EXPERIMENTAL INVESTIGATION OF THE SAND-STABILIZATION POTENTIAL OF A PLANT-DERIVED BIO-MASS

by

PAUL ANDREW BARTLEY

B.S., Kansas State University, 2009

A THESIS

submitted in partial fulfillment of the requirements for the degree

MASTER OF SCIENCE

Department of Civil Engineering
College of Engineering

KANSAS STATE UNIVERSITY
Manhattan, Kansas

2011

Approved by:

Major Professor
Dr. Dunja Perić

Abstract

The main objective of this study was to experimentally investigate the Mohr-Coulomb strength parameters of masonry sand mixed with varying amounts of water and lignin. Lignin is a plant-derived biomass, which is a co-product of bio-fuel production. It exhibits binding qualities when mixed with water thus making it an ideal candidate for sustainable non-traditional sand stabilization.

An experimental program was devised and carried out to quantify the compaction and early age stress-strain and dilatancy responses of sand-lignin mixes. The program included sieve analysis, Atterberg limit tests, standard Proctor tests, and direct shear tests. The experimental results were used to find the cohesion and the angle of internal friction of the tested material, therefore determining the influence of the amount of lignin and water on the strength of the samples. An extensive data analysis was subsequently completed to gain deeper understanding of the underlying strength gain mechanism.

It was found that the normalized cohesion benefit due to lignin is controlled by two variables; water to lignin ratio and void ratio. The lignin and water create a paste, which provides particle bonding at the contacts of sand particles, thus increasing the stress-bearing cross sectional area. Increase in the portion of cross-sectional area occupied by water and lignin normalized by gravimetric lignin content, increases the normalized cohesion up to a point, while the cohesion per gravimetric lignin content decreases with the increasing area ratio. This in turn indicates that cohesion increases only up to 6% of lignin, beyond which it starts to decrease due to the presence of too much fine material within the pores. The presence of lignin in the pores consistently decreases the angle of internal friction. However, for all configurations with lignin tested herein, cohesion was larger than for dry sand, thus indicating strength benefits at low confining pressures or at normal stresses below the so-called limiting normal stress.

Table of Contents

List of Figures vi
List of Tables xiii
Acknowledgements xiv
Chapter 1 - Introduction 1
1.1 Scope of Work 2
Chapter 2 - Background 4
2.1 History 4
2.2 Production 5
2.3 Environmental Impact 8
2.4 Recent Work 8
2.4.1 Federal Highway Administration Wildlife Refuge Studies 8
2.4.2 Iowa State University 13
2.4.2 U.S. Army Engineer Research and Development Center 13
Chapter 3 - Material Properties 14
3.1 Sand Description 14
3.2 Lignin Description 15
3.3 Water Description 15
3.4 Phase Relationships 15
3.5 Basic Definitions 18
3.5.1 Volume Relationships 18
3.5.2 Mass Relationships 19
3.5.3 Mass-Volume Relationships 20
3.5.4 Derived Relationships 22
3.6 Proctor Tests 23
3.6.1 Standard Proctor Test Procedure 23
3.6.2 Standard Proctor Test Results 23
3.7 Atterberg Limit Tests 29
Chapter 4 - Experimental Equipment, Techniques, and Program 31

4.1 Direct Shear Test Apparatus 31
4.1.1 Shear Box 34
4.1.2 Linear Variable Displacement Transducers 34
4.1.3 “S” Type Load Cell 35
4.1.4 Digital Input/Drive Unit Housing 36
4.1.4 Autonomous Data Acquisition Unit (ADU) 37
4.1.5 Loading Assembly 37
4.1.6 Carriage Assembly 39
4.1.7 DataSystem 7 Geotechnical Software 41
4.2 Direct Shear Test Procedure 41
4.2.1 Direct Shear Test Program 41
4.2.2 Test Specimen Preparation 42
4.2.3 Direct Shear Apparatus Preparation 49
4.2.4 Direct Shear Apparatus Test Procedure 50
4.2.5 Consolidation Stage 50
4.2.6 Shear Stage 50
4.2.7 Final Measurements 51
Chapter 5 - Experimental Results 52
5.1 Direct Shear Test Results 52
5.1.1 Gravimetric Lignin Content (0%) 53
5.1.2 Gravimetric Lignin Content (2%) 56
5.1.3 Gravimetric Lignin Content (9%) 61
5.1.4 Gravimetric Lignin Content (14%) 66
5.2 Information about Direct Shear Specimens 72
5.2.1 Water Content Data 72
5.2.2 Updated Void Ratios 76
5.2.3 Specimen Photographs 78
Chapter 6 - Analysis and Discussion 82
6.1 Determination of Mohr-Coulomb’s Strength Parameters 82
6.2 Further Analysis 87
Chapter 7 - Conclusions and Recommendations 138

7.1 Conclusions 138
7.2 Recommendations 140
References 141
Appendix A - Additional Direct Shear Testing Results 144
A.1.1 Gravimetric Lignin Content (4%) 144
A.1.2 Gravimetric Lignin Content (6%) 149
Appendix B - Additional Direct Shear Analysis Plots 154
B.1.1 Analysis Plots for Determination of c and Φ 154

List of Figures

Figure 2-1: Paper Pulping and Lignin Production Process 7
Figure 2-2: Spray application of Lignin product to bladed surface. 10
Figure 2-3: Blending of borrow material with lignin product 10
Figure 2-4: Rolling and compaction of blended material surface. 11
Figure 2-5: Application of Lignin-based product at Seedskadee National Wildlife Refuge. 12
Figure 3-1: Grain size distribution curve of masonry sand 14
Figure 3-2: Phase diagram showing separate constituents 16
Figure 3-3: Phase diagram showing lignin and water as a single constituent 16
Figure 3-4: Phase diagram showing various degrees of saturation and masses 17
Figure 3-5: Summary of Standard Proctor Tests 24
Figure 3-6: Summary of Standard Proctor Tests showing $\rho_{d,s+l}$ 25
Figure 3-7: Standard Proctor Test for χ_l = 0% 26
Figure 3-8: Standard Proctor Test for χ_l = 2% 26
Figure 3-9: Standard Proctor Test for χ_l = 4% 27
Figure 3-10: Standard Proctor Test for χ_l = 6% 27
Figure 3-11: Standard Proctor Test for χ_l = 9% 28
Figure 3-12: Standard Proctor Test for χ_l = 14% 28
Figure 3-13: Liquid Limit Test Summary 29
Figure 3-14: Liquid Limit versus Gravimetric Lignin Content 30
Figure 4-1: Photograph of Shear Box Components 34
Figure 4-2: Photograph of Linear Variable Displacement Transducers 35
Figure 4-3: Photograph of “S” Type Load Cell 36
Figure 4-4: Photograph of Digital Input Box 36
Figure 4-5: Photograph of Autonomous Data Acquisition Unit 37
Figure 4-6: Schematic of Direct Shear Apparatus Load Frame [ELE, 2006] 38
Figure 4-7: Plot of vertical force vs. deflection of frame. 39
Figure 4-8: Schematic of Shear Box Carriage Assembly [ELE, 2006] 40
Figure 4-9: Summary of Direct Shear Sample Configurations 43

Figure 4-10: Example of planned position of points A, B, C, D, E (No scale). 44
Figure 4-11: Phase Diagram for χ_l = 0%..... 46
Figure 4-12: Phase Diagram for χ_l = 2%..... 46
Figure 4-13: Phase Diagram for χ_l = 4%..... 47
Figure 4-14: Phase Diagram for χ_l = 6%..... 47
Figure 4-15: Phase Diagram for χ_l = 9%..... 48
Figure 4-16: Phase Diagram for χ_l = 14%..... 48
Figure 4-17: Photograph of Shear Box Placed into Carriage 49
Figure 5-1: Shear Stress vs. Horizontal Displacement, χ_l = 0% (A)..... 53
Figure 5-2: Change in Thickness vs. Horizontal Displacement, χ_l = 0% (A)..... 53
Figure 5-3: Shear Stress vs. Horizontal Displacement, χ_l = 0% (E) 54
Figure 5-4: Change in Thickness vs. Horizontal Displacement, χ_l = 0% (E) 54
Figure 5-5: Shear Stress vs. Horizontal Displacement, χ_l = 0% (C)..... 55
Figure 5-6: Change in Thickness vs. Horizontal Displacement, χ_l = 0% (C) 55
Figure 5-7: Shear Stress vs. Horizontal Displacement, χ_l = 2% (A)..... 56
Figure 5-8: Change in Thickness vs. Horizontal Displacement, χ_l = 2% (A)..... 56
Figure 5-9: Shear Stress vs. Horizontal Displacement, χ_l = 2% (E) 57
Figure 5-10: Change in Thickness vs. Horizontal Displacement, χ_l = 2% (E) 57
Figure 5-11: Shear Stress vs. Horizontal Displacement, χ_l = 2% (C)..... 58
Figure 5-12: Change in Thickness vs. Horizontal Displacement, χ_l = 2% (C) 58
Figure 5-13: Shear Stress vs. Horizontal Displacement, χ_l = 2% (D)..... 59
Figure 5-14: Change in Thickness vs. Horizontal Displacement, χ_l = 2% (D)..... 59
Figure 5-15: Shear Stress vs. Horizontal Displacement, χ_l = 2% (B)..... 60
Figure 5-16: Change in Thickness vs. Horizontal Displacement, χ_l = 2% (B) 60
Figure 5-17: Shear Stress vs. Horizontal Displacement, χ_l = 9% (A)..... 61
Figure 5-18: Change in Thickness vs. Horizontal Displacement, χ_l = 9% (A)..... 61
Figure 5-19: Shear Stress vs. Horizontal Displacement, χ_l = 9% (E) 62
Figure 5-20: Change in Thickness vs. Horizontal Displacement, χ_l = 9% (E) 62
Figure 5-21: Shear Stress vs. Horizontal Displacement s, χ_l = 9% (C) 63
Figure 5-22: Change in Thickness vs. Horizontal Displacement, χ_l = 9% (C) 63
Figure 5-23: Shear Stress vs. Horizontal Displacement, χ_l = 9% (D)..... 64

Figure 5-24: Change in Thickness vs. Horizontal Displacement, χ_l = 9% (D) 64
Figure 5-25: Shear Stress vs. Horizontal Displacement, χ_l = 9% (B) 65
Figure 5-26: Change in Thickness vs. Horizontal Displacement, χ_l = 9% (B) 65
Figure 5-27: Shear Stress vs. Horizontal Displacement, χ_l = 14% (A) 66
Figure 5-28: Change in Thickness vs. Horizontal Displacement, χ_l = 14% (A) 66
Figure 5-29: Shear Stress vs. Horizontal Displacement, χ_l = 14% (E) 67
Figure 5-30: Change in Thickness vs. Horizontal Displacement, χ_l = 14% (E) 67
Figure 5-31: Shear Stress vs. Horizontal Displacement, χ_l = 14% (C) 68
Figure 5-32: Change in Thickness vs. Horizontal Displacement, χ_l = 14% (C) 68
Figure 5-33: Shear Stress vs. Horizontal Displacement, χ_l = 14% (D) 69
Figure 5-34: Change in Thickness vs. Horizontal Displacement, χ_l = 14% (D) 69
Figure 5-35: Shear Stress vs. Horizontal Displacement, χ_l = 14% (B) 70
Figure 5-36: Change in Thickness vs. Horizontal Displacement, χ_l = 14% (B) 70
Figure 5-37: Updated phase diagram for χ_l = 0% 73
Figure 5-38: Updated phase diagram for χ_l = 2% 73
Figure 5-39: Updated phase diagram for χ_l = 4% 74
Figure 5-40: Updated phase diagram for χ_l = 6% 74
Figure 5-41: Updated phase diagram for χ_l = 9% 75
Figure 5-42: Updated phase diagram for χ_l = 14% 75
Figure 5-43: Magnified Image of χ_l = 0%, w = 0% (dry sand) 78
Figure 5-44: Magnified Image of χ_l = 0%, w = 4% (moist sand) 79
Figure 5-45: Magnified Image of χ_l = 2% 79
Figure 5-46: Magnified Image of χ_l = 4% 79
Figure 5-47: Magnified Image of χ_l = 6% 80
Figure 5-48: Magnified Image of χ_l = 9% 80
Figure 5-49: Magnified Image of χ_l = 14% 80
Figure 6-1: Peak Shear Stress vs. Normal Stress for χ_l = 9% (A) 83
Figure 6-2: Peak Shear Stress vs. Normal Stress for χ_l = 9% (E) 83
Figure 6-3: Peak Shear Stress vs. Normal Stress for χ_l = 9% (C) 84
Figure 6-4: Peak Shear Stress vs. Normal Stress for χ_l = 9% (D) 84
Figure 6-5: Peak Shear Stress vs. Normal Stress for χ_l = 9% (B) 85

Figure 6-6: Summary of Cohesion for All Configurations 86
Figure 6-7: Summary of Angle of Friction for All Configurations 87
Figure 6-8: Schematic depicting load-bearing cross-sectional area 91
Figure 6-9: Plot Depicting Limit Stress of Sand-Lignin-Water Mixture 92
Figure 6-10: Normalized Limit Stress vs. Gravimetric Lignin Content (All pts.; power) 93
Figure 6-11: Normalized Limit Stress vs. Gravimetric Lignin Content (All pts.; log) 93
Figure 6-12: Stress in Lignin+Water vs. Area Ratio (All pts.) 94
Figure 6-13: Stress in Lignin+Water vs. Area Ratio (All pts.) 94
Figure 6-14: Normalized Cohesion vs. Normalized Area Ratio (All pts.) 96
Figure 6-15: Normalized Cohesion vs. Normalized Area Ratio (w/o 2%) 96
Figure 6-16: Normalized Cohesion vs. Normalized Area Ratio (w/o 2A, 2E, 2C, 2D) 97
Figure 6-17: Normalized Cohesion vs. Normalized Area Ratio (2%) 97
Figure 6-18: Normalized Cohesion vs. Normalized Area Ratio (4%) 98
Figure 6-19: Normalized Cohesion vs. Normalized Area Ratio (6%) 98
Figure 6-20: Normalized Cohesion vs. Normalized Area Ratio (9%) 99
Figure 6-21: Normalized Cohesion vs. Normalized Area Ratio (14%) 99
Figure 6-22: Normalized Cohesion vs. Normalized Area Ratio (4 and 6%) 100
Figure 6-23: Normalized Cohesion vs. Normalized Area Ratio (6 and 9%) 101
Figure 6-24: Normalized Cohesion vs. Normalized Area Ratio (9 and 14%) 101
Figure 6-25: Normalized Cohesion vs. Normalized Area Ratio (4, 6, 9%) 102
Figure 6-26: Normalized Cohesion vs. Normalized Area Ratio (6, 9, 14%) 102
Figure 6-27: Normalized Cohesion vs. Normalized Area Ratio (4, 6, 9, 14%) 103
Figure 6-28: Normalized Cohesion vs. Normalized Area Ratio (All pts., A) 104
Figure 6-29: Normalized Cohesion vs. Normalized Area Ratio (4, 6, 9, 14%, A) 105
Figure 6-30: Normalized Cohesion vs. Normalized Area Ratio (All pts., E) 105
Figure 6-31: Normalized Cohesion vs. Normalized Area Ratio (4, 6, 9, 14%, E) 106
Figure 6-32: Normalized Cohesion vs. Normalized Area Ratio (All pts., C) 106
Figure 6-33: Normalized Cohesion vs. Normalized Area Ratio (4, 6, 9, 14%, C) 107
Figure 6-34: Normalized Cohesion vs. Normalized Area Ratio (All pts.; D, E, B) 108
Figure 6-35: Normalized Cohesion vs. Normalized Area Ratio (D, E, B, w/o 2D, 2E) 108
Figure 6-36: Normalized Cohesion vs. Normalized Area Ratio (4 and 6%; D, E, B) 109

Figure 6-37: Normalized Cohesion vs. Normalized Area Ratio (6 and 9%; D, E, B) 109
Figure 6-38: Normalized Cohesion vs. Normalized Area Ratio (9 and 14%; D, E, B) 110
Figure 6-39: Normalized Cohesion vs. Normalized Area Ratio (4, 6, 9%; D, E, B) 110
Figure 6-40: Normalized Cohesion vs. Normalized Area Ratio (6, 9, 14%; D, E, B) 111
Figure 6-41: Normalized Cohesion vs. Area Ratio (All pts.) 112
Figure 6-42: Normalized Cohesion vs. Area Ratio (4, 6, and 9%) 113
Figure 6-43: Cohesion Normalized to Area Ratio vs. Area Ratio (All pts.) 114
Figure 6-44: Normalized Area Ratio vs. Water to Lignin Ratio (All pts.) 116
Figure 6-45: Normalized Area Ratio vs. Water Content (All pts. 116
Figure 6-46: Normalized Area Ratio vs. Void Ratio (All pts.) 117
Figure 6-47: Normalized Area Ratio vs. Gravimetric Lignin Content (All pts.) 117
Figure 6-48: Angle of Friction vs. Gravimetric Lignin Content (All pts.) 119
Figure 6-49: Angle of Friction vs. Gravimetric Lignin Content (All pts.) 120
Figure 6-50: Angle of Friction vs. Area Ratio (All pts., individual) 121
Figure 6-51: Angle of Friction vs. Area Ratio (All pts.) 121
Figure 6-52: Tangent of Friction Angle vs. Normalized Area Ratio (All pts.) 122
Figure 6-53: Cohesion vs. Gravimetric Lignin Content (All pts.) 123
Figure 6-54: Cohesion vs. Gravimetric Lignin Content (All pts.) 124
Figure 6-55: Cohesion vs. Area Ratio (All pts.) 125
Figure 6-56: Cohesion vs. Area Ratio (All pts.) 125
Figure 6-57: Normalized Cohesion vs. Normalized Area Ratio (Select pts., w/o 9B) 128
Figure 6-58: Normalized Cohesion vs. Normalized Area Ratio (Select pts., 4, 6, 9% w/o 9B) 128
Figure 6-59: Cohesion vs. Gravimetric Lignin Content (Select pts.) 129
Figure 6-60: Cohesion vs. Gravimetric Lignin Content (Select pts.) 130
Figure 6-61: Cohesion vs. Area Ratio (Select pts.) 131
Figure 6-62: Cohesion vs. Area Ratio (Select pts.) 131
Figure 6-63: Angle of Friction vs. Gravimetric Lignin Content (Select pts.) 132
Figure 6-64: Angle of Friction vs. Gravimetric Lignin Content (Select pts.) 133
Figure 6-65: Angle of Friction vs. Area Ratio (Select pts.) 134
Figure 6-66: Angle of Friction vs. Area Ratio (Select pts.) 134
Figure 6-67: Normalized Cohesion vs. Normalized Area Ratio (Select pts., 6 & 9% w/o 9B) 135

Figure 6-68: Normalized Cohesion vs. Normalized Area Ratio (Select pts., DEB, w/o 9B) 135
Figure 6-69: Normalized Cohesion vs. Normalized Area Ratio (Select pts., DEB, w/o 9B) 136
Figure 6-70: Tangent of Friction Angle vs. Normalized Area Ratio (Select pts.) 136
Figure A-1: Shear Stress vs. Horizontal Displacement, χ_l = 4% (A) 144
Figure A-2: Change in Thickness vs. Horizontal Displacement, χ_l = 4% (A) 144
Figure A-3: Shear Stress vs. Horizontal Displacement, χ_l = 4% (E) 145
Figure A-4: Change in Thickness vs. Horizontal Displacement, χ_l = 4% (E) 145
Figure A-5: Shear Stress vs. Horizontal Displacement, χ_l = 4% (C) 146
Figure A-6: Change in Thickness vs. Horizontal Displacement, χ_l = 4% (C) 146
Figure A-7: Shear Stress vs. Horizontal Displacement, χ_l = 4% (D) 147
Figure A-8: Change in Thickness vs. Horizontal Displacement, χ_l = 4% (D) 147
Figure A-9: Shear Stress vs. Horizontal Displacement, χ_l = 4% (B) 148
Figure A-10: Change in Thickness vs. Horizontal Displacement, χ_l = 4% (B) 148
Figure A-11: Shear Stress vs. Horizontal Displacement, χ_l = 6% (A) 149
Figure A-12: Change in Thickness vs. Horizontal Displacement, χ_l = 6% (A) 149
Figure A-13: Shear Stress vs. Horizontal Displacement, χ_l = 6% (E) 150
Figure A-14: Change in Thickness vs. Horizontal Displacement, χ_l = 6% (E) 150
Figure A-15: Shear Stress vs. Horizontal Displacement, χ_l = 6% (C) 151
Figure A-16: Change in Thickness vs. Horizontal Displacement, χ_l = 6% (C) 151
Figure A-17: Shear Stress, vs. Horizontal Displacement, χ_l = 6% (D) 152
Figure A-18: Change in Thickness vs. Horizontal Displacement, χ_l = 6% (D) 152
Figure A-19: Shear Stress vs. Horizontal Displacement, χ_l = 6% (B) 153
Figure A-20: Change in Thickness vs. Horizontal Displacement, χ_l = 6% (B) 153
Figure B-1: Plot of Normal Stress v. Peak Stress for χ_l = 0% (A 154
Figure B-2: Plot of Normal Stress v. Peak Stress for χ_l = 0% (E) 155
Figure B-5: Plot of Normal Stress v. Peak Stress for χ_l = 2% (E) 156
Figure B-6: Plot of Normal Stress v. Peak Stress for χ_l = 2% (C) 157
Figure B-7: Plot of Normal Stress v. Peak Stress for χ_l = 2% (D) 157
Figure B-8: Plot of Normal Stress v. Peak Stress for χ_l = 2% (B) 158
Figure B-9: Plot of Normal Stress v. Peak Stress for χ_l = 4% (A) 158
Figure B-10: Plot of Normal Stress v. Peak Stress for χ_l = 4% (E) 159

Figure B-11: Plot of Normal Stress v. Peak Stress for χ_I = 4% (C) 159
Figure B-12: Plot of Normal Stress v. Peak Stress for χ_I = 4% (D) 160
Figure B-13: Plot of Normal Stress v. Peak Stress for χ_I = 4% (B) 160
Figure B-14: Plot of Normal Stress v. Peak Stress for χ_I = 6% (A) 161
Figure B-15 Plot of Normal Stress v. Peak Stress for χ_I = 6% (E) 161
Figure B-16: Plot of Normal Stress v. Peak Stress for χ_I = 6% (C) 162
Figure B-17: Plot of Normal Stress v. Peak Stress for χ_I = 6% (D) 162
Figure B-18: Plot of Normal Stress v. Peak Stress for χ_I = 6% (B) 163
Figure B-19: Plot of Normal Stress v. Peak Stress for χ_I = 14% (A) 163
Figure B-22: Plot of Normal Stress v. Peak Stress for χ_I = 14% (D) 165
Figure B-23: Plot of Normal Stress v. Peak Stress for χ_I = 14% (B) 165

List of Tables

Table 4-1: Direct Shear Apparatus Specifications and Dimensions [ELE, 2006] 33
Table 4-2: Description of Direct Shear Sample Configurations 43
Table 4-3: Planned Direct Shear Test Program 45
Table 5-1: Actual water contents for direct shear tests. 72
Table 5-2: Change in height and void ratios for all configurations 77
Table 6-1: Values of Cohesion and Angle of Friction for All Test Points 82
Table 6-2: Rankings of R^2 values for individual configurations 100
Table 6-3: Rankings of R^2 values for different combinations of configurations 103
Table 6-4: Rankings of R2 values for configurations A, E, and C plots 107
Table 6-5: Rankings of R^2 values for configurations D, E, B combinations 111
Table 6-6: Calculation of Amount of Fines in Sand-Lignin-Water Mix 127

Acknowledgements

This thesis would not have been possible without the gracious contributions and support of many talented and caring individuals. For all of the encouraging, thoughtful and constructive words, and the assistance with tasks both small and large, I must give thanks and acknowledge the following individuals and groups.

I would like to begin by thanking the faculty and staff in the Department of Civil Engineering at Kansas State University. I am thankful to the faculty for many acts of guidance over the years; notably Dr. Yacoub Najjar and Dr. Robert Stokes for being part of my Supervisory Committee. In addition, I want to thank Danita Deters and Peggy Selvidge in the Civil Engineering office for their invaluable knowledge and help during my time at Kansas State. Every one of my questions, whether about payroll or figuring out which form needed to be submitted next, was met with a quick and informed answer that solved the issue immediately.

I would like to thank the University Transportation Center and its director, Dr. Robert Stokes, for providing me with funding for my education through scholarships. Kansas State University is fortunate to have such a program. My graduate education would not have been possible without it.

Roland Taft and Mike Schoenherr from Borregaard Lignotech also deserve thanks for contributing a generous supply of lignin for testing and a wealth of knowledge concerning their product. Dr. Mbaki Onyango is due thanks for her investigation involving this material and for establishing some testing parameters that I was able to work with. I also thank Dr. Lawrence Davis from the Department of Biochemistry at Kansas State for similar contributions.

I would also like to express my gratitude to my colleagues, Mr. Hakan Yasarer and Mr. Wilson Smith. Hakan and Wilson have provided me with an amount of help and support that is impossible to quantify. In addition to academic work, I have come to regard them as great friends as well.

I thank my advisor, Dr. Dunja Perić, for all she has done during the course of my graduate work. I thank her for keeping me on task and challenging me to always be persistent in investigating the work one step further so that my thesis is something that I am truly proud of. The countless hours she has dedicated to me to teach and guide me during this time could never

be repaid. I always appreciated knowing that she would make time to answer my questions, sometimes from halfway around the world. Her dedication to her job is second to none and I hope to take that influence into my career.

Finally, I owe the biggest debt of gratitude to my family. Graduate school is a frequently frustrating and stressful experience and I couldn't imagine getting through it without them. They have put up with me in a way that only family can. To my brothers, Ross and Eric, I thank them for keeping me grounded at all times and not allowing me to take anything too seriously. To my parents, I thank them for supporting me and helping me out with any issue imaginable as well as instilling the drive to never give up. Without their encouragement and perspective, it is certain that I would not be where I am today.

Chapter 1 - Introduction

It is the inherent instability of dry sands at low confining pressures that necessitates maintenance of unpaved roads, which often serve as the main transportation lifelines in rural areas. In Kansas alone there are more than 98,000 miles of unpaved gravel roads, which comprises about 72.5 % of the total road mileage in the state and accounts for about 10% of annual vehicle miles traveled [Dissanayake, *et al.*, 2009]. Sloped embankments, which are highly susceptible to erosion and require occasional maintenance, can also be found along most roadways.

Traditional methods of stabilizing soils to improve strength and durability of unpaved roadways have included the use of cement, lime, fly ash, and asphalt emulsion [Newman, *et al.*, 2004]. Although these materials are relatively inexpensive and easy to apply, they require intensive industrial processes to manufacture and have not been found to be of substantial benefit to silty, sandy soil types [Newman, *et al.*, 2004]. Recently, a variety of non-traditional soil stabilization additives from commercial sectors have proved viable such as polymer emulsions, acids, lignosulfonate derivatives, enzymes, tree resin emulsions, and silicates [Newman, *et al.*, 2004]. Other recent studies have investigated the use of alternative materials, such as a rapidly renewable resource like compost, for prevention of erosion of sandy and silty soils [Reddi, *et al.*, 2010].

Lignin is an essential component of all primary plant life that bonds the cellulose fibers together in plant cell walls, whereby the later provide the tensile strength. Lignin is the second most abundant biological material on the planet, exceeded only by cellulose and hemicellulose and comprising 15-25% of the dry weight of woody plants [Ragauskas, 2011]. Though lignin has long been known as a co-product of the paper industry, it has only recently become a co-product of the biofuel industry. The most common use of lignin today is as a dust palliative, however in the future lignin could prove to be an effective and sustainable method for preventing slope erosion and possibly as a stabilizer for paved road beds and slopes. The importance of lignin could also increase substantially in the future due to its status as a highly sustainable and rapidly renewable material. The sustainability of soil additives is an increasing topic of relevance. For example, the production of cement, a common soil additive, accounts for approximately 5% of

man-made carbon dioxide emissions to the atmosphere, making it a major contributor to global greenhouse gas emissions [DCN Digital Media, 2011].

Consequently, it is of a particular interest to assess the increase in cohesion and any accompanying changes in friction of soil-lignin mixes in comparison to dry sands. To this end the first phase of this research, where the main goal was assessing strength benefits of sand-lignin mixes immediately upon mixing, has been completed. This will provide baseline values for a future study, whose goal will be to assess the strength benefits after different periods of air drying. During the testing program visual and tactile observations indicated that the sand-lignin mixtures rapidly gained stiffness and strength due to air drying. A quantitative assessment of these gains is presently being carried out and will be the subject of another M.S. thesis.

1.1 Scope of Work

The scope of the work for this study includes the following:

1. A background investigation of lignin.
2. The preliminary material characterization.
3. The direct shear testing.
4. Analysis of direct shear test results.
5. Conclusions & Recommendations

The background investigation consisted of reviewing sources of information about lignin's history, production, usage and previous research studies. While lignin has long been a marketed product, it has primarily been used for small, specific uses. As a result, most information collected is produced by lignin manufacturers or as a portion of a larger piece about wood pulping and paper production. A limited amount of case studies were found as part of the background investigation and are reported on in Chapter 2.

The preliminary characterization of materials was performed by means of sieve analysis, standard Proctor testing, and Atterberg limits tests. The strength characterization was carried out by direct shear testing. The sieve analysis was conducted on the oven-dried, masonry sand obtained from Midwest Concrete Materials in Manhattan, KS, and was used in all tests herein. Standard Proctor tests were conducted on six different combination of sand and gravimetric lignin content; 0, 2, 4, 6, 9, and 14%. The results of the Proctor tests provided a basis for

planning of the direct shear testing program. Atterberg limit tests were performed, where possible, to determine whether the sand-lignin mixes exhibited any clay-like behavior.

The direct shear tests were conducted on the six gravimetric lignin contents. The samples containing lignin were tested at five different configurations, while tests on sand alone were performed at only three different configurations. All samples were tested at five different normal stresses for a total of 140 tests. The samples were thoroughly mixed individually before each direct shear test in a bowl, carefully placed in the direct shear box, compacted to a predetermined value of relative compaction and then mounted inside the apparatus. Moisture contents were determined by placing portions of the mixed sample in the oven for drying before direct shear tests. Additionally, portions of direct shear samples were placed in the oven upon the completion of tests for direct determination of moisture contents at the end of tests.

The cohesion and angle of friction were determined based on the measured peak shear stress. The results of direct shear tests were subjected to further extensive analysis in order to qualitatively and quantitatively assess the mechanism of the cohesion gain and accompanying changes in friction.

Chapter 2 - Background

Lignin is a part of plant biomass where it forms a bio-composite together with cellulose fibers. While the fibers provide primarily tensile-strength, the lignin bonds the fibers together. A widely available and abundant material, lignin is traditionally extracted from wood by the pulping process necessary to create paper. Lignin used in this study is also known as calcium lignosulfonate. More recently, lignin has also been extracted as a co-product of bio-fuel production. Lignin has been produced and marketed for several decades, mostly as a niche product without a broad industrial use. As an environmentally friendly, highly sustainable resource that is widely available, it seems like only a matter of time before lignin is utilized for a larger purpose.

2.1 History

Lignin was first discovered by Anselme Payen in 1838. He discovered that treatment of wood with nitric acid and an alkaline solution yielded an insoluble residue he referred to as "cellulose" and dissolved incrustants [Wang, 2011]. It wasn't until later, in 1865, that Schulze designated these incrustants as lignin, a term derived from the Latin word "lignum" meaning "wood" that was coined by the Swiss botanist Augustin Pyramus de Candolle in 1819 [Glasser, 2000]. Extensive work has been done following the initial experiments of Payen to find ways to selectively stabilize lignins with either sulfurous acid or alkaline solutions in order to separate useful cellulose fibers [Glasser, 2000]. In the years that followed until now, a myriad of research papers have been produced in the field of organic chemistry leading to the discovery and fundamental knowledge of the chemical structure of lignin.

Lignin has been used to suppress dust emissions from unpaved roads in America and Europe since the 1920's [Calbinder, 2001]. Dust emissions are a concern for several reasons. Dust can carry unwanted chemicals and other irritants into the eyes and lungs of humans as well as animals. Dust can also obstruct visibility on roads, particularly near construction sites, and cause accidents [Muckel, 2004]. Initially, raw lignin solutions (liquor) were taken from pulp mills and sprayed on unpaved roads to suppress dust [Glasser, 2000]. This practice was validated when research showed that lignosulfonates bind soil particles together and draw air from the atmosphere (i.e. hydroscopic) to maintain a measure of moistness in unpaved roads,

therefore reducing dust generation. It has also been established that lignosulfonates applied at a higher rate and deeper mixing level can be used to stabilize subgrade or base materials containing fine particles, providing a firm, mostly dust-free surface [Kestler, 2009]. Lignin is also widely used for stabilization of parking lots, driveways and road shoulders, as a more economical alternative to pavement [Reed]. It should be noted, however, that while lignin has been extensively used for several decades, little research has been done concerning the strength and stability of sand-lignin mixtures.

The use of lignin has not been limited to roadway applications. As far back as the 1880s lignin was used in leather tanning and dye baths [ILI, 2000]. Lignins have been used in food products, used as emulsifiers in animal feed and as a raw material in the production of vanillin, a widely used ingredient in food flavor, in pharmaceuticals and a fragrance in perfumes and odor-masking products. The adhesive, "glue"–like property of lignin has made the material a useful component in the making of charcoal briquettes, ceramics, linoleum paste, plywood and particle board.

2.2 Production

Lignin is produced as a by-product of wood pulping, produced by two different methods; sulfate (also known as kraft) and sulfite pulping. The primary difference between the two types is in the chemicals used in the process. The chemicals are used to dissolve the lignin, which makes up approximately 20-35 percent of the wood, to create pulp and liquor [Brady, *et al.*, 1998]. After the "digestion" stage, "washing" is directed to recover the liquor containing the lignin. Washing removes the weaker black liquor from the pulp which is sent to the chemical recovery process. Dilute liquor is treated and concentrated to 50-60% solids by evaporating water. From this base material, the products known as lignins and lignosulfonates are produced [Ragauskas, 2011]. Figure 2-1 shows the pulp process in more detail.

Recently, an interest in using biomass as a source of lignin has significantly increased. Agricultural biomass conversion to produce biofuels, such as ethanol, has been a rising trend in the industry. A major source of biomass, for cellulosic ethanol in particular, is corn stover, the residue of corn harvesting. It is estimated that approximately 75 million dry tons of corn stover are produced annually [Fox, 2006], which would go to waste since there is no other practical

industrial use for the product. Of this amount it is estimated that 11.4% of the content contains lignin, therefore corn stover could provide 8.5 million tons of lignin a year [Fox, 2006].

Similar to wood pulping, chemicals are used to separate lignin from biomass. A weak mineral acid is used to pretreat the biomass then the carbohydrate is depolymerized and extracted by either continuing acid hydrolysis or by enzymatic treatment. In a second process known as steam explosion, the biomass is briefly subjected to high pressure and temperature (200-250°C) before being rapidly released to atmospheric conditions. The lignin can be extracted by aqueous alkaline solvents [Fox, 2006].

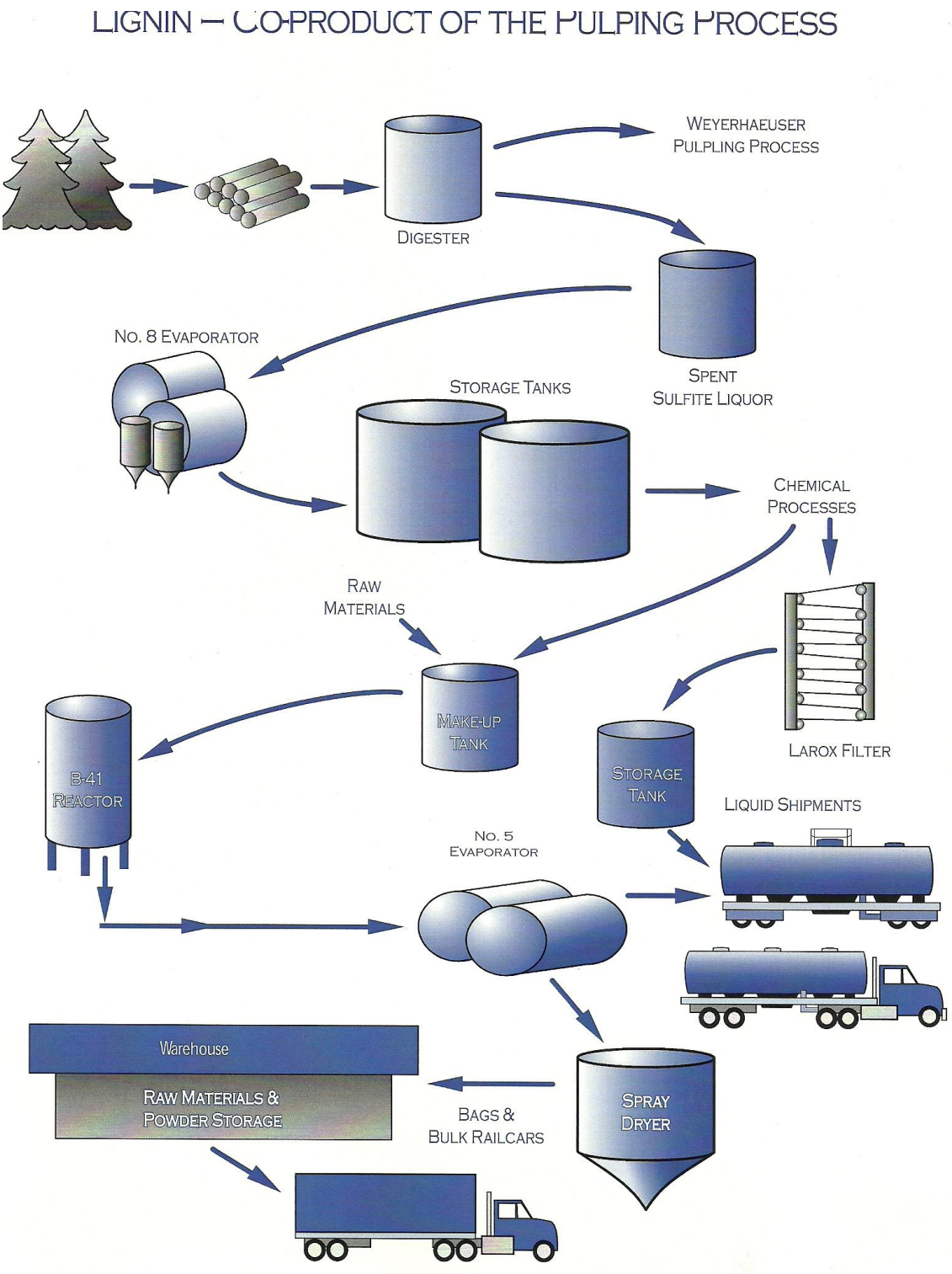

Figure 2-1: Paper Pulping and Lignin Production Process [source: Lignotech Brochure]

2.3 Environmental Impact

The impact on the environment from applying lignosulfonates has been found to be negligible [Adams, 1988]. Lignin has been applied to roads, used as an ingredient in animal feeds, and even used in many human foods for decades without incident. There is no presence of dioxins (toxic chemicals acquired from paper bleaching processes) or any other organics present at hazardous levels in lignin. Lignin is non-toxic to animals, however minor irritation could occur if exposed to eyes or directly to skin due to its extremely small particle size. Data indicates that there is minimal risk of groundwater contamination at concentrations of less than 10 kg per square meter [Stepanian and Shea, 1986].

The effects of corrosion from lignin have considerably smaller consequence than those of other chemical treatments typically used for dust suppression such as calcium chloride or magnesium chloride [Adams, 1988]. Because of the nature of their bonding mechanism, lignins mix with soils to form cohesive bonds. Therefore lignin, as a treatment, is not as easily transferable as, for example, calcium chloride, where the chemical is loosely concentrated on the surface and is more readily passed to automobiles.

2.4 Recent Work

While work concerning lignin as a sustainable additive to road building materials has been limited, the studies recently completed have shown that it is effective. The following briefly summarizes two successful field studies and some laboratory investigations.

2.4.1 Federal Highway Administration Wildlife Refuge Studies

The Federal Highway Administration (FHWA) has recently taken some interest in investigating the potential of lignin as an unpaved road surface stabilizer. Citing the problems of dust generation from road user traffic and overall difficulty of maintenance for unpaved roads, the FHWA has funded two studies to broaden the knowledge about dust control products. Lignin was compared to several other products. The first study took place at Buenos Aires National Wildlife Refuge in south-central Arizona in October 2005, while the Seedskadee National Wildlife Refuge in southwestern Wyoming was the location of the second study, which took place in September 2008.

In the first study, at Buenos Aires National Wildlife Refuge [Surdahl, *et al*, 2005], six different road stabilizer and dust-suppression products were applied to a surface course comprised of borrow material classified as poorly graded sand by AASHTO and ASTM classification standards. The duration of the study was 24 months. The intention of the study was to evaluate the six products for long-term performance. The investigation sought to rate each product performance in dust control, rutting, washboarding, raveling and soil stabilization over a 24-month period. Of the six products, two were lignin based; a magnesium/lignosulfonate mixture and a lignosulfonate product. The performance of the materials was monitored at 6-month intervals for 2 years starting after the first 6 months following application.

All products were applied to a depth of 6 inches in windrows; blade mixed, and then compacted with a 9.4 Mg (12-ton) 9-wheel pneumatic roller. The application of the lignin-based products was done by blading off 3 inches of top material and windrowed to the side of the road. The product was then applied to the bladed surface in two passes, with the 3 inches of bladed material replaced following application. The products were then applied again to the top surface of the replaced material in three passes, followed by additional blading for leveling. Finally, the material was compacted with a 9-wheel pneumatic roller [Surdahl, *et al*, 2005]. The process can be seen in Figures 2-2 through 2-4 below.

Figure 2-2: Spray application of Lignin product to bladed surface [source: Surdahl *et al*, 2005].

Figure 2-3: Blending of borrow material with lignin product [source: Surdahl *et al*, 2005]

.

Figure 2-4: Rolling and compaction of blended material surface [source: Surdahl *et al*, 2005].

The monitoring consisted of visual inspection, Dynamic Cone Penetrometer tests, silt load evaluations, nuclear density gauge readings, and GeoGage Soil Stiffness tests. Overall, the lignin products performed well. The products were approximately average in terms of visual inspection, above average in stabilization performance, and average in relative cost and application rate [Surdahl, *et al*., 2005].

The second study at Seedskadee National Wildlife Refuge [Surdahl, *et al*., 2008] used the same lignin based products, magnesium-lignosulfonate and lignosulfonate, as in the Buenos Aires study. At this site the surfacing material was classified as an A-1-b material, defined as well-graded finer stone fragments, gravel and sand by the AASHTO M 145 classification system. This soil fell into three classifications by the ASTM D 2487 standard; poorly graded sand with silt, poorly graded sand with clay, and silty clayey sand. These classification differences were not thought to be significant.

In the Seedskadee NWR trial, application of the lignin products was processed by scarification of the aggregate surface course to 5 inches depth with the grader while the water

truck added 2,320 gallons of the product solution. The water truck then attached to the front of a CMI 650 pulverizer where the solution was applied to the surface course through liquid dispersion nozzles as it was milled to a 5 inch depth. The mixture was then graded and rolled [Surdahl, *et al*, 2008].

In this trial the lignin products consistently ranked near the top in the same inspection parameters of visual inspection, physical inspection, relative cost and application rate as the Buenos Aires NWR trial [Surdahl, *et al.*, 2008].

Figure 2-5: Application of Lignin-based product at Seedskadee National Wildlife Refuge [source: Surdahl *et al*, 2008].

Possible drawbacks to the FHWA studies are the environment in which they were applied, less-traveled wildlife preserves in mostly dry climates. Although dry climate is typical for both of these locations, Seedskadee experienced more precipitation and wind than Buenos Aires during the course of these studies. While these studies were set in somewhat ideal locales, the potential of lignin as a soil stabilization and dust palliative material was demonstrated effectively.

2.4.2 Iowa State University

An investigation of effects of lignin in in the form of oil and powder, both derived from biomass, on clay was recently completed at Iowa State University [Ceylan, *et al.*, 2010]. The intent of this study was to determine whether or not lignin provided a significant strength improvement. The trials found that strengths comparable to soils enhanced with fly ash could be achieved with the combination of a liquid-based lignin product and a powdered lignin product added to clay and from the combination of the same liquid-based lignin product and fly ash added to clay. It was concluded that lignin served as a suitable, environmentally safe clay stabilizer [Ceylan, *et al.*, 2010].

2.4.2 U.S. Army Engineer Research and Development Center

An investigation of the stabilization potential of a moist silty-sand material with twelve non-traditional additives was conducted at the U.S. Army Engineer Research and Development Center in Vicksburg, MS. The additives investigated in the study were 1 acid, 4 enzymes, 2 lignosulfonates, 1 petroleum emulsion, 3 polymers, and 1 tree resin. The authors of the study choose to omit the product names of the materials used.

Each mixture was represented by six specimens. Two specimens were allowed to cure for 1 day, two were allowed to cure for 7 days, and 2 were allowed to cure for 28 days. Three of the specimens were subjected to "dry" unconfined compression testing, one for each curing period. The remaining three were subjected to "wet" unconfined compression testing in which the cured specimen was soaked in water on one side for 15 minutes and then allowed to drain for 5 minutes prior to testing. The silty-sand was uniform throughout testing, with the water content being equal prior to the addition of all additives at the desired amount.

Neither Lignosulfonate 1 nor Lignosulfonate 2 displayed a marked improvement over the control sample in the "dry" test. Lignosulfonate 1 showed improved unconfined compressive strength for the wet condition, as well as a resistance to disintegration in the water. Lignosulfonate 2 began to disintegrate once placed into the water for the wet test, which reduced the unconfined compressive strength. Lignosulfonate 1 did show an increase in strength at 28 days over the control specimen, where Lignosulfonate 2 did not. This test would seem to imply that curing time is a significant factor in the compressive strength gain of lignin-modified soils. Curing time is a topic to be discussed in future research.

Chapter 3 - Material Properties

Materials used in this study include sand, lignin, and water. Follow up sections provide more detailed description of these materials.

3.1 Sand Description

The sand used in this study was obtained from Midwest Concrete Materials in Manhattan, Kansas. A sieve analysis was performed in accordance with ASTM D 422. The coefficients of uniformity and curvature of the sand were found to be equal to 2.75 and 1.45, respectively. Thus, according to the Unified Soil Classification system, this sand is poorly graded (SP). The specific gravity of the sand was found to be 2.64 by using the ASTM D 854 method. According to ASTM D 2487 this sand is medium to fine sand that is also known as masonry sand.

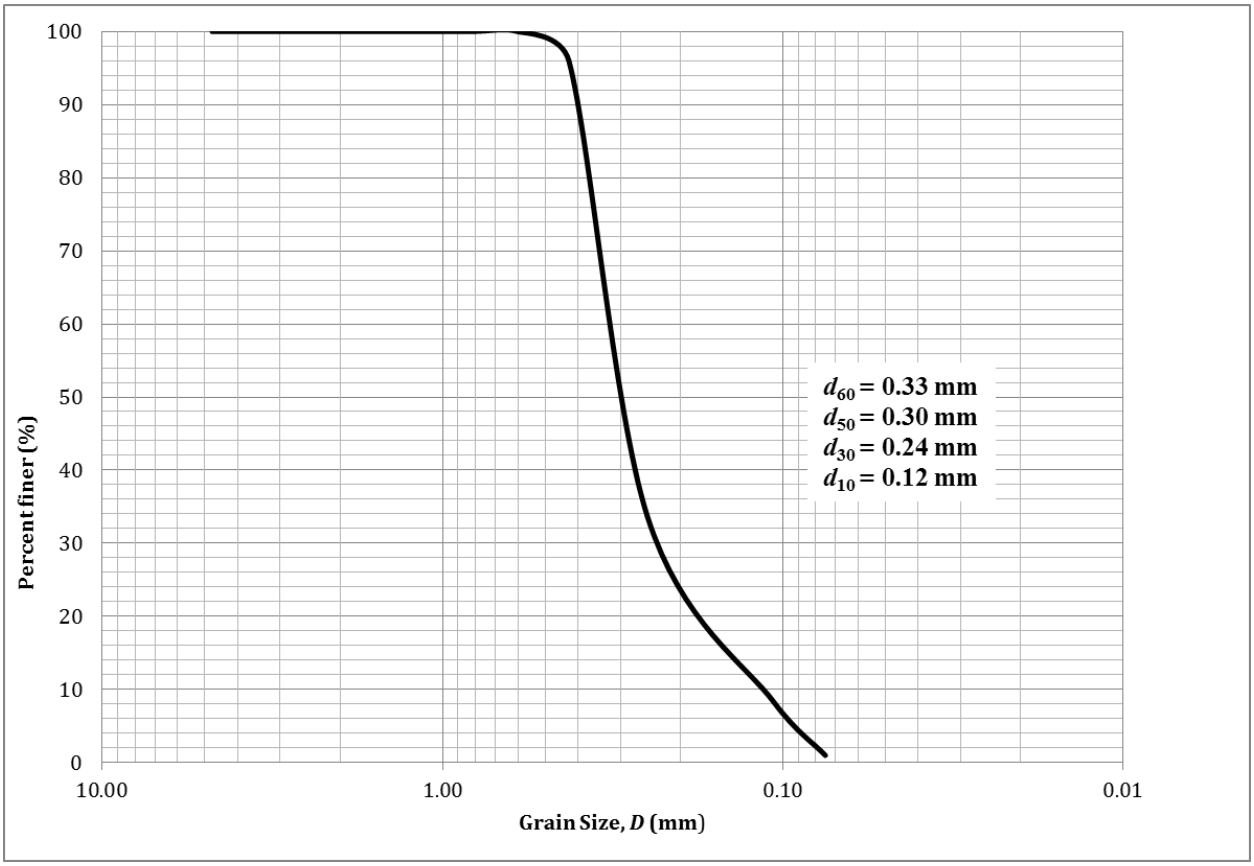

Figure 3-1: Grain size distribution curve of masonry sand

3.2 Lignin Description

The lignin used in this study is Norlig A, a commercially marketed purified calcium lignosulfonate-based product obtained from Lignotech USA. It is used in a wide variety of organic and inorganic industrial binding applications such as the agglomeration of limestone, coal, ceramics and fertilizer. Other uses include, but are not limited to, dust control of unpaved roads and stockpiles and as a low-cost dispersant of various substrates including gypsum and concrete [Lignotech, 2008].

Norlig A is a brown powder, with a pH value of 4.0. It contains 0.4% sodium, 5% moisture, 4.4% calcium, 5% sulfonate sulfur, 5% total sulfur, and 17.9% HPLC sugars with a bulk density of 36 lbs/ft^3.

3.3 Water Description

Water used in this study was non-potable water taken from the tap in the laboratory.

3.4 Phase Relationships

The multiphase nature of a soil-lignin mix is illustrated in the phase diagrams shown in Figures 3-2, 3-3-3 and 3-4. In this study the typical constituents, which are solid particles, water and air, are augmented by the addition of a lignin powder. The lignin powder is a renewable material that may be considered as either an individual component or as a partition of the cementation component of the soil. Figure 3-2 illustrates the composition of the soil including sand solids, lignin and water as separate constituents. Figure 3-3 displays water and lignin as a single constituent while Figure 3-4 depicts the definitions of the degrees of saturations of each constituent: lignin, water, and air. The basic definitions and phase relationships among the constituents in terms of masses and volumes follow the phase diagrams.

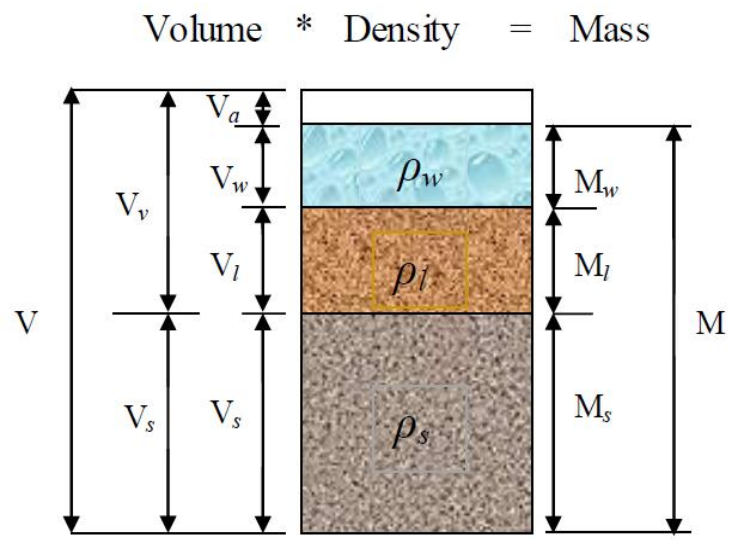

Figure 3-2: Phase diagram showing separate constituents

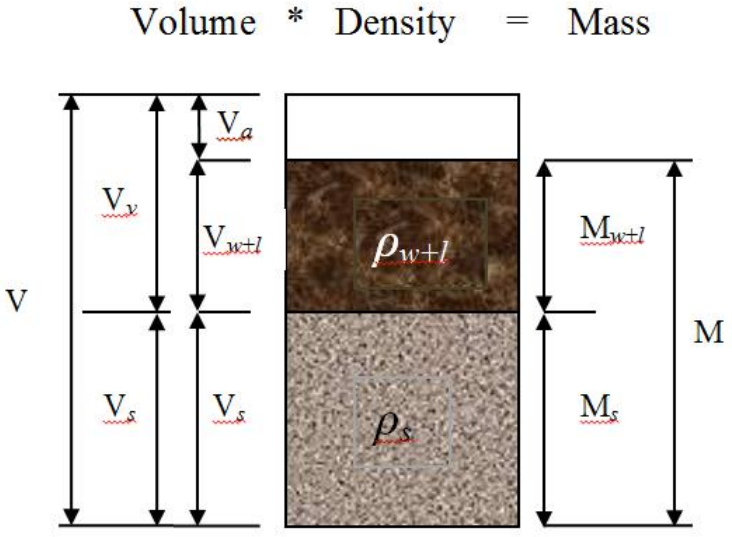

Figure 3-3: Phase diagram showing lignin and water as a single constituent

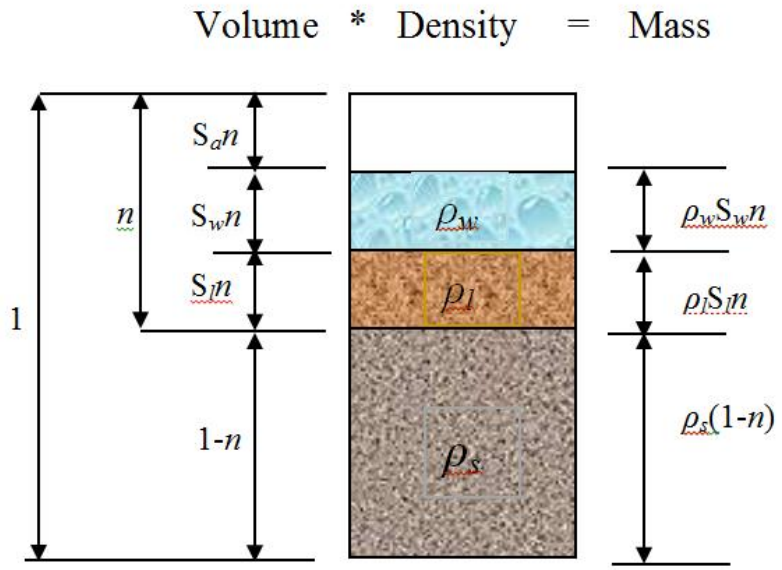

Figure 3-4: Phase diagram showing various degrees of saturation and masses

3.5 Basic Definitions

Basic definitions describing the phase relationships are grouped in three sections comprising volume, mass and volume/mass relationships.

3.5.1 Volume Relationships

3.5.1.1 Void Ratio (e)

$$e = \frac{V_v}{V_s} \tag{1}$$

3.5.1.2 Porosity (n)

$$n = \frac{V_v}{V} \longrightarrow n = \frac{e}{1+e} \quad \text{and} \quad e = \frac{n}{1-n} \tag{2}$$

3.5.1.3 Degree of Water Saturation (S_w)

$$S_w = \frac{V_w}{V_v} \tag{3}$$

3.5.1.4 Degree of Lignin Saturation (S_l)

$$S_l = \frac{V_l}{V_v} \tag{4}$$

3.5.1.5 Degree of Air Saturation (S_a)

$$S_a = \frac{V_a}{V_v} \tag{5}$$

and the following holds

$$S_w + S_l + S_a = 1 \longrightarrow \left(\frac{V_w + V_l + V_a}{V_v} = 1\right) \tag{6}$$

3.5.2 Mass Relationships

3.5.2.1 Gravimetric Water Content (w)

$$w = \frac{M_w}{M_s} \tag{7}$$

3.5.2.2 Modified Gravimetric Water Content ($\bar{w}$)

$$\bar{w} = \frac{M - M_{dry}}{M_{dry}} = \frac{w}{1 + \chi_l} \tag{8}$$

3.5.2.3 Gravimetric Lignin Content (χ_l)

$$\chi_l = \frac{M_l}{M_s} \tag{9}$$

3.5.2.4 Gravimetric Water/Lignin Ratio ($w_{w/l}$)

$$w_{w/l} = \frac{M_w}{M_l} \longrightarrow w_{w/l} = \frac{w}{\chi_l} \quad \text{or} \quad w = w_{w/l}\chi_l \tag{10}$$

also

$$w_{w/l} = \frac{1}{G_l}\frac{S_w}{S_l}$$

3.5.3 Mass-Volume Relationships

3.5.3.1 Mass Density of Water (ρ_w)

$$\rho_w = \frac{M_w}{V_w} \tag{11}$$

It is assumed that ρ_w = 1.0 g/cm^3 = 62.4 lb/ft^3

3.5.3.2 Mass Density of Sand Solids (ρ_s)

$$\rho_s = \frac{M_s}{V_s} \tag{12}$$

For masonry sand used in the study ρ_s = 2.6 g/cm^3 = 162.24 lb/ft^3

3.5.3.3 Mass Density of Lignin Solids (ρ_l)

$$\rho_l = \frac{M_l}{V_l} \tag{13}$$

For this study ρ_l = 1.6 g/cm^3 = 99.84 lb/ft^3 according to Lignotech USA Inc.

3.5.3.4 Dry Mass Density (ρ_d)

$$\rho_d = \frac{M_s}{V} \tag{14}$$

3.5.3.5 Total Mass Density (of Soil-Lignin Mixture) (ρ)

$$\rho = \frac{M}{V} \tag{15}$$

3.5.3.6 Dry Mass Density of Sand Solids and Lignin ($\rho_{d,s\&l}$)

$$\rho_{d,s\&l} = \frac{M_s + M_l}{V} \tag{16}$$

3.5.4 Derived Relationships

Based on the definition given in Eqn. (15) and Fig. 3 the following is obtained:

$$\rho = (1-n)\rho_s + nS_w\rho_w + nS_l\rho_l \tag{17}$$

or

$$\rho = [(1-n)G_s + n(S_w + S_l G_l)]\rho_w \tag{18}$$

and by substituting the expression for void ratio from Eqn. (2) the following alternate expression is obtained:

$$\rho = \frac{[G_S + e(S_w + S_l G_l)]\rho_w}{1+e} \tag{19}$$

Based on the definition given in Eqn. (16), Fig. (3) and Eqn. (18) the following is obtained:

$$\rho_{s\&l} = [(1-n)G_s + nS_l G_l]\rho_w \tag{20}$$

and by substituting the expression for void ratio from Eqn. (2) the following alternate expression is obtained:

$$\rho_{s\&l} = \frac{(G_s + eS_l G_l)\rho_w}{1+e} \tag{21}$$

3.6 Proctor Tests

Standard Proctor Tests (ASTM D 698-Procedure A) were performed on the mix of dry sand, lignin powder and water for six different gravimetric lignin contents corresponding to 0%, 2%, 4%, 6%, 9%, and 14%.

3.6.1 Standard Proctor Test Procedure

The test was conducted by applying a standard compaction effort to samples containing 2500 grams of sand mixed with different quantities of lignin, specified above. For each value of gravimetric lignin content several different configurations having different water contents defined by Eqn. (7) were tested. These constituents were thoroughly mixed and compacted in a mold having a volume of 943 cm^3.

3.6.2 Standard Proctor Test Results

Summary compaction curves for all tests are shown in Figure 3-5 and 3-6. These figures depict the experimentally observed relationship between the dry mass density given by Eqn. (14) and moisture content, w. The results of each individual test are shown in Figures 3-7 through Figure 3-12. These figures depict the zero-air-voids-curve (Z.A.V.C.), which represents the relationship between the dry mass density and water content at zero air content or when all voids are completely filled with water and lignin. This state is not attainable by compaction. The greater proximity of the Z.A.V.C. to the experimentally obtained compaction curve indicates that a smaller amount of air is present in the voids. In addition, the constant water and air saturation curves are shown whereby the degrees of water and air saturation correspond to their values at the optimum water contents. Figures 3-7 through 3-12 also contain the detailed information including void ratios, lignin and air saturations, and gravimetric water to lignin ratios at the optimum moisture contents. In addition, the values of the optimum moisture contents and maximum dry densities are provided.

These results show that the maximum dry density of sand-lignin mix decreases with the increasing lignin content indicating that the smaller amount of sand can be packed into the standard volume size by using the standard compactive effort. However, the increasing amount of lignin causes the increase in the dry mass density of sand and lignin [Eqn. (21)]. Furthermore,

while the air saturation decreases the water saturation increases with the increasing lignin content, except in the case of zero lignin content shown in Figure 3-7.

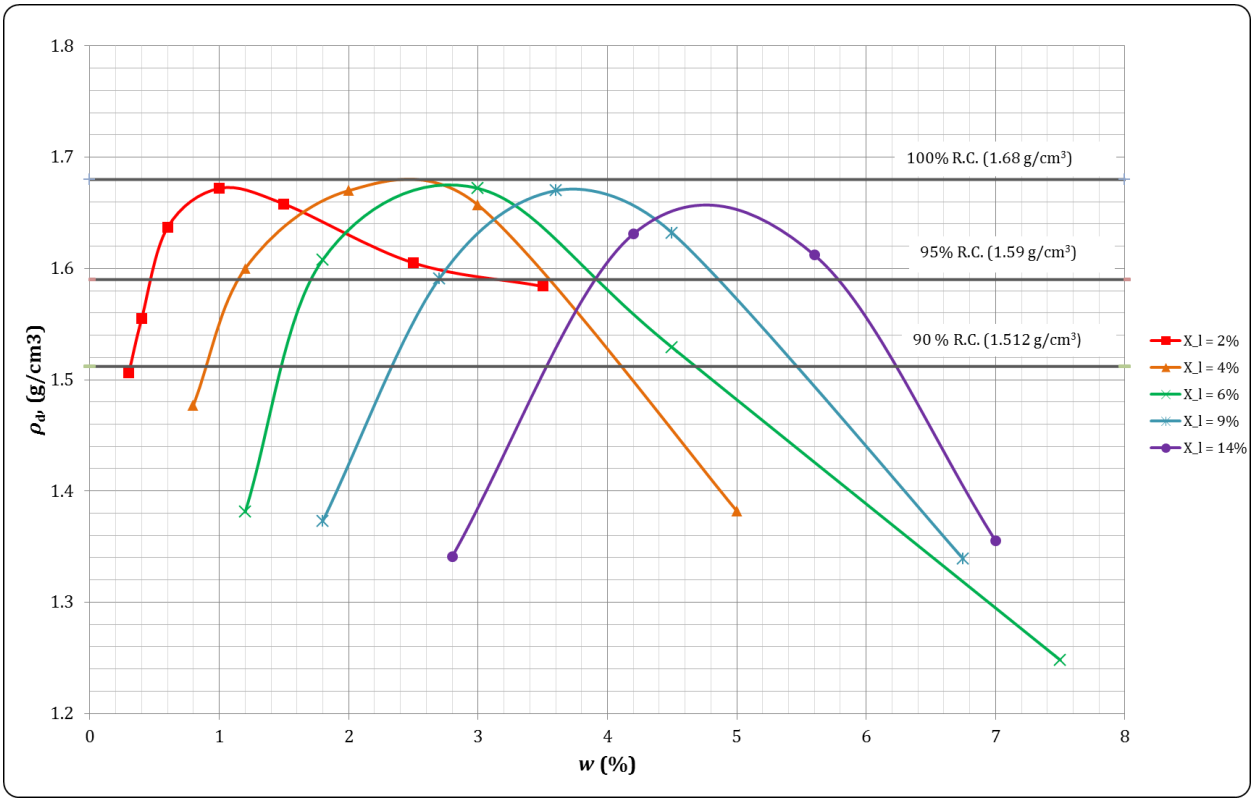

Figure 3-5: Summary of Standard Proctor Tests

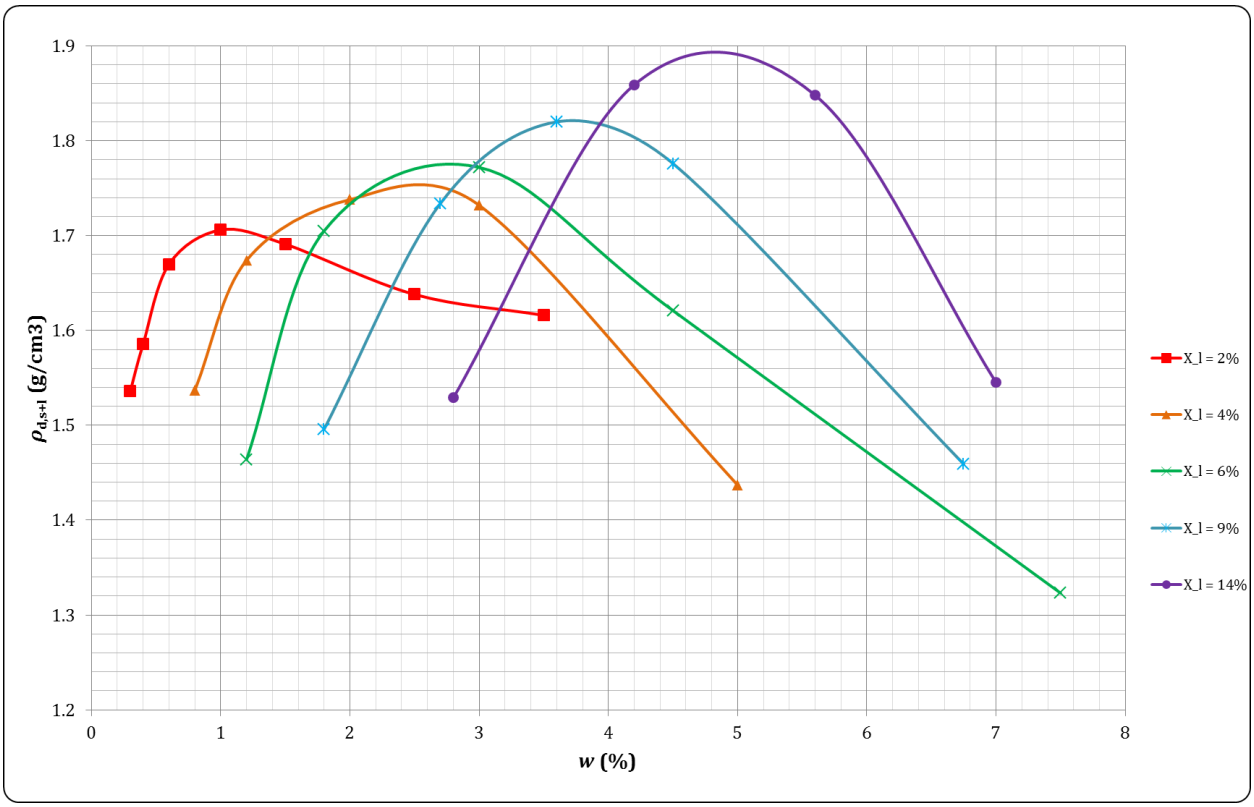

Figure 3-6: Summary of Standard Proctor Tests showing $\rho_{d,s+l}$

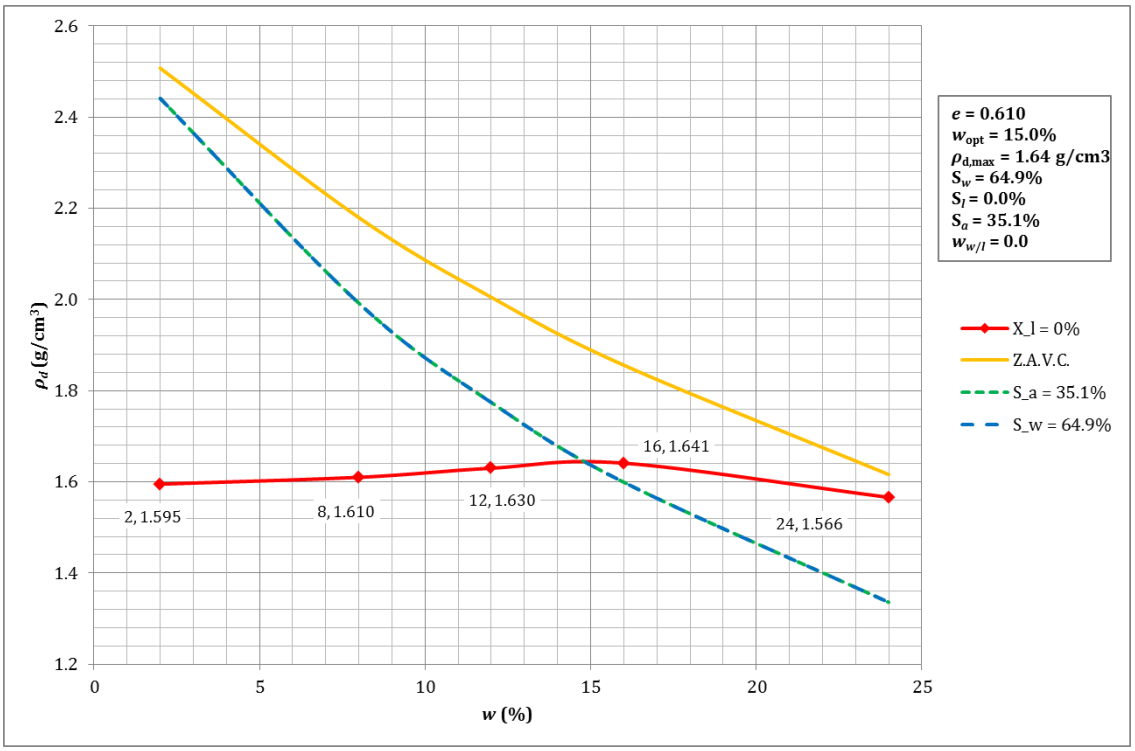

Figure 3-7: Standard Proctor Test for χ_l = 0%

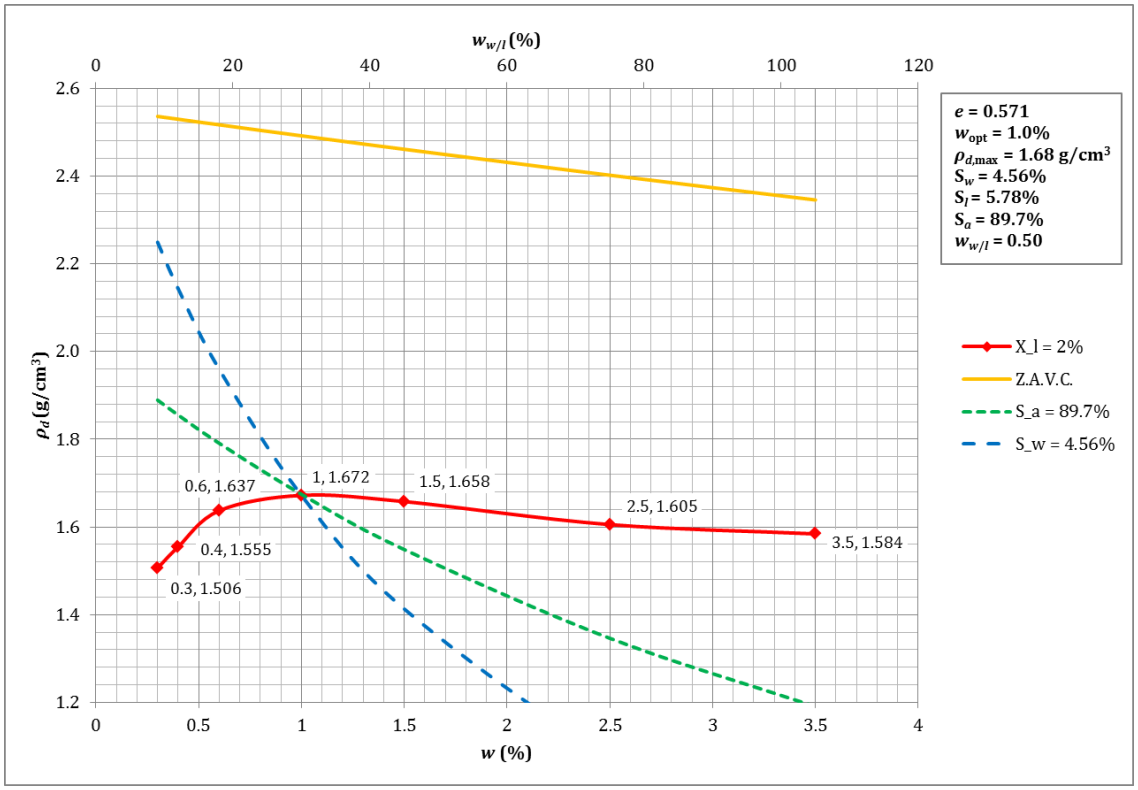

Figure 3-8: Standard Proctor Test for χ_l = 2%

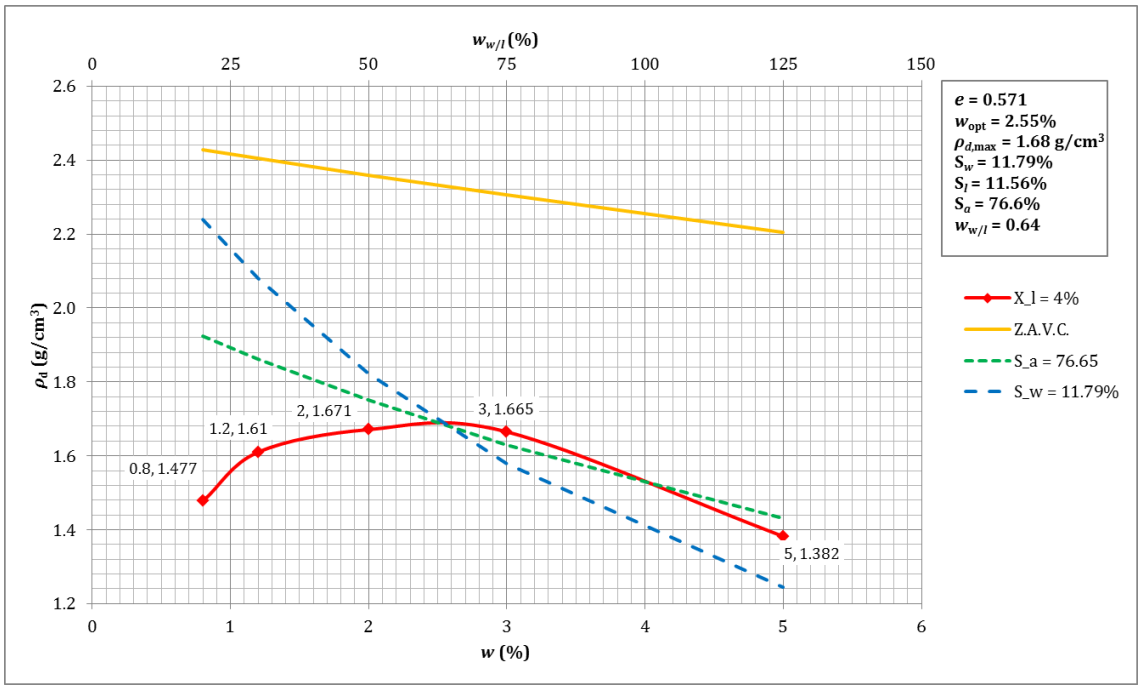

Figure 3-9: Standard Proctor Test for χ_l = 4%

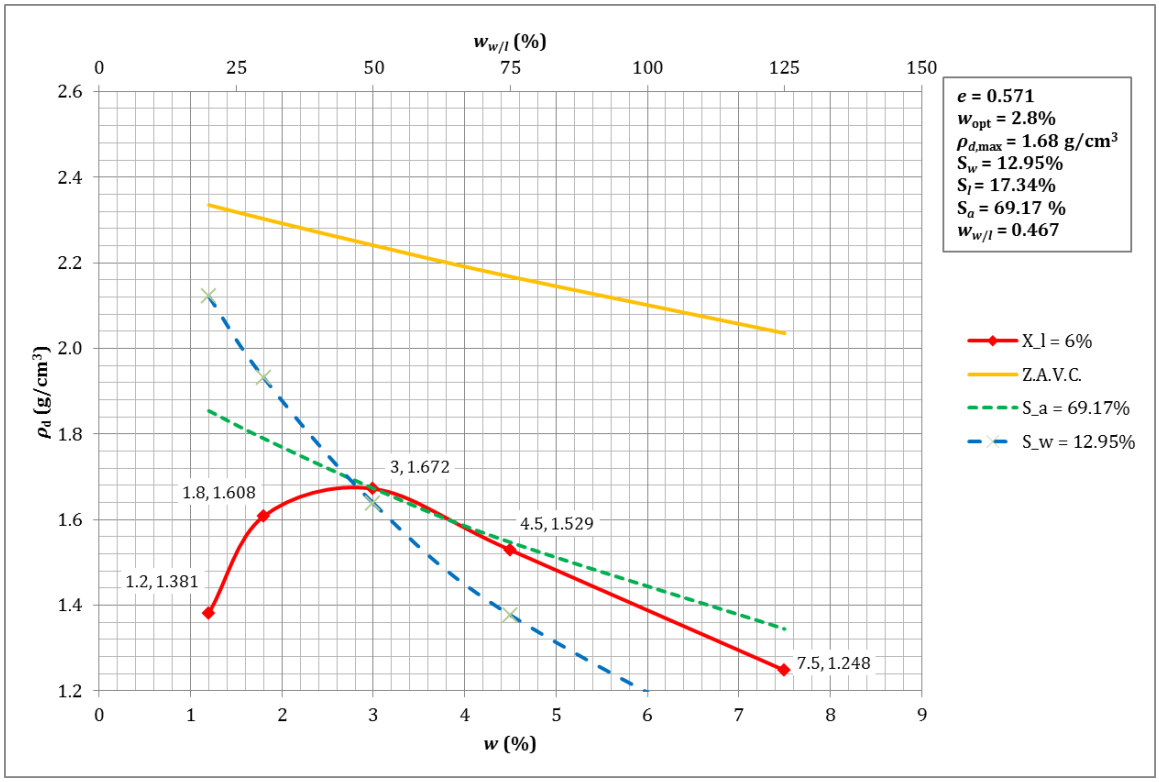

Figure 3-10: Standard Proctor Test for χ_l = 6%

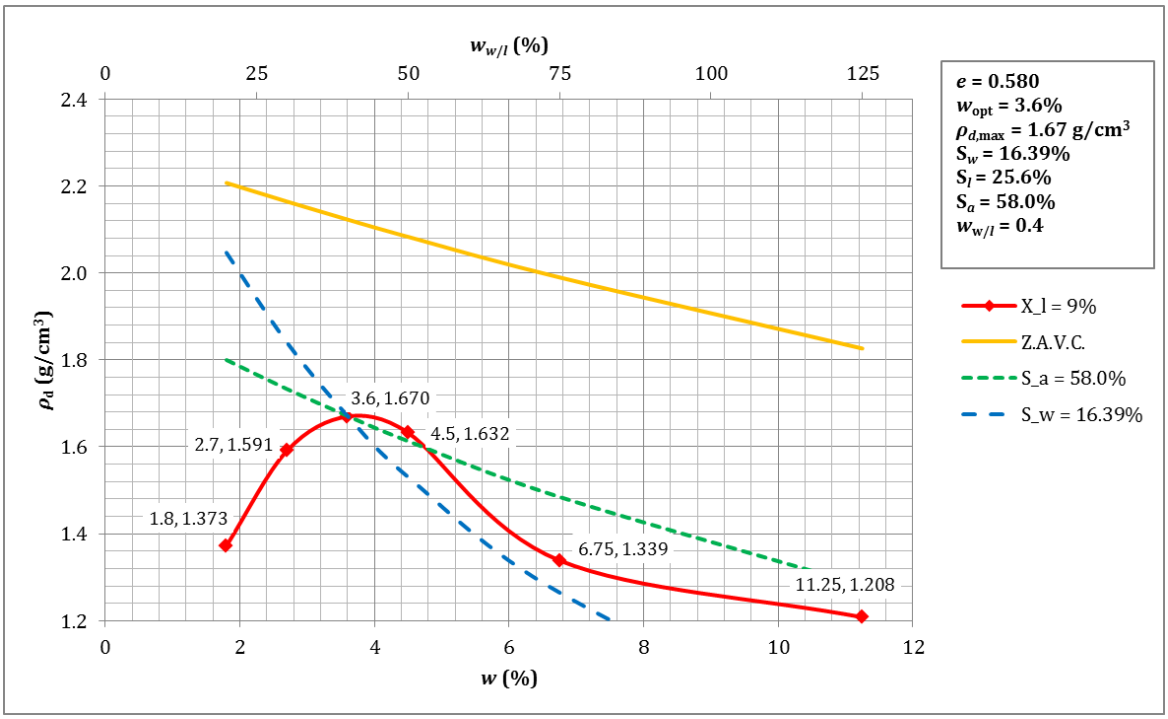

Figure 3-11: Standard Proctor Test for χ_l = 9%

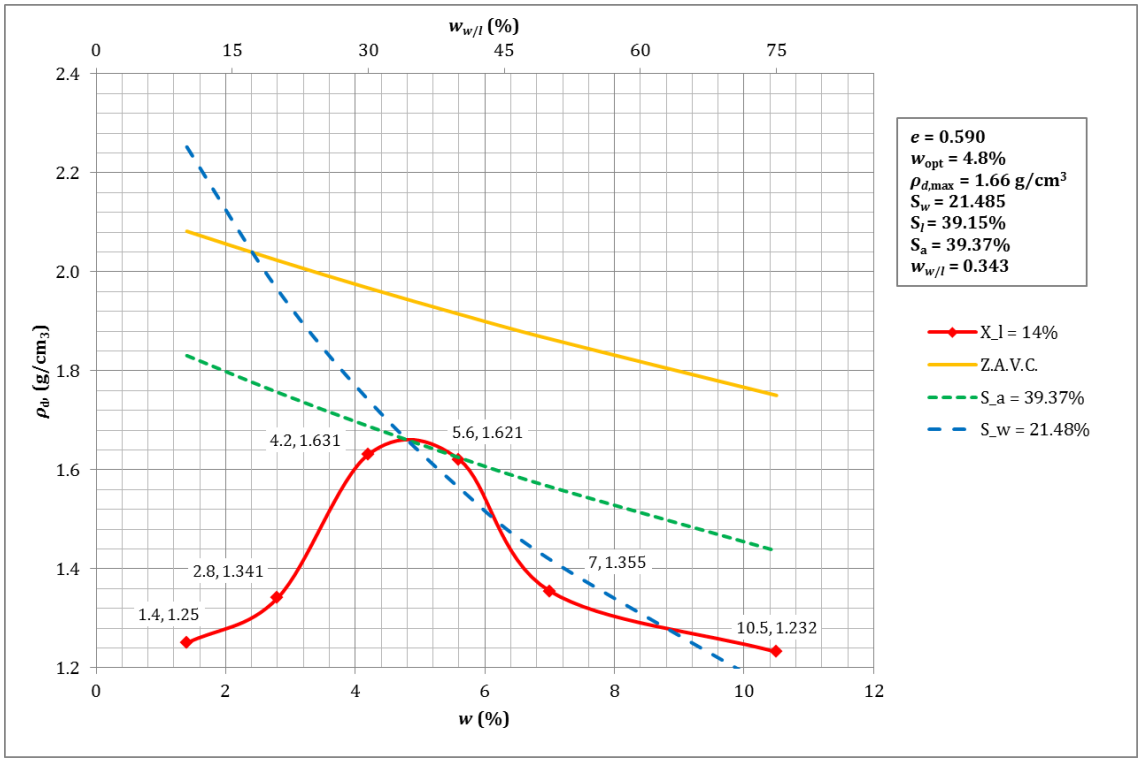

Figure 3-12: Standard Proctor Test for χ_l = 14%

3.7 Atterberg Limit Tests

Liquid limits (ASTM D-4318), of the sand-lignin mix, were determined in this study. Atterberg limit tests are typically conducted for fine-grained soils. However, the addition of lignin to sand adds a quantifiable cohesive quality making Atterberg limit tests relevant as a supplemental part of the overall investigation. The liquid limit test was conducted for all gravimetric lignin contents except for 2%, where the results proved inconclusive. The plastic limit test could not be performed due to the non-plastic nature of the material. The results of the liquid limit test are presented in Figure 3-13 below. Figure 3-14 shows that the increase of liquid limit with increased gravimetric lignin content follows a nearly linear trend.

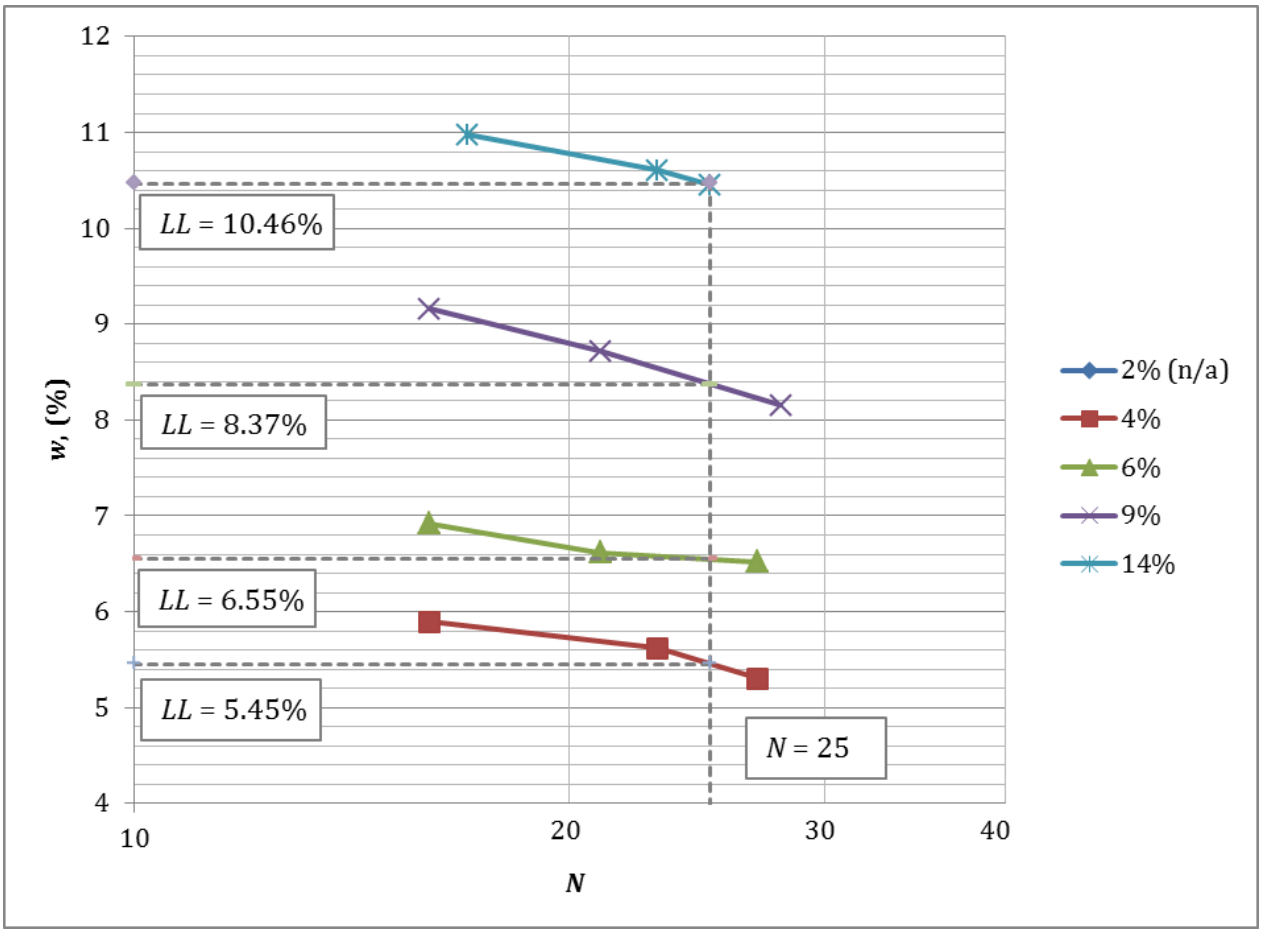

Figure 3-13: Liquid Limit Test Summary

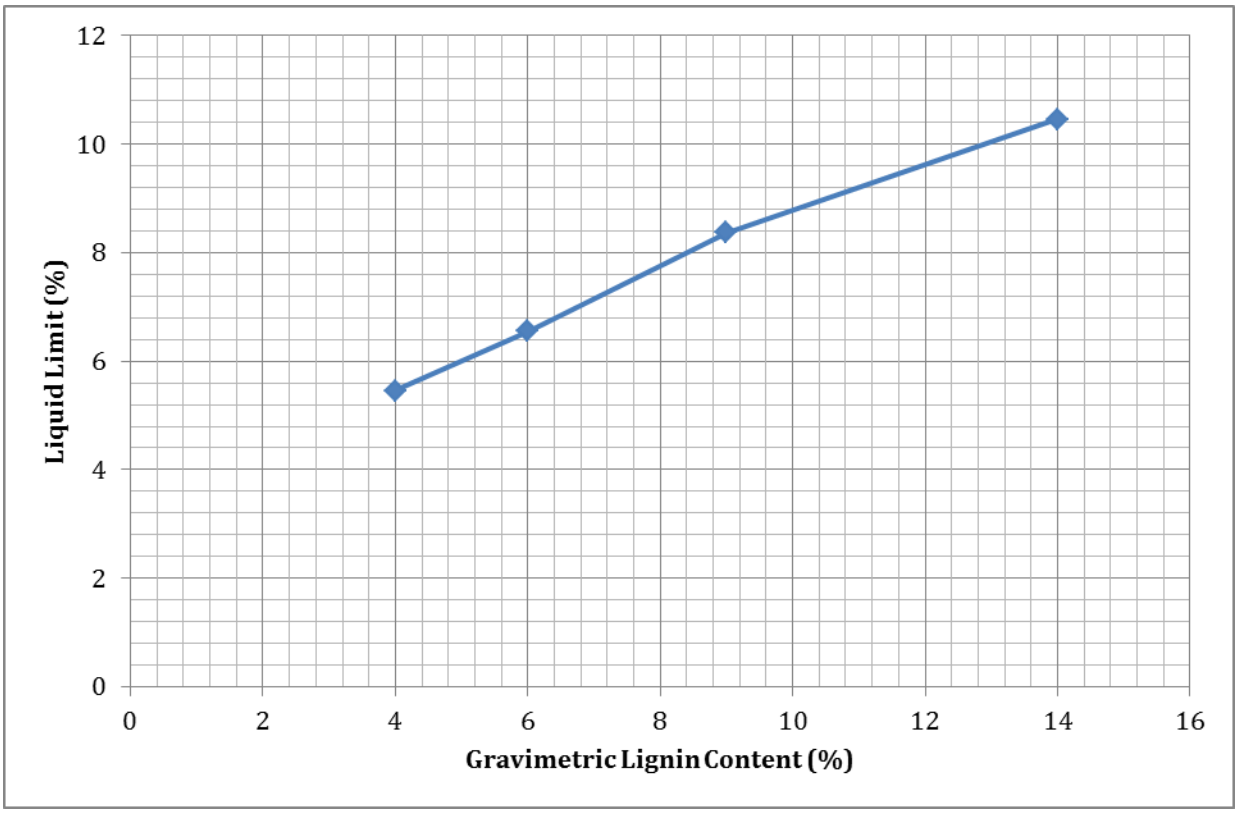

Figure 3-14: Liquid Limit versus Gravimetric Lignin Content

Chapter 4 - Experimental Equipment, Techniques, and Program

The program of direct shear tests was selected based on the results of the Proctor tests and in an effort to assess the effect of void ratio and water content as well as water to lignin ratio on the strength of lignin-sand mixtures.

The direct shear test is used herein to measure the friction angle and, cohesion, which are necessary for, failure analysis of foundations and slopes. The shear strength τ of a dry or fully saturated sand or gravel may be expressed by the equation

$$\tau = \sigma' \tan \Phi' \tag{21}$$

where σ' = the effective normal stress acting on the failure surface

Φ' = the effective angle of internal friction of soil

The angle of internal friction is a function of the relative density of coarse grained soils, and their grain size, shape, and grain size distribution. For example, an increase in the void ratio of sand will result in a decrease of the friction angle. However, for a given void ratio, an increase in the angularity of the sand particles will produce a higher value of its friction angle [Das, 1997].

The direct shear test is desirable because it is known as the simplest, the oldest, and the most straightforward procedure for measuring the shear strength of soils. The direct shear test has some disadvantages, the most immediate being the pre-determined failure plane [Head, 1994].

4.1 Direct Shear Test Apparatus

The direct shear apparatus used in this study belongs to the Geotechnical Laboratories located in the Civil Engineering Department at Kansas State University. It consists of a shear box, two linear variable displacement transducers (LVDTs), an "S" type load cell, digital input head, an autonomous data acquisition unit (ADU), and the loading/carriage assembly. The prepared specimen is transferred to the shear box, which is then placed into the carriage assembly on the loading frame. The shearing of the specimen is controlled by the digital input

on the drive unit housing. The vertical and horizontal displacements of the specimen are measured by the two LVDTs. The horizontal force is measured by the load cell, sends the data electronically to the ADU, which is connected to a personal computer that displays the test progress in real-time and stores the results. The computer runs ELE DS7 Geotechnical software to facilitate the data recording and analysis. The specifications and dimensions of the direct shear apparatus are provided in Table 4-1.

Table 4-1: Direct Shear Apparatus Specifications and Dimensions [ELE, 2006]

Manufacturer	ELE International
Model	26-2114
Max Specimen Size	100 mm
Max Design Normal Load	1000 kg
Specimen 60 mm square 10:1 ratio Shear Force	100 kg 2.8 N/mm^2 (272.5 kPa)
Max Design Shear Force	5.0 kN
Weight (approximate)	70 kg (155 lbs)
Approximate Dimensions (L x H x W)	320 x 1135 x 1260 mm
Enclosure	Metal casing with painted finish
Temperature	5° C to 40° C
Supply Voltage(s)	115 VAC 50/60 Hz 230 VAC, 50/60 Hz
Power Consumption	26W

4.1.1 Shear Box

The shear box is a split metal-frame "box" consisting of an upper and lower half. The inside, which houses soil samples, is round. There are a total of six screws included and associated with the shear box. Four Teflon-tipped screws are used to assist the procedure by controlling the space between the upper and lower parts, thereby reducing friction between the two halves of the box. Two locking-pin screws that are removed before testing are used to fasten the box together during sample preparation. Upper and lower porous stones are used to drain water from samples. In addition, upper and lower serrated pressure pads are necessary for testing to minimize slippage at the interface between the soil and shear box and also to improve the transfer of the normal load to the soil. Filter papers are placed at the top and bottom surfaces of a sample, between the sample and the porous stones.

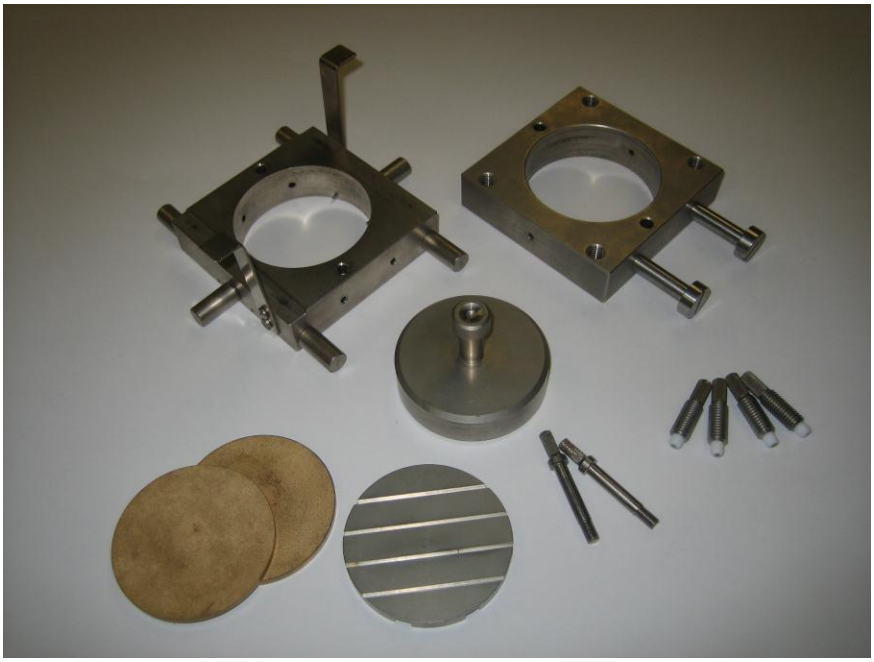

Figure 4-1: Photograph of Shear Box Components

4.1.2 Linear Variable Displacement Transducers

A Linear Variable Displacement Transducer (LVDT) is a type of electronic transducer used for measuring displacements. The transducer has three solenoid coils placed end-to-end

around a tube. The center coil is the primary, and the two outer coils act as secondary coils. A cylindrical ferromagnetic core, attached to the object whose position is to be measured, slides along the axis of the tube. The motion induces an electrical current in the coils, whose voltage depends on the magnitude of the motion. The LVDTs are used in this case to measure the horizontal and vertical displacements of the soil sample during testing. The two LVDTs used for shear testing are identical and interchangeable, therefore one is used for the measurement of vertical displacement and the other is used for the measurement of horizontal displacement.

Figure 4-2: Photograph of Linear Variable Displacement Transducers

4.1.3 "S" Type Load Cell

The load cell is an electronic transducer that is used to measure an acting force by an electrical signal. This measurement is indirect and happens in two stages. Through a mechanical arrangement, the force being sensed deforms a strain gauge. The strain gauge converts the deformation to electrical signals that are relayed to the ADU and in turn to the computer as the measured force on the sample. The load cell is placed so as to measure the amount of horizontal force. The load cell below is shown attached to extension pieces and mounting bracket screws.

Figure 4-3: Photograph of "S" Type Load Cell

4.1.4 Digital Input/Drive Unit Housing

The operation of the direct shear apparatus is controlled by the digital input located on the drive unit housing. The input features a digital keyboard on the facing of the housing that allows the user to input the rate of shear displacement for the test, a range of 0.00001 mm/min to 9.99999 mm/min. The housing contains a small motor that drives a piston that applies the force to the soil sample and load cell. The motor assembly includes a limit switch that automatically stops the motor at 10 mm.

Figure 4-4: Photograph of Digital Input Box

4.1.4 Autonomous Data Acquisition Unit (ADU)

The autonomous data acquisition unit is a data storage facility with on-board intelligence and memory capability. The ADU allows communication between the LVDTs, load cell, and computer that is to be used for testing; therefore acting as a bridge between the direct shear apparatus and the computer. The LVDTs and load cell are connected directly to the ADU, each to one of the eight channels included on the input panel. While eight channels are available, the ADU allows for expansion of an additional eight channels for each panel for a maximum of 32 total channels.

Figure 4-5: Photograph of Autonomous Data Acquisition Unit

4.1.5 Loading Assembly

The loading assembly consists of three parts: the load frame, load hanger, and the loading lever arm. The load frame is connected to the lever loading arm, which is in turn connected to the load hanger, shown in Figure 4-6. The amount of vertical force applied to the sample is predetermined by placing any combination of weights on the load hanger. The load hanger is offset from the location where the force is applied by the length of the lever arm to multiply the weight by a factor of ten, i.e. one Newton equals ten Newtons of the vertical force. If no weight is placed on the load hanger, then the force on the sample from the load frame is assumed to be zero. A calibration curve showing the deflection of the frame due to loading versus the amount

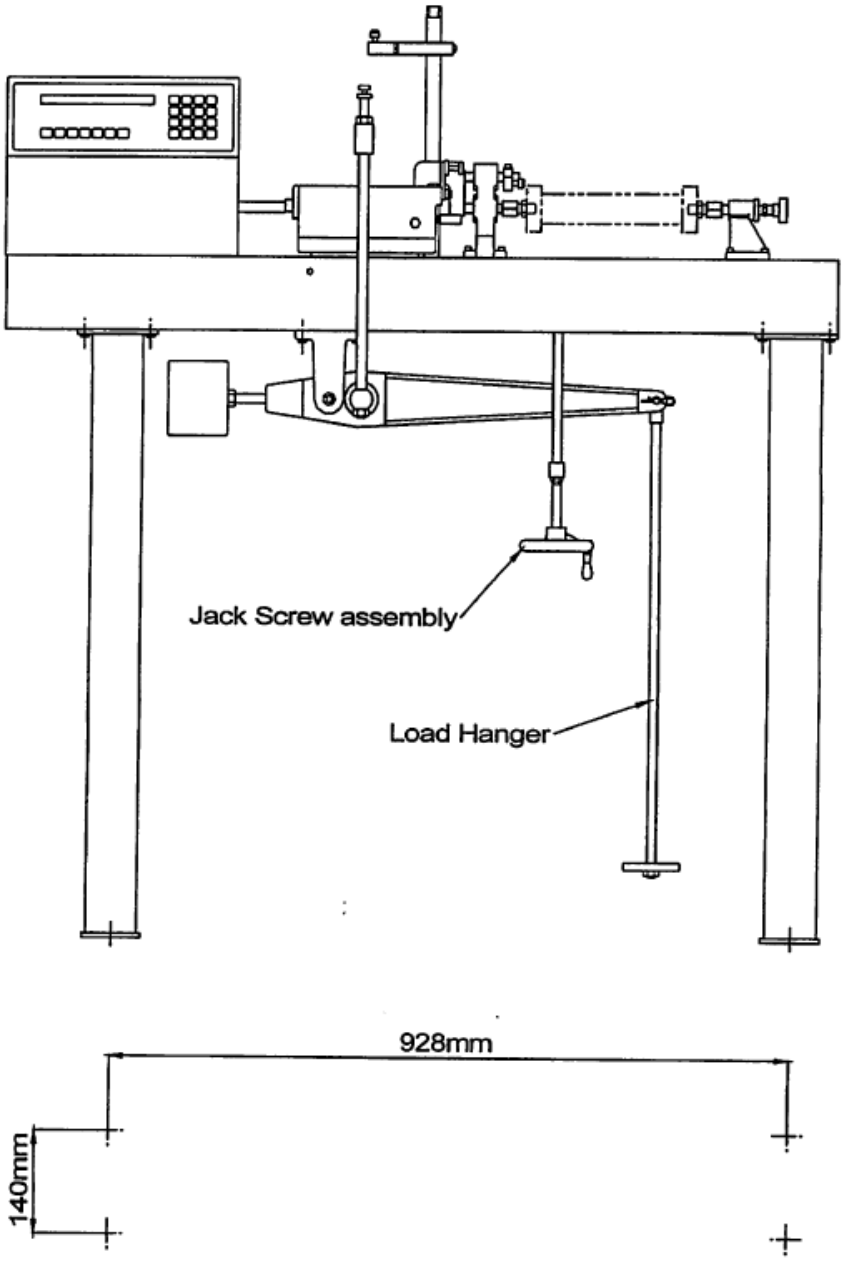

Figure 4-6: Schematic of Direct Shear Apparatus Load Frame [ELE, 2006]

of the vertical stress acting on a dummy steel sample is depicted in Figure 4-7.

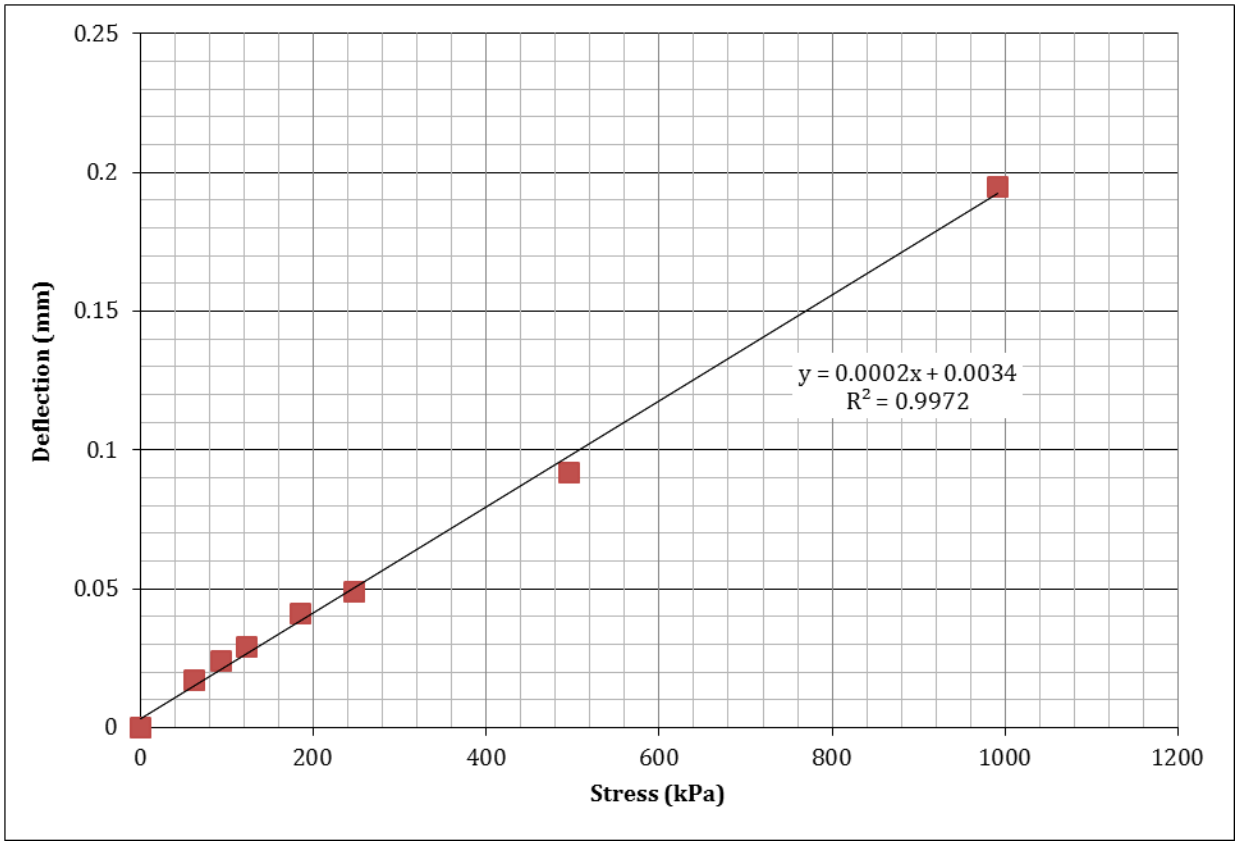

Figure 4-7: Plot of vertical force vs. deflection of frame.

4.1.6 Carriage Assembly

The carriage assembly holds the direct shear box and moves during the application of a horizontal force. The carriage rests on two ball-race tracks to allow the movement. After the sample is prepared in the shear box it is carefully placed in the box carriage and attached screws are tightened to secure the specimen. A load pad is placed on the sample to evenly distribute the pressure and the load frame is moved into position. After the horizontal and vertical LVDTs are placed in the correct position, the sample is ready for testing. A schematic of the carriage assembly is shown in Figure 4-8.

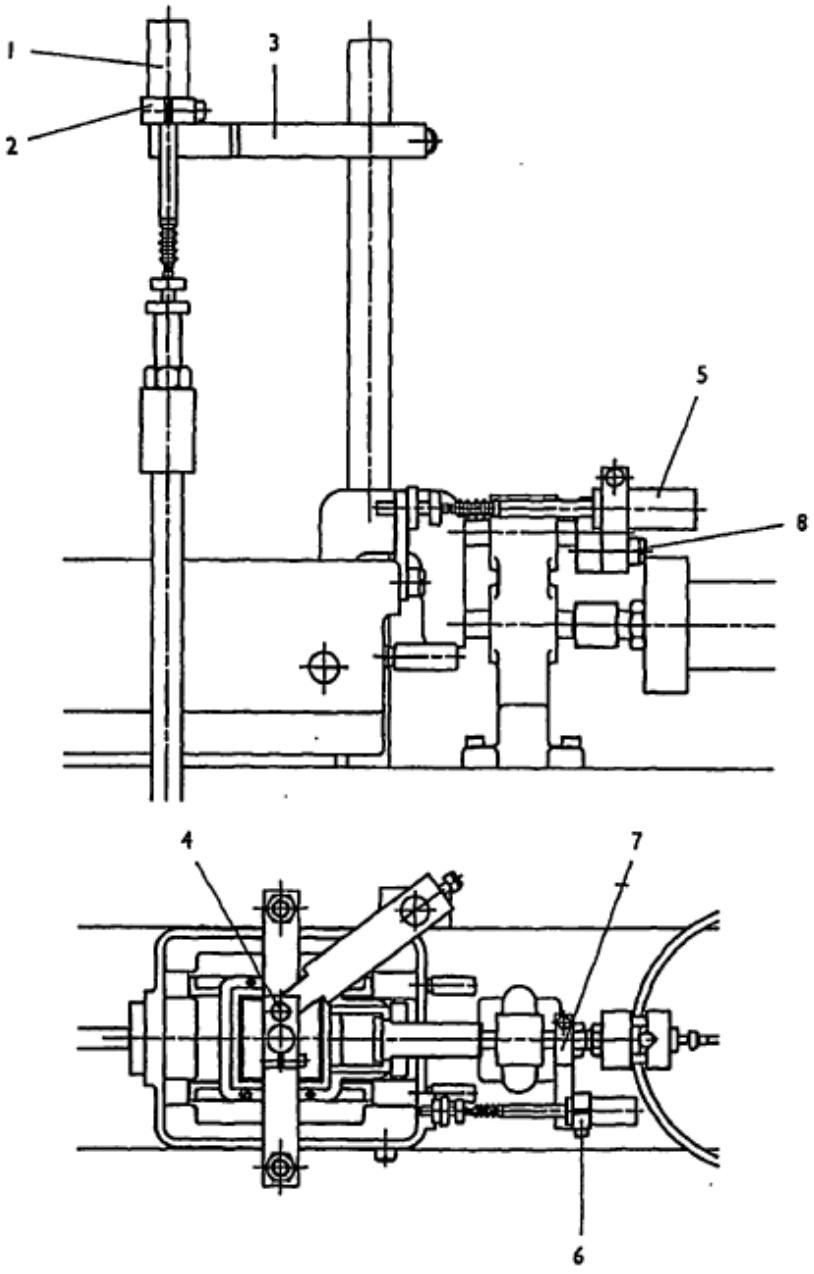

Key

1 Vertical displacement transducer
2 Split bracket
3 Upstand arm
4 Thumbscrew
5 Horizontal displacement transducer
6 Split bracket
7 Swan neck guide shaft arm
8 Thumbscrew

Figure 4-8: Schematic of Shear Box Carriage Assembly [ELE, 2006]

4.1.7 DataSystem 7 Geotechnical Software

DataSystem 7 (DS 7) Geotechnical software is a data analysis and reporting software suite designed to work in concert with ELE's ADU data logger and transducers. The software incorporates advanced features such as intelligent data analysis, automatic report generation, and data exchange compatibility.

4.2 Direct Shear Test Procedure

The direct shear test procedure (ASTM D-3080) was designed to produce uniform and repeatable test results. The procedure consisted of thoroughly mixing dry sand with lignin powder at the desired gravimetric lignin contents. The preselected amounts of water were then added to the dry mix, depending on the desired configuration, and mixed thoroughly. The predetermined amounts of prepared samples were then placed in the shear box and compacted to the desired height using a Proctor test sample ejector before being placed in the carriage assembly for testing. This sample preparation procedure enabled attainment of desired initial dry densities.

4.2.1 Direct Shear Test Program

The program of direct shear tests was selected based on the results of the Proctor tests and in an effort to assess the effect of void ratio and water content as well as of the gravimetric water to lignin ratio on the strength of lignin-sand mixtures. The samples for direct shear tests were prepared at void ratios of 0.571, 0.654, and 0.746 representing 100%, 95%, and 90% relative compactions, respectively. A number of different water contents were selected including optimum, dry and wet of optimum whereby most of them are located on the standard Proctor compaction curves, except at $\chi_l = 14\%$ where the minimum void ratio was 0.590. The schematic of the planned experimental program depicting all testing configurations is shown in Figure 4-9 and Table 4-3. The planned positioning of points A, B, C, D, E is shown in Figure 4-10 and described in Table 4-2.

Phase diagrams for each planned configuration are shown in Figures 4-11 through 4-16. These phase relationships were carefully devised and represent the material as mixed; they represent exactly what comprises the mixture. However, the effect of long-term drying on the mixtures is as of the time of writing unknown. Therefore, the phase relationships may change

with time but that phenomena will not be addressed in this study. The samples discussed herein were tested immediately upon mixing so the phase relationships presented here should be close to the actual state of the samples tested. These phase diagrams are presented in Chapter 5 representing actual water contents.

4.2.2 Test Specimen Preparation

Sand-lignin mix samples for the direct shear testing were prepared as follows:

1. An amount of oven-dried sand, calculated based on the target dry density value, was measured and placed in a bowl.
2. The amount of lignin powder to be used was calculated according to Table 4-3 and mixed thoroughly with the measured amount of sand.
3. Amount of water was calculated according to Table 4-3 and thoroughly mixed into dry sand-lignin supply.
4. Mass of sand to be used was determined in accordance with the target void ratio or dry density assuming the final compacted height of 24 mm. The sand was placed into the shear box in a total of three lifts. Each lift was compacted manually to a desired height by using a wooden compaction tool. The top porous stone was then placed on top of the sample in box.
5. The shear box containing the sample was placed on a hydraulic jack with a 7" stroke and 6000 lb-f (26.7 kN) total pushing force.
6. All samples were compacted to uniform 24 mm initial height.
7. Sample was then placed in direct shear apparatus carriage for testing.

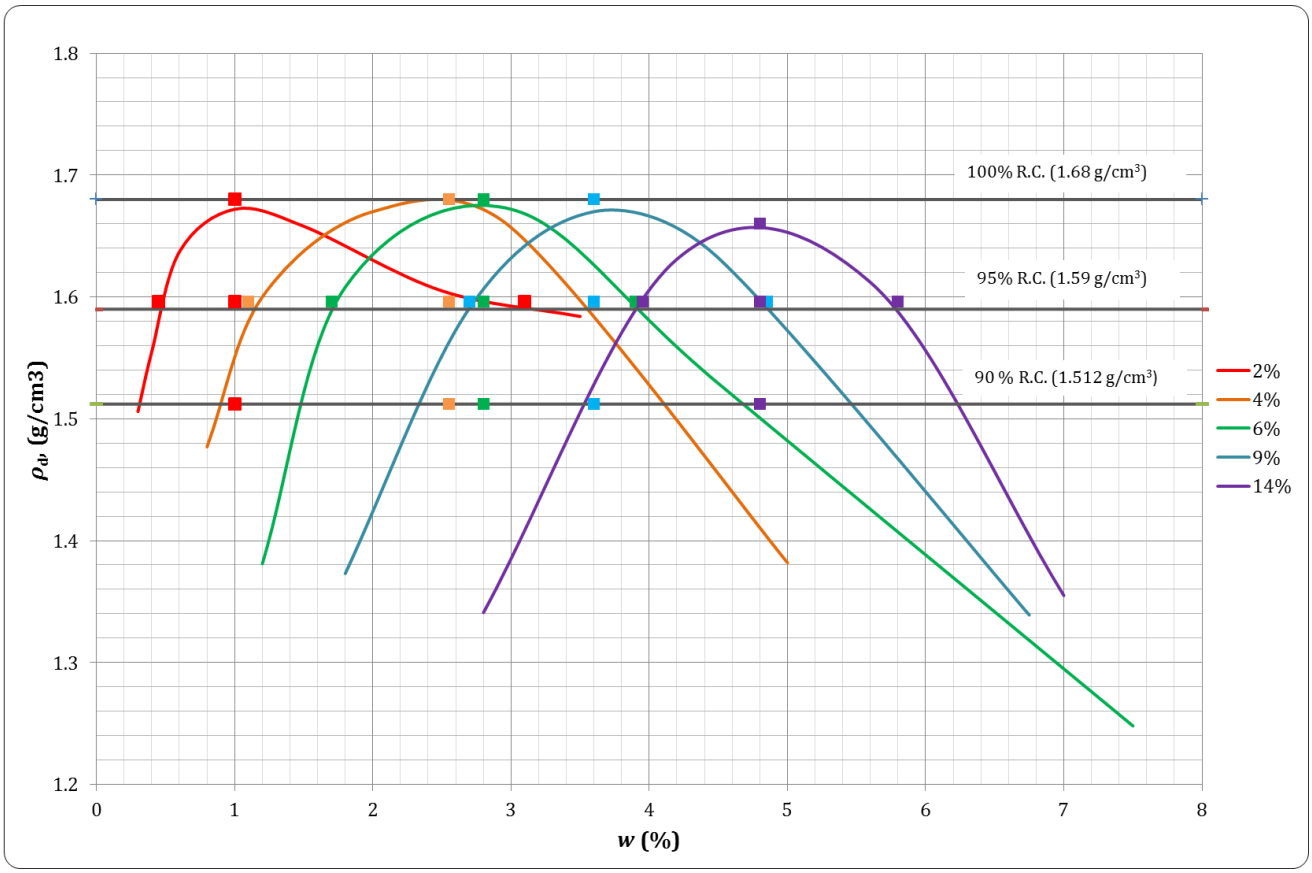

Figure 4-9: Summary of Direct Shear Sample Configurations

Table 4-2: Description of Direct Shear Sample Configurations

Test Pt.	Description	Void Ratio, *e*
A	100% density, optimum moisture	0.571
E	95% density, optimum moisture	0.654
C	90% density, optimum moisture	0.746
D	95% density, dry of optimum moisture	0.654
B	95% density, wet of optimum moisture	0.654

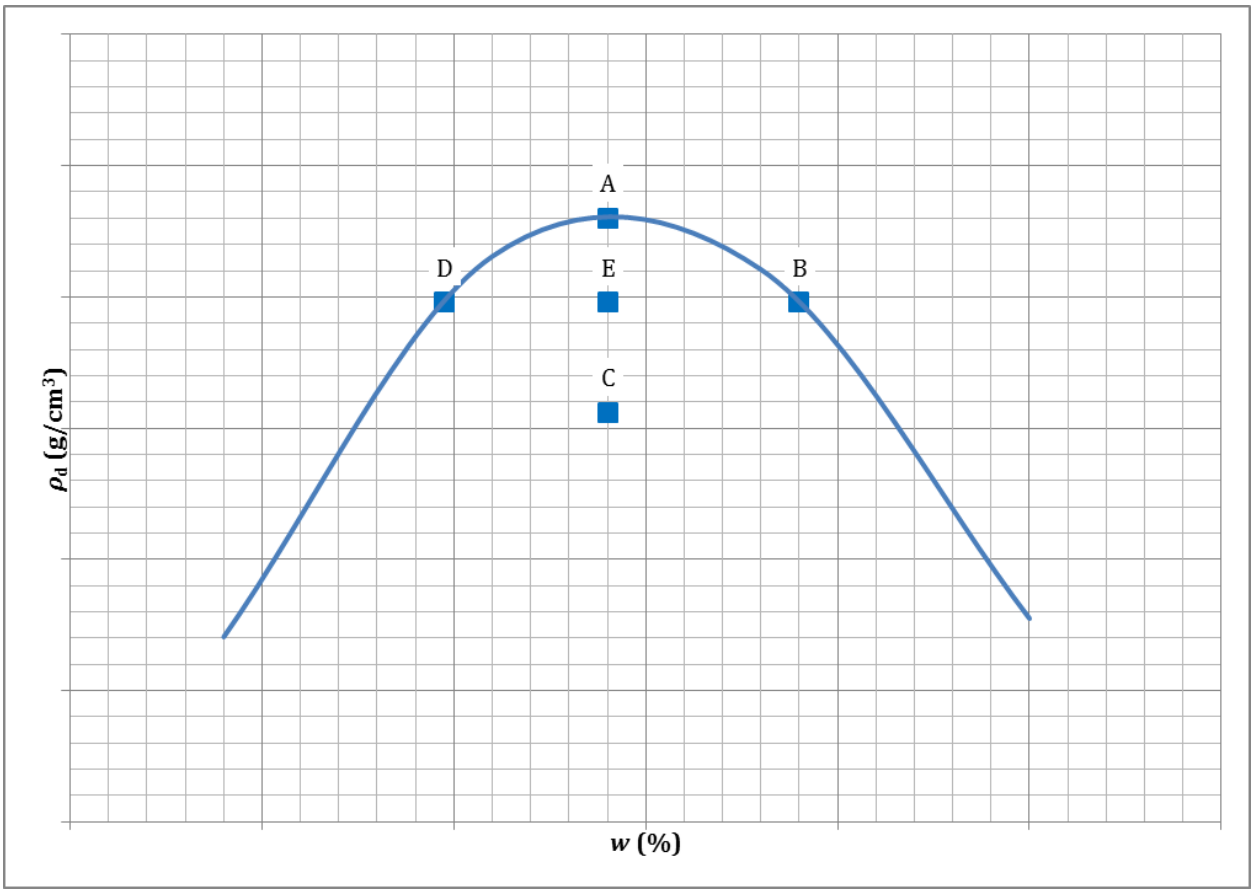

Figure 4-10: Example of planned position of points A, B, C, D, E (No scale).

Table 4-3: Planned Direct Shear Test Program

χ_l (%)	Pt.	w (%)	ρ_d (g/cm^3)	e
0	A	0.00	1.680	0.571
0	E	0.00	1.596	0.654
0	C	0.00	1.512	0.746
2	A	1.00	1.680	0.571
2	E	1.00	1.596	0.654
2	C	1.00	1.512	0.746
2	D	0.45	1.596	0.654
2	B	3.10	1.596	0.654
4	A	2.55	1.680	0.571
4	E	2.55	1.596	0.654
4	C	2.55	1.512	0.746
4	D	1.10	1.596	0.654
4	B	3.60	1.596	0.654
6	A	2.80	1.680	0.571
6	E	2.80	1.596	0.654
6	C	2.80	1.512	0.746
6	D	1.70	1.596	0.654
6	B	3.90	1.596	0.654
9	A	3.60	1.670	0.580
9	E	3.60	1.596	0.654
9	C	3.60	1.512	0.746
9	D	2.70	1.596	0.654
9	B	4.85	1.596	0.654
14	A	4.80	1.660	0.590
14	E	4.80	1.596	0.654
14	C	4.80	1.512	0.746
14	D	3.95	1.596	0.654
14	B	5.80	1.596	0.654

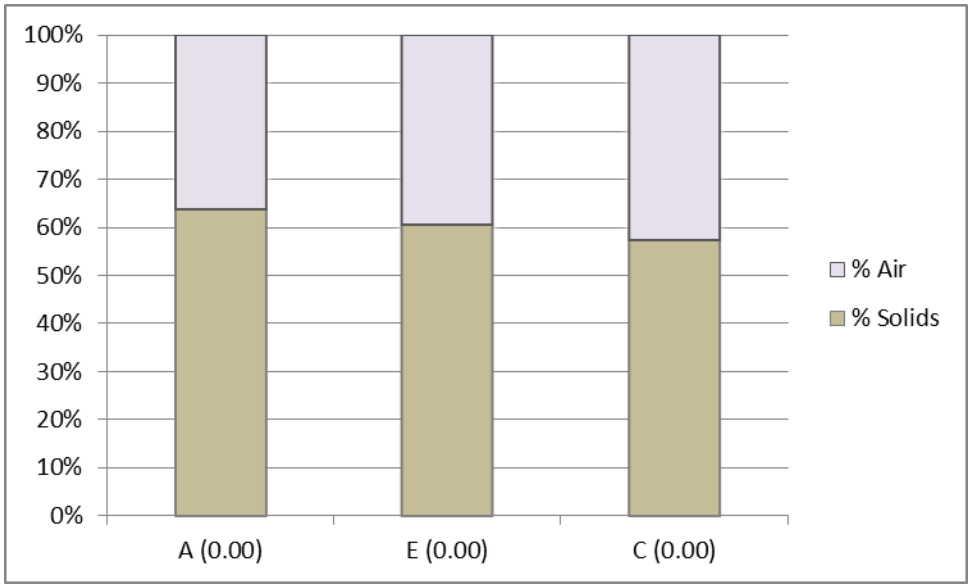

Figure 4-11: Phase Diagram for χ_l = 0%

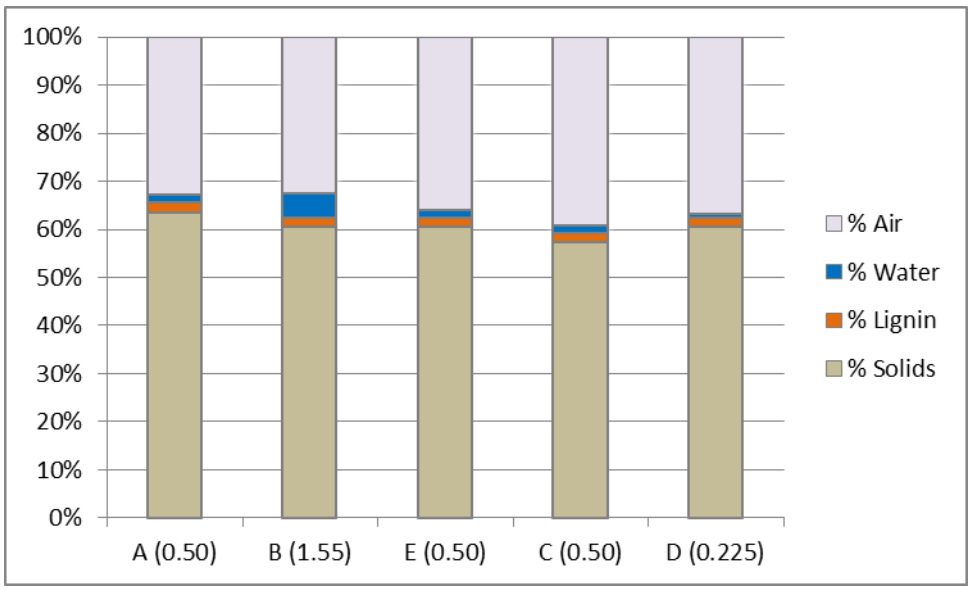

Figure 4-12: Phase Diagram for χ_l = 2%

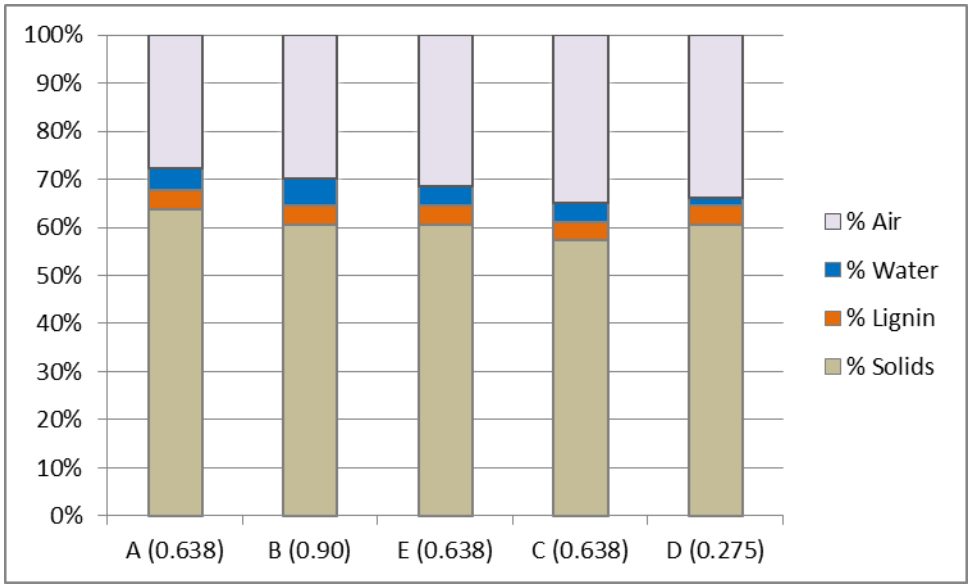

Figure 4-13: Phase Diagram for χ_l = 4%

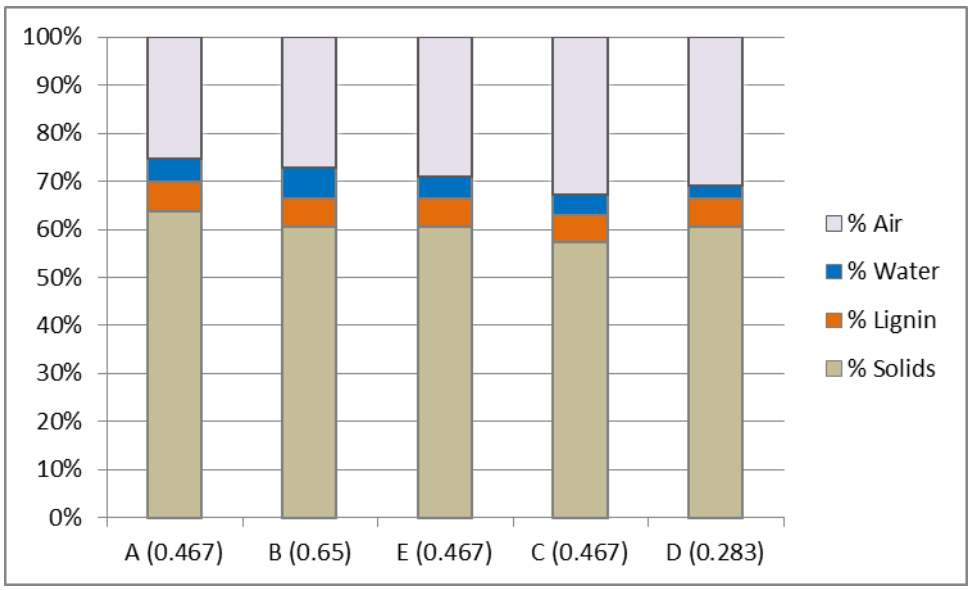

Figure 4-14: Phase Diagram for χ_l = 6%

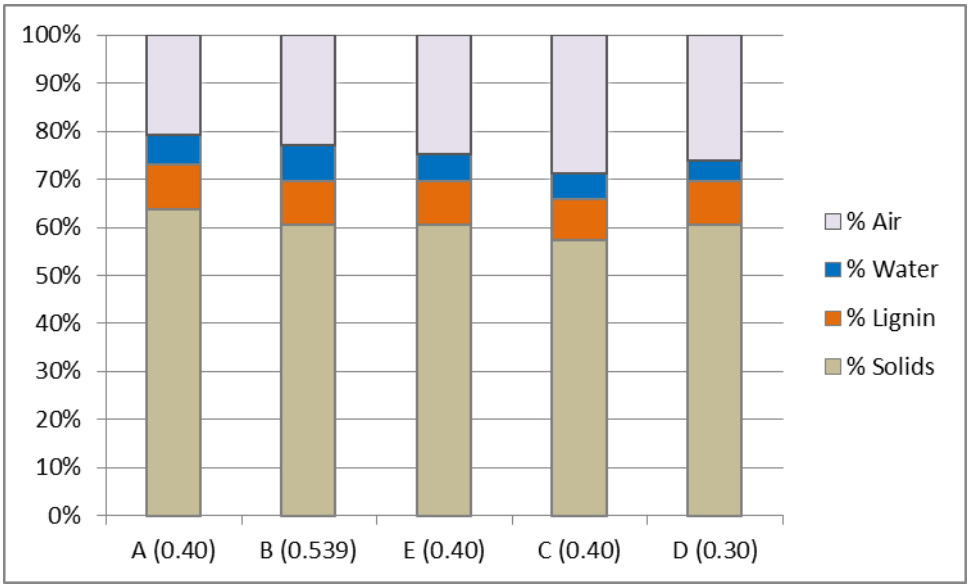

Figure 4-15: Phase Diagram for χ_l = 9%

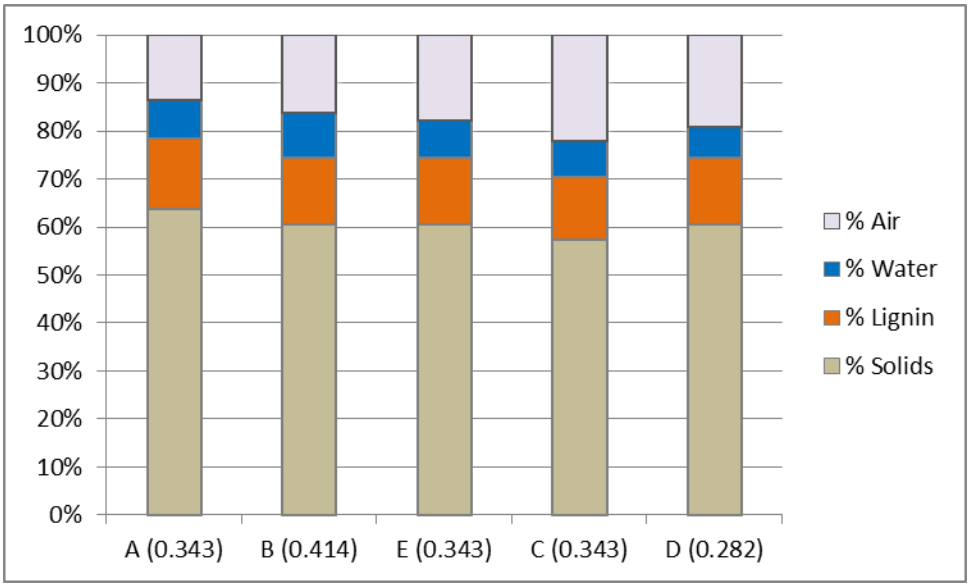

Figure 4-16: Phase Diagram for χ_l = 14%

4.2.3 Direct Shear Apparatus Preparation

The direct shear apparatus is turned on along with the ADU and computer prior to testing. The DS7 software must be loaded as well. After the sample is prepared in the shear box, the machine is set up, and the computer settings are ready, the sample is ready to be mounted in the shear box carriage on the direct shear apparatus.

The box is lifted by the two "lugs" and placed in a level manner into the carriage, as shown in Figure 4-8. The two adjustment screws below the swan neck yoke are tightened to secure the shear box.

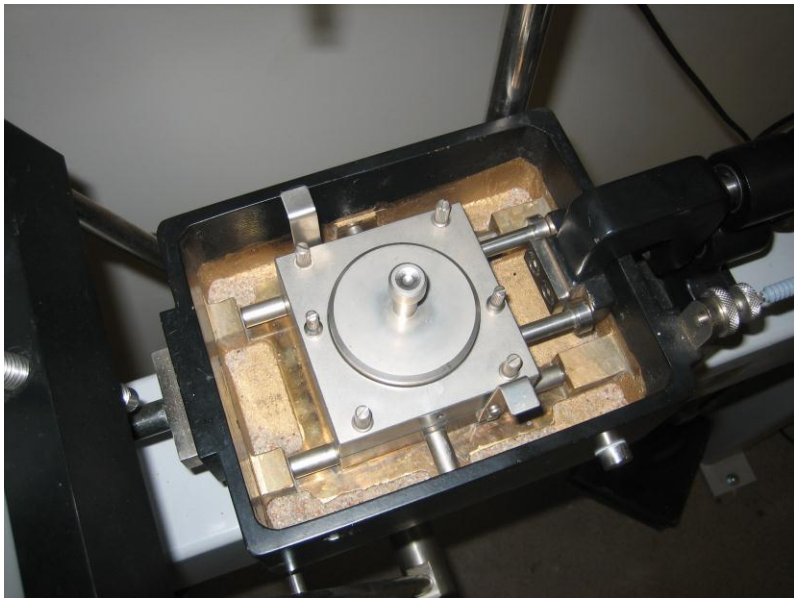

Figure 4-17: Photograph of Shear Box Placed into Carriage

After the shear box is placed into the carriage, the loading frame is fixed in the testing position, with the load application screw fitting into the indention on the load pad on the sample just tight enough to hold it in position. The vertical LVDT assembly is then adjusted so as to center the tip on the top of the load screw. If the jack screw is still properly secured, the desired amount of weight is placed on the load hanger.

4.2.4 Direct Shear Apparatus Test Procedure

The testing procedure consists of five stages that the software guides the user through sequentially. The first stage is the test initialization. Sample weight, height, and specimen condition (dry, wet, etc.) are input into the program.

4.2.5 Consolidation Stage

The consolidation stage can be used to calculate the rate of displacement using the square-root-of time method as a result of finding the value of t_{90}, (the time for 90% consolidation), and dD/dt, the rate of vertical displacement. The jack screw is carefully released and the normal force is applied to the sample. The consolidation stage was allowed to run until the vertical deformation visibly ceased (based on the reading from the computer screen display). The DS7 software collects the amount of vertical displacement and plots it versus the square root time on the computer screen. The rate of displacement is calculated from this plot. The rate of displacement is then input into the digital input on the machine.

While the program provides a reliable method for calculating rate of displacement, typically in the range of 0.25 to 0.45 mm/min, this value was not used for this study. Since the sand-lignin mixture contained more than 5% fines therefore the rate should be calculated as dense sand with fines, by ASTM D-3080. ASTM states that the displacement rate, d_r, is equal to d_f/t_f, which is shear displacement at failure divided by time to failure. Conservative estimates of time to failure needed to ensure fully drained conditions are estimated to be 60 minutes with the displacement to failure estimate equal to 5 mm, resulting in an estimated rate of 0.083 mm/min. Therefore the conservative estimated displacement rate that was used for all direct shear tests is 0.08 mm/min.

4.2.6 Shear Stage

The shear stage is the stage of the test which leads to soil failure. A logging rate of 0.008 mm/min was used to ensure that a sufficient amount of data is collected. To begin the test, the locking pins are removed and the Teflon-tipped spacing screws are tightened and released to separate the two halves of the shear box. The test is then initiated and allowed to continue to failure, which occurs when the real-time plot of shear stress versus horizontal displacement

reaches an apparent maximum or approximately constant value for a significant amount of horizontal displacement.

4.2.7 Final Measurements

The final stage of the program allows the user to interpret the maximum shear stress and the corresponding shear displacement. A test report that includes a consolidation plot, a shear stress versus horizontal displacement plot, and a vertical displacement versus horizontal displacement plot can then be generated. Multiple tests at different confining pressures for a given sample configuration can be grouped together to determine an angle of friction and cohesion of the sample. While the DS7 software provides an acceptable plot of the cohesion and angle of friction, the parameters for this study were determined using linear regression analysis in Microsoft Excel.

Chapter 5 - Experimental Results

The direct shear tests were performed on sand-lignin mixes having gravimetric lignin contents of 0, 2, 4, 6, 9 and 14%. Each sand-lignin mixture was tested at five configurations, which were described in more detail in Tables 4-2 and 4-3, and Figures 4-11 through 4-16. For each configuration five specimens were tested corresponding to the normal stresses of 62.0, 92.9, 123.9, 185.9, and 247.6 kPa.

5.1 Direct Shear Test Results

Shear force, horizontal and vertical displacements were continuously recorded during the shear phase of direct shear tests by using the DataSystem 7 Geotechnical software. Failure was defined by the first attainment of the maximum shear stress. The corresponding horizontal and vertical displacements were also recorded.

Results for gravimetric lignin contents of 0, 2, 9, and 14% results are presented in Figures 5-1 through 5-36 as shear stress versus horizontal displacement for each configuration at each confining stress and as vertical displacement versus horizontal displacement for each configuration point at each confining stress. The corresponding plots for gravimetric lignin contents of 4 and 6% are included in Appendix A due to the repetitive nature of the plots. It should be noted that an increase in the sample thickness indicates dilation, which is negative herein. A decrease in the sample thickness represents compaction, which is positive.

5.1.1 Gravimetric Lignin Content (0%)

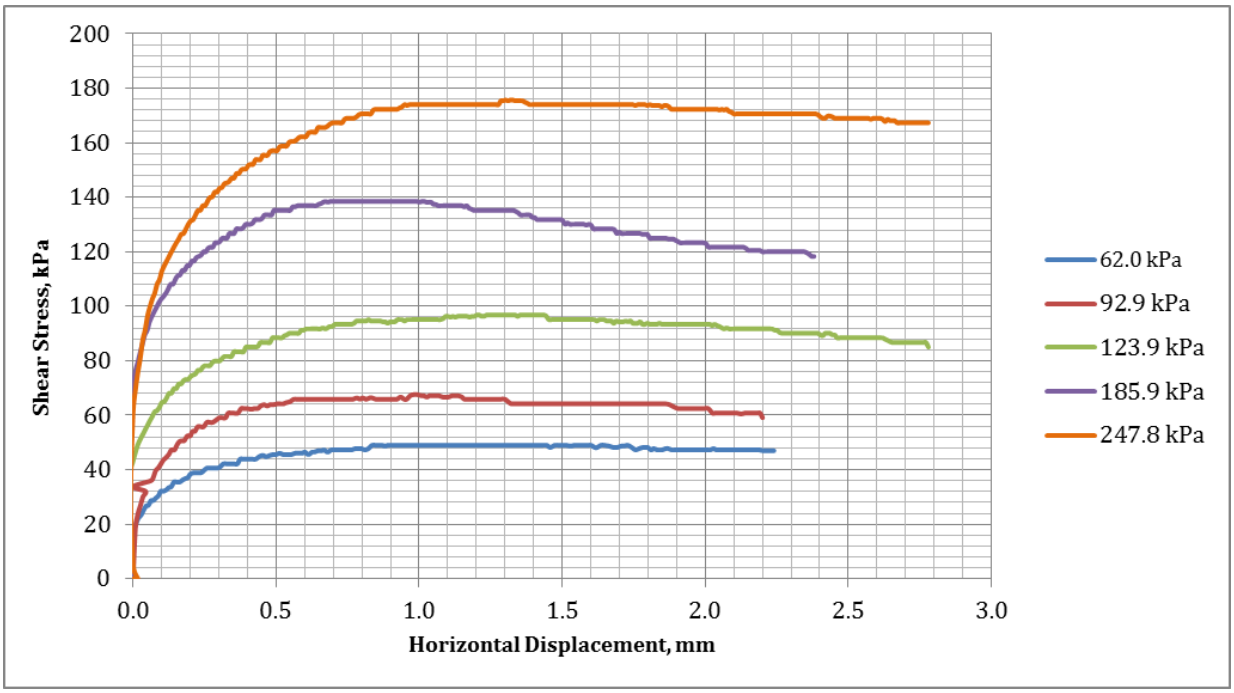

Figure 5-1: Shear Stress vs. Horizontal Displacement, χ_l = 0% (A)

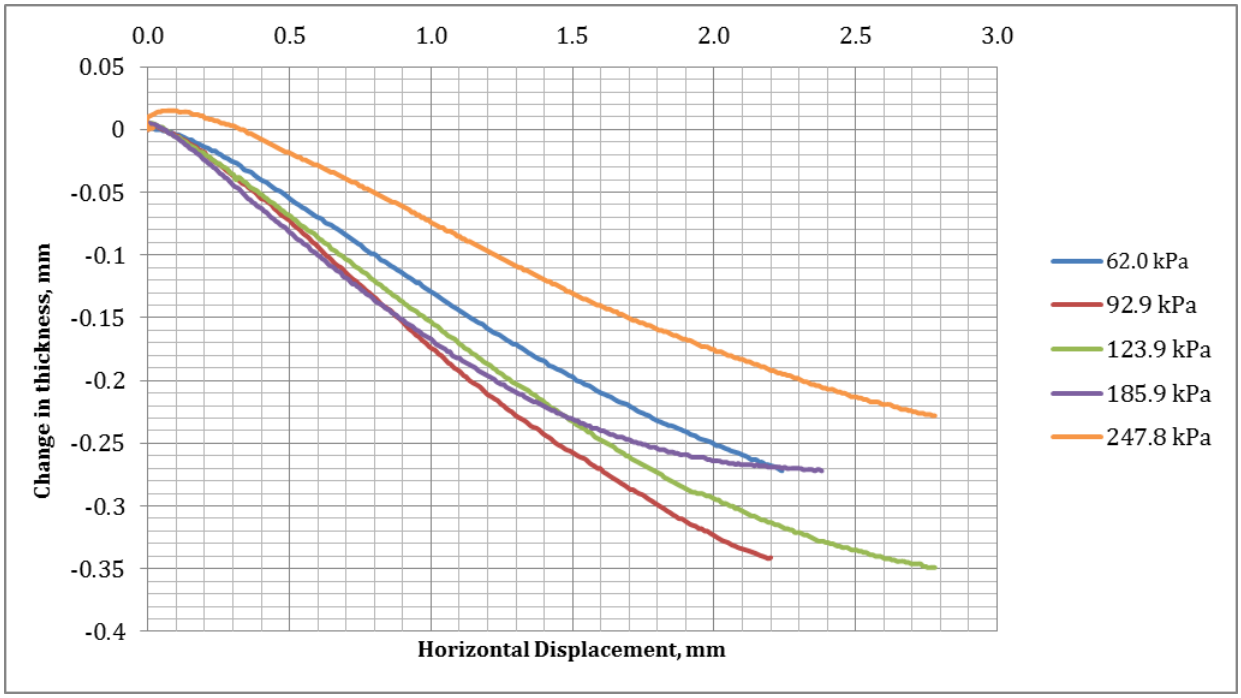

Figure 5-2: Change in Thickness vs. Horizontal Displacement, χ_l = 0% (A)

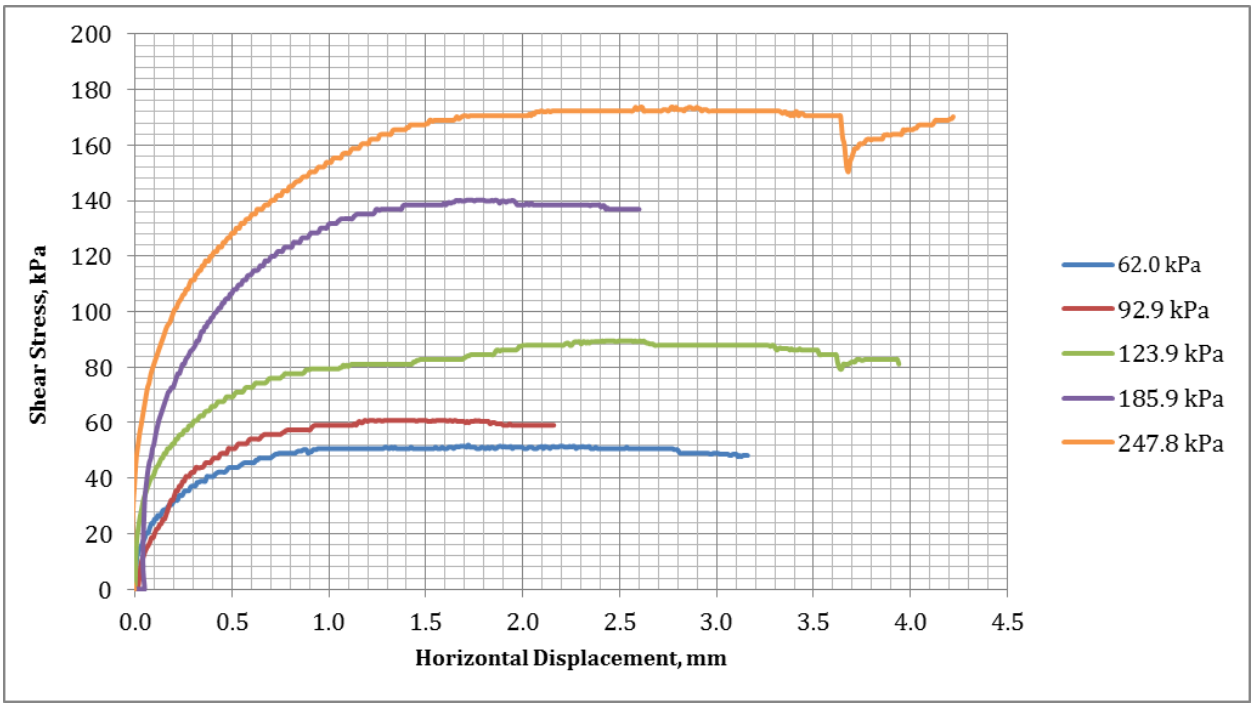

Figure 5-3: Shear Stress vs. Horizontal Displacement, χ_l = 0% (E)

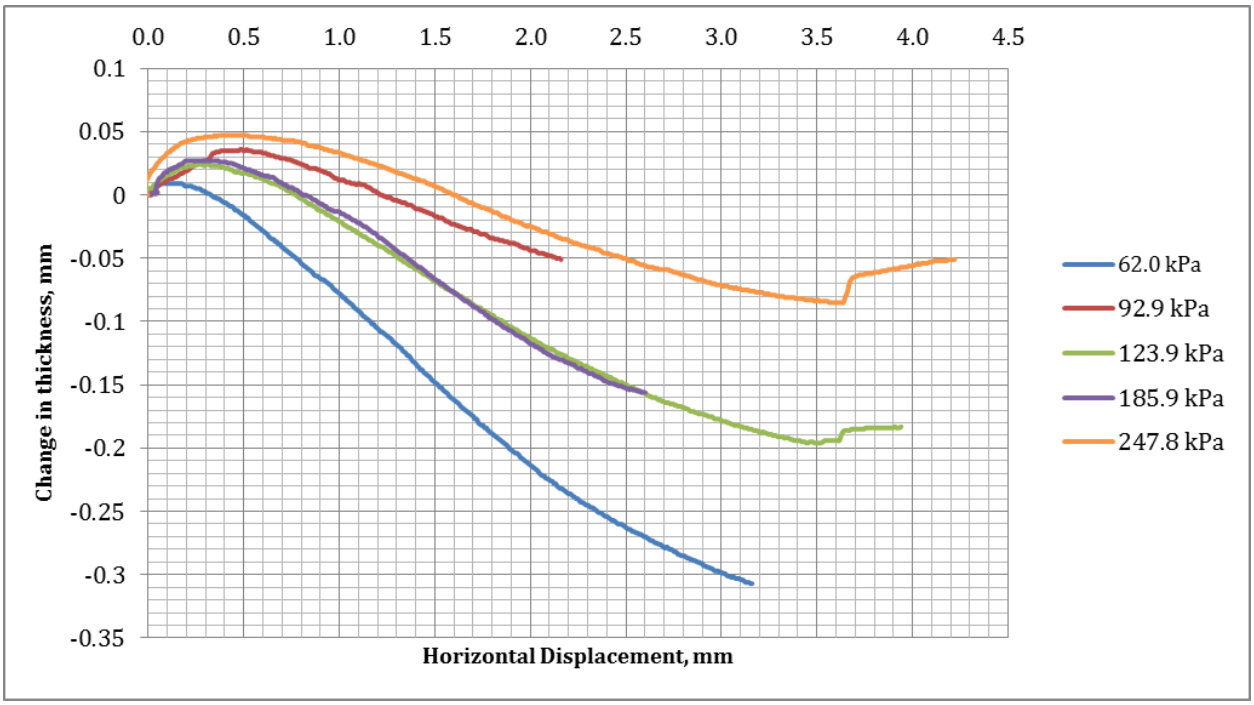

Figure 5-4: Change in Thickness vs. Horizontal Displacement, χ_l = 0% (E)

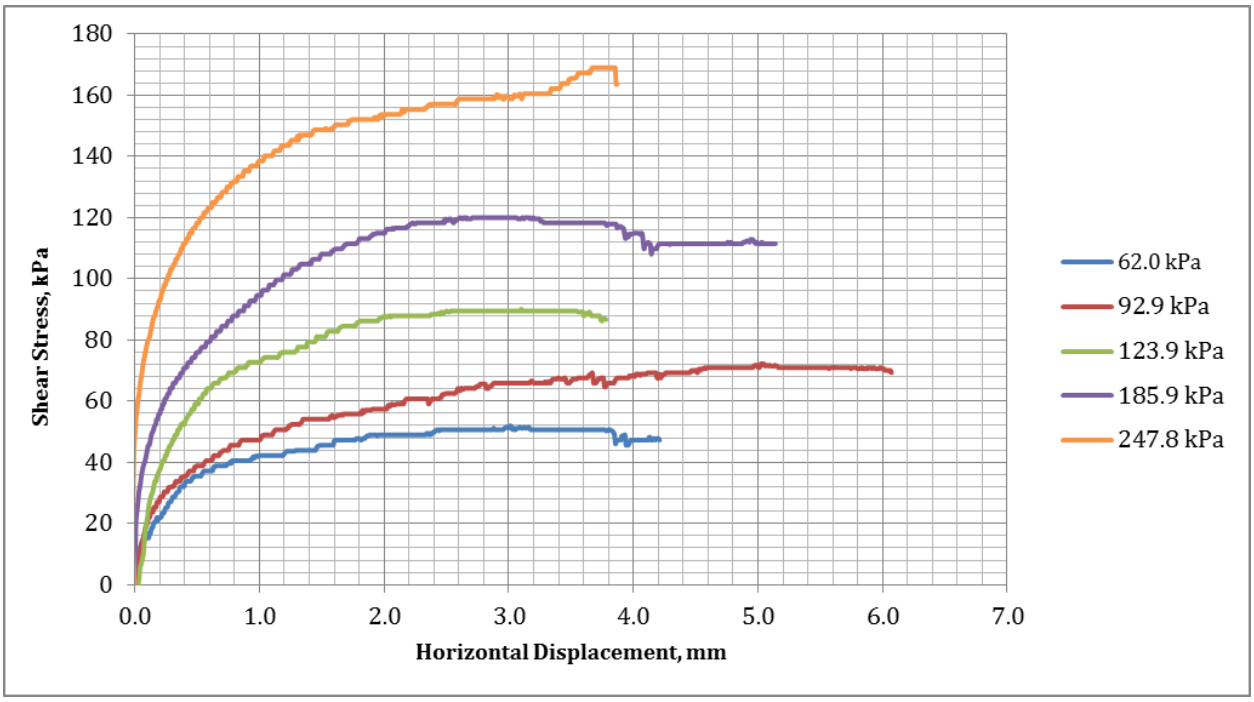

Figure 5-5: Shear Stress vs. Horizontal Displacement, χ_I = 0% (C)

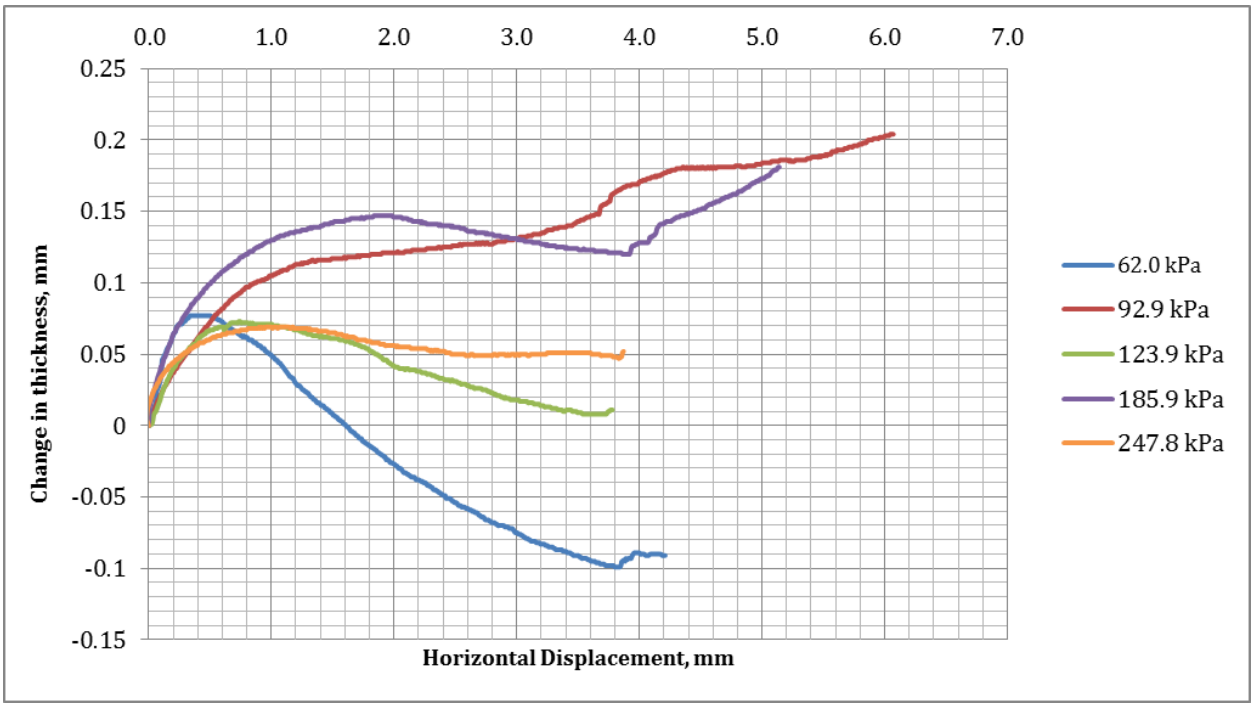

Figure 5-6: Change in Thickness vs. Horizontal Displacement, χ_I = 0% (C)

5.1.2 Gravimetric Lignin Content (2%)

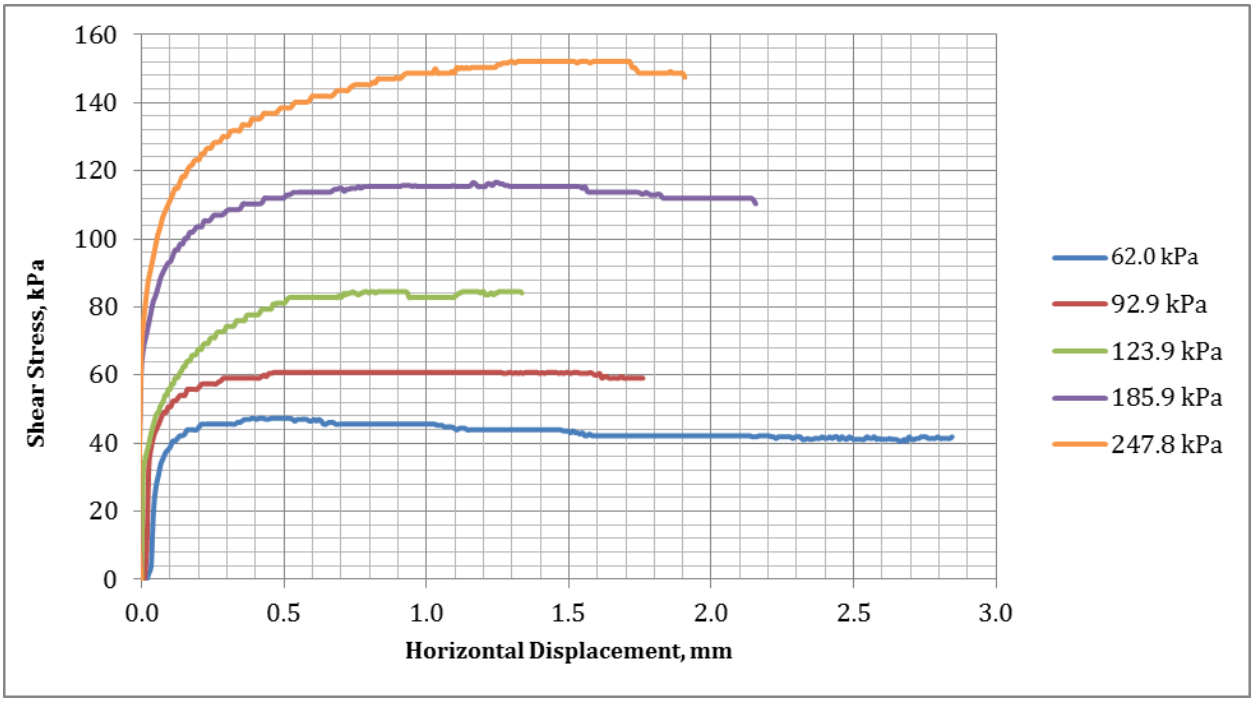

Figure 5-7: Shear Stress vs. Horizontal Displacement, χ_l = 2% (A)

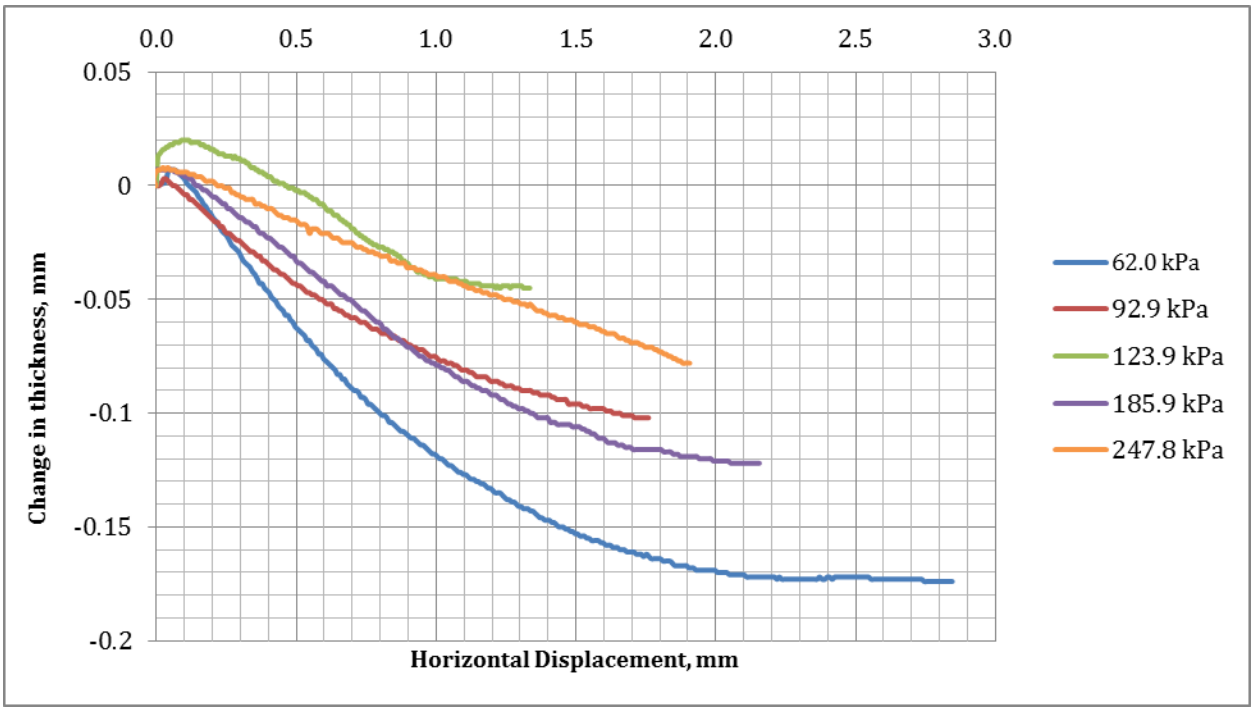

Figure 5-8: Change in Thickness vs. Horizontal Displacement, χ_l = 2% (A)

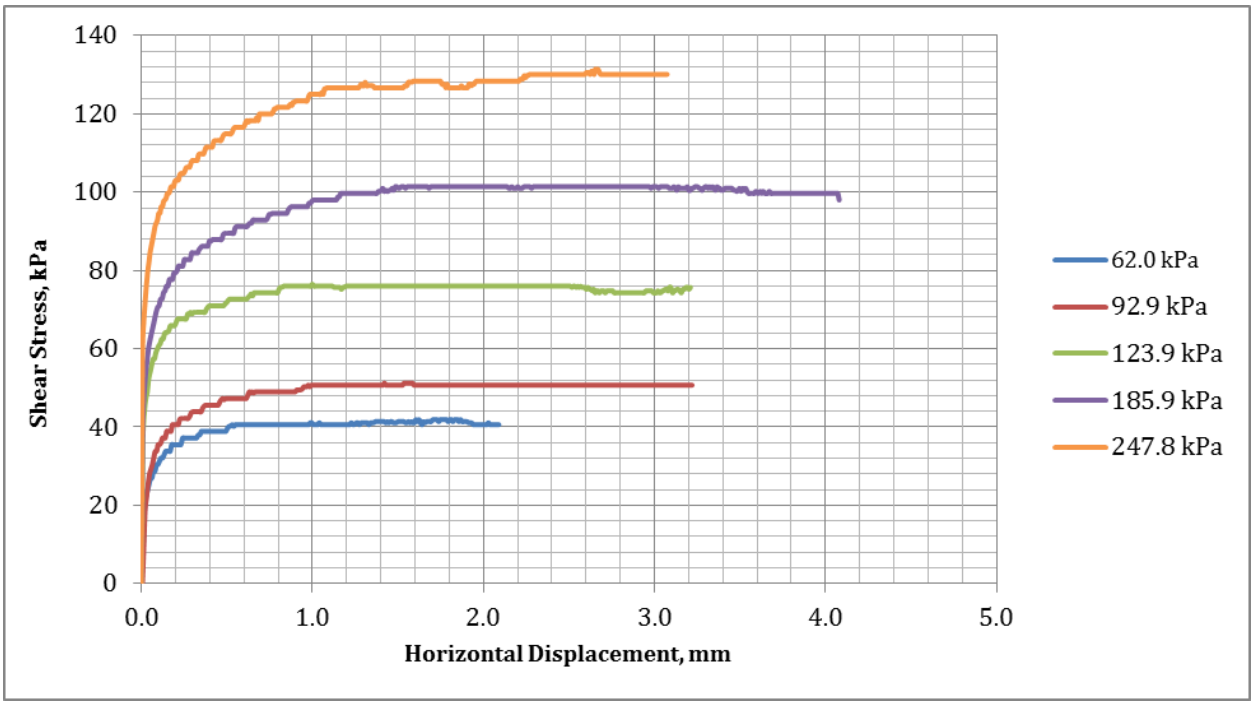

Figure 5-9: Shear Stress vs. Horizontal Displacement, χ_J = 2% (E)

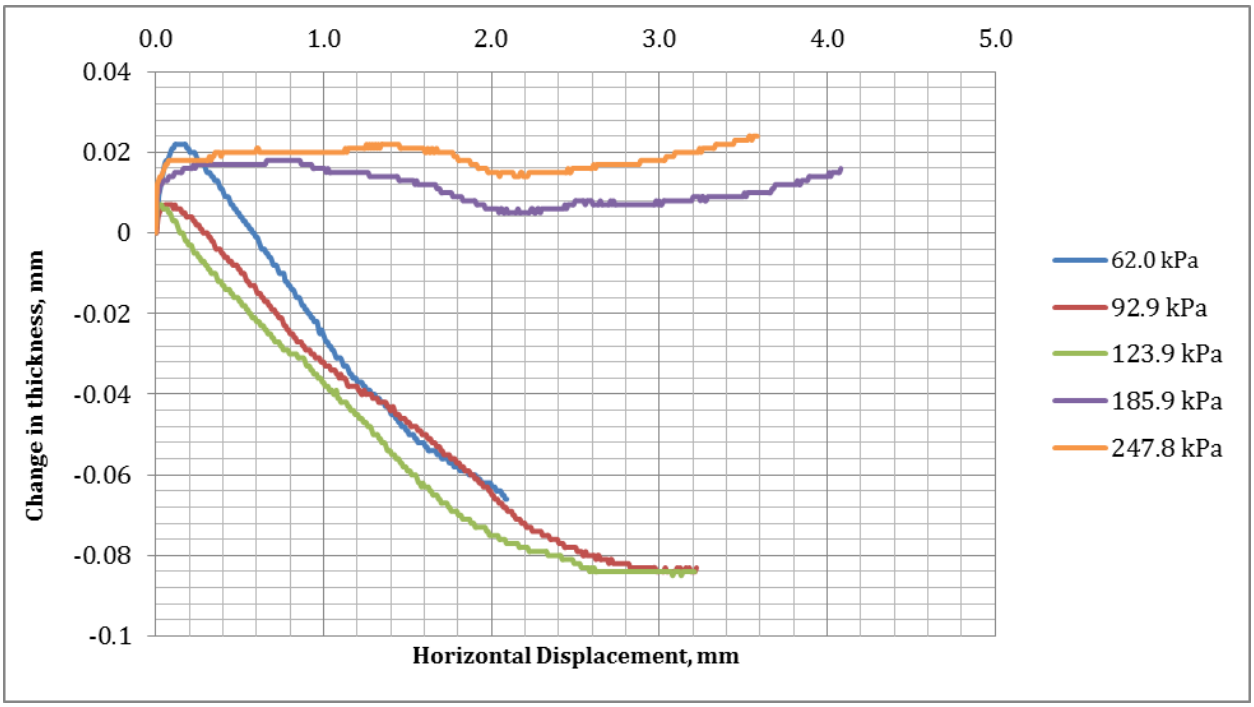

Figure 5-10: Change in Thickness vs. Horizontal Displacement, χ_J = 2% (E)

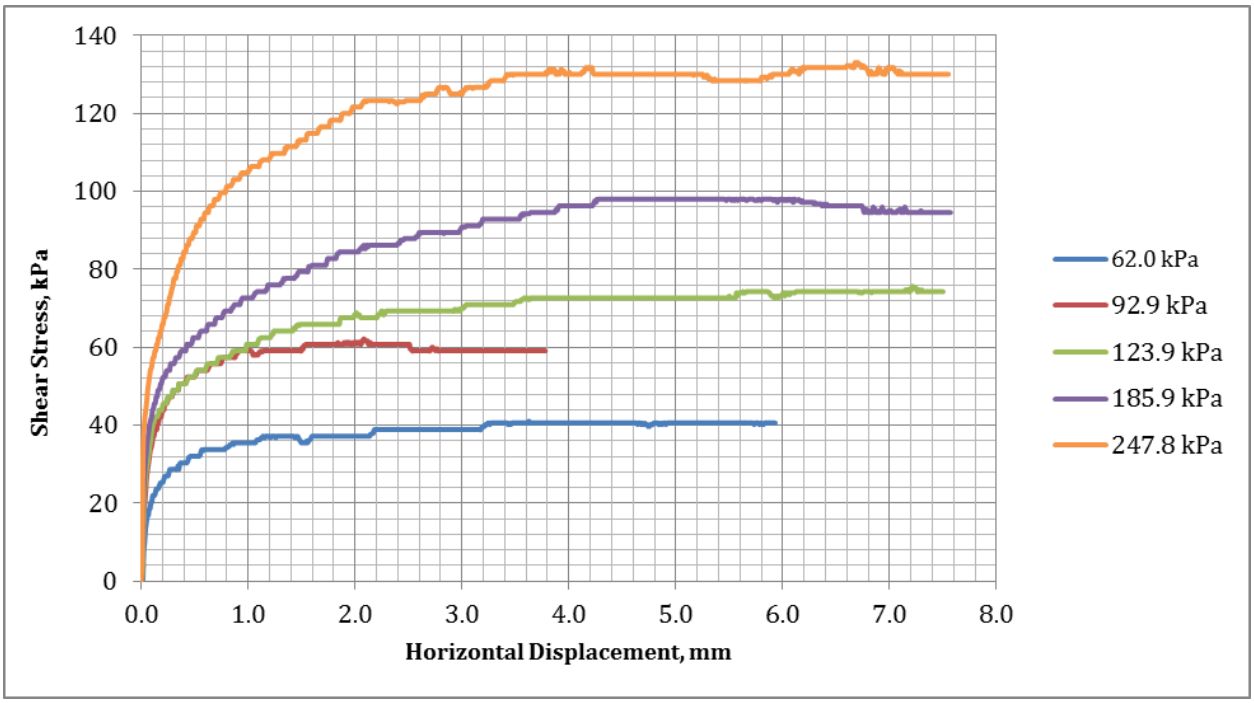

Figure 5-11: Shear Stress vs. Horizontal Displacement, χ_l = 2% (C)

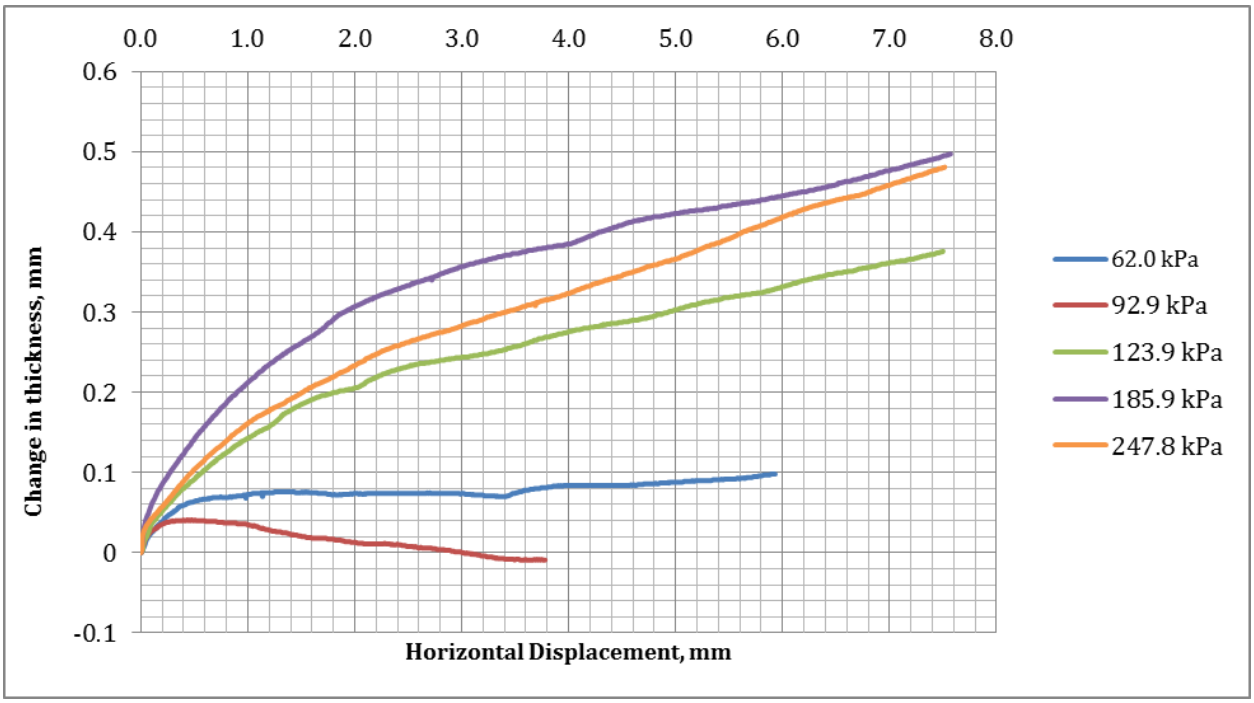

Figure 5-12: Change in Thickness vs. Horizontal Displacement, χ_l = 2% (C)

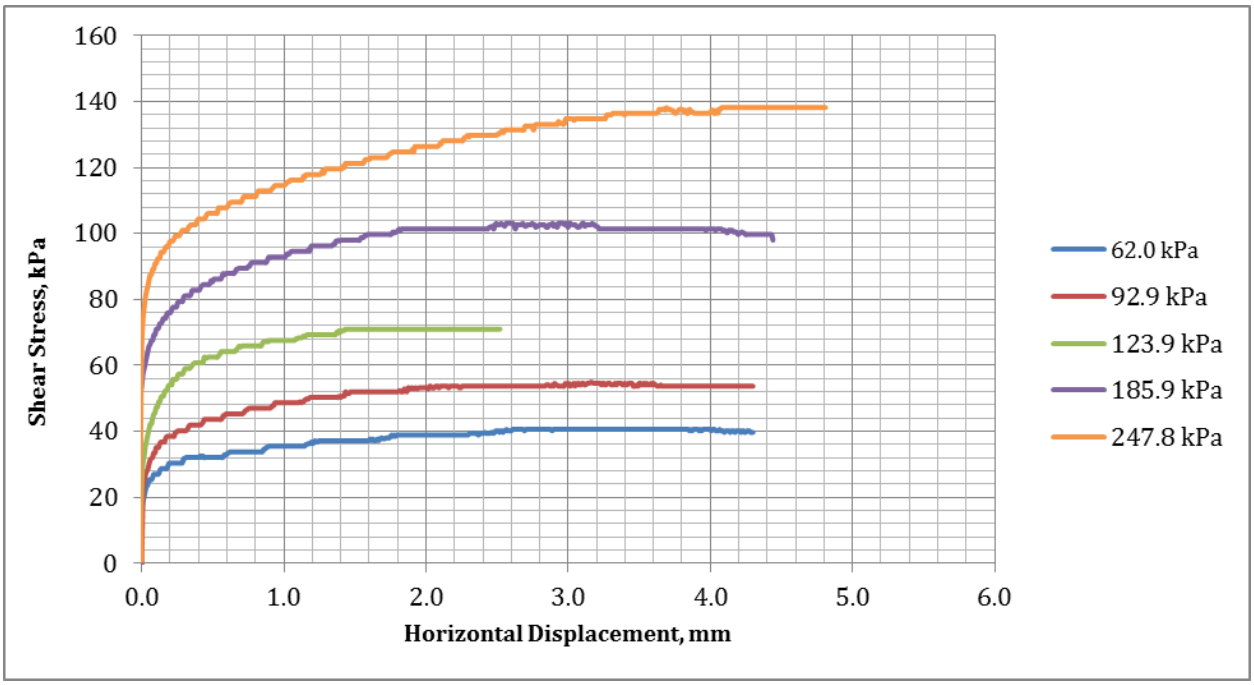

Figure 5-13: Shear Stress vs. Horizontal Displacement, χ_l = 2% (D)

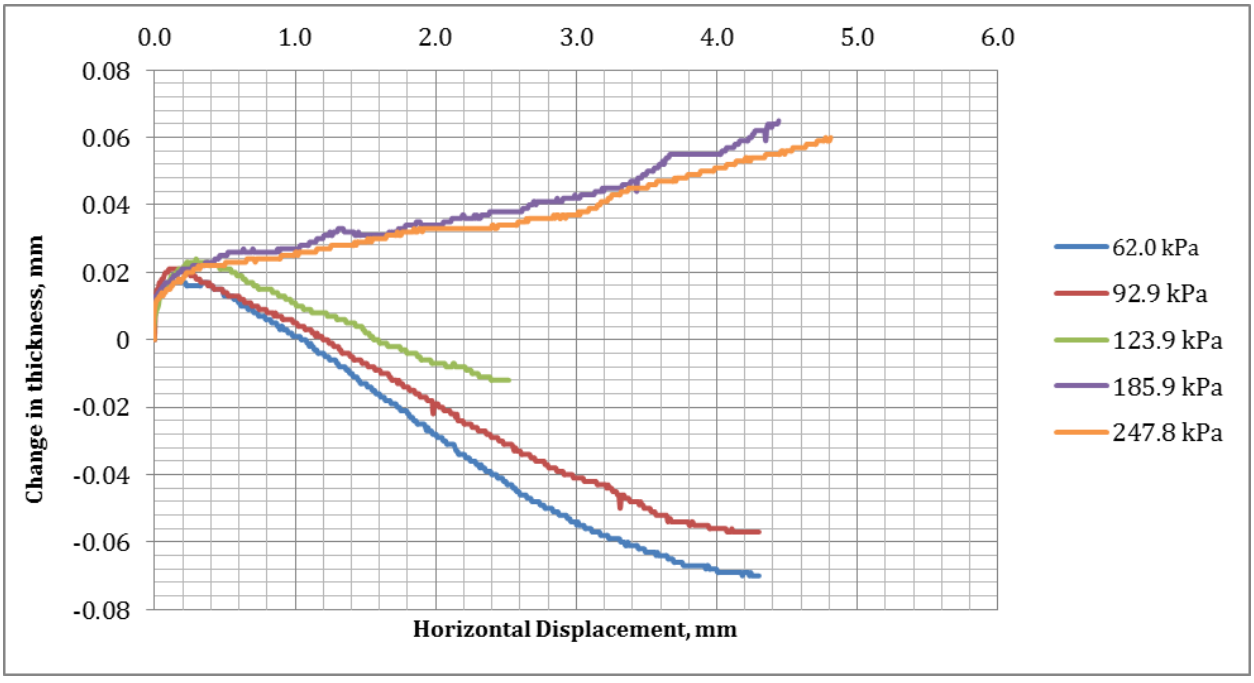

Figure 5-14: Change in Thickness vs. Horizontal Displacement, χ_l = 2% (D)

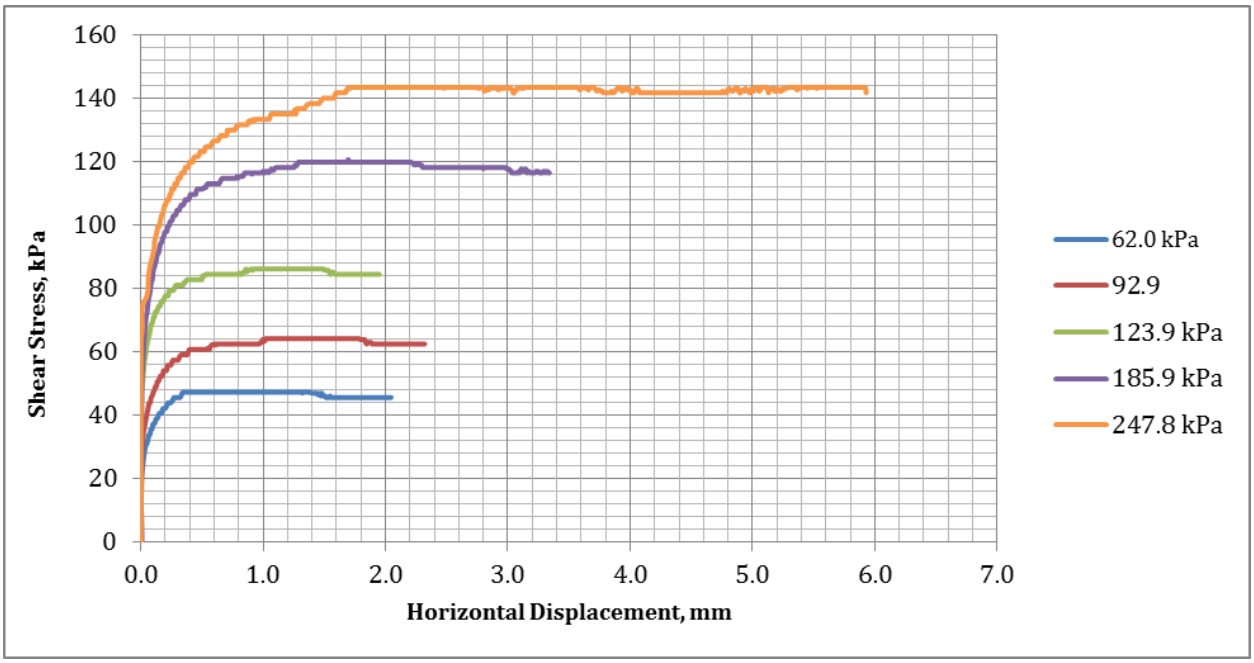

Figure 5-15: Shear Stress vs. Horizontal Displacement, χ_I = 2% (B)

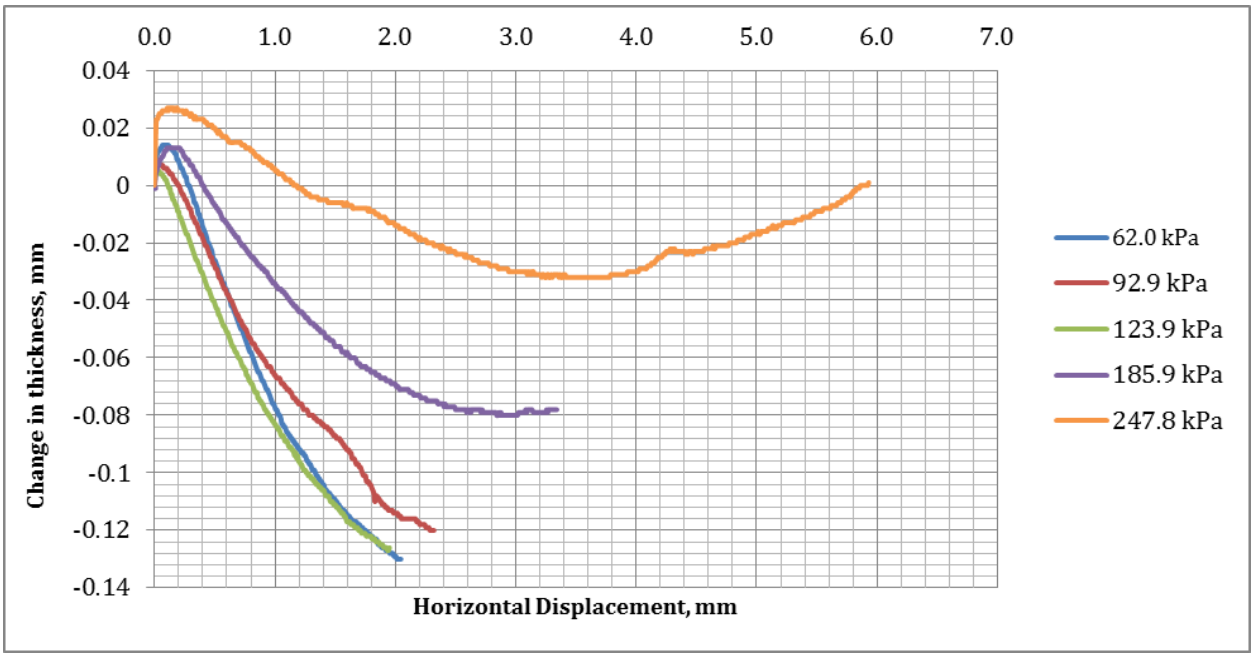

Figure 5-16: Change in Thickness vs. Horizontal Displacement, χ_I = 2% (B)

5.1.3 Gravimetric Lignin Content (9%)

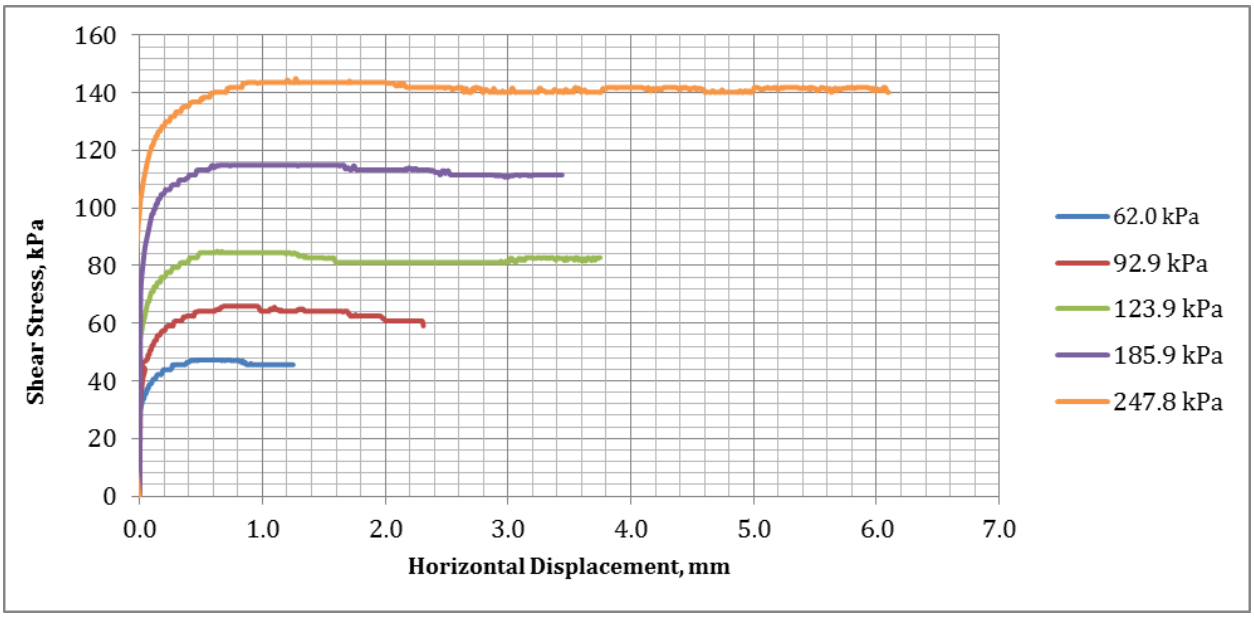

Figure 5-17: Shear Stress vs. Horizontal Displacement, χ_l = 9% (A)

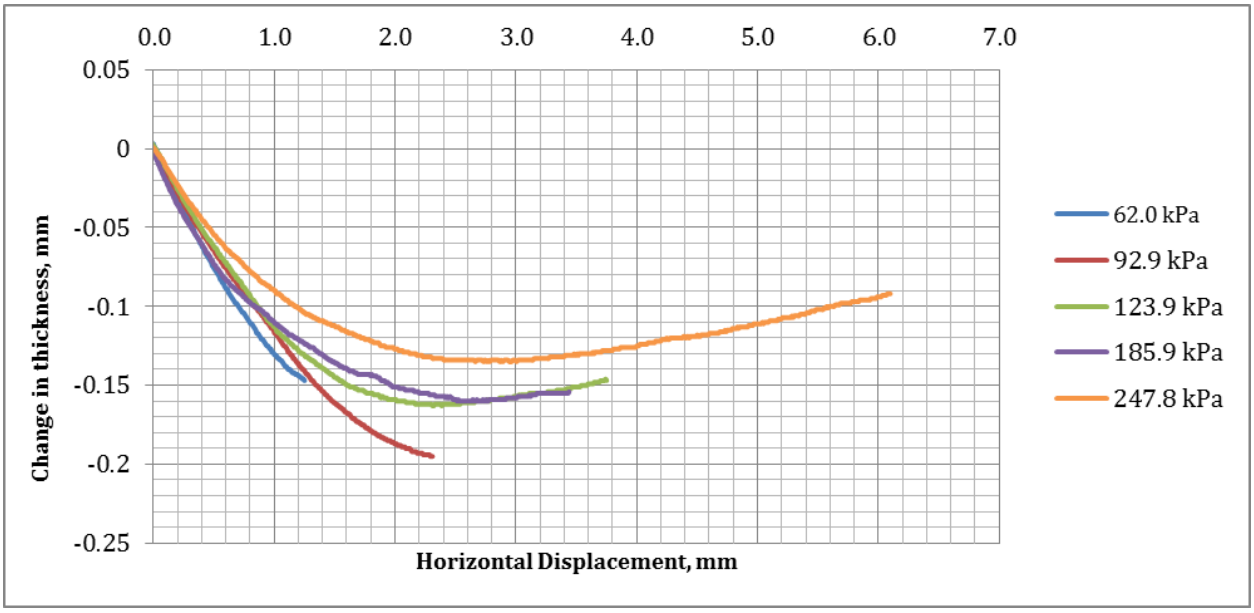

Figure 5-18: Change in Thickness vs. Horizontal Displacement, χ_l = 9% (A)

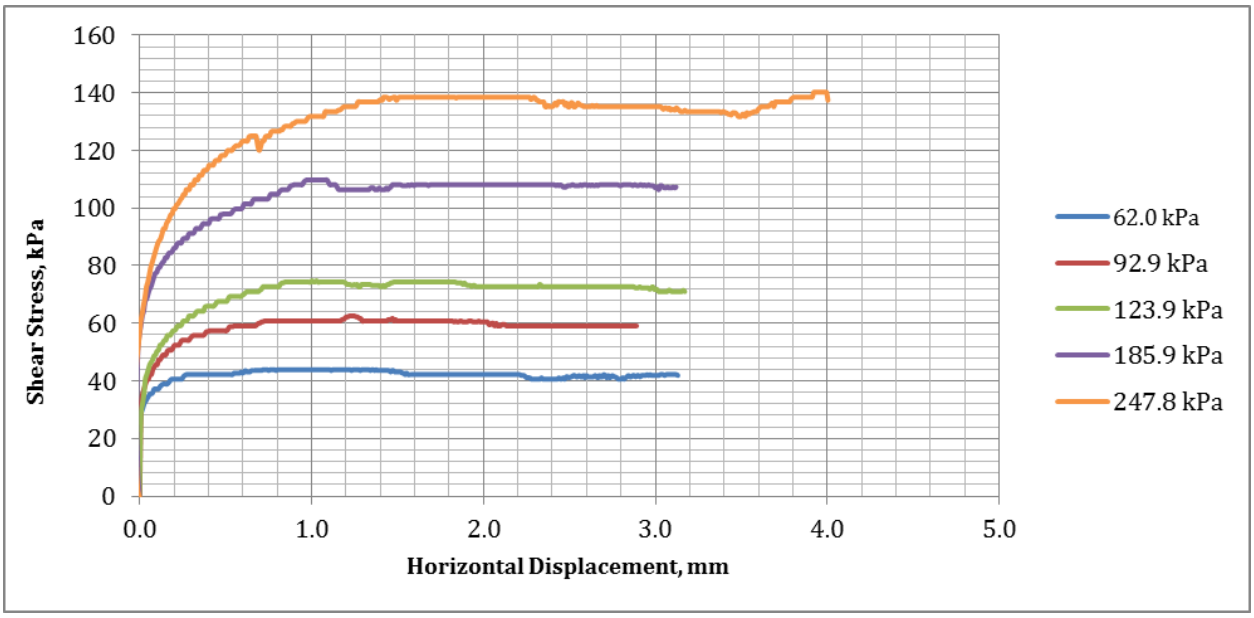

Figure 5-19: Shear Stress vs. Horizontal Displacement, χ_l = 9% (E)

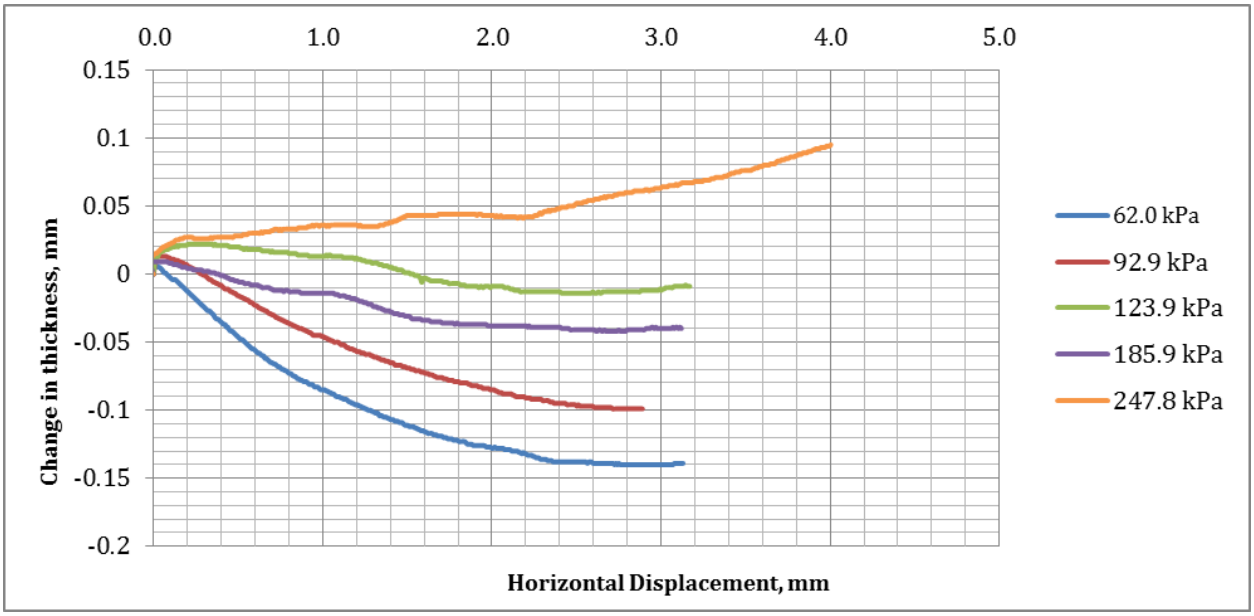

Figure 5-20: Change in Thickness vs. Horizontal Displacement, χ_l = 9% (E)

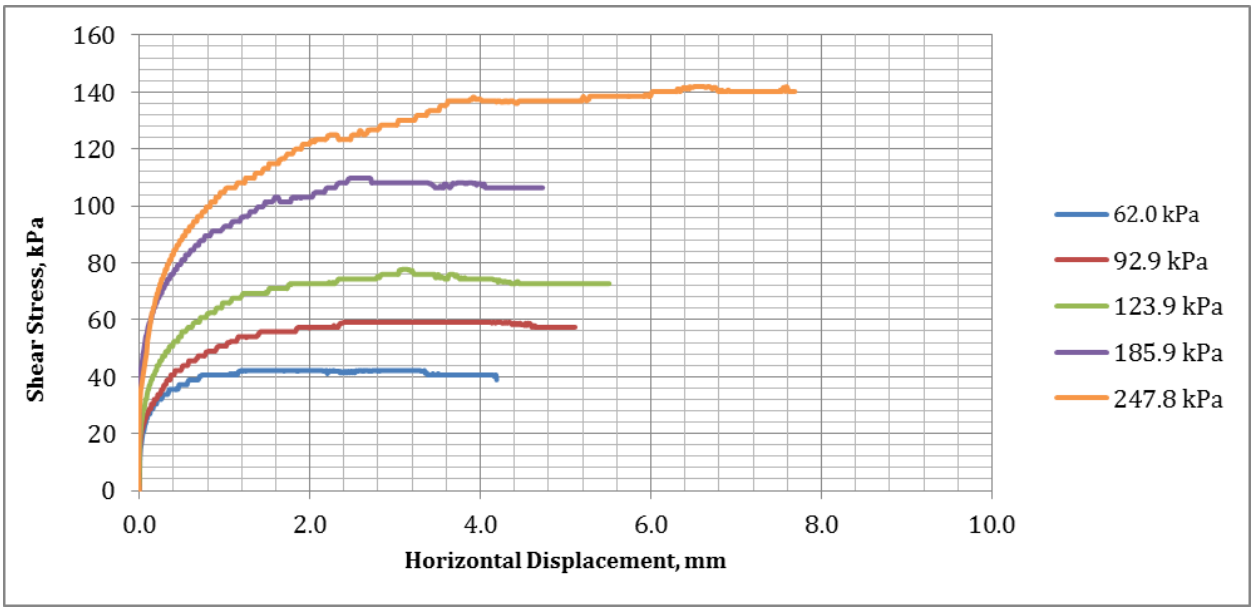

Figure 5-21: Shear Stress vs. Horizontal Displacement s, χ_l = 9% (C)

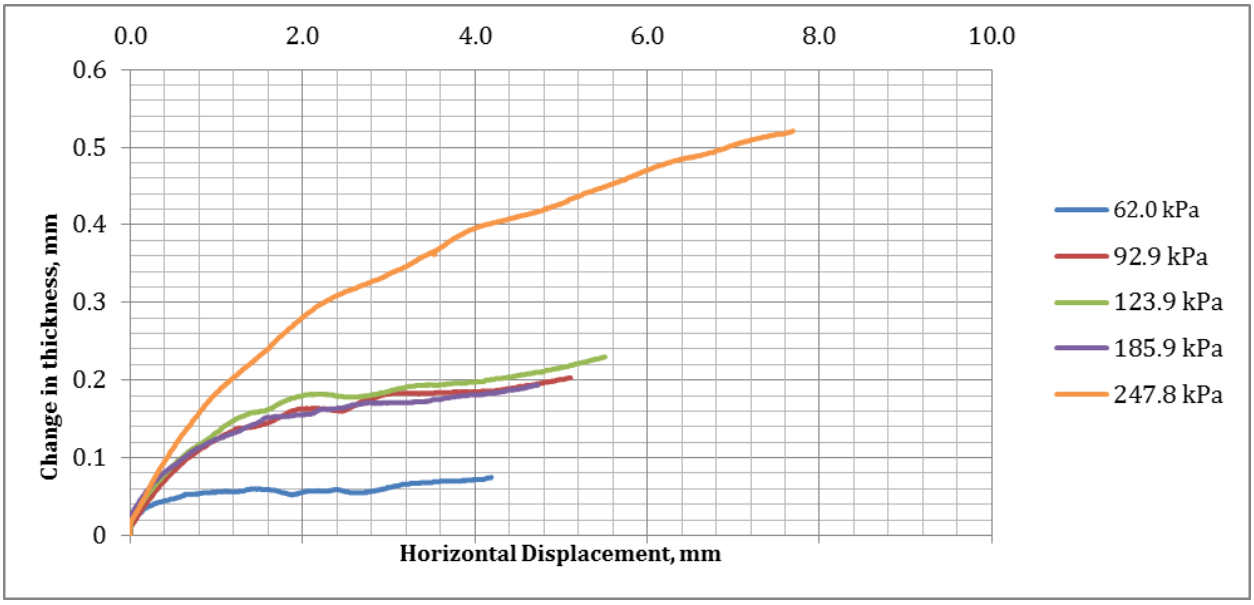

Figure 5-22: Change in Thickness vs. Horizontal Displacement, χ_l = 9% (C)

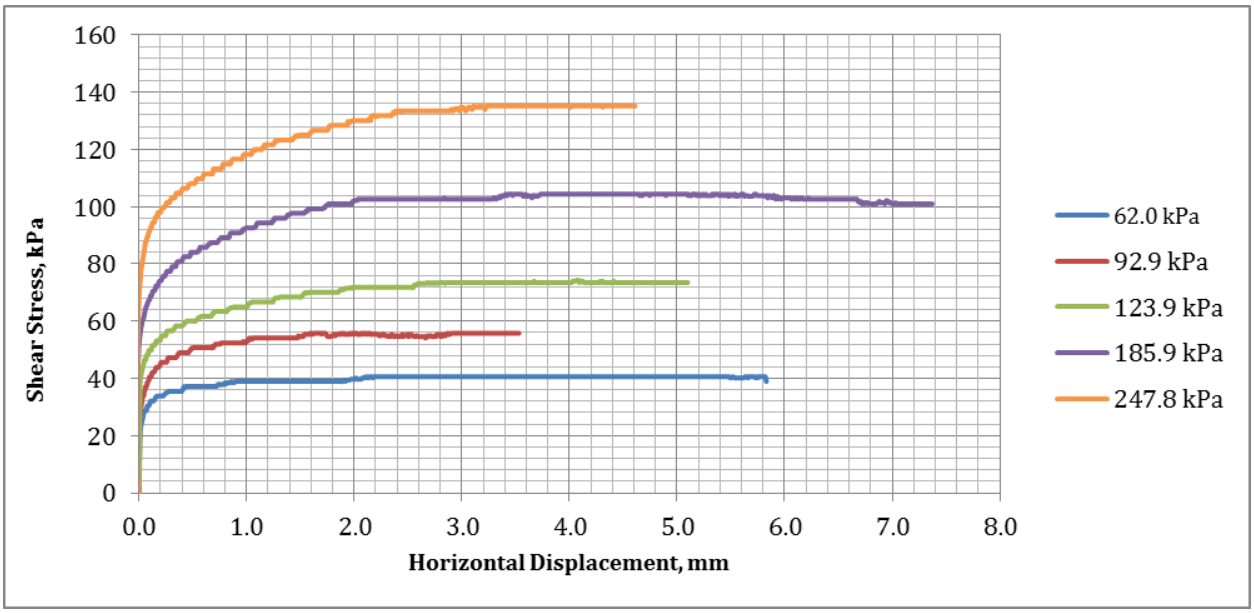

Figure 5-23: Shear Stress vs. Horizontal Displacement, χ_I = 9% (D)

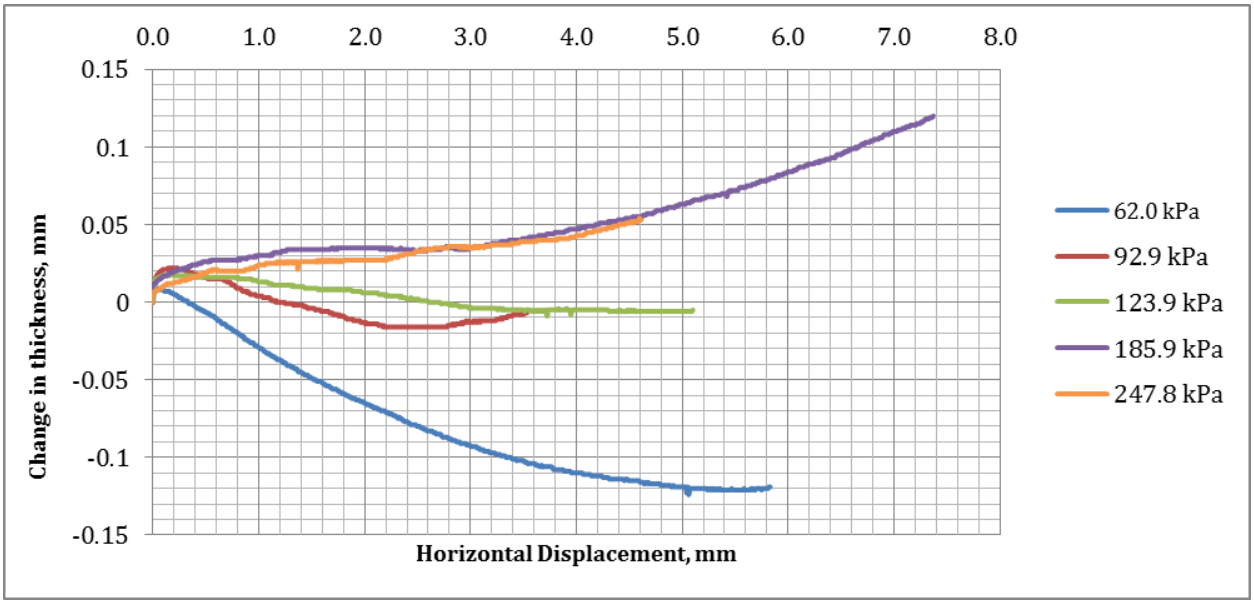

Figure 5-24: Change in Thickness vs. Horizontal Displacement, χ_I = 9% (D)

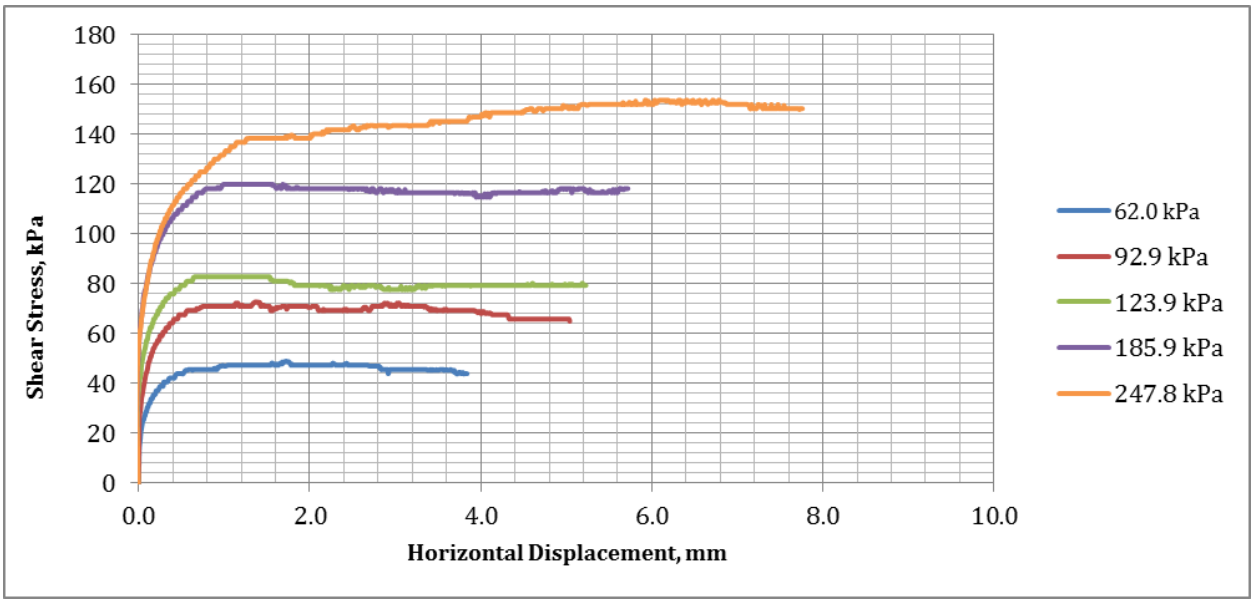

Figure 5-25: Shear Stress vs. Horizontal Displacement, χ_I = 9% (B)

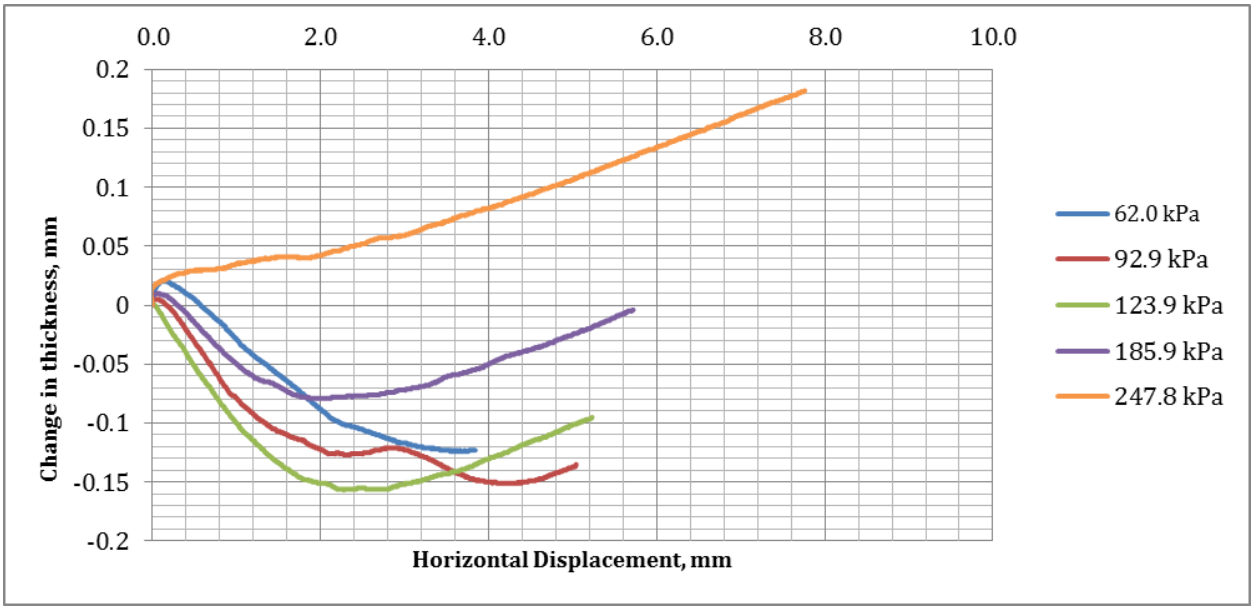

Figure 5-26: Change in Thickness vs. Horizontal Displacement, χ_I = 9% (B)

5.1.4 Gravimetric Lignin Content (14%)

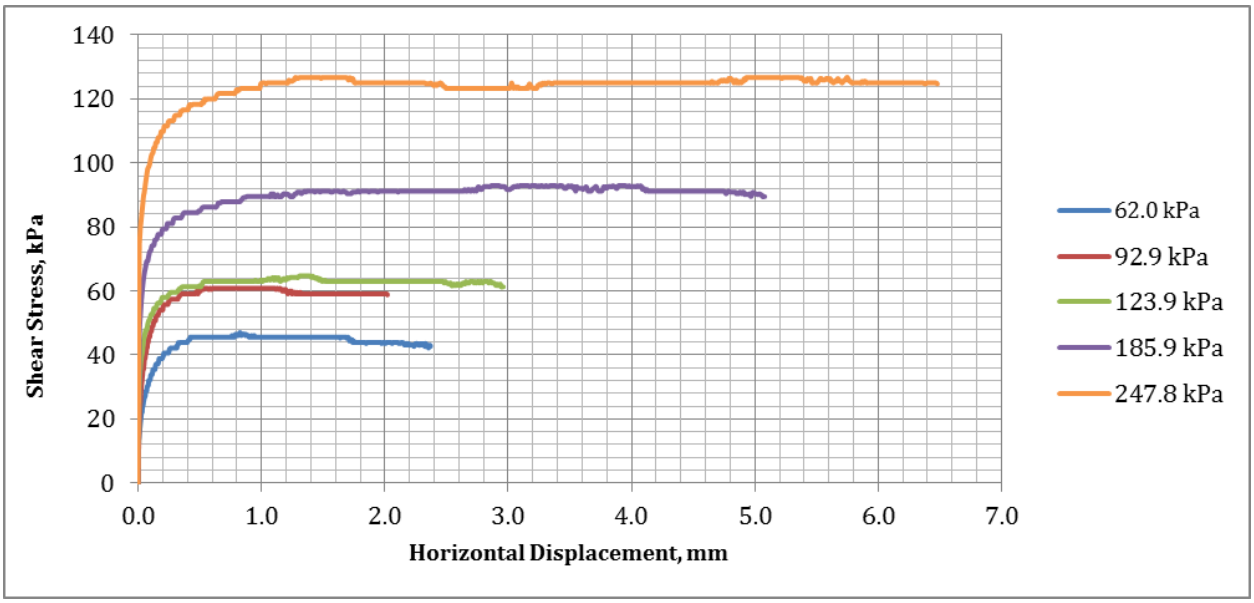

Figure 5-27: Shear Stress vs. Horizontal Displacement, χ_l = 14% (A)

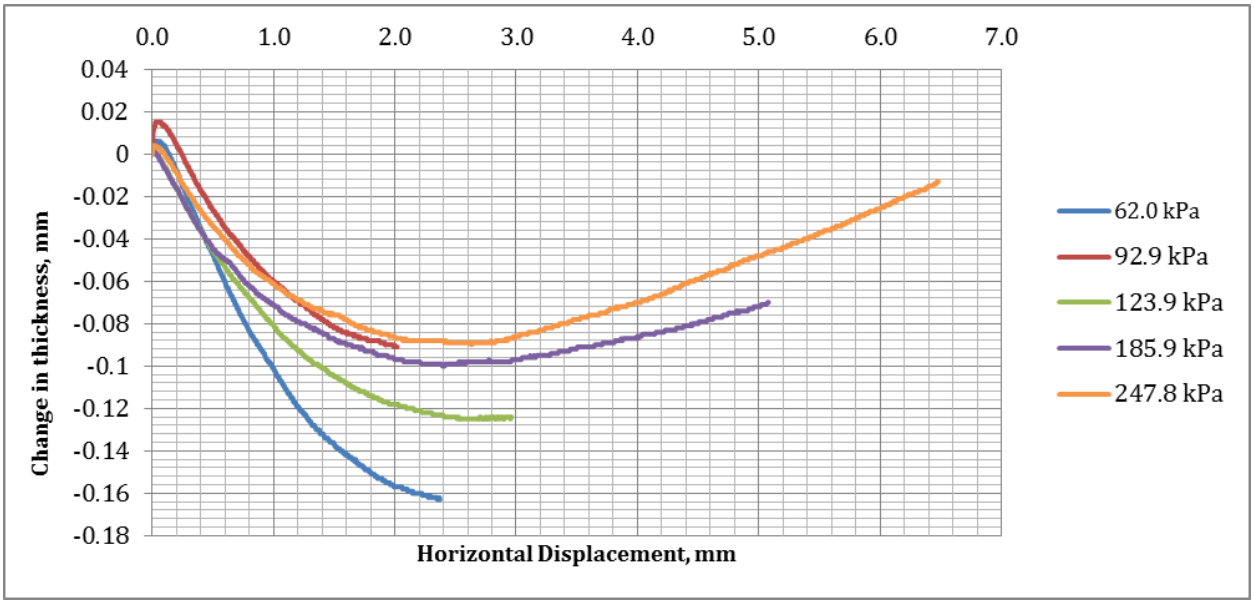

Figure 5-28: Change in Thickness vs. Horizontal Displacement, χ_l = 14% (A)

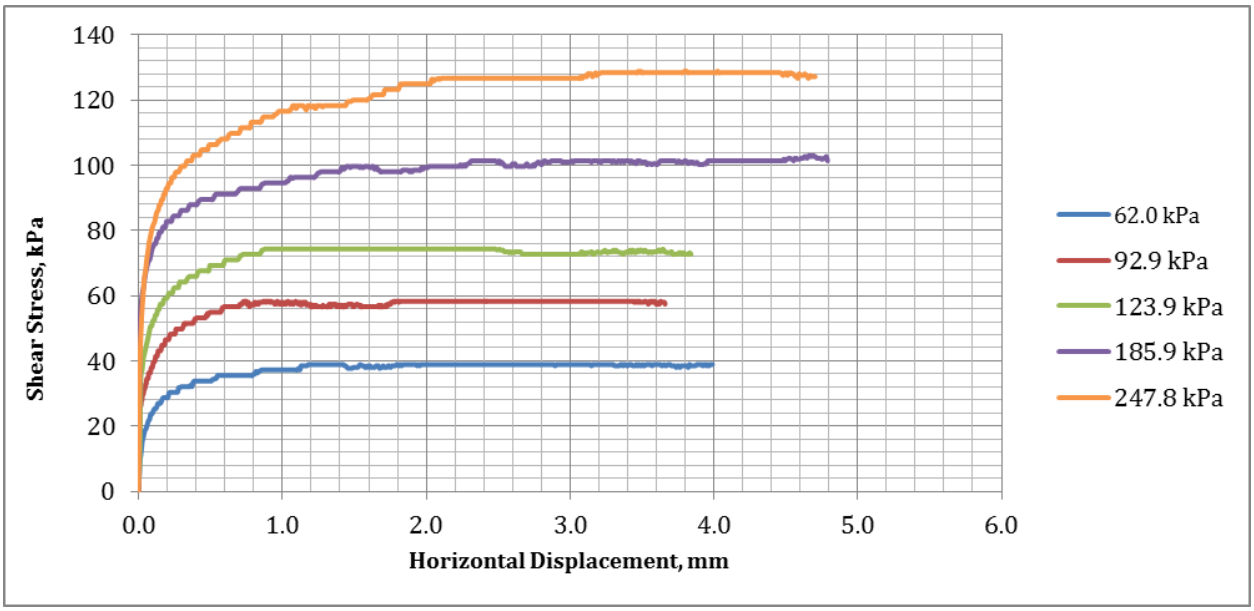

Figure 5-29: Shear Stress vs. Horizontal Displacement, χ_l = 14% (E)

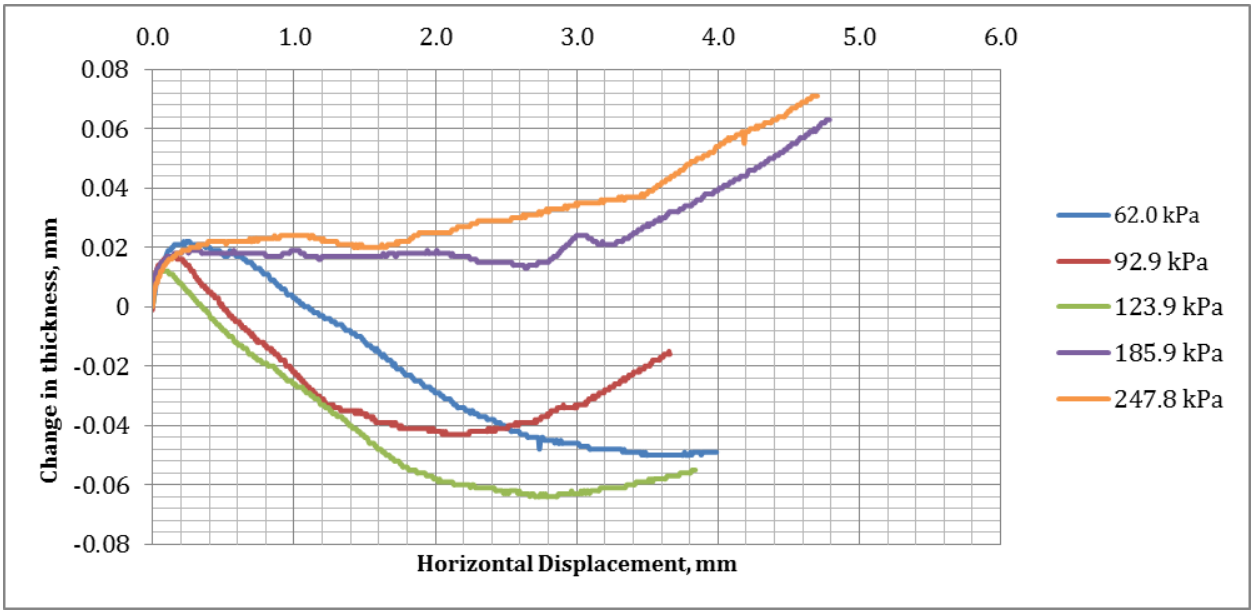

Figure 5-30: Change in Thickness vs. Horizontal Displacement, χ_l = 14% (E)

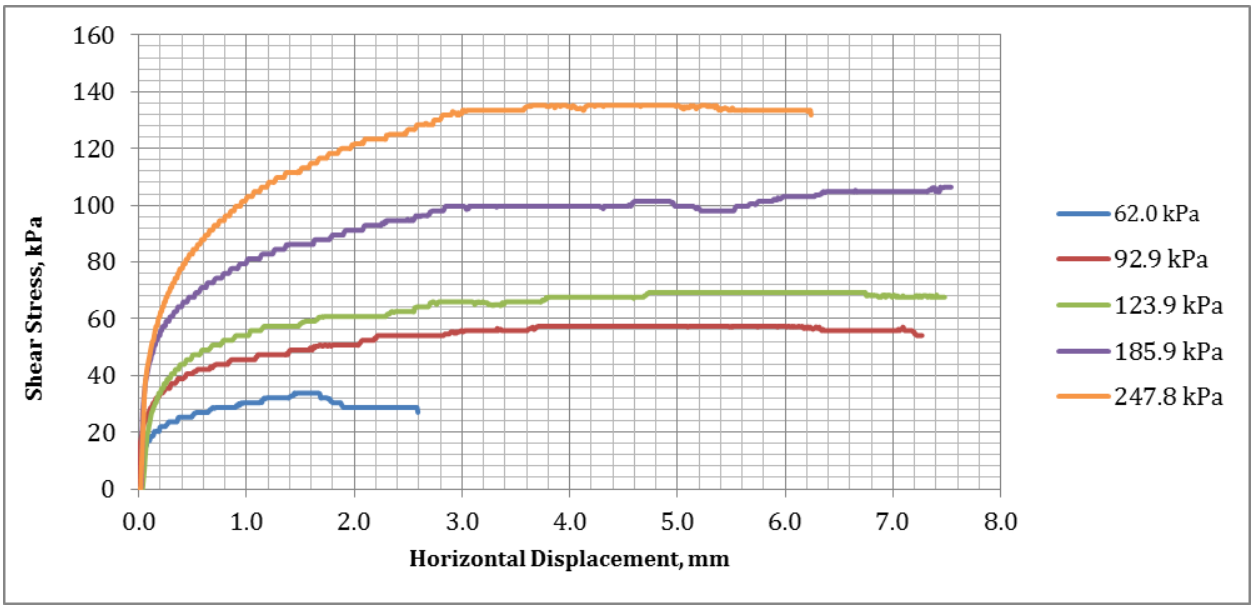

Figure 5-31: Shear Stress vs. Horizontal Displacement, χ_I = 14% (C)

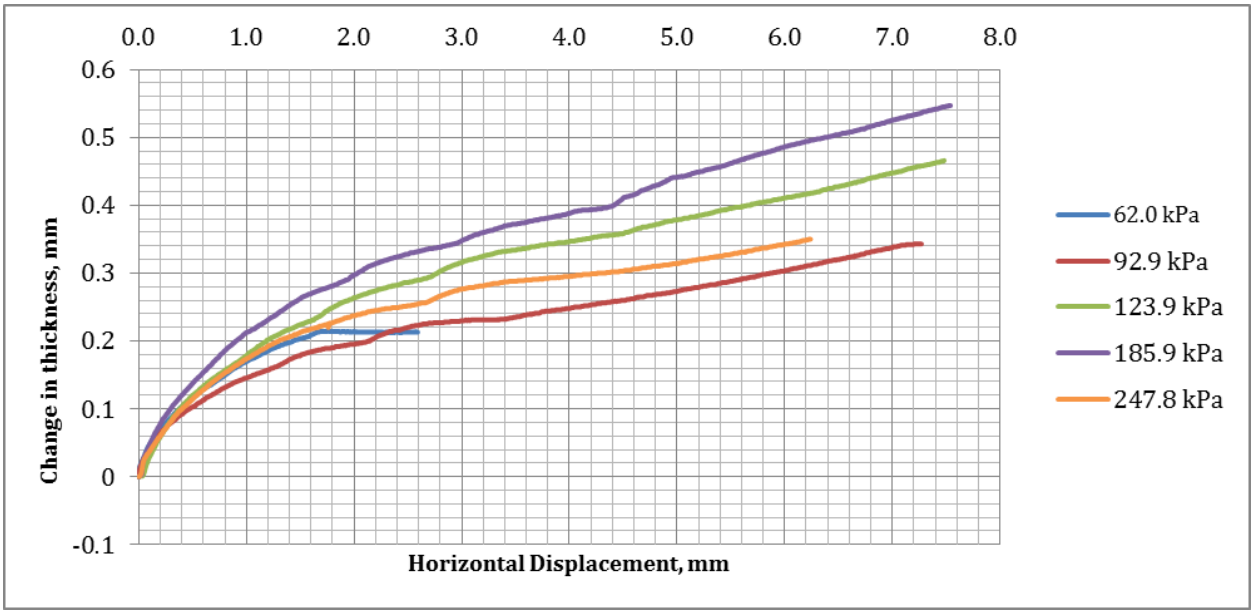

Figure 5-32: Change in Thickness vs. Horizontal Displacement, χ_I = 14% (C)

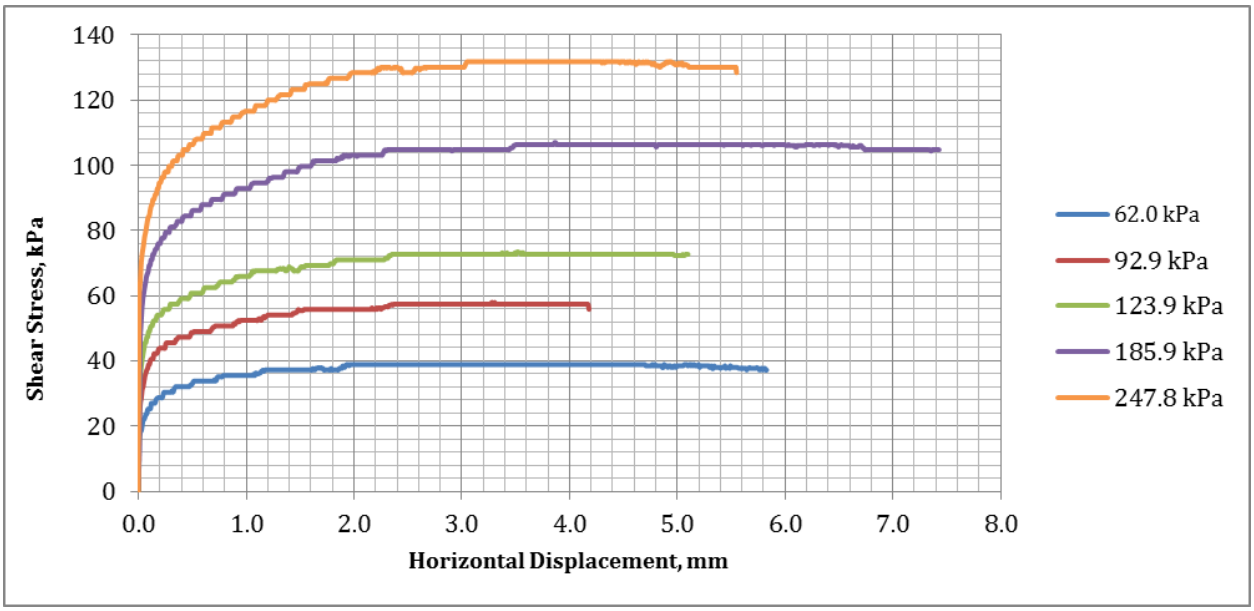

Figure 5-33: Shear Stress vs. Horizontal Displacement, χ_l = 14% (D)

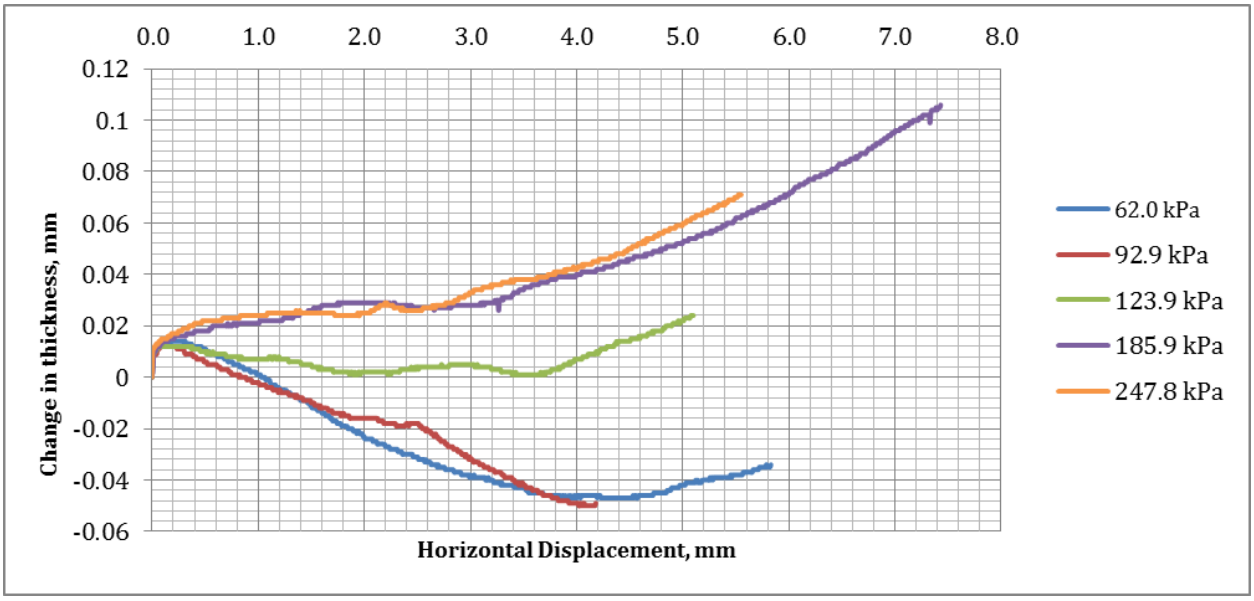

Figure 5-34: Change in Thickness vs. Horizontal Displacement, χ_l = 14% (D)

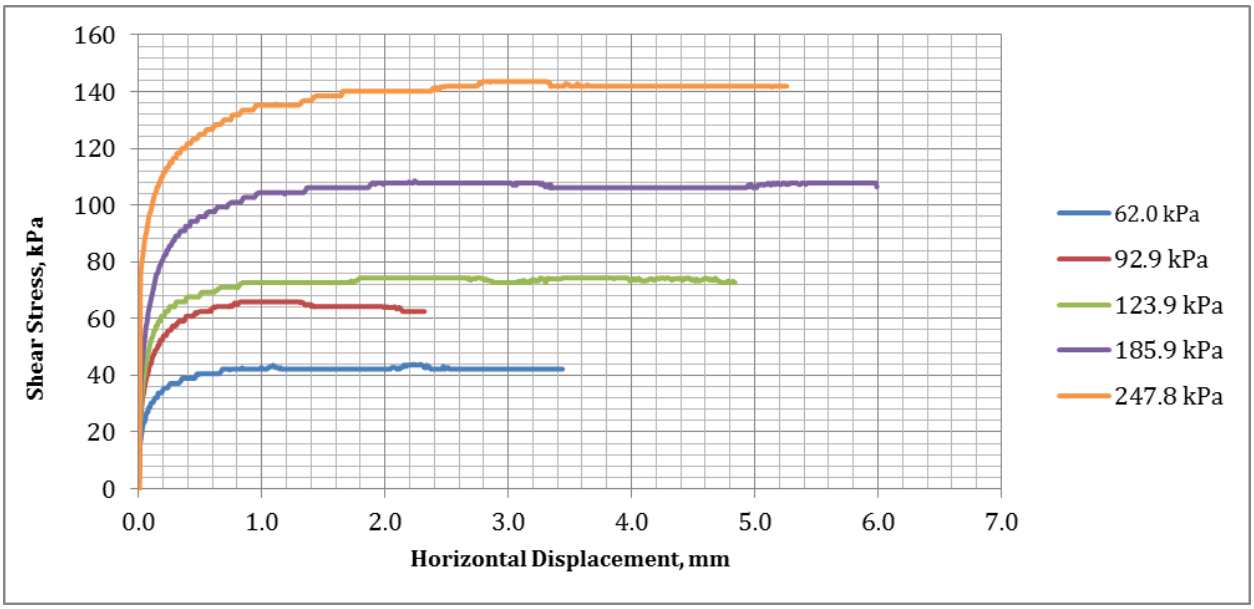

Figure 5-35: Shear Stress vs. Horizontal Displacement, χ_I = 14% (B)

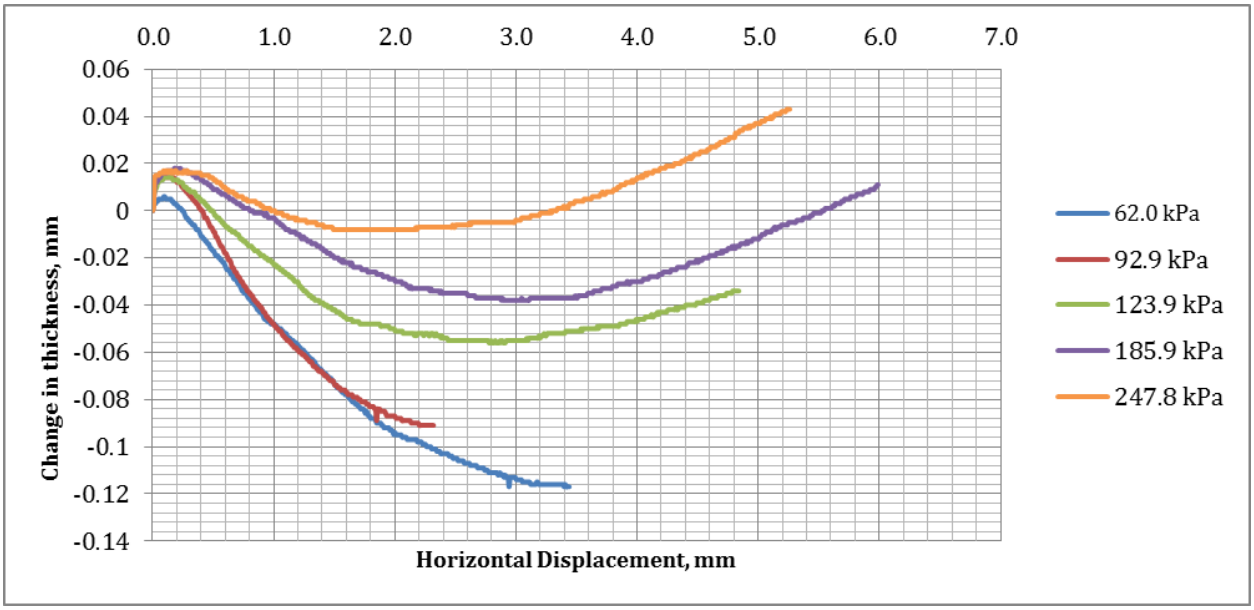

Figure 5-36: Change in Thickness vs. Horizontal Displacement, χ_I = 14% (B)

While the maximum allowable horizontal displacement is 10 mm, the shear phase of any test can be stopped when desired. Shear stress occasionally experiences a very slight to slight post peak drop; this is not significant.

The plots showing vertical displacement versus lateral displacement are different for each test. Two behavioral trends are exhibited, compression (or contraction) and dilation. With some exception, dilation typically occurs at lower normal stresses and contraction occurs at higher normal stresses. Initial level of relative compaction dictates the trends as well. Higher initial relative compaction (or higher dry density) produces more dilatant behavior, while lower initial relative compaction (or lower dry density) results in more contractant behavior.

Addition of lignin decreases dilatancy whereby the highest dilatancy occurs generally at point A, which is followed by B, E, D, and C. Among D, E, and B, the configurations which have equal initial void ratios, the material at point B is often the most dilatant and it produces the highest shear stress at failure. Furthermore, a small amount of lignin significantly decreases the dilatancy of dry sand. The maximum dilatancy of sand-lignin mixes for configurations A and B is reached at χ_l = 6%, for configuration E is reached at χ_l = 4%, for configuration C is reached at χ_l = 4%, and at configuration D is reached at χ_l = 14%.

5.2 Information about Direct Shear Specimens

5.2.1 Water Content Data

Moist samples of the lignin-sand mix were taken and placed into an oven at 105 ℃ for drying for at least 8 hours before and after each test. This was done to measure the actual water content of the samples. The results of the moisture are presented in Table 5-1.

Table 5-1: Actual water contents for direct shear tests.

χ_l (%)	Pt.	After *w* avg. (%)
2	A	1.13
2	E	1.48
2	C	1.18
2	D	0.77
2	B	3.23
4	A	3.30
4	E	2.80
4	C	2.62
4	D	1.52
4	B	3.35
6	A	3.03
6	E	3.08
6	C	2.85
6	D	2.12
6	B	4.02
9	A	3.74
9	E	4.01
9	C	4.08
9	D	2.29
9	B	5.12
14	A	5.41
14	E	5.48
14	C	5.61
14	D	4.82
14	B	6.38

In addition to the samples taken from the mix prior to direct shear testing, the samples were taken from the top half of the specimen after shearing. The samples mounted inside the shear box were covered from all sides and test duration was relatively short, thus significantly inhibiting the drying process. The phase diagrams shown in Figures 4-11 through 4-16 are updated in Figures 5-37 through 5-42 to reflect the actual water content.

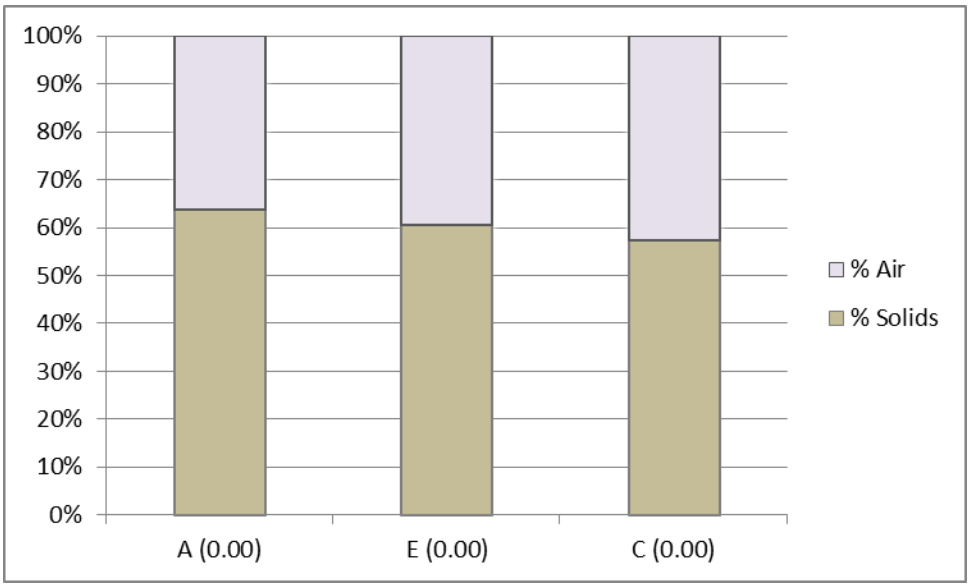

Figure 5-37: Updated phase diagram for χ_l = 0%

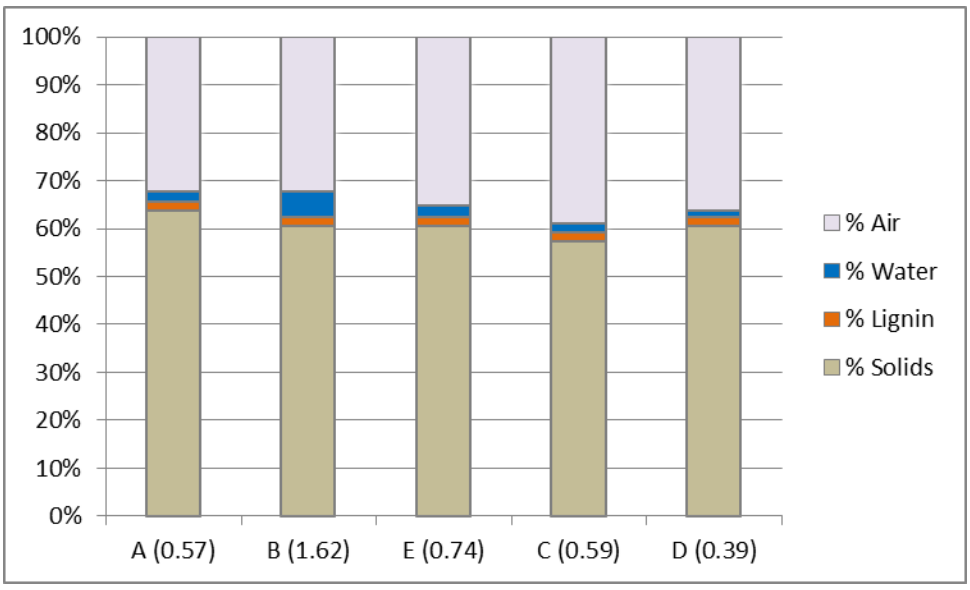

Figure 5-38: Updated phase diagram for χ_l = 2%

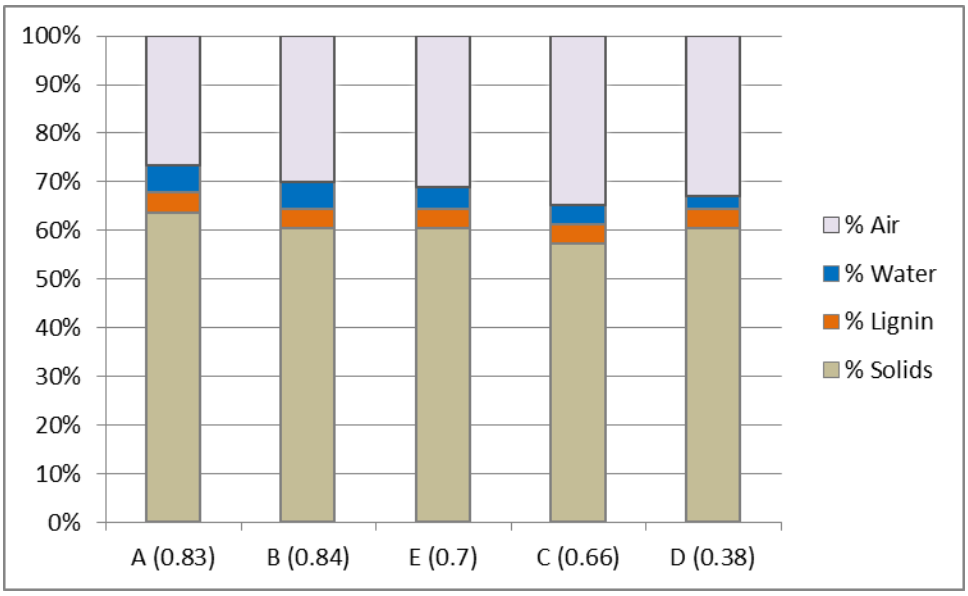

Figure 5-39: Updated phase diagram for χ_l = 4%

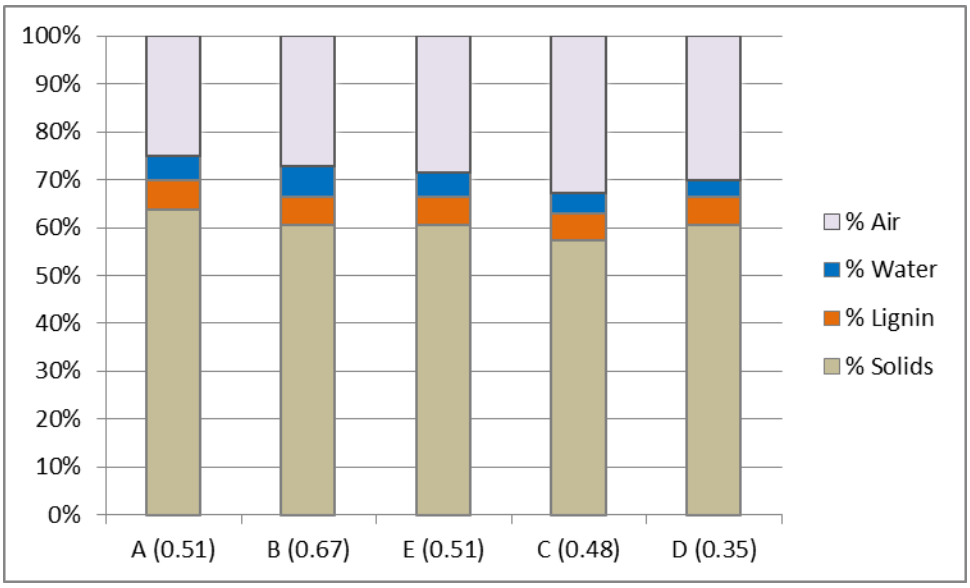

Figure 5-40: Updated phase diagram for χ_l = 6%

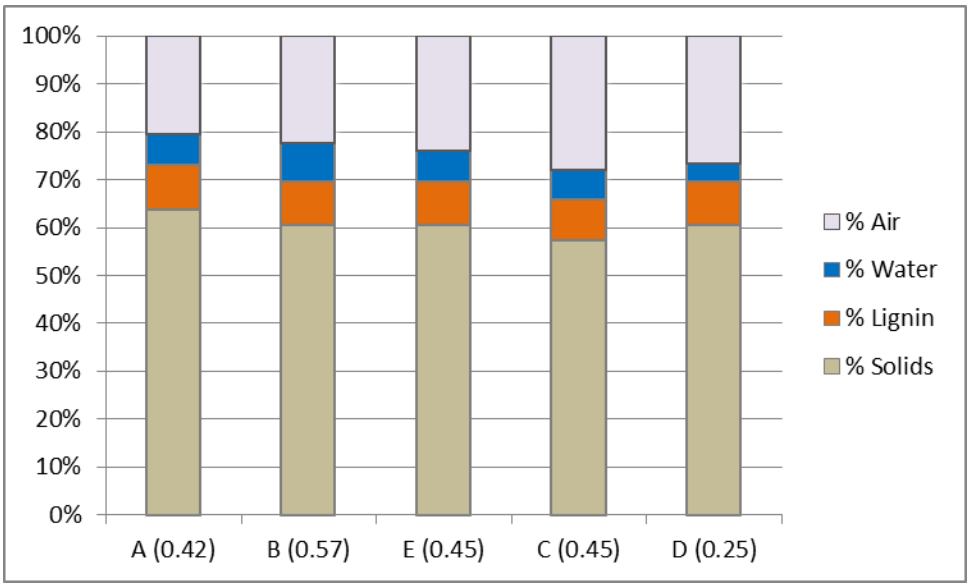

Figure 5-41: Updated phase diagram for χ_l = 9%

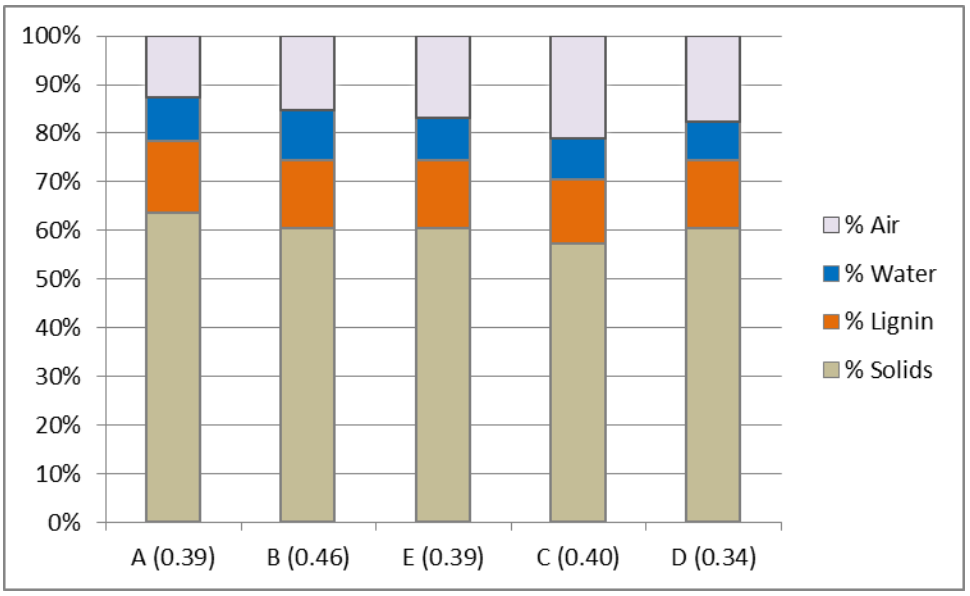

Figure 5-42: Updated phase diagram for χ_l = 14%

5.2.2 Updated Void Ratios

Similar to the water contents, the initial void ratios of the samples changed due to testing conditions. Specifically, the consolidation (or compression) stage decreased the heights of the specimens and as a result they were sheared at the initial void ratio, which was slightly smaller than the one achieved after the compaction. Table 5-2 depicts the changes in heights recorded after consolidation and the corresponding (updated) void ratios, which were used for the analysis presented in Chapter 6. The updated void ratios were calculated by using the following equation:

$$e_1 = e_0 - \frac{\Delta H_{avg}}{H_0}(1 + e_0) \tag{22}$$

Where e_0 is the value of the void ratio before the application of normal stress, and e_1 is the updated value of the void ratio at the end of the compression. The height change ΔH_{avg} is averaged over all normal stresses for a given sample configuration.

Table 5-2: Change in height and void ratios for all configurations

χ_l (%)	Pt.	e_0	ΔH_{avg} (mm)	e_1
0	A	0.571	0.493	0.539
0	E	0.654	0.643	0.610
0	C	0.746	0.706	0.695
2	A	0.571	0.519	0.537
2	E	0.654	0.497	0.620
2	C	0.746	0.698	0.695
2	D	0.654	0.542	0.617
2	B	0.654	0.494	0.620
4	A	0.571	0.493	0.539
4	E	0.654	0.426	0.625
4	C	0.746	0.770	0.690
4	D	0.654	0.538	0.617
4	B	0.654	0.490	0.620
6	A	0.571	0.426	0.543
6	E	0.654	0.466	0.622
6	C	0.746	0.801	0.688
6	D	0.654	0.450	0.623
6	B	0.654	0.392	0.627
9	A	0.571	0.389	0.546
9	E	0.654	0.465	0.622
9	C	0.746	0.828	0.686
9	D	0.654	0.350	0.630
9	B	0.654	0.504	0.619
14	A	0.590	0.567	0.552
14	E	0.654	0.561	0.615
14	C	0.746	0.918	0.679
14	D	0.654	0.473	0.621
14	B	0.654	0.627	0.611

5.2.3 Specimen Photographs

Photographs of each specimen were taken at the end of direct shear tests with a Canon PowerShot SD1200 IS 10 megapixel digital camera. To capture the images, specimens were placed under a Nikon SMZ-2T microscope with 10x/23 eye pieces fixed with a Javenlin SmartCam to the vertical photo tube that was attached to a computer monitor. From the image on the computer monitor, the images were captured.

Many of the images are very similar in appearance due to the somewhat repetitive nature of the sample configurations. Therefore, only one image has been selected to provide a direct view of the specimen compositions. In addition, the images of sand alone at 0% and 4% moistures have been included for the sake of comparison. These images are displayed in Figures 5-43 through 5-49.

Figure 5-43: Magnified Image of χ_l = 0%, w = 0% (dry sand)

Figure 5-44: Magnified Image of χ_l = 0%, w = 4% (moist sand)

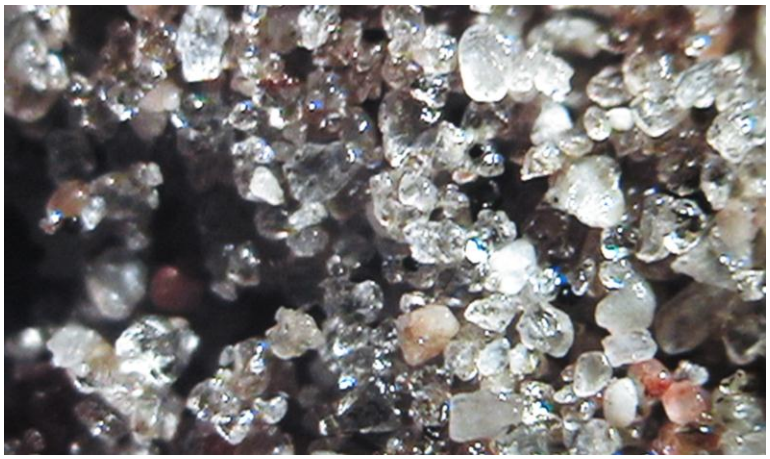

Figure 5-45: Magnified Image of χ_l = 2%

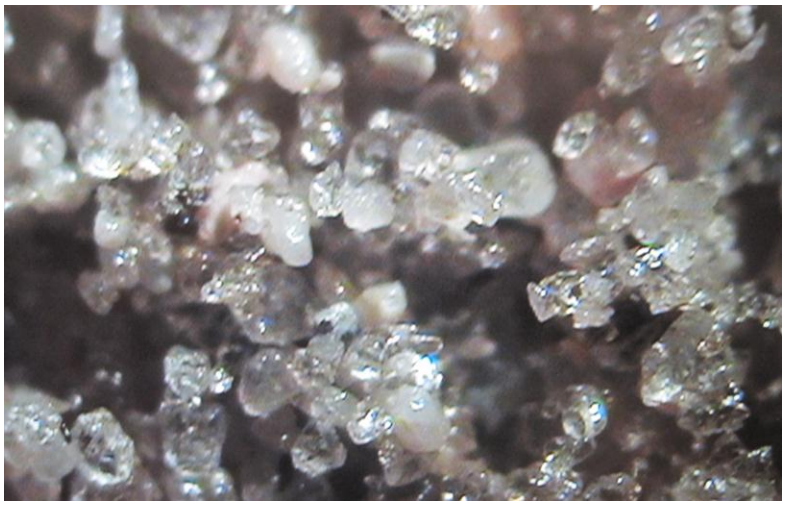

Figure 5-46: Magnified Image of χ_l = 4%

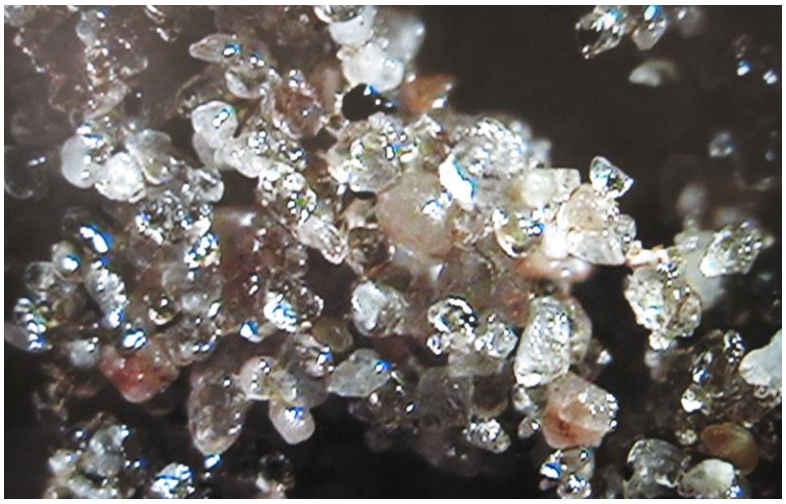

Figure 5-47: Magnified Image of χ_l = 6%

Figure 5-48: Magnified Image of χ_l = 9%

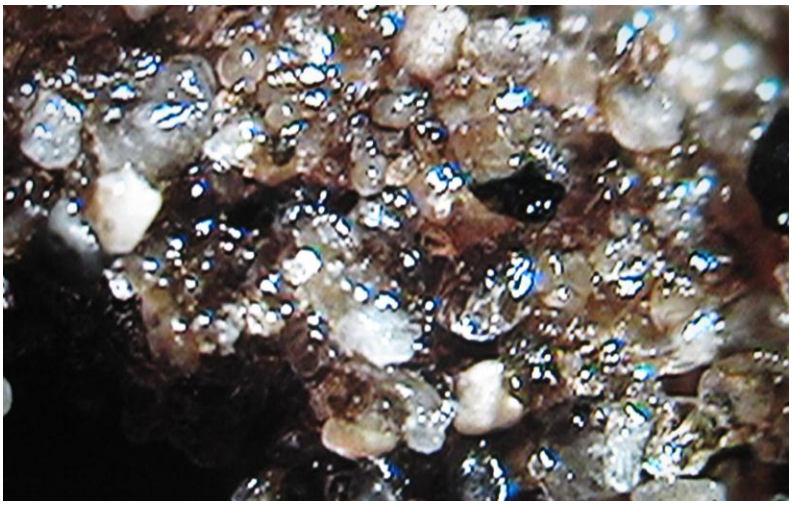

Figure 5-49: Magnified Image of χ_l = 14%

The effect of the increasing amount of lignin+water is evident in these photographs. In Figure 5-43 the dry sand particles are surrounded by voids filled with air. Figure 5-44 shows moist sand, whereby sand particles are surrounded by water and air. The sand particles appear to be better bonded together than in Figure 5-43 due to the presence of water menisci. Figure 5-45 shows a structure similar to that of the wet sand, but the coloration is slightly darker and the "finish" on the particles is glossier, reflecting the presence of a lignin paste. In Figure 5-46 through 5-48 the increasing amount of lignin is evident. The balance of lignin, water and sand appears to be optimum in the photographs of χ_l = 4 and 6% because the lignin appears to coat the sand particles evenly without evidence of much inert lignin. From this point on the amount of lignin+water appears to increase to the point in Figure 5-49 where it is evident that there is an overabundance of lignin and the particles may be over lubricated and formed apart from each other.

Chapter 6 - Analysis and Discussion

Plots showing normal stresses versus shear stresses at failure were generated for all tests to determine the angle of friction, Φ and the cohesion, c, which are also known as Mohr-Coulomb's strength parameters. Additional plots were generated following the determination of c and Φ with the primary intent of analyzing the effect of lignin on cohesion.

6.1 Determination of Mohr-Coulomb's Strength Parameters

The plots of maximum shear stress versus normal stress for gravimetric lignin content 9% can be found in Figures 6-1 through 6-5. Plots for other gravimetric lignin contents are found in Figures B-1 through B-23 in Appendix B. A summary of the Mohr-Coulomb's strength parameters, which were determined based on these plots, is shown in Table 6-1.

Table 6-1: Values of Cohesion and Angle of Friction for All Test Points

χ_l	0%		2%		4%		6%		9%		14%	
	c (kPa)	Φ (°)	c (kPa)	Φ (°)	c (kPa)	Φ (°)	c (kPa)	Φ (°)	c (kPa)	Φ (°)	c (kPa)	Φ (°)
A	0	36.4	13	28.1	16.5	29.2	18.2	27.6	16.1	27.3	14	23.8
E	0	35.4	11.3	28.6	11.5	27.6	14.7	26.1	13.2	27	10.8	25.7
C	0	32.2	10.9	27.2	9.5	25.1	9.8	26.8	9.8	28.2	7.4	26.3
D	0	35.4	8.7	26.7	7.6	26.9	8	27	9.1	27	8.1	27
B	0	35.4	8.2	32.3	15.6	28.7	16.8	31	16.8	29	12.5	27.6
c_{avg} (kPa)	0		10.42		12.14		13.5		13		10.56	
Φ_{avg}(°)		35.0		28.6		27.5		27.7		27.7		26.1

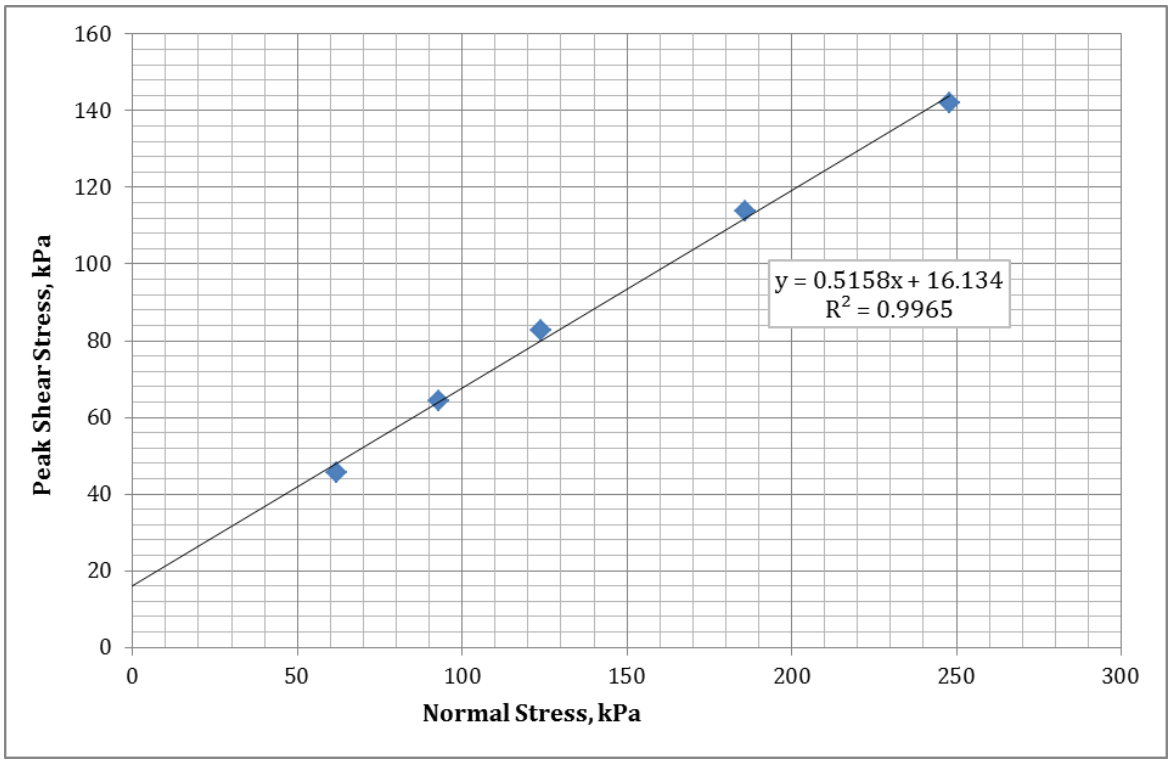

Figure 6-1: Peak Shear Stress vs. Normal Stress for χ_l = 9% (A)

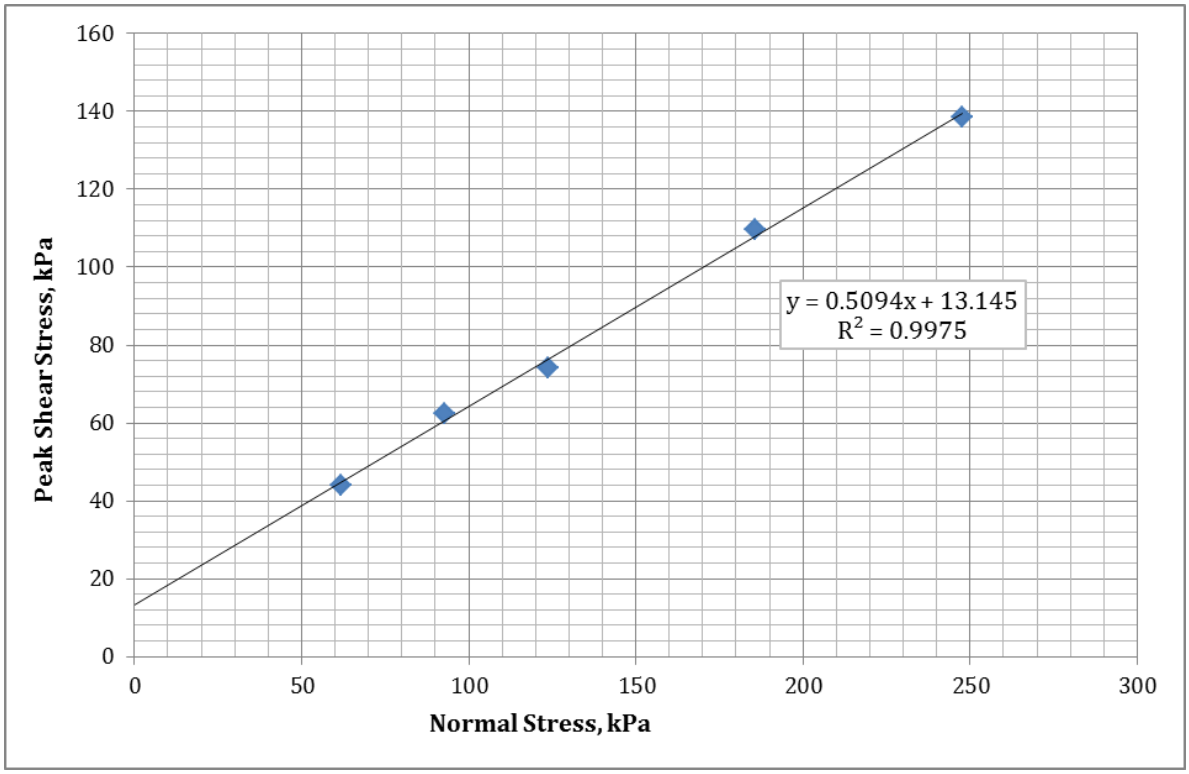

Figure 6-2: Peak Shear Stress vs. Normal Stress for χ_l = 9% (E)

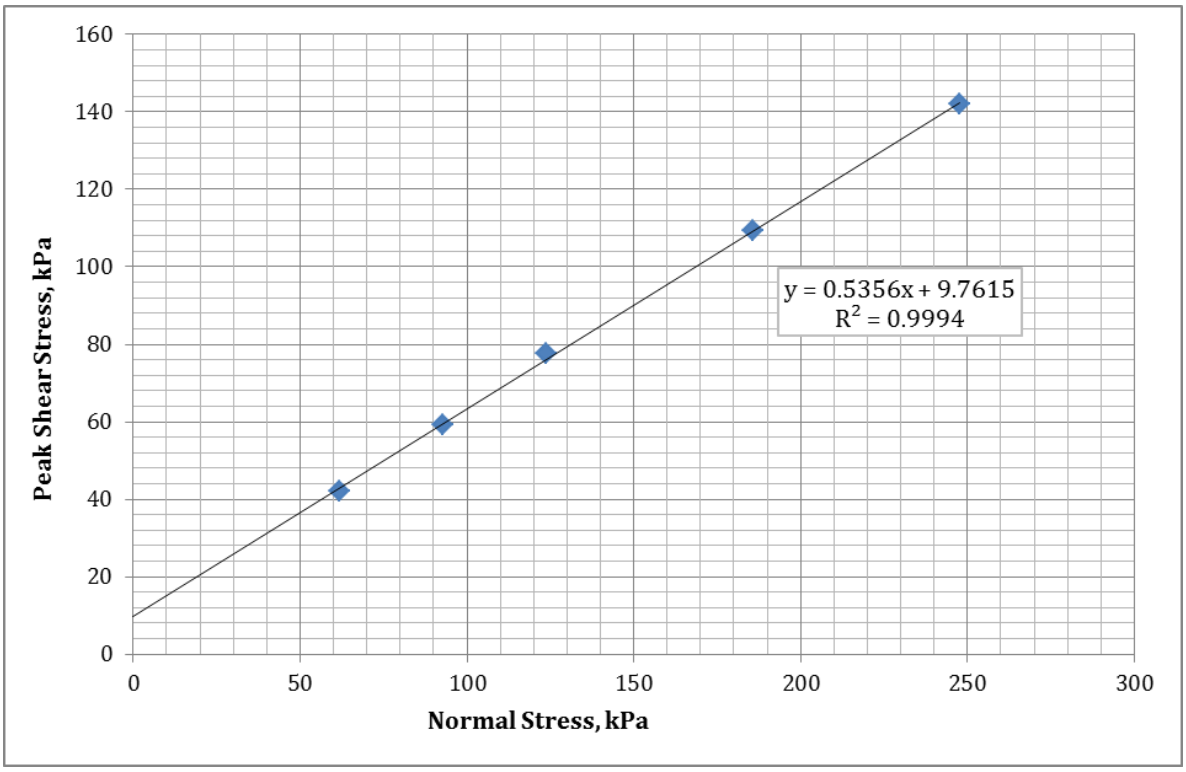

Figure 6-3: Peak Shear Stress vs. Normal Stress for χ_I = 9% (C)

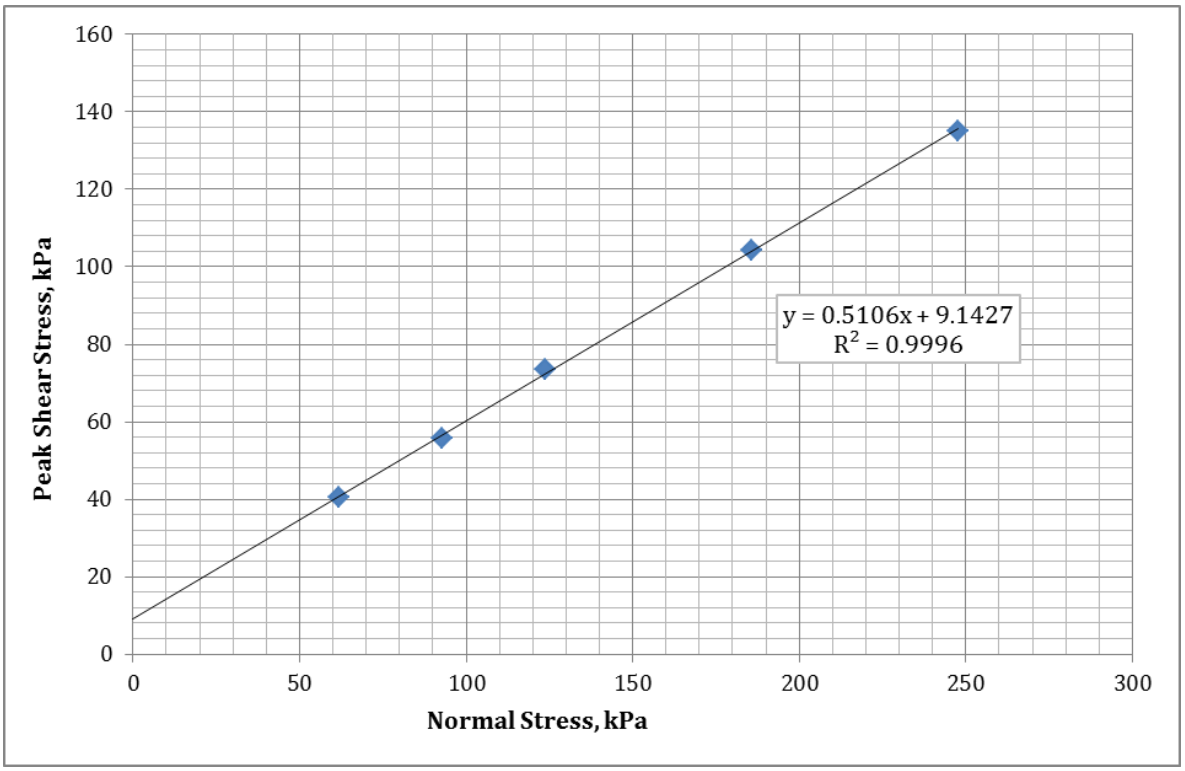

Figure 6-4: Peak Shear Stress vs. Normal Stress for χ_I = 9% (D)

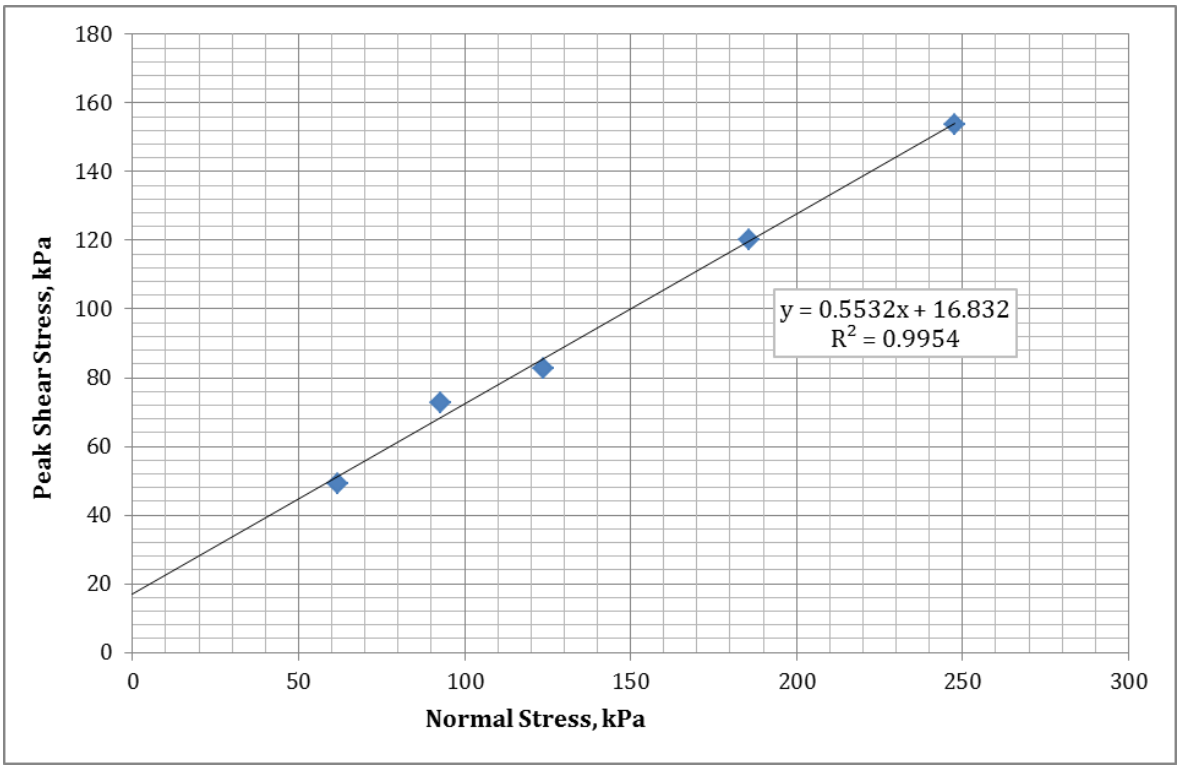

Figure 6-5: Peak Shear Stress vs. Normal Stress for χ_l = 9% (B)

The coefficient of determination (R^2) for all tests varied in range from 0.97 to greater than 0.99, with most being 0.99 or higher. The trend of cohesion seems consistent; it is the highest at configurations A or B, then configuration E, configuration C and finally configuration D. This trend makes intuitive sense; the highest cohesion is brought about by 100% relative compaction and optimum water content or by 95% relative compaction wet of optimum. It then follows that point E is at the midpoint in the range of the cohesion values as it exhibits 95% relative compaction and optimum water. Point C is at 90% relative compaction and has optimum water content while point D has 95% relative compaction and the least amount of water of the five tested configurations. Points C and D rank fourth and fifth in cohesion, respectively. Exceptions occur to these trends at 2-B and 14-C. The sample configuration 2-B is unique in that it has by far the highest water to lignin ratio, equal to 161.5%, while having a very small amount of lignin. The sample configuration 14-C is likely unique in that it exhibits the presence of a relatively high amount of lignin and a high amount of water, while being very loosely compacted. Figure 6-6 summarizes the results for cohesion.

It is more difficult to find a trend for the results of the angle of friction. The angle of friction for all sample configuration ranges from 23.8 to 36.4 degrees, and from 23.8 to 32.3 degrees for sand-lignin mixes. This clearly indicates a reduction of magnitude of the angle of friction from dry sand (32.2° to 36.4°). The reason for the decreasing angle of internal friction with the increasing lignin content is most likely due to an increasing amount of fine lignin particles, which also decrease the dilatancy. Figure 6-7 summarizes the results for the angle of friction.

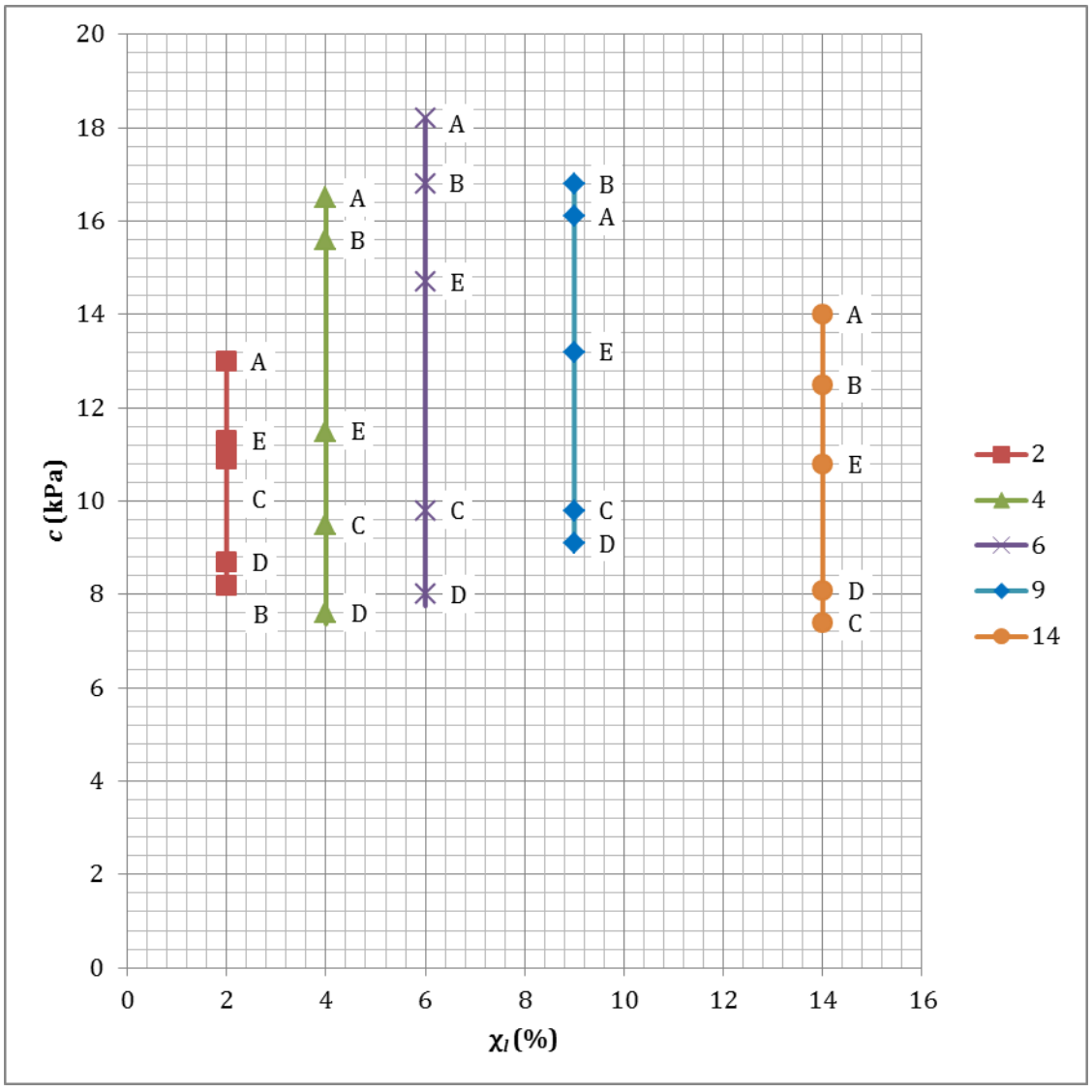

Figure 6-6: Summary of Cohesion for All Configurations

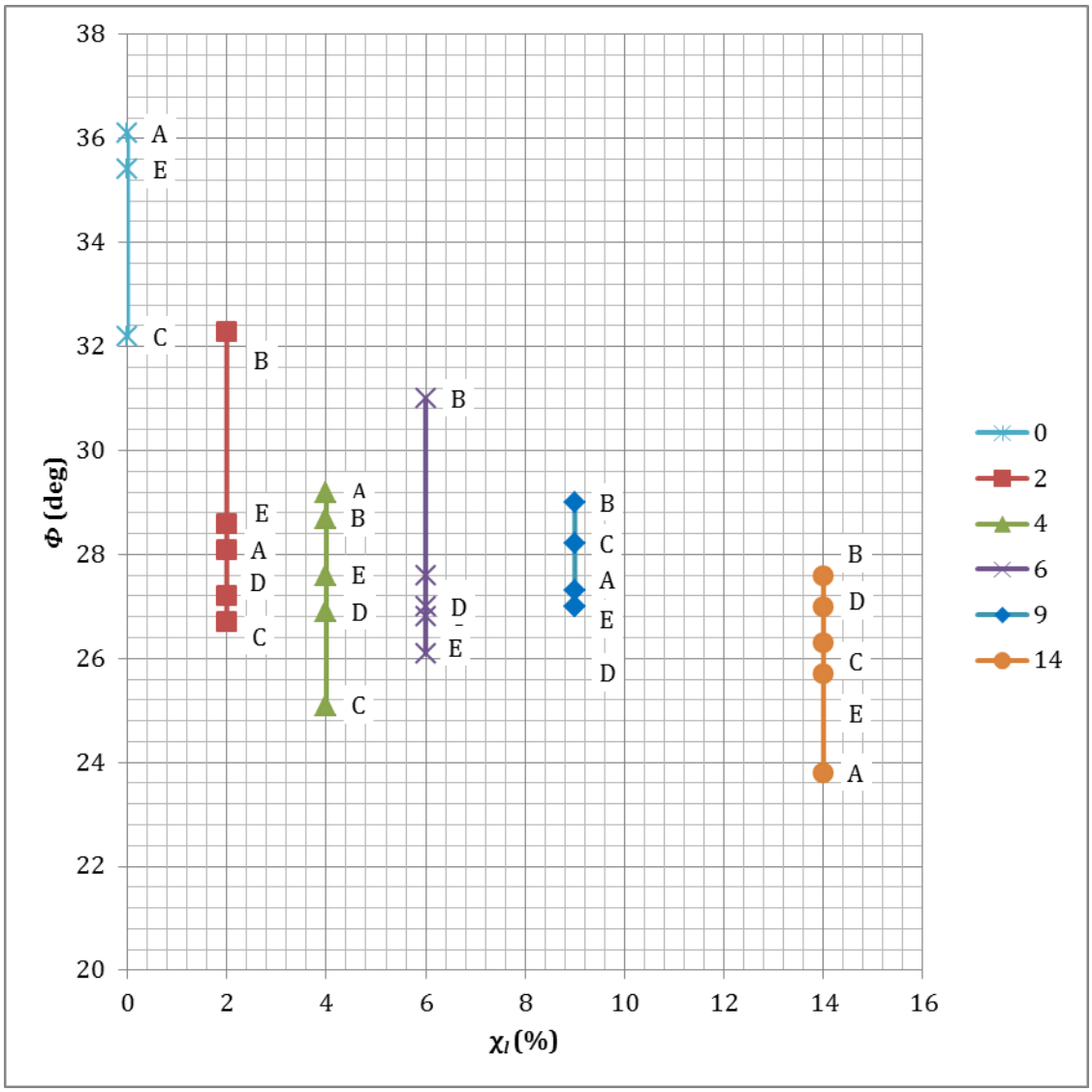

Figure 6-7: Summary of Angle of Friction for All Configurations

6.2 Further Analysis

In addition to the cohesion and angle of friction, further analysis is necessary to achieve a more complete understanding of the relationships at work between sand, lignin, and water. To aid this understanding, additional equations have been derived from the basic definitions of phase relationships given in Chapter 3. These expressions provide basis for the estimation of the portion of the total cross sectional area, which is occupied by water and lignin paste. Alternatively, the paste can be partitioned into lignin+water and portions of the total cross sectional area occupied by each of the constituents can be computed. A schematic of load bearing cross sectional area is shown in Figure 6-8.

From the definition of the degree of water saturation (Equation 3) the following is obtained:

$$S_w = \frac{V_w}{V_v} = \frac{G_s w}{e} \tag{23}$$

from where it follows

$$\frac{A_w}{A} = \left(\frac{V_w}{V_v}\right)\left(\frac{V_v}{V}\right) = S_w n = S_w \frac{e}{1+e} = \frac{G_s w}{1+e} \tag{24}$$

Similarly for lignin area ratio the following is obtained:

$$\frac{A_l}{A} = \frac{G_s \chi_l}{G_l(1+e)} \tag{25}$$

And by adding Equations (24) and (25) the following is obtained:

$$\frac{A_w}{A} + \frac{A_l}{A} = \frac{A_{w+l}}{A} \tag{26}$$

$$\frac{A_{w+l}}{A} = \frac{G_s}{1+e}\left(w + \frac{\chi_l}{G_l}\right) \tag{27}$$

From where it follows that:

$$\frac{A_{w+l}}{A\chi_l} = \frac{G_s}{1+e}\left(w_{w/l} + \frac{1}{G_l}\right) \tag{28}$$

Equation (27) is important because it shows that water content, gravimetric lignin content, and void ratio affect the size of the cross sectional area occupied by lignin and water.

As shown in Figure 3-2, which depicts the phase diagrams, there are three different constituents carrying the stress: lignin and water, and solids contacts. Water and lignin together form a paste, which acts as a binding agent. This concept is illustrated in Figure 6-8.

From the equilibrium of forces depicted in Figure 6-8, it follows that the external or total normal force is carried by these three constituents as follows:

$$F = F_c + F_{l+w} = \sigma_c A_c + \sigma_{l+w} A_{l+w} \tag{29}$$

And by dividing this equation by the entire cross sectional area, A, the following is obtained:

$$\sigma = \sigma_c \frac{A_c}{A} + \sigma_{l+w} \frac{A_{l+w}}{A} = \sigma' + \sigma_{l+w} \frac{A_{l+w}}{A} \tag{30}$$

thus, in addition to the portion of the external or total stress carried by the contacts of sand particles, which is also known as the effective stress, there is a portion carried by the lignin and water paste, which is denoted as σ_{l+w}. Moreover, adding lignin and water increases the cross-sectional area engaged in carrying the normal stress.

By applying the Mohr-Coulomb criterion, which is satisfied based on the experimental results obtained in this study, the following holds:

$$\tau = \sigma \tan\phi \tag{31}$$

where Φ is the friction angle of the sand-water-lignin mix in terms of total stress. Next, equation (31) is combined with Equation (30) resulting in

$$\tau = \sigma' \tan\phi + \sigma_{l+w} \frac{A_{l+w}}{A} \tan\phi = \sigma' \tan\phi + c \tag{32}$$

and the second term in Equation (32) can be interpreted as cohesion, which is given by

$$c = \sigma_{l+w} \frac{A_{l+w}}{A} \tan\phi = \frac{F_{l+w}}{A} \tan\phi \tag{33}$$

Thus, the amount of cohesion depends on the portion of the total cross-sectional area, which is occupied by lignin and water, stress in the lignin and water and the angle of friction of the sand

lignin mix (Φ). In addition, Equation (33) shows that this material possesses some tensile strength, which is clearly derived from lignin-water paste.

The following is obtained from Equation (33)

$$\sigma_{l+w} = \frac{c}{\frac{A_{l+w}}{A}\tan\phi} \tag{34}$$

and Equation (35) provides means of determining normal stress in the lignin and water paste from the experimental results.

Next, the expression for the limit normal stress, which is the maximum normal stress that can be applied to the sand-lignin-water mix while still providing a cohesion benefit over dry sand, is obtained. For normal stresses larger than the limiting stress the sand-lignin-water mix is superseded in ranking of peak shear stress by the dry sand. This concept is illustrated in Figure 6-9.

$$\sigma_{Limit} = \frac{c}{\left(\tan\phi_{\chi_l=0\%} - \tan\phi\right)} \tag{35}$$

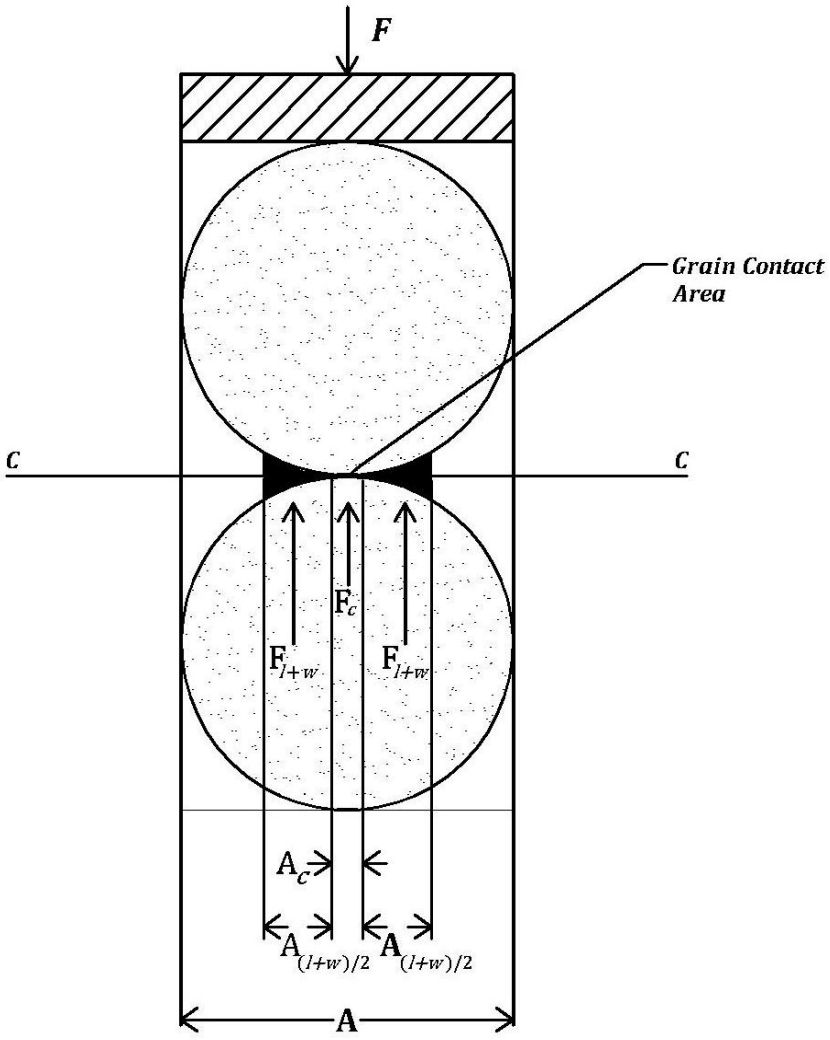

Figure 6-8: Schematic depicting load-bearing cross-sectional area

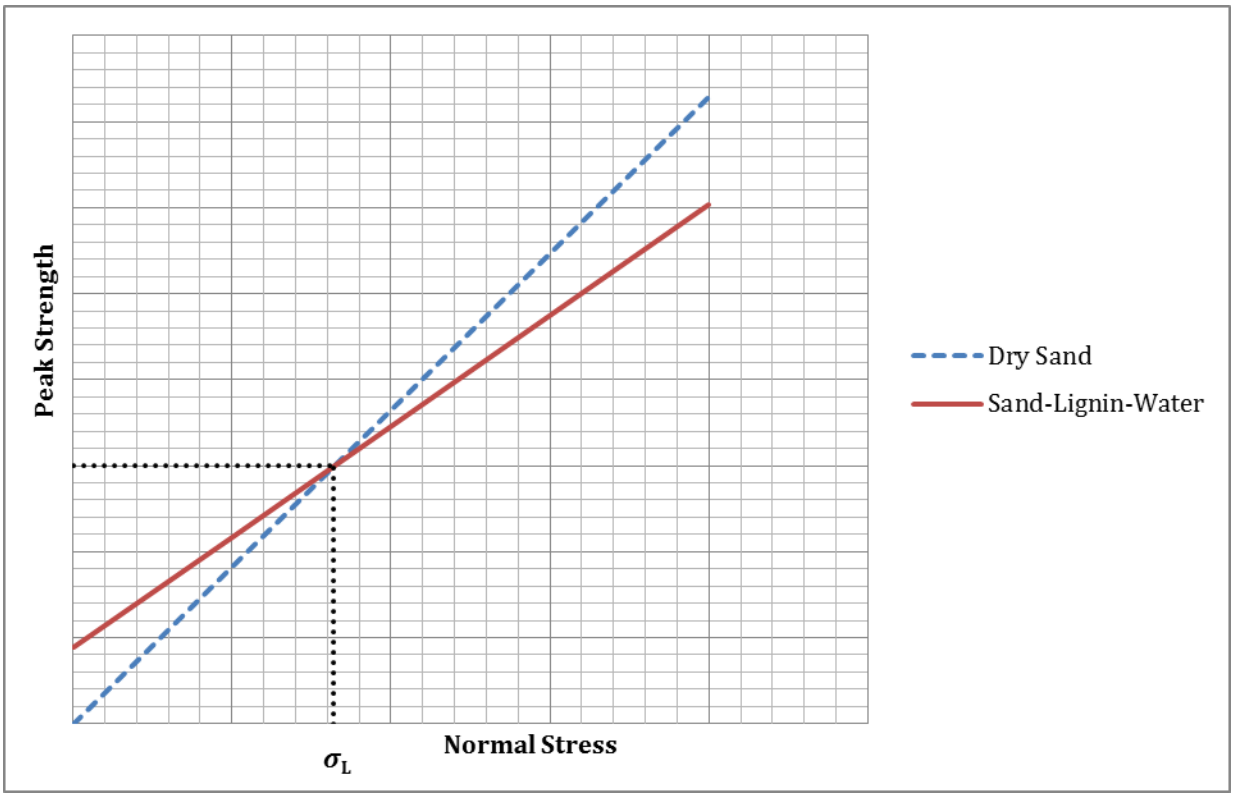

Figure 6-9: Plot Depicting Limit Stress of Sand-Lignin-Water Mixture

The plots that follow show several important data trends which were found by extensive analysis of experimental results. The first plot, displayed in Figure 6-10 is a plot of normalized limit stress versus gravimetric lignin content. Figure 6-11 is the same plot as 6-10 but the data are fitted by a logarithmic regression analysis. Thus, the limiting normal stress provided by each additional percent of lignin content decreases with the increasing lignin content. It remains the largest in configuration B, followed by C, E, A, and D. Configuration C is positioned high because of the lowest value of the friction angle in dry sand at relative compaction of 90%.

Figures 6-12 and 6-13 are showing normal stress in the lignin-water paste versus the area ratio for each set of configurations individually and all configurations together. The normal stress carried by lignin-water decreases with the increase in the portion of the total cross sectional area occupied by lignin-water.

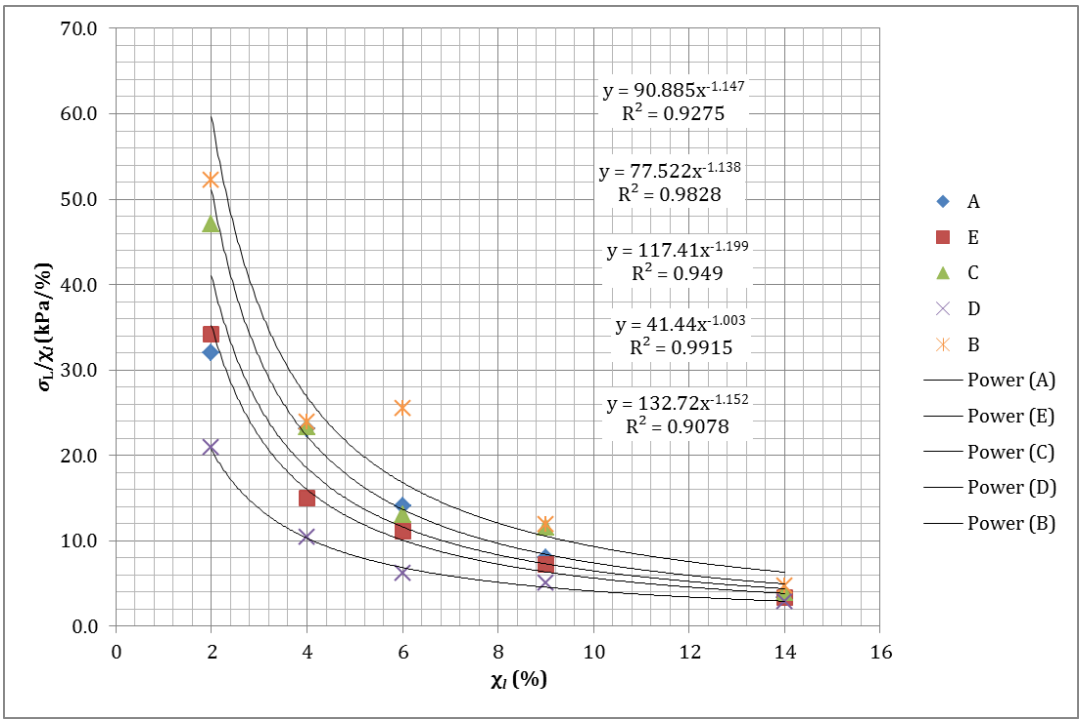

Figure 6-10: Normalized Limit Stress vs. Gravimetric Lignin Content (All pts.; power)

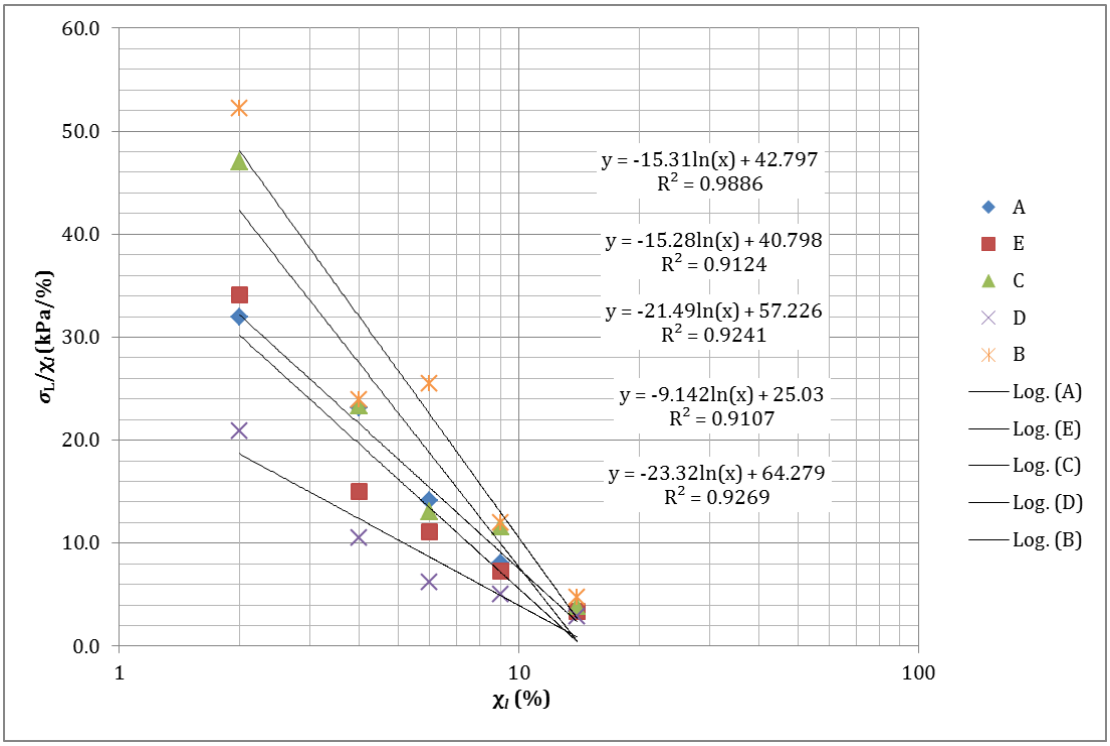

Figure 6-11: Normalized Limit Stress vs. Gravimetric Lignin Content (All pts.; log)

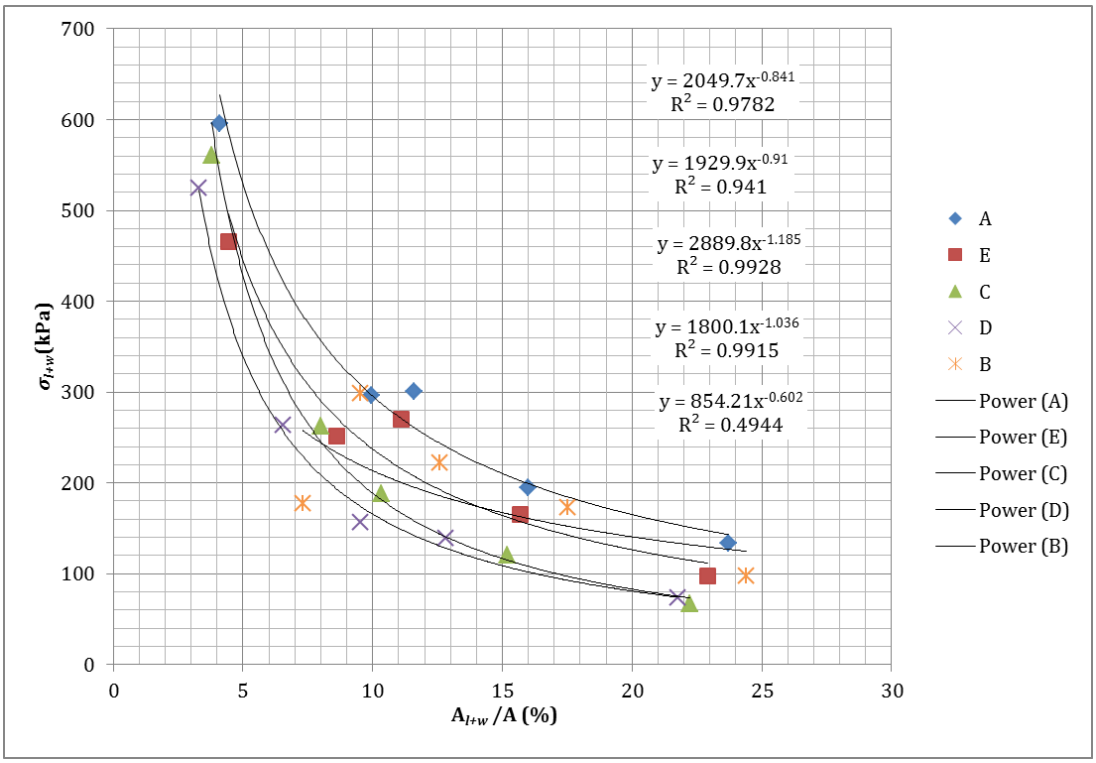

Figure 6-12: Stress in Lignin+Water vs. Area Ratio (All pts.)

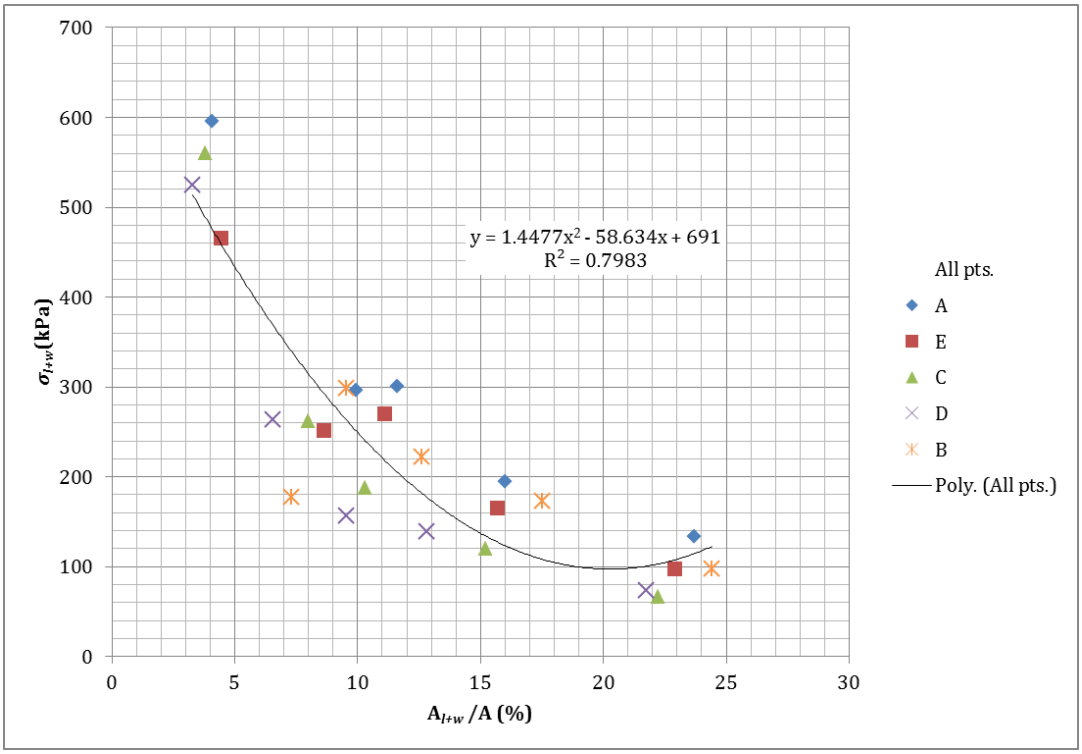

Figure 6-13: Stress in Lignin+Water vs. Area Ratio (All pts.)

Figures 6-14 and 6-15 illustrate that an increase in the ratio of the areas of lignin+water and the total cross sectional area normalized by the lignin content enhances the normalized cohesion of the mixture, whereby normalization is carried out by dividing by gravimetric lignin content.

While gravimetric lignin content of 2% is low, the accompanying water contents are extremely low, thus making it very difficult if not impossible to achieve homogeneous samples. A probable exception to this is configuration 2B, which contains more water resulting in the highest water to lignin ratio among all samples, equal to 161.5%. Thus, in Figure 5-14, configuration 2B appears to fit the data for higher gravimetric lignin contents. At the other extreme, gravimetric lignin content 14% appears to contain too much lignin-water, which is lubricating the sand particles to a diminished strength gain. It is also noted that sample configurations corresponding to 14% plot slightly further away from remaining configurations in Figure 6-15, whereby those representing gravimetric lignin content of 2% have already been removed due to likely non-homogeneities.

Figure 6-16 depicts all data points except those corresponding to configurations 2A, 2C, 2D and 2E. It is because configurations 2A, 2C, 2D and 2E plot furthest away from the remaining data points that they are removed from further analysis. This is most likely the consequence of the inability to achieve a homogenous mixture in these configurations.

Figures 6-17 through 6-27 present the data for gravimetric lignin contents individually and in different combinations of configurations. The best correlation of points exists in Figure 6-22, which is the combined analysis of χ_l = 4 and 6% and it is followed by the combination of χ_l = 4, 6, and 9% in Figure 6-25. Although the combination of 4% and 6% show the best correlation (R^2 = 0.88), the combination of 4, 6, and 9% holds second place with the R^2 value of 0.86, simply because the data for 9% show slightly worse fit than those for 4% and 6%. Adding 14% to any combination decreases R^2 value with the lowest value (R^2 = 0.61) for 9% and 14%. Figures 6-28 through 6-29 show response for configurations A, while Figures 6-30 through 6-31 show the response for configurations E. Finally, Figures 6-32 through 6-33 show the response for configurations C. Tables ranking the values of coefficient of determination for each set of configuration plots are presented in Tables 6-2 through 6-5.

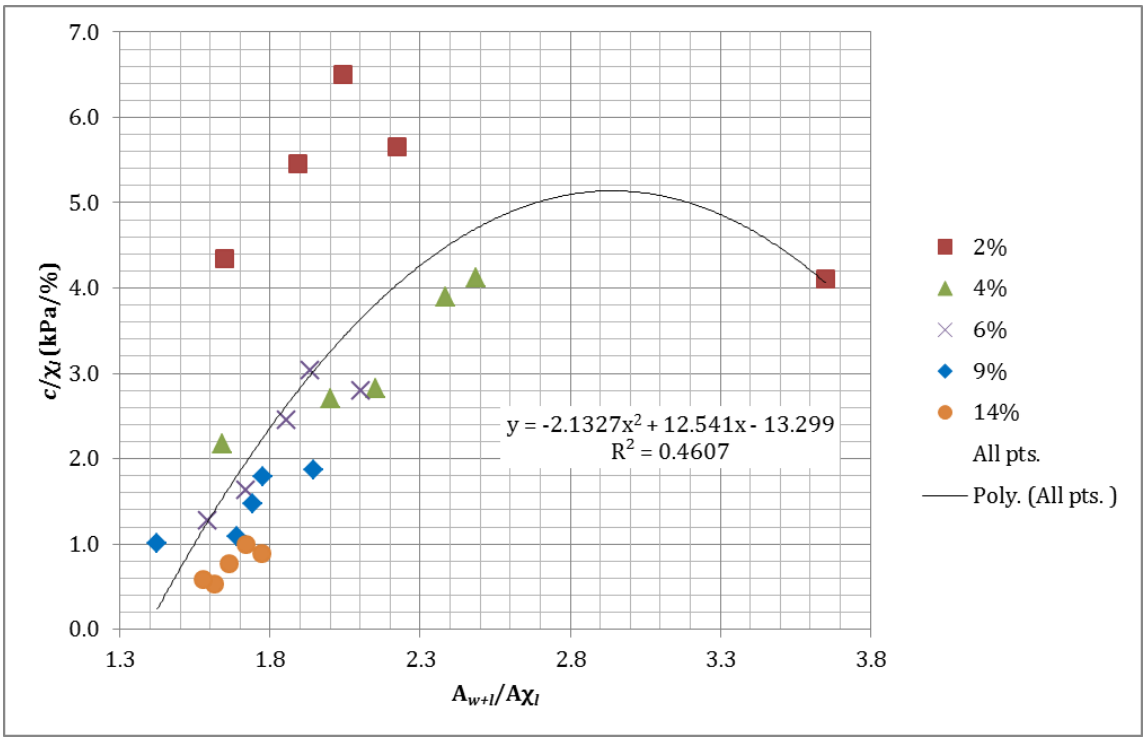

Figure 6-14: Normalized Cohesion vs. Normalized Area Ratio (All pts.)

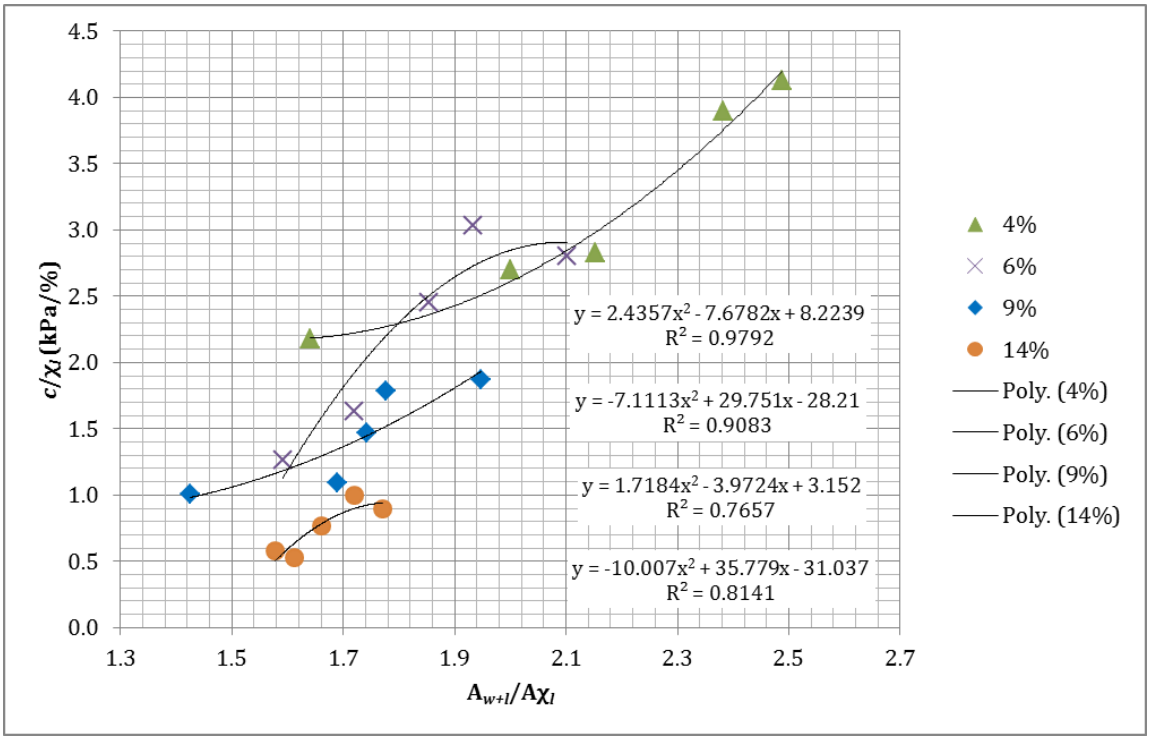

Figure 6-15: Normalized Cohesion vs. Normalized Area Ratio (w/o 2%)

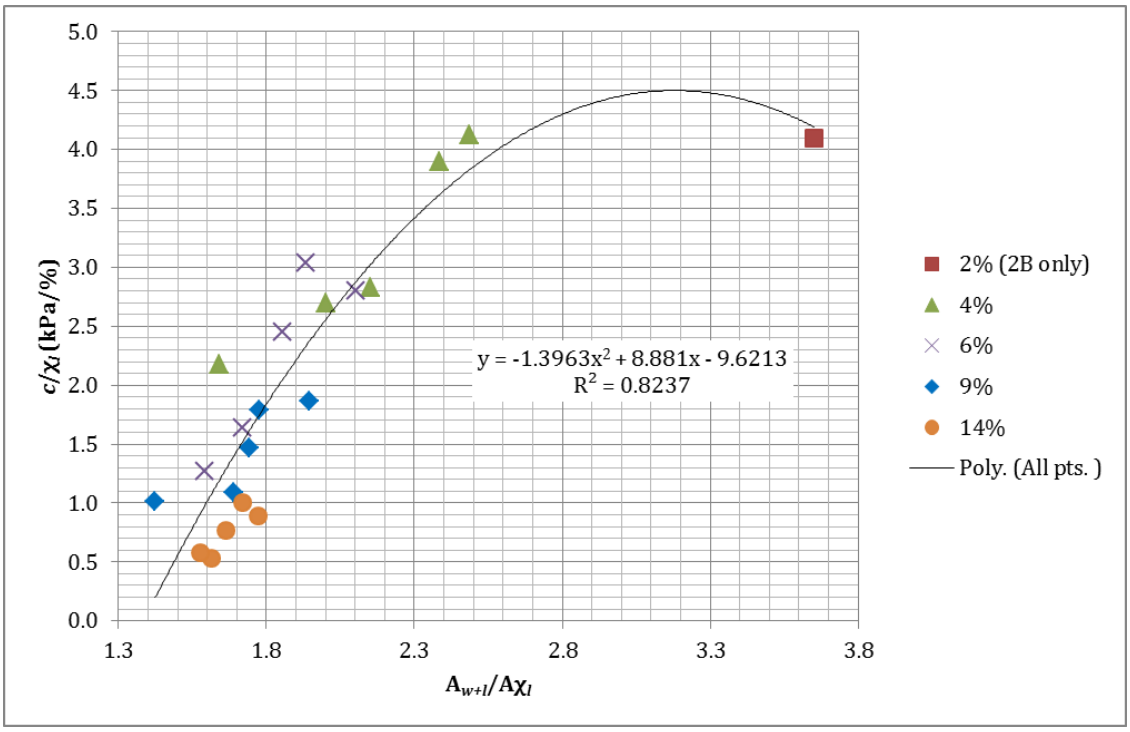

Figure 6-16: Normalized Cohesion vs. Normalized Area Ratio (w/o 2A, 2E, 2C, 2D)

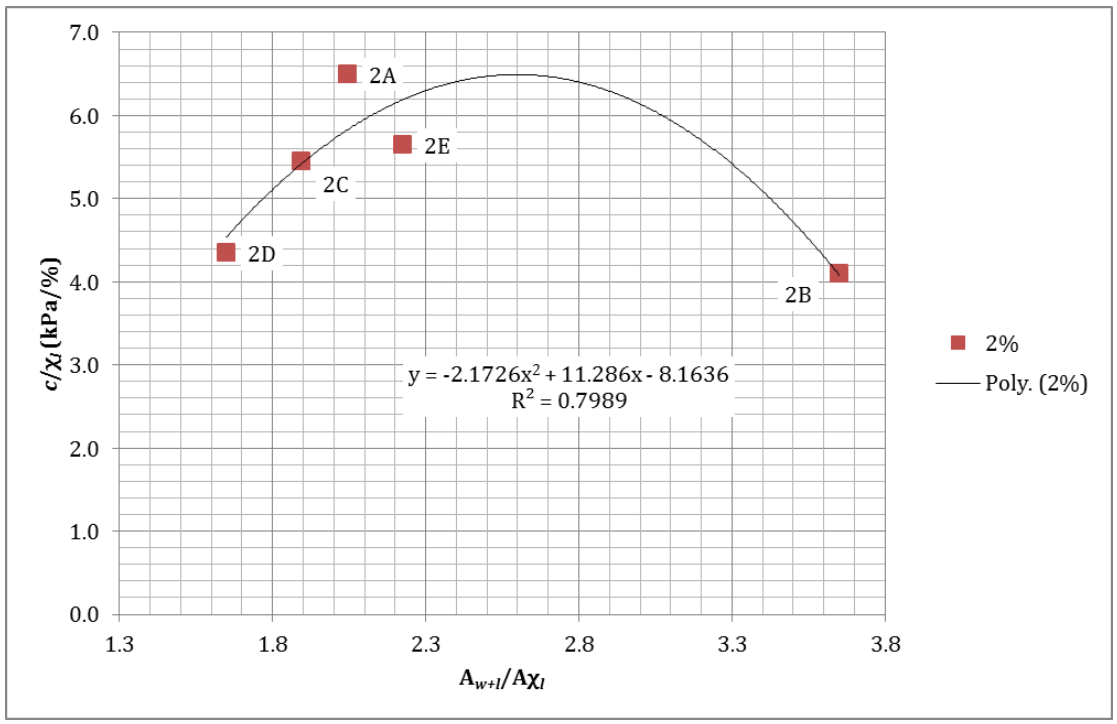

Figure 6-17: Normalized Cohesion vs. Normalized Area Ratio (2%)

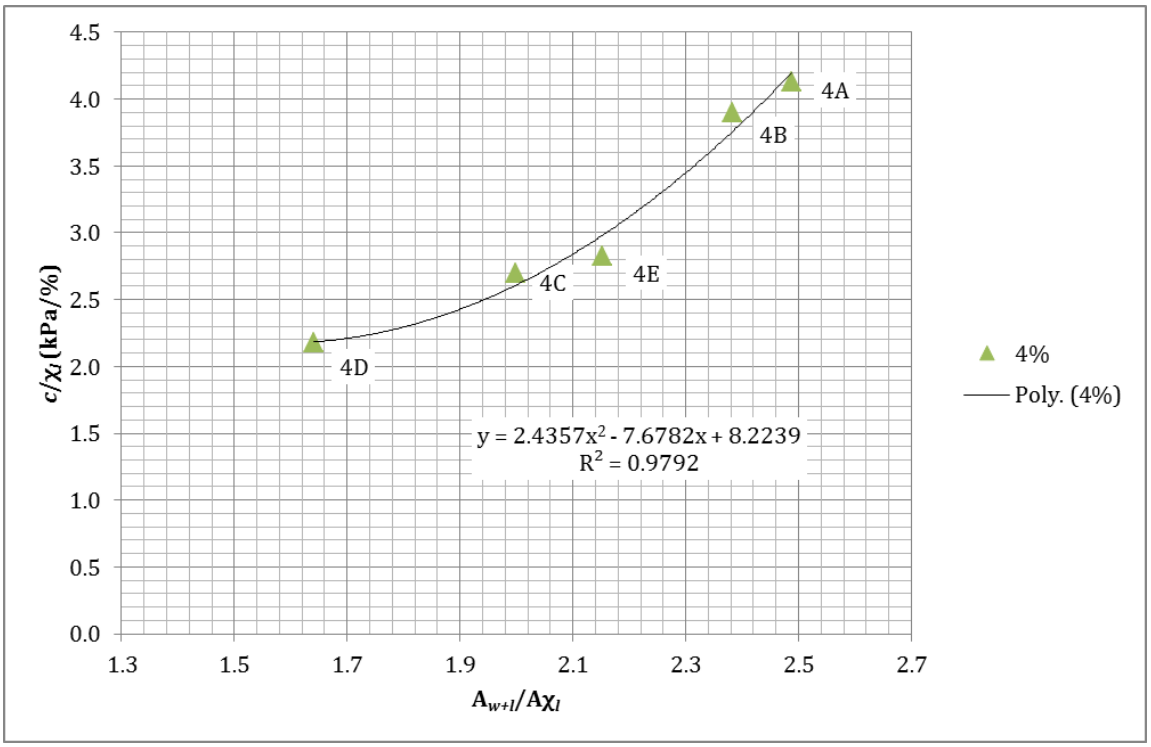

Figure 6-18: Normalized Cohesion vs. Normalized Area Ratio (4%)

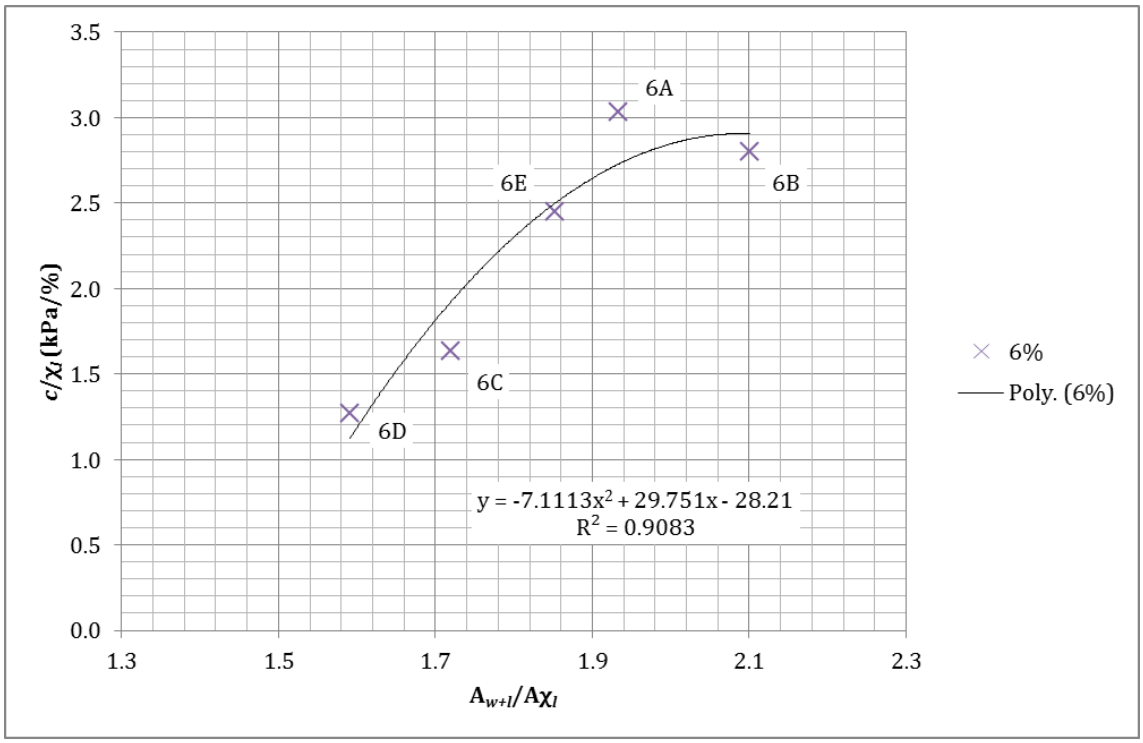

Figure 6-19: Normalized Cohesion vs. Normalized Area Ratio (6%)

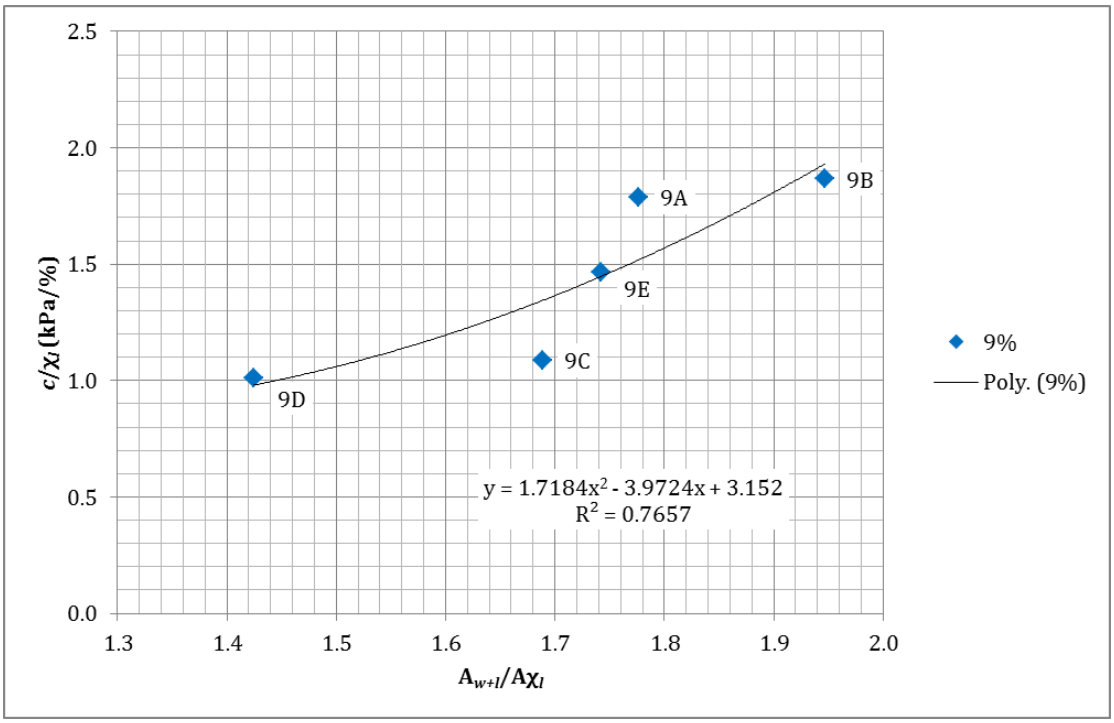

Figure 6-20: Normalized Cohesion vs. Normalized Area Ratio (9%)

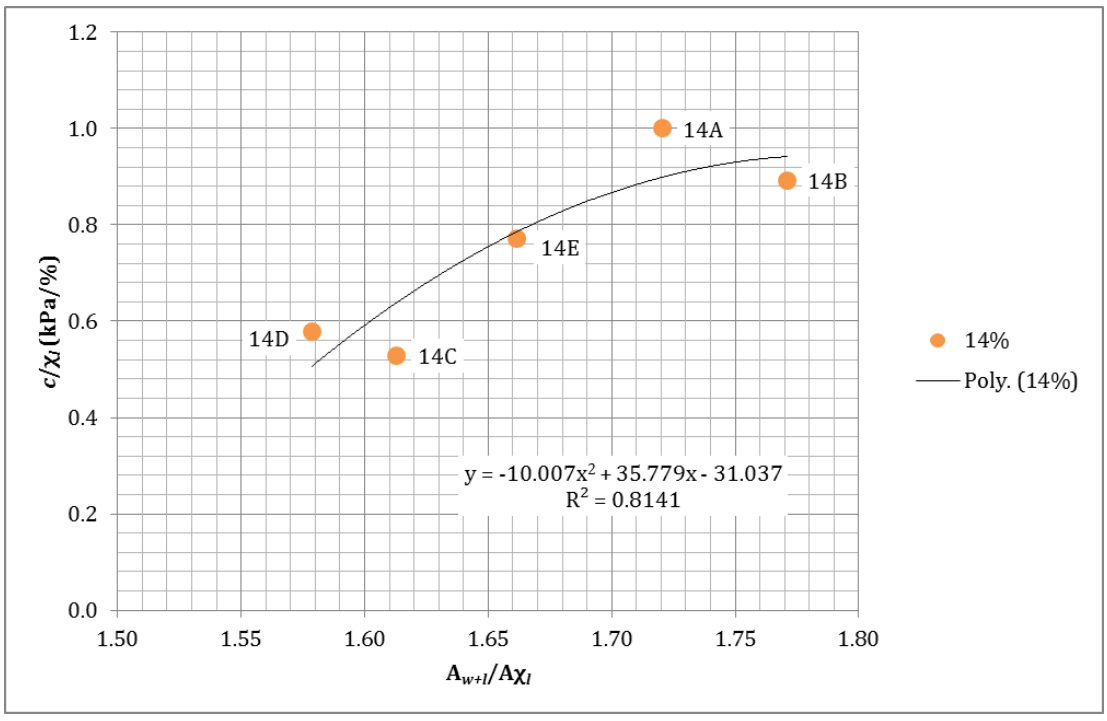

Figure 6-21: Normalized Cohesion vs. Normalized Area Ratio (14%)

Table 6-2: Rankings of R^2 values for individual configurations

χ_l (%)	R^2	Rank
2	0.80	4
4	0.98	1
6	0.91	2
9	0.77	5
14	0.81	3

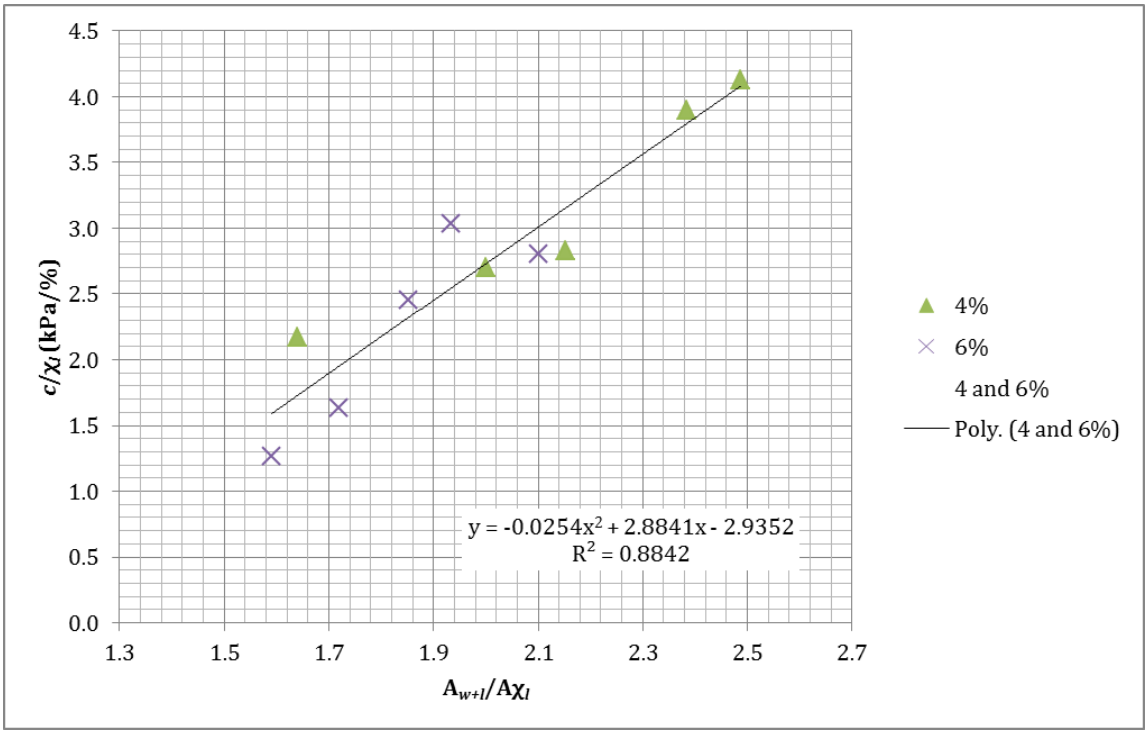

Figure 6-22: Normalized Cohesion vs. Normalized Area Ratio (4 and 6%)

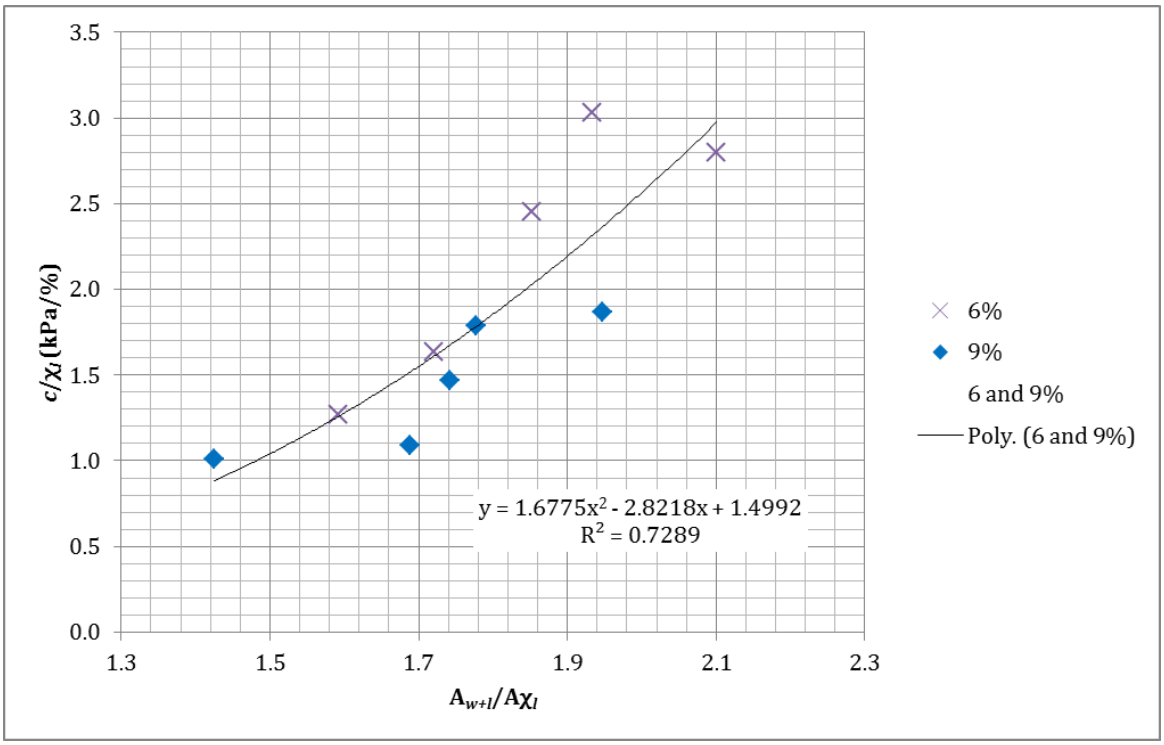

Figure 6-23: Normalized Cohesion vs. Normalized Area Ratio (6 and 9%)

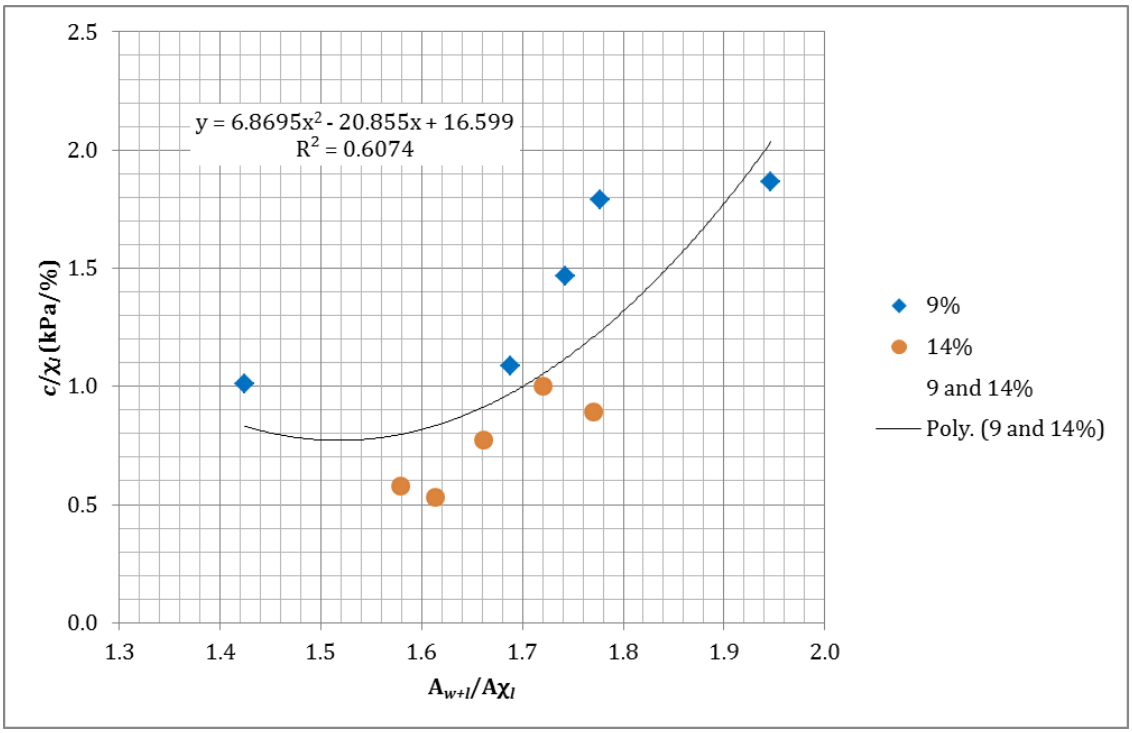

Figure 6-24: Normalized Cohesion vs. Normalized Area Ratio (9 and 14%)

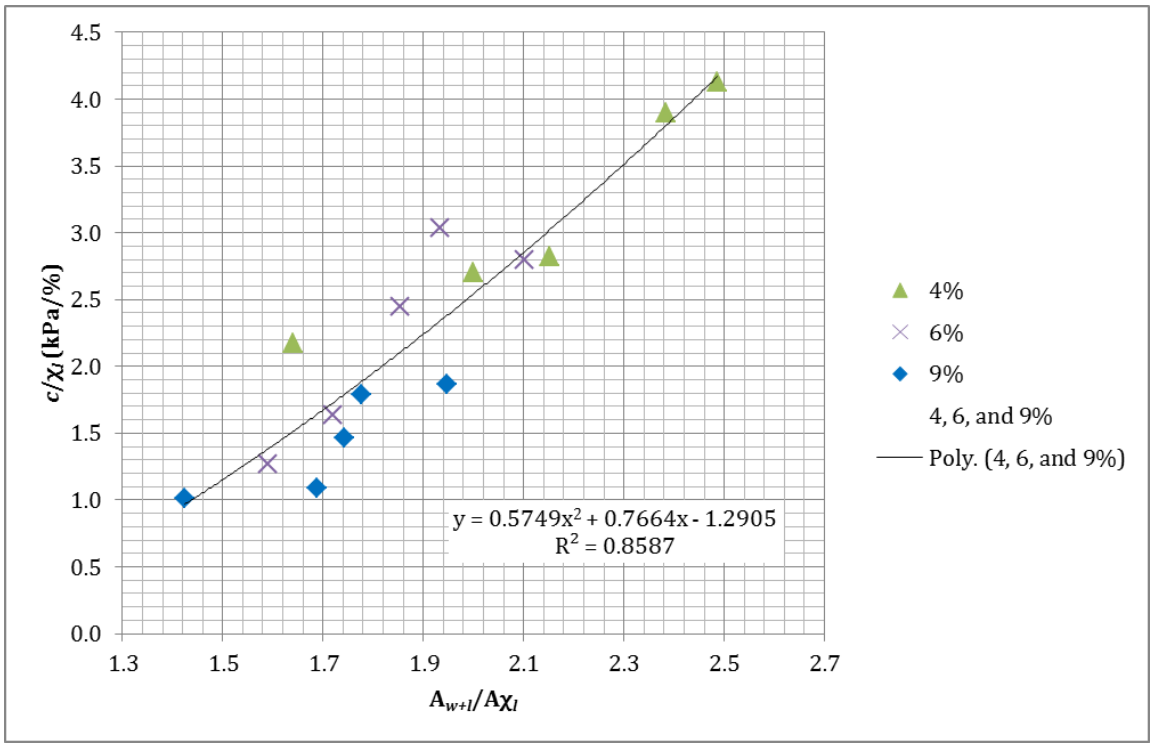

Figure 6-25: Normalized Cohesion vs. Normalized Area Ratio (4, 6, 9%)

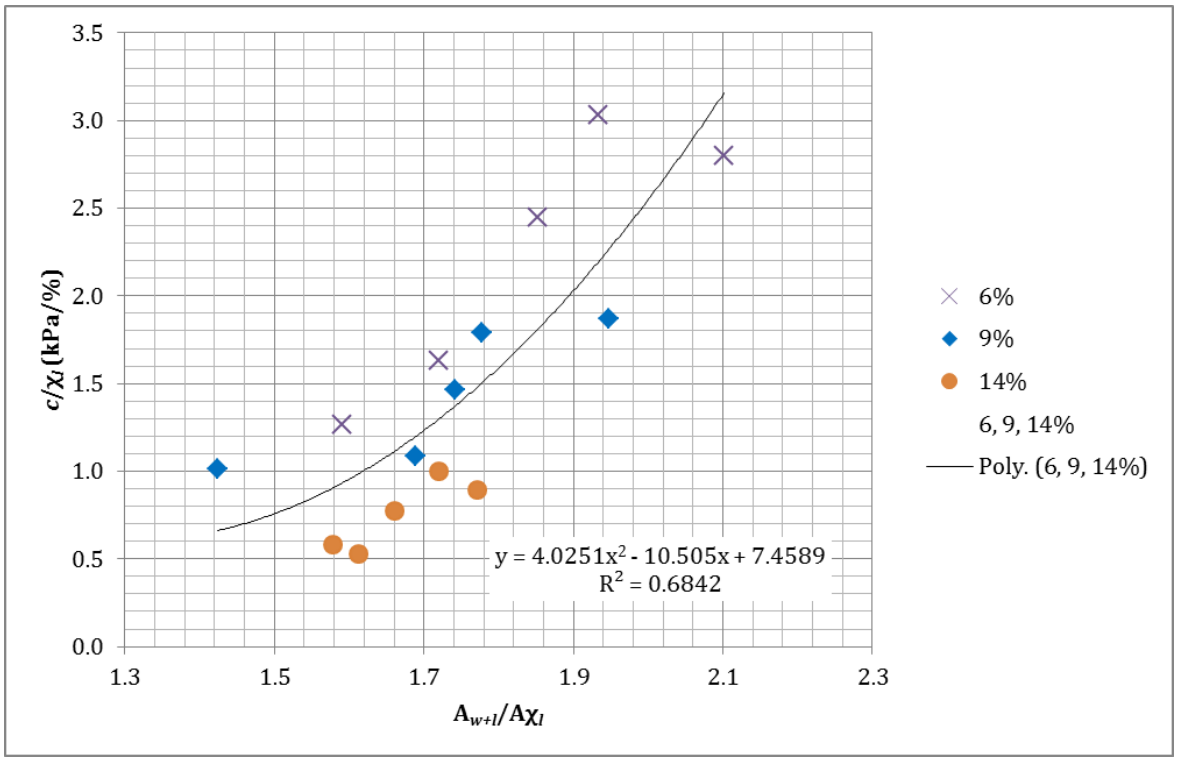

Figure 6-26: Normalized Cohesion vs. Normalized Area Ratio (6, 9, 14%)

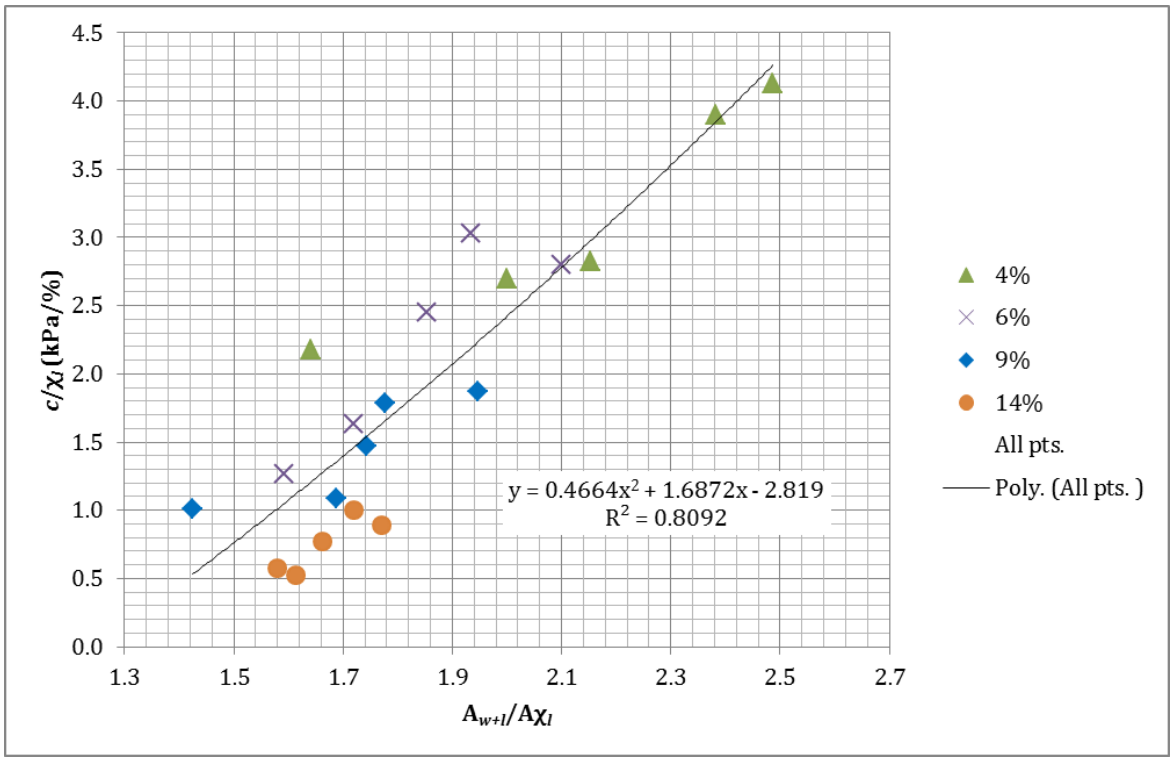

Figure 6-27: Normalized Cohesion vs. Normalized Area Ratio (4, 6, 9, 14%)

Table 6-3: Rankings of R^2 values for different combinations of configurations

Combination (%)	R^2	Rank
4, 6	0.88	1
6, 9	0.73	4
9, 14	0.61	6
4, 6, 9	0.86	2
6, 9, 14	0.68	5
4, 6, 9, 14	0.81	3

Figures 6-28 through 6-39 plot the same data points separated into four groups as follows:

1) Configurations A illustrate the effect of water to gravimetric lignin ratio at the relative compaction of 100%.
2) Configurations E illustrate the effect of water to lignin ratio at the relative compaction of 95%.
3) Configurations C illustrate the effect of water to lignin ratio at the relative compaction of 90%.
4) Configurations DEB illustrate the effect of water to gravimetric lignin ratio at constant void ratio corresponding to the relative compaction of 95%.

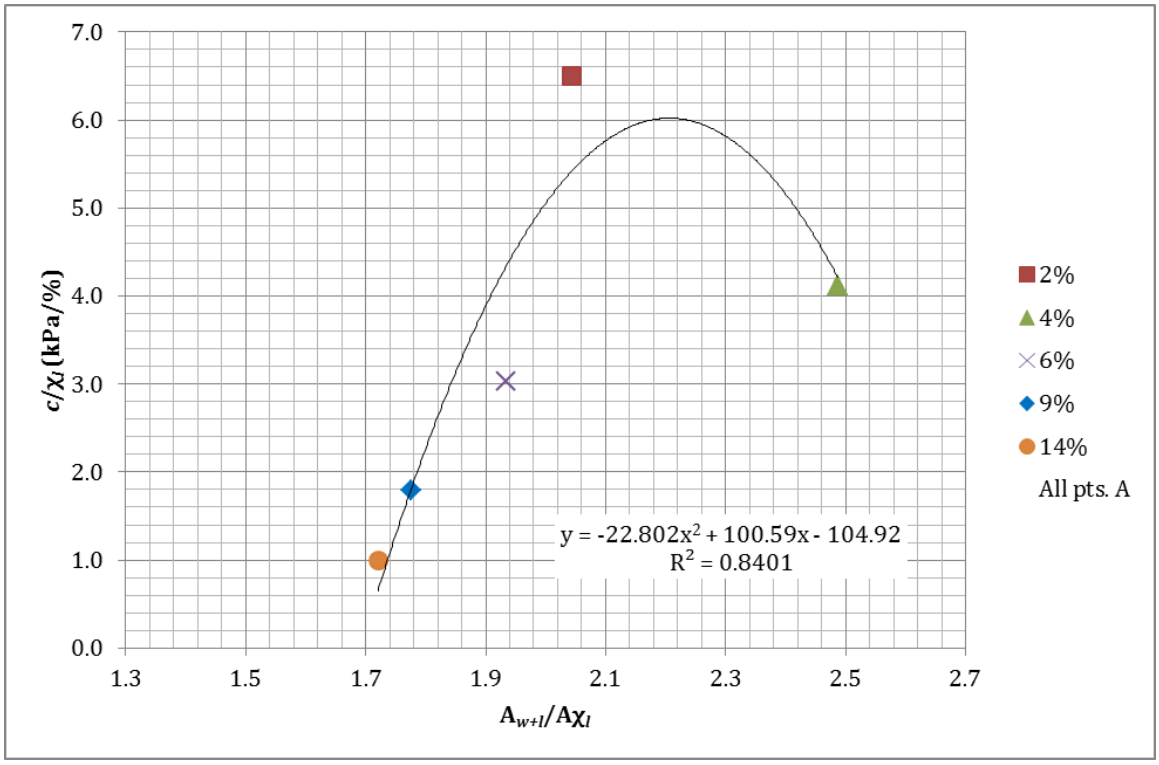

Figure 6-28: Normalized Cohesion vs. Normalized Area Ratio (All pts., A)

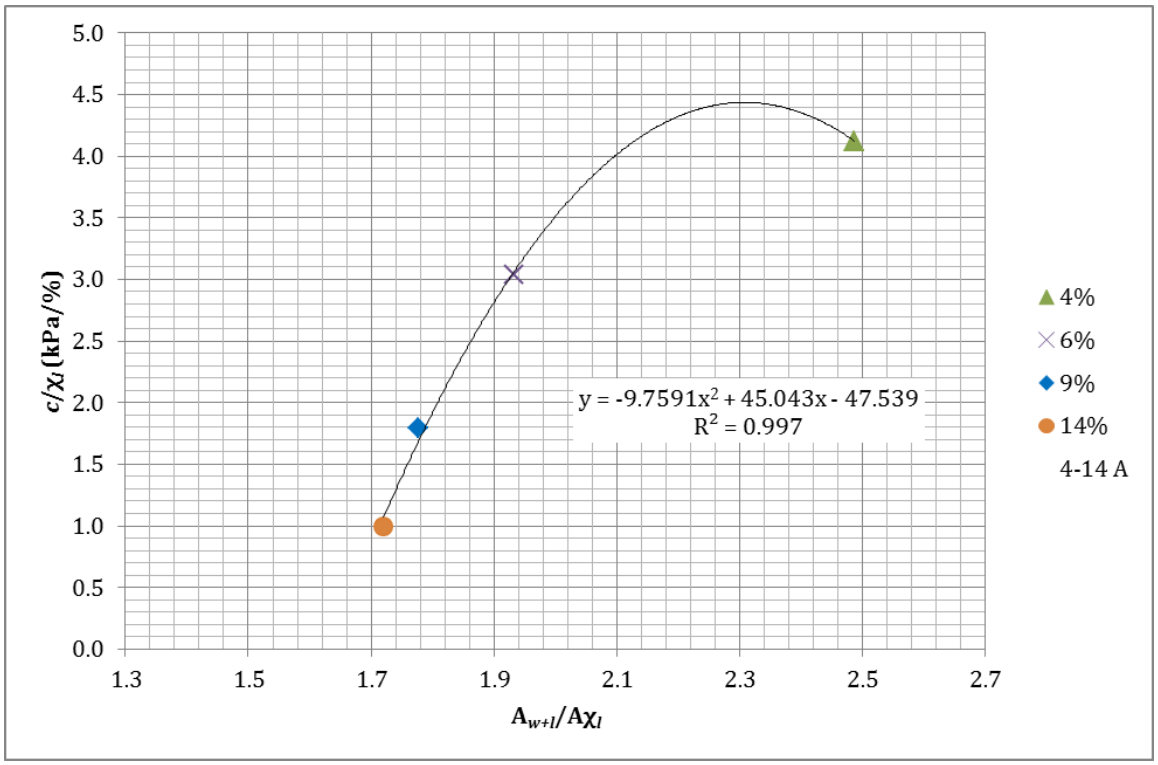

Figure 6-29: Normalized Cohesion vs. Normalized Area Ratio (4, 6, 9, 14%, A)

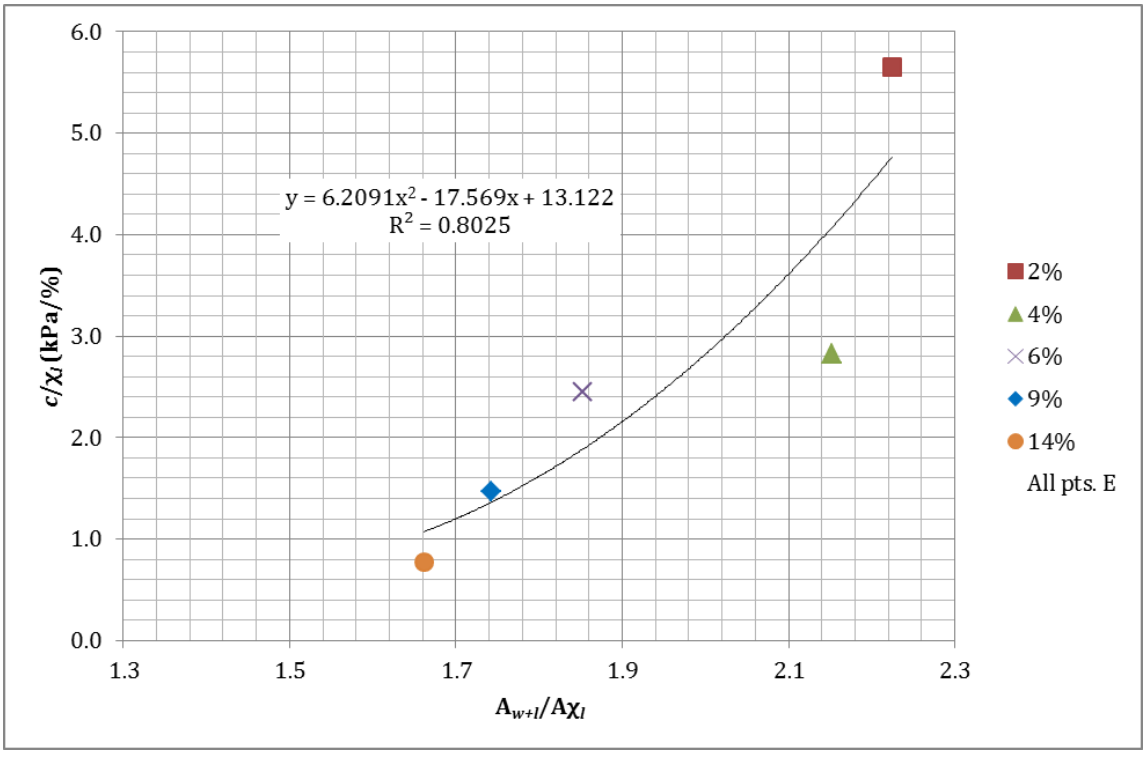

Figure 6-30: Normalized Cohesion vs. Normalized Area Ratio (All pts., E)

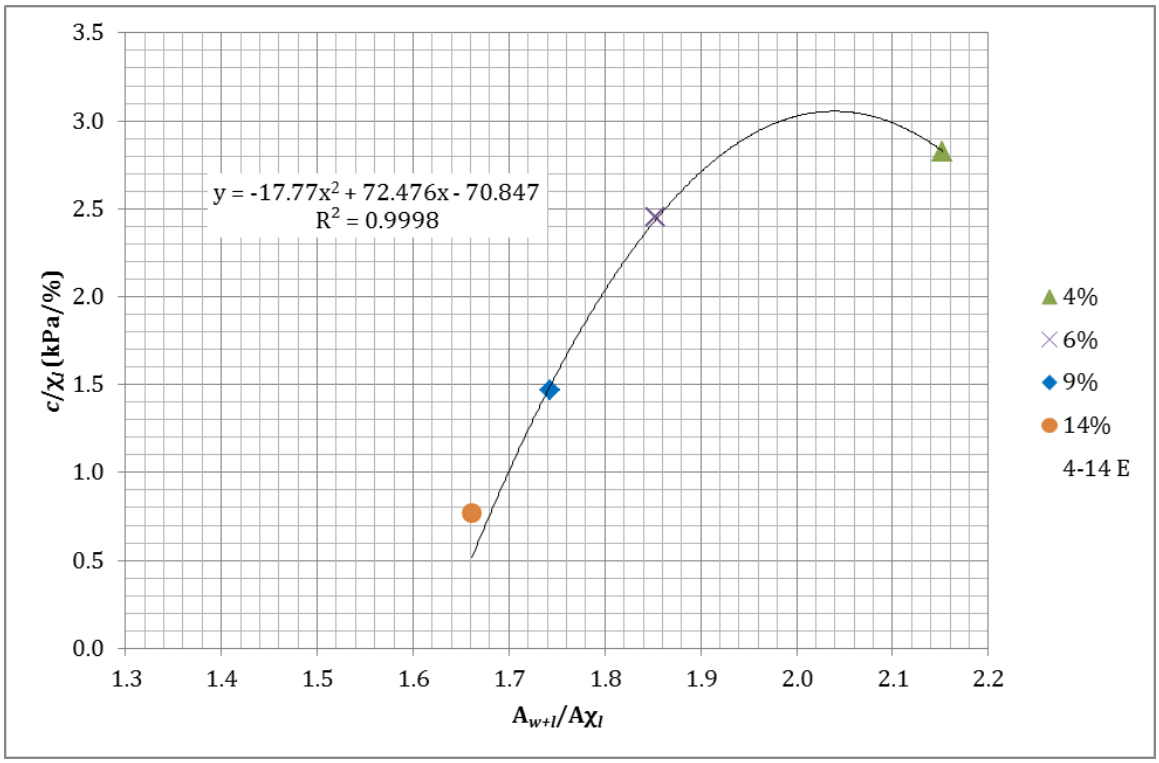

Figure 6-31: Normalized Cohesion vs. Normalized Area Ratio (4, 6, 9, 14%, E)

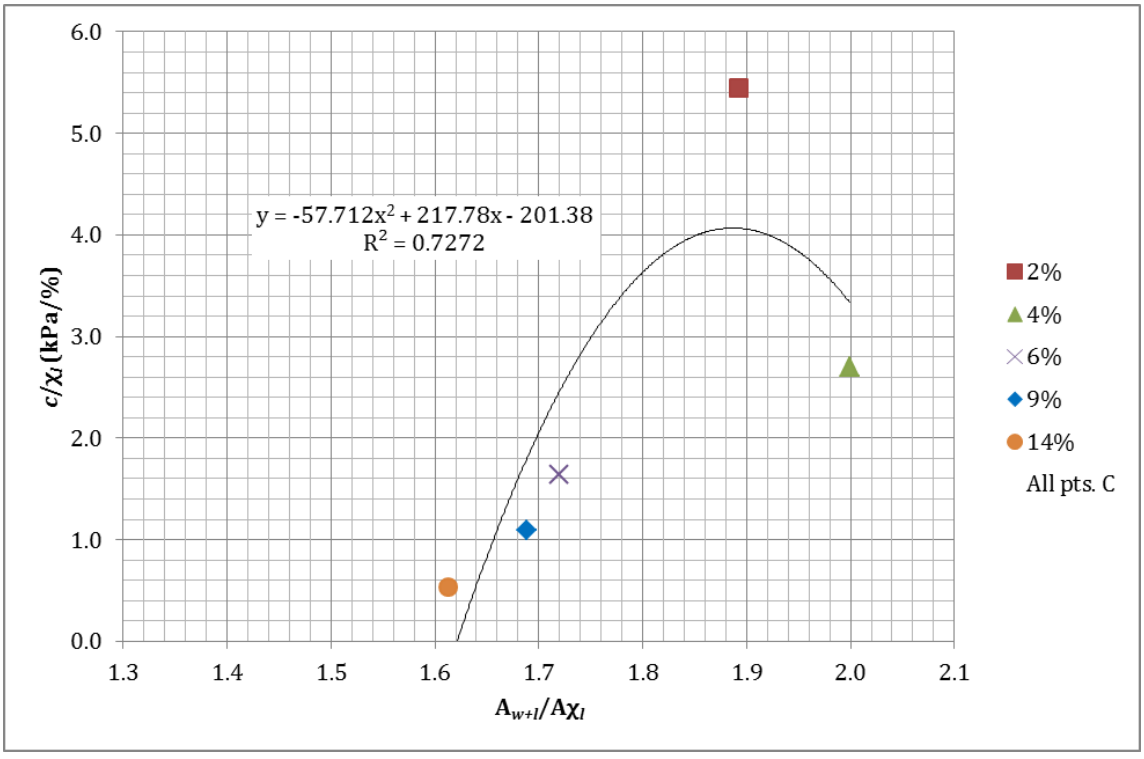

Figure 6-32: Normalized Cohesion vs. Normalized Area Ratio (All pts., C)

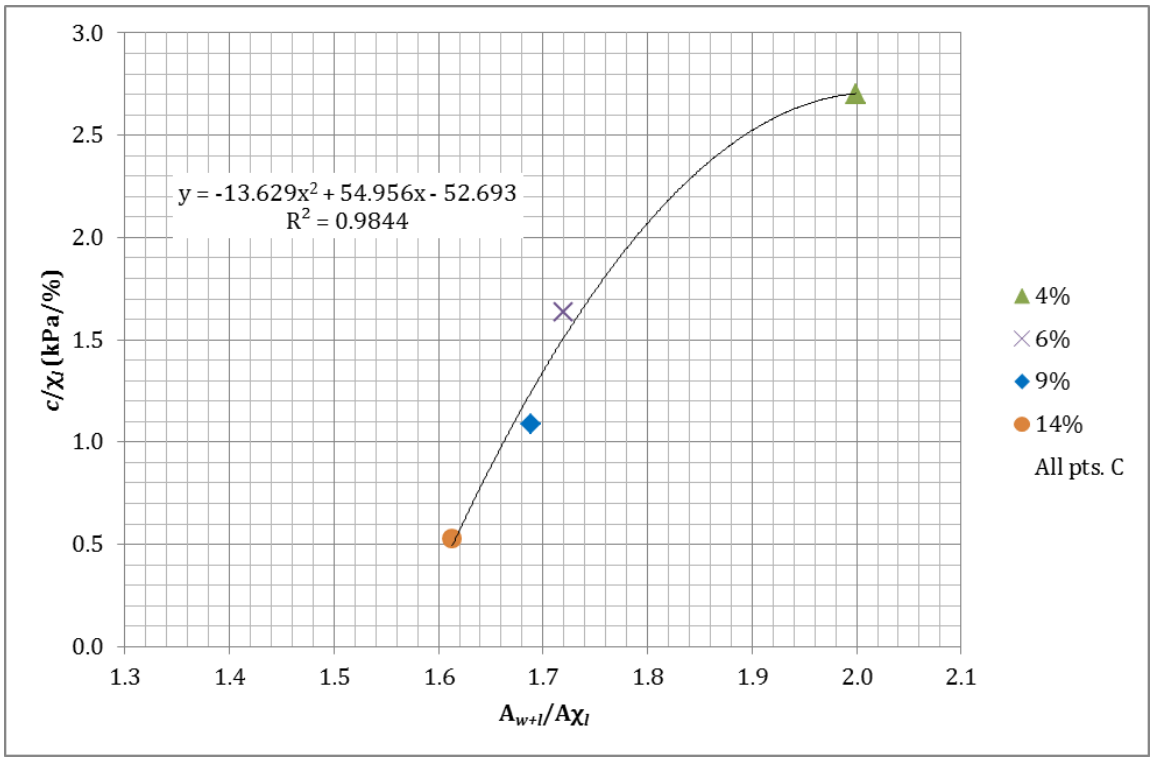

Figure 6-33: Normalized Cohesion vs. Normalized Area Ratio (4, 6, 9, 14%, C)

Table 6-4: Rankings of R2 values for configurations A, E, and C plots

Configurations	R^2	Rank
A (all)	0.840	4
A (w/o 2A)	0.997	2
E (all)	0.803	5
E (w/o 2E)	0.999	1
C (all)	0.727	6
C (w/o 2C)	0.984	3

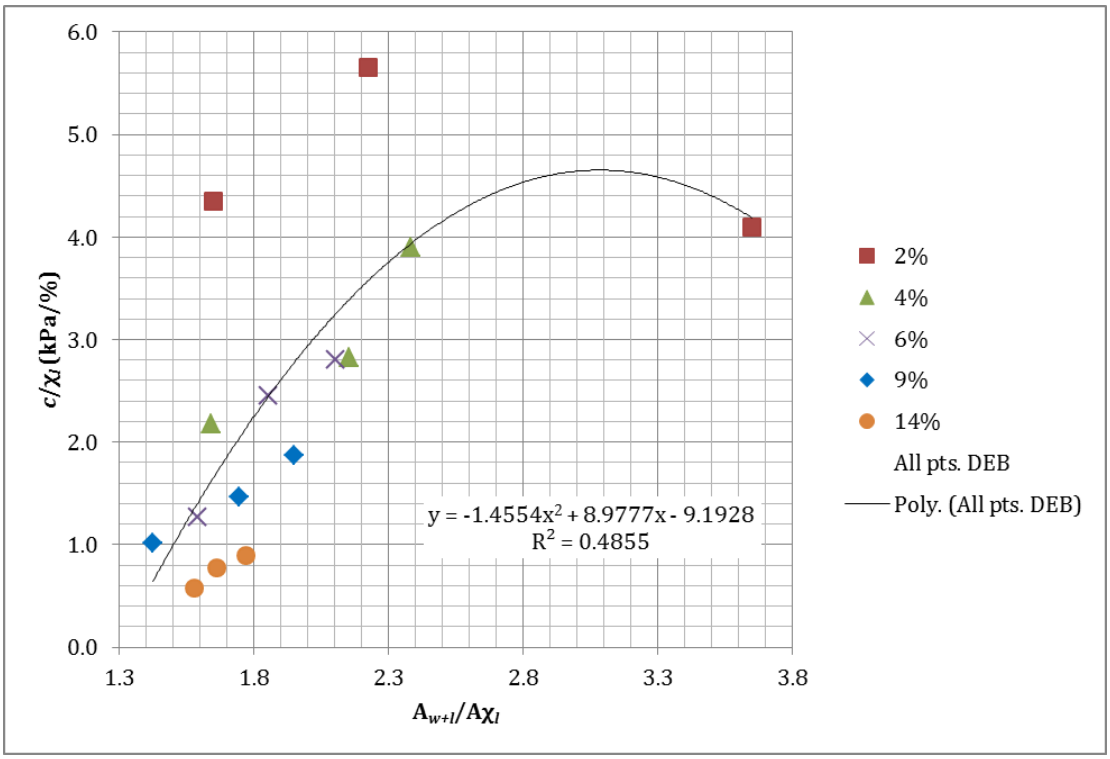

Figure 6-34: Normalized Cohesion vs. Normalized Area Ratio (All pts.; D, E, B)

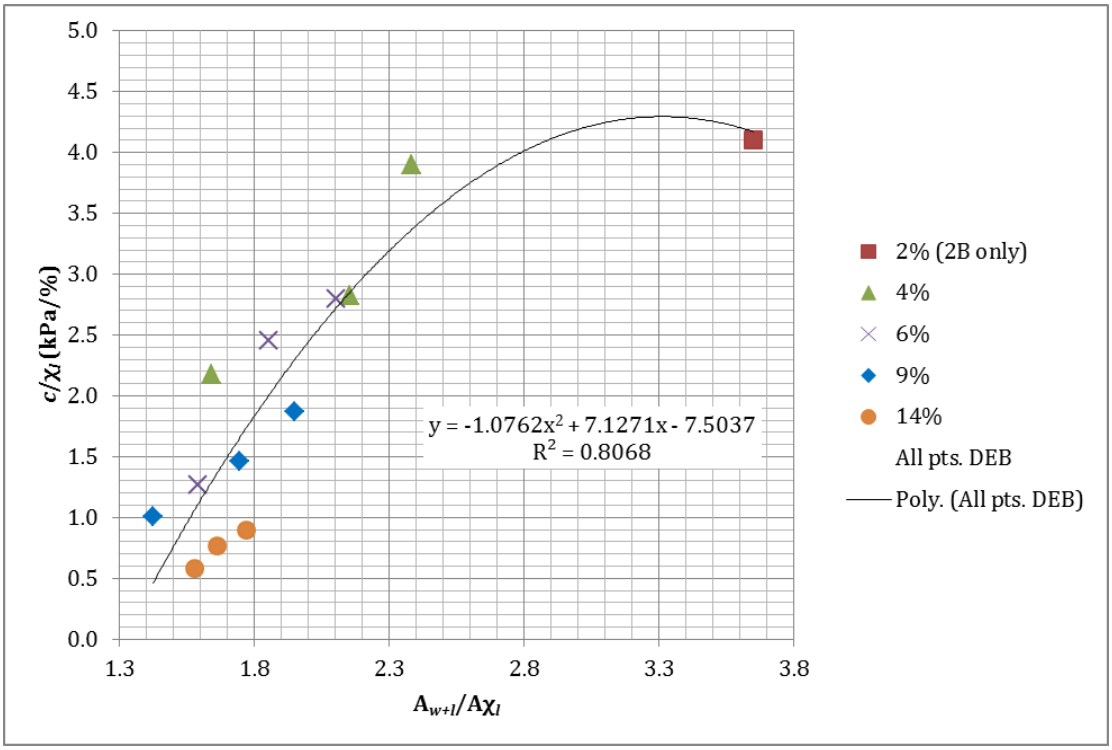

Figure 6-35: Normalized Cohesion vs. Normalized Area Ratio (D, E, B, w/o 2D, 2E)

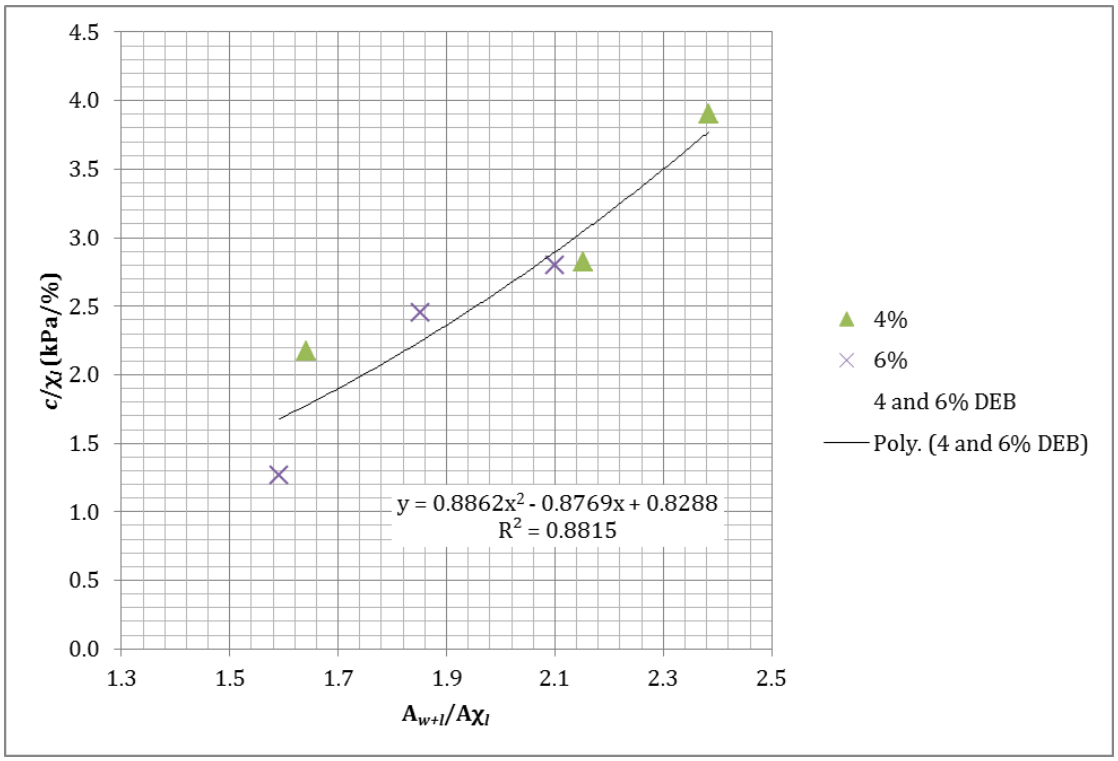

Figure 6-36: Normalized Cohesion vs. Normalized Area Ratio (4 and 6%; D, E, B)

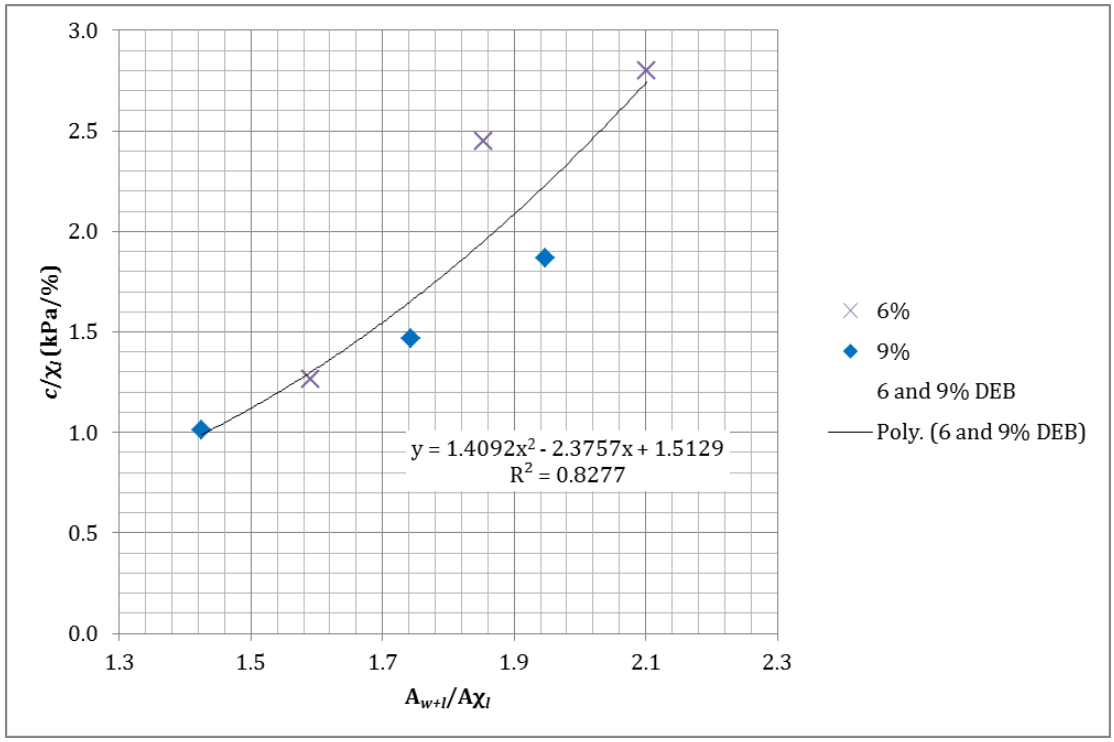

Figure 6-37: Normalized Cohesion vs. Normalized Area Ratio (6 and 9%; D, E, B)

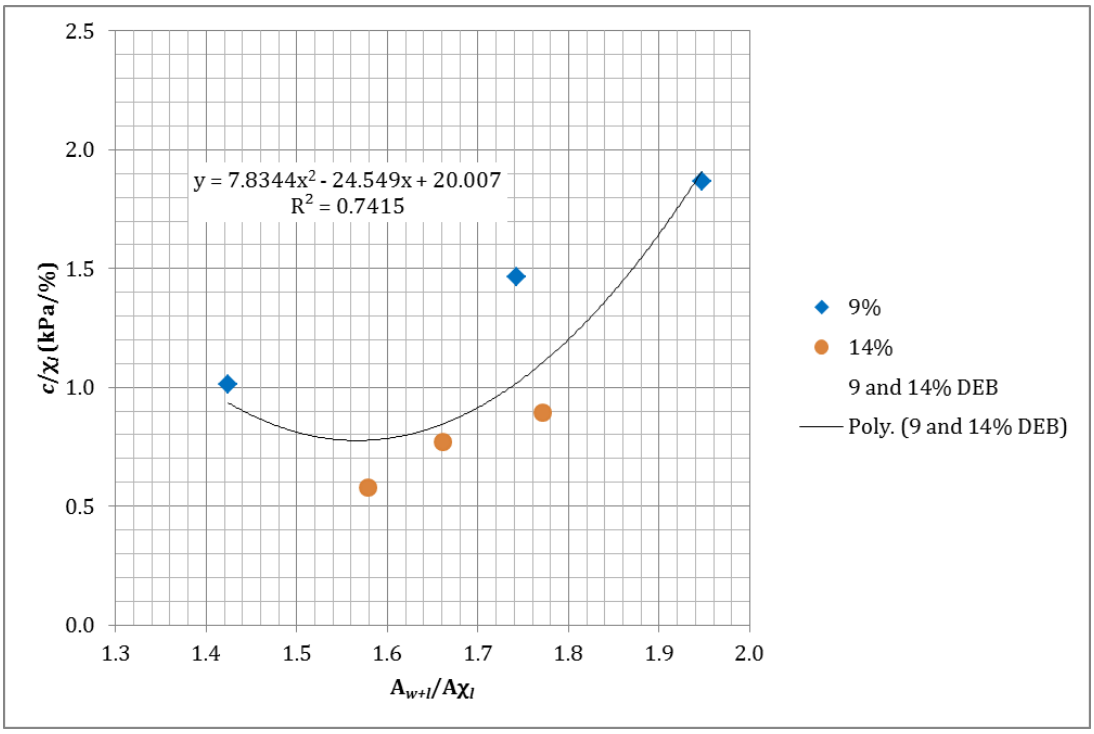

Figure 6-38: Normalized Cohesion vs. Normalized Area Ratio (9 and 14%; D, E, B)

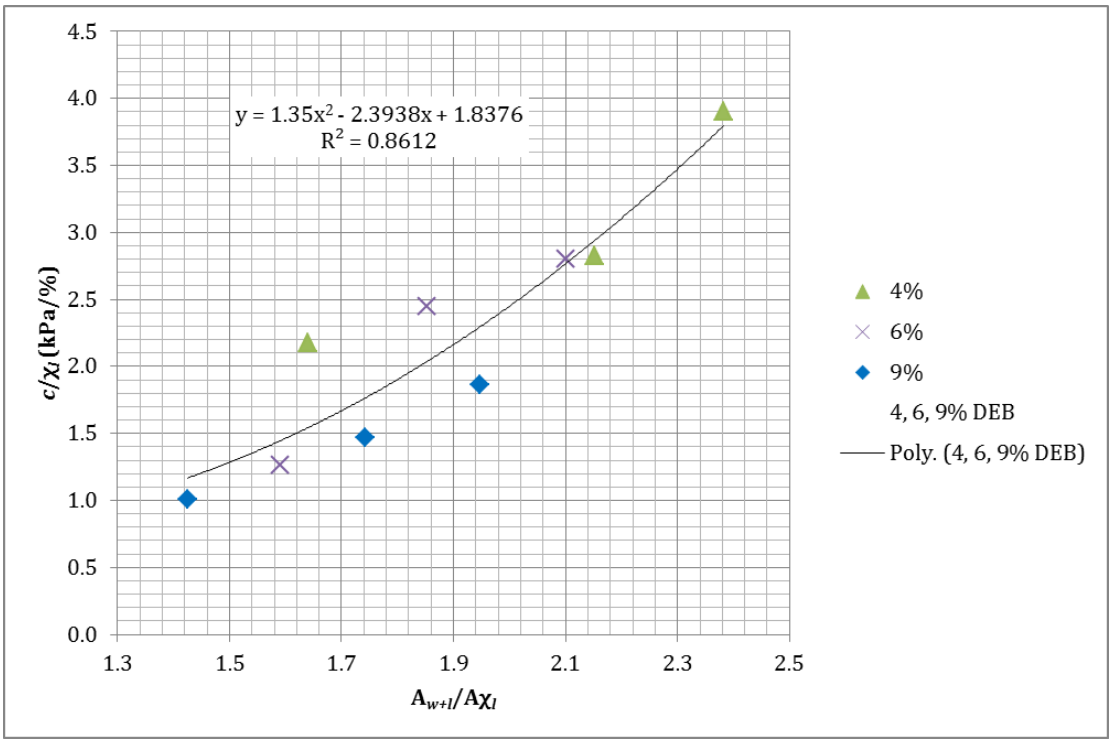

Figure 6-39: Normalized Cohesion vs. Normalized Area Ratio (4, 6, 9%; D, E, B)

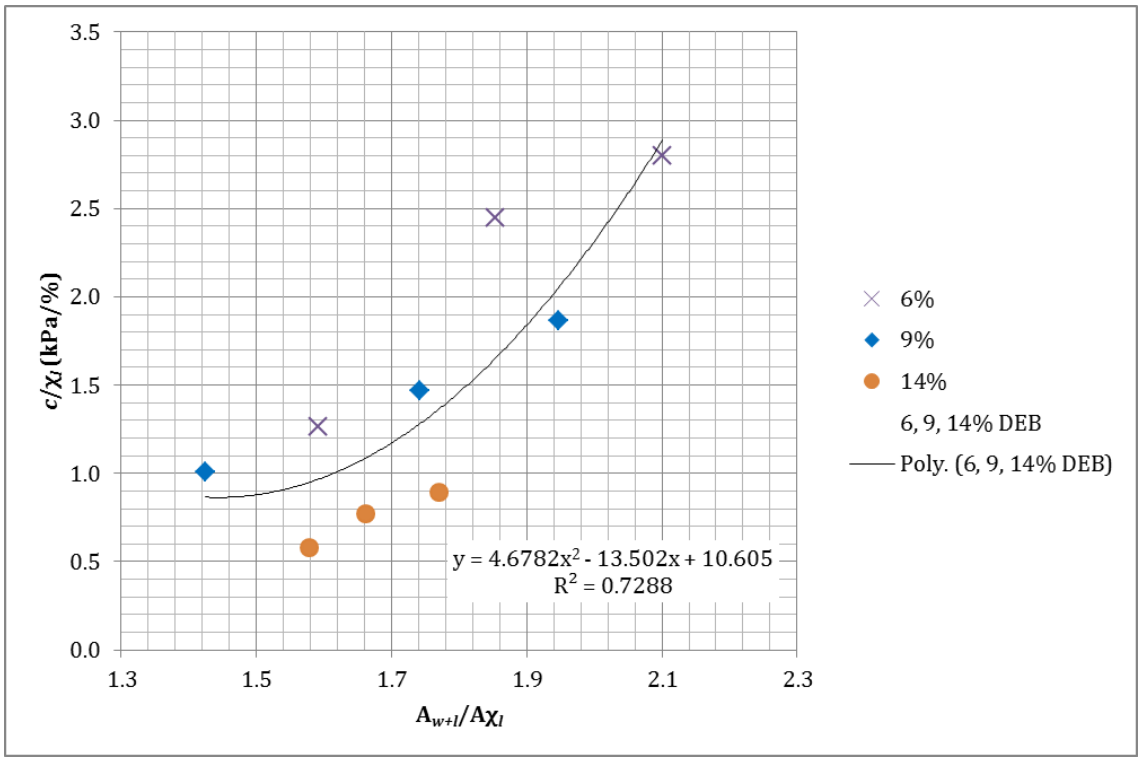

Figure 6-40: Normalized Cohesion vs. Normalized Area Ratio (6, 9, 14%; D, E, B)

Table 6-5: Rankings of R^2 values for configurations D, E, B combinations

Combination (%)	R^2	Rank
4, 6	0.88	1
6, 9	0.83	3
9, 14	0.74	6
4, 6, 9	0.86	2
6, 9, 14	0.73	7
4, 6, 9, 14	0.79	5
2B, 4, 6, 9, 14	0.81	4

Tables 6-2 through 6-5 show the ranking of various configurations in different categories. Rankings are based on the values of the coefficients of determination. Among individual lignin contents, the best fit is achieved for 4%, which is followed by 6%. The worse fit is obtained for χ_l = 9%, but the corresponding value of the coefficient of determination is close to that belonging to the combination of χ_l = 2 and 14%. All values of R^2 are larger than 0.77.

In various combinations, including all testing configurations, χ_l = 4 and 6% has the top ranking (R^2 = 0.86). Adding χ_l = 14% to any combination decreases R^2 more significantly then

adding χ_l = 9%, thus indicating that the material response changes at χ_l = 14%, resulting in a different behavior.

Combinations involving points D, E, and B confirm this observation, whereby the top three rankings belong to χ_l = 4 and 6%, χ_l = 4, 6, and 9%, and χ_l = 6 and 9%. It is noted that the only χ_l = 2% configuration included in the group rankings is configuration 2B due to the previous observations.

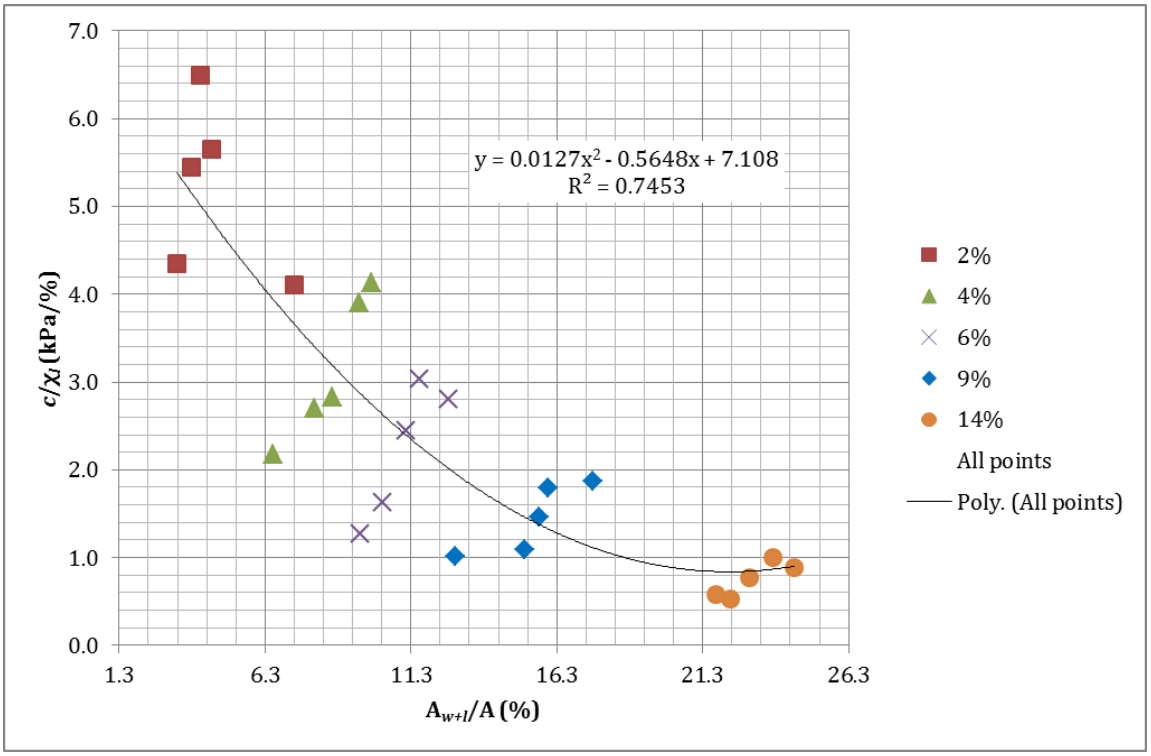

Figure 6-41: Normalized Cohesion vs. Area Ratio (All pts.)

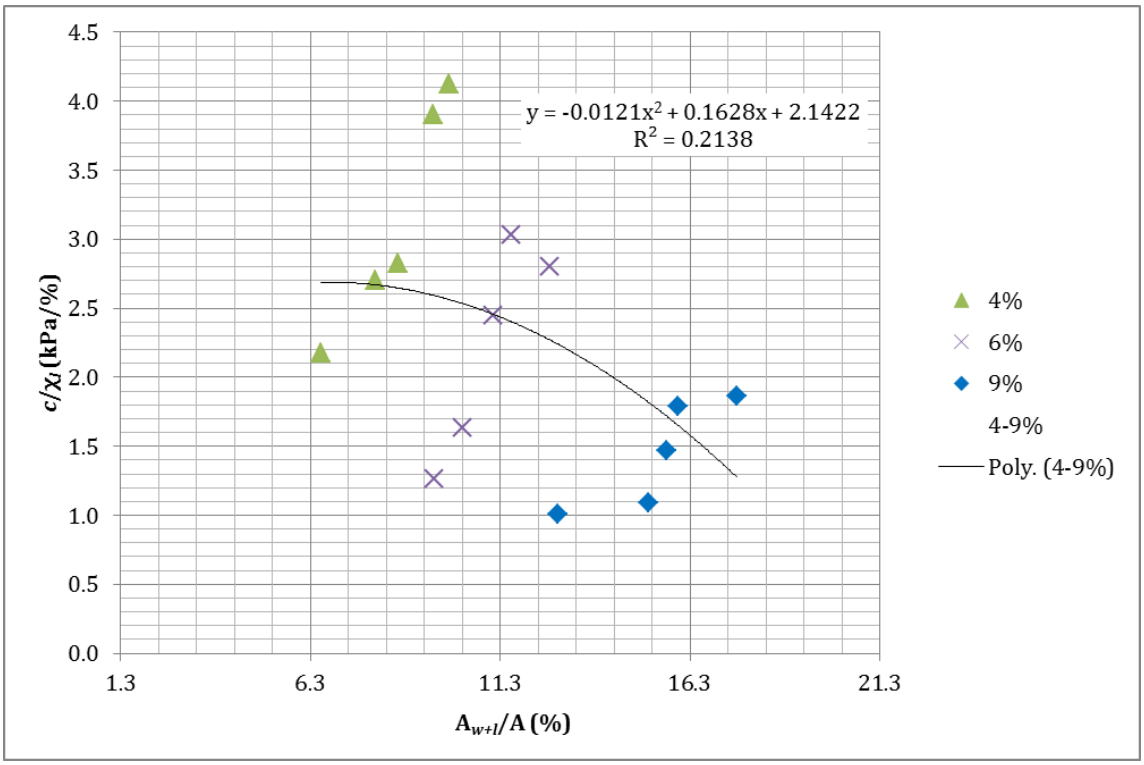

Figure 6-42: Normalized Cohesion vs. Area Ratio (4, 6, and 9%)

Figure 6-41 plots normalized cohesion versus the non-normalized area ratio. This plot differs from the plots of normalized cohesion versus normalized area ratio in that the fit is better for all sample configurations than for the cohesion of gravimetric lignin content of 4%, 6% and 9%.

Figure 6-43 plots cohesion normalized by area ratio versus the area ratio. This plot illustrates the same trend as the plot in Figure 6-41.

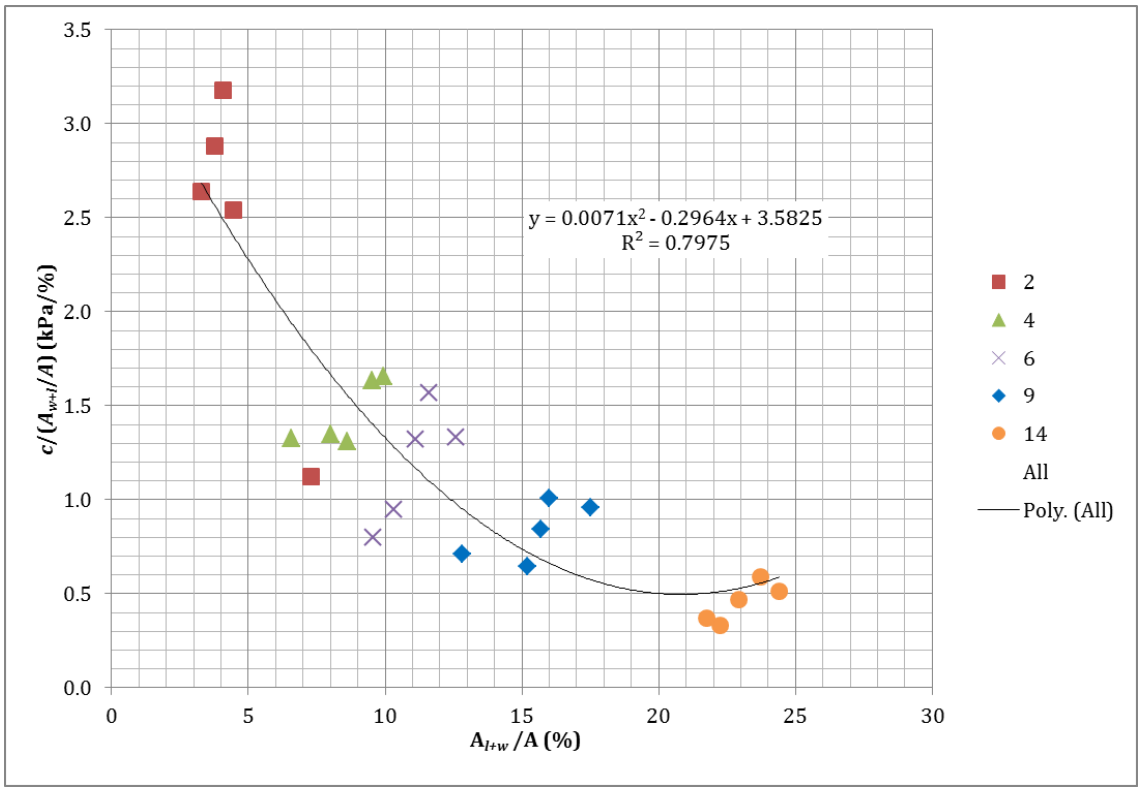

Figure 6-43: Cohesion Normalized to Area Ratio vs. Area Ratio (All pts.)

Figures 6-44 through 6-46 illustrate the ranges of water to lignin ratios, water contents, and void ratios used in the experimental program. Figure 6-44 plots normalized area ratio versus actual water to lignin ratio. It is noted that the relationship between normalized area ratio and water to lignin ratio is linear for constant void ratio (Equation 28). Thus, it is because void ratios are not constant for all sample configurations that the determination coefficient is slightly smaller than one. Water to lignin ratio values for the most part range from approximately 24% to 84%, with only one exception occurring at configuration 2B (161.5%); resulting in the normalized area ratios ranging from approximately 1.4 to 2.5, with the exception of configuration 2B (3.79). It is also noted that sample configurations with lower gravimetric lignin contents are located closer to the upper bounds of these ranges. Figure 6-45 shows the range of water contents and corresponding normalized area ratios used in the experimental program. It shows that water content values ranging from 0.8 to 6.4% were used in the experimental program.

Figure 6-46 plots normalized area ratios versus actual void ratios after the consolidation phase. All points are clustered around three distinct values of void ratios reflecting three different levels of relative compaction, whereby configuration 14A was compacted slightly below other A configurations. Finally, Figure 6-47 plots normalized area ratio versus gravimetric lignin content. This plot illustrates how the range of normalized area ratio ultimately decreases with the increasing lignin content.

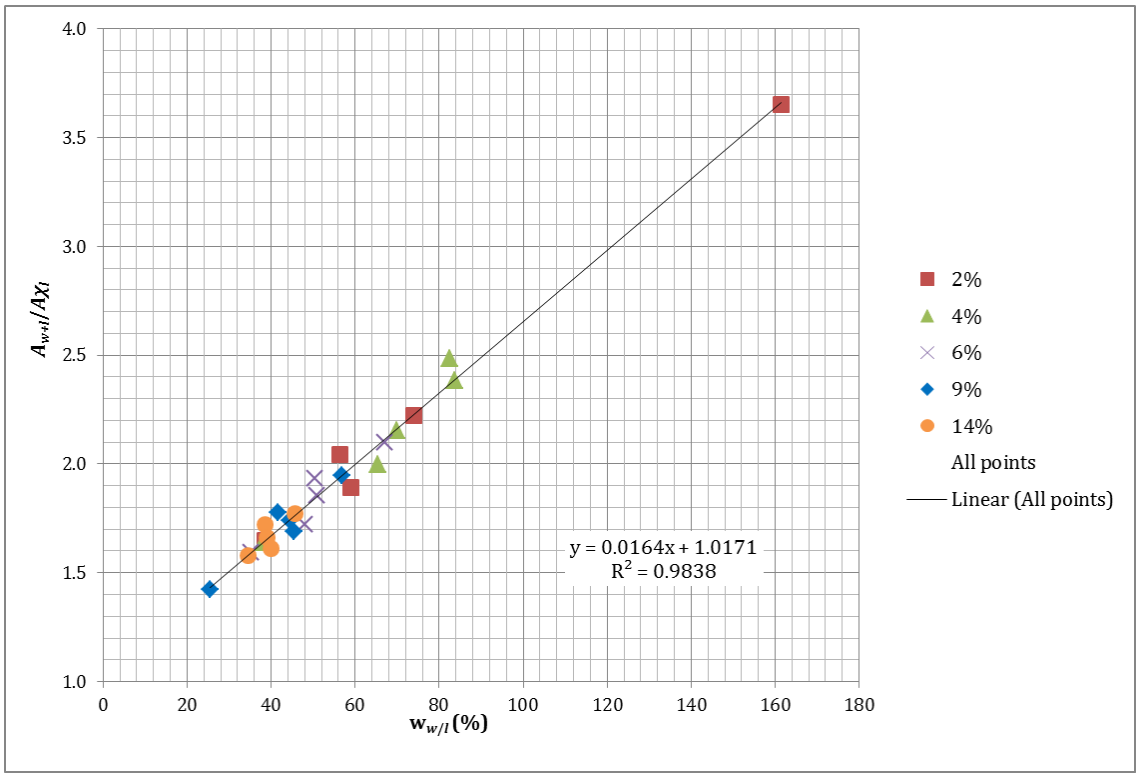

Figure 6-44: Normalized Area Ratio vs. Water to Lignin Ratio (All pts.)

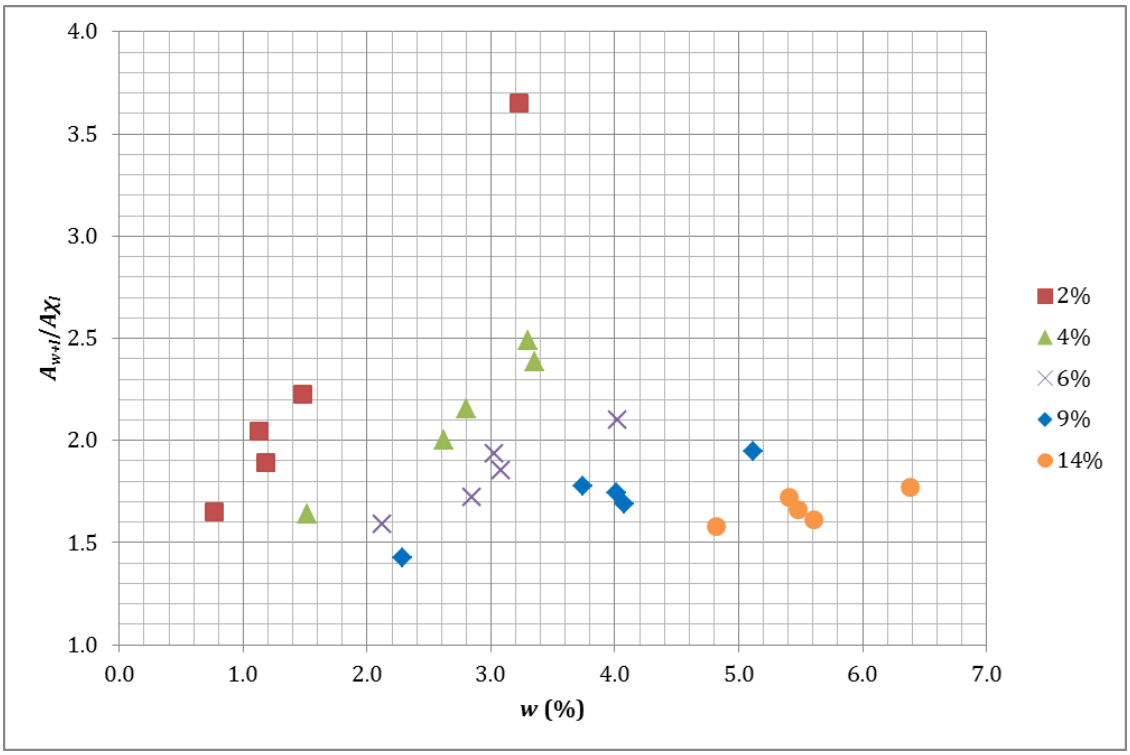

Figure 6-45: Normalized Area Ratio vs. Water Content (All pts.

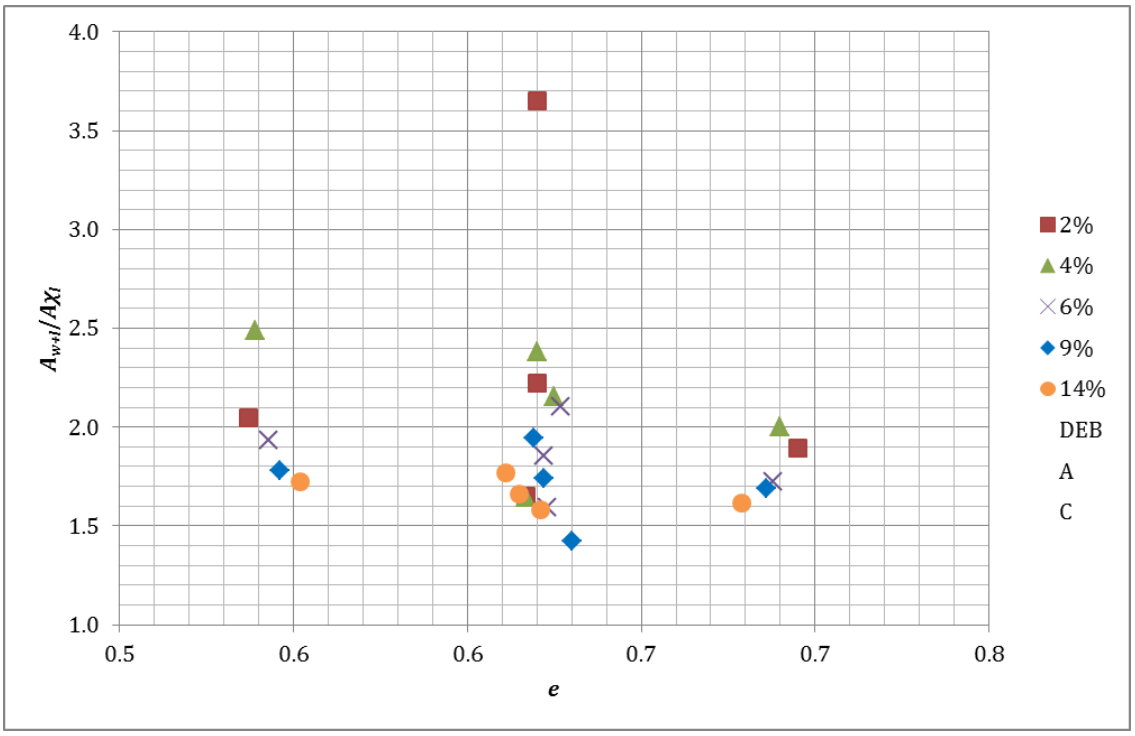

Figure 6-46: Normalized Area Ratio vs. Void Ratio (All pts.)

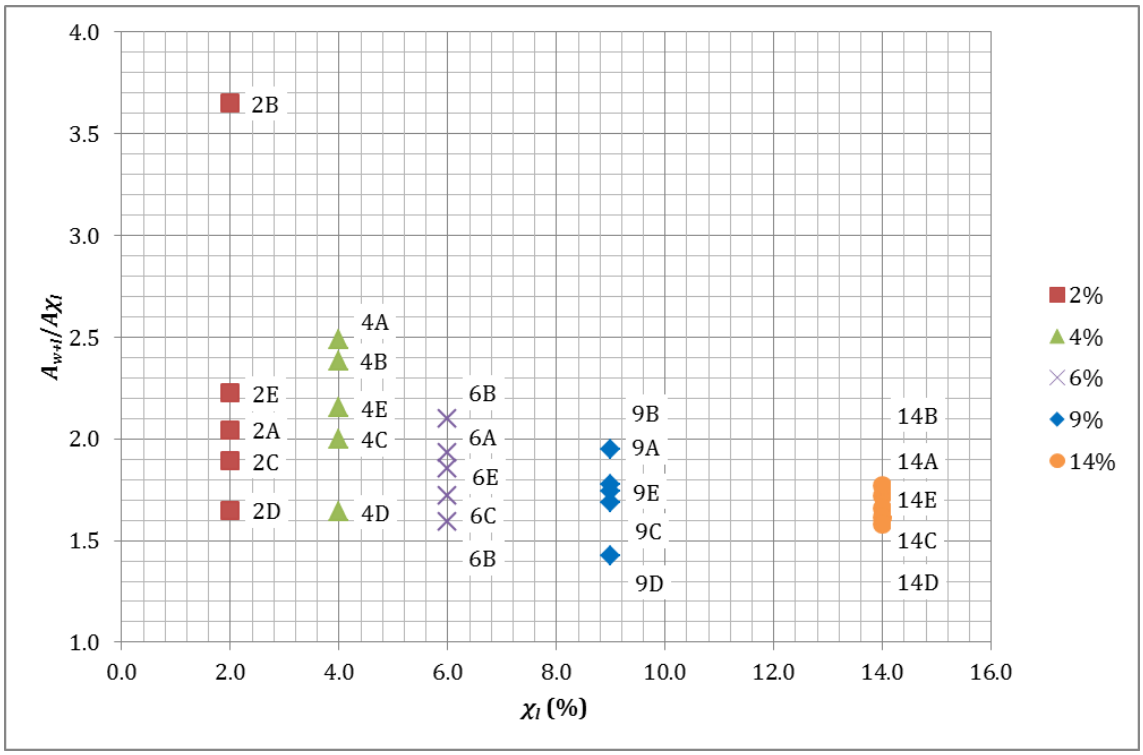

Figure 6-47: Normalized Area Ratio vs. Gravimetric Lignin Content (All pts.)

The following sets of plots are related to the internal friction angle of the specimens. Figure 6-48 is Figure 6-7 with trend lines drawn for the configurations, A, E, C, D, and B. Figure 6-49 represents the same data as Figure 6-48 but with all configurations analyzed together. The plots detect decreasing friction angle with the increasing gravimetric lignin ratio for configurations A, B and E. This trend is not as evident at configurations C and D. This could be because configuration C is under compacted and configuration D contains low moisture content levels. Both factors could impact the trends of the angle of friction. Figures 6-50 and 6-51 plot the angles of friction versus area ratio.

Figure 6-52 is a plot of the tangent of the angle of friction versus the normalized area ratio. The trend is evident, with the exception of points 6B and 14A.

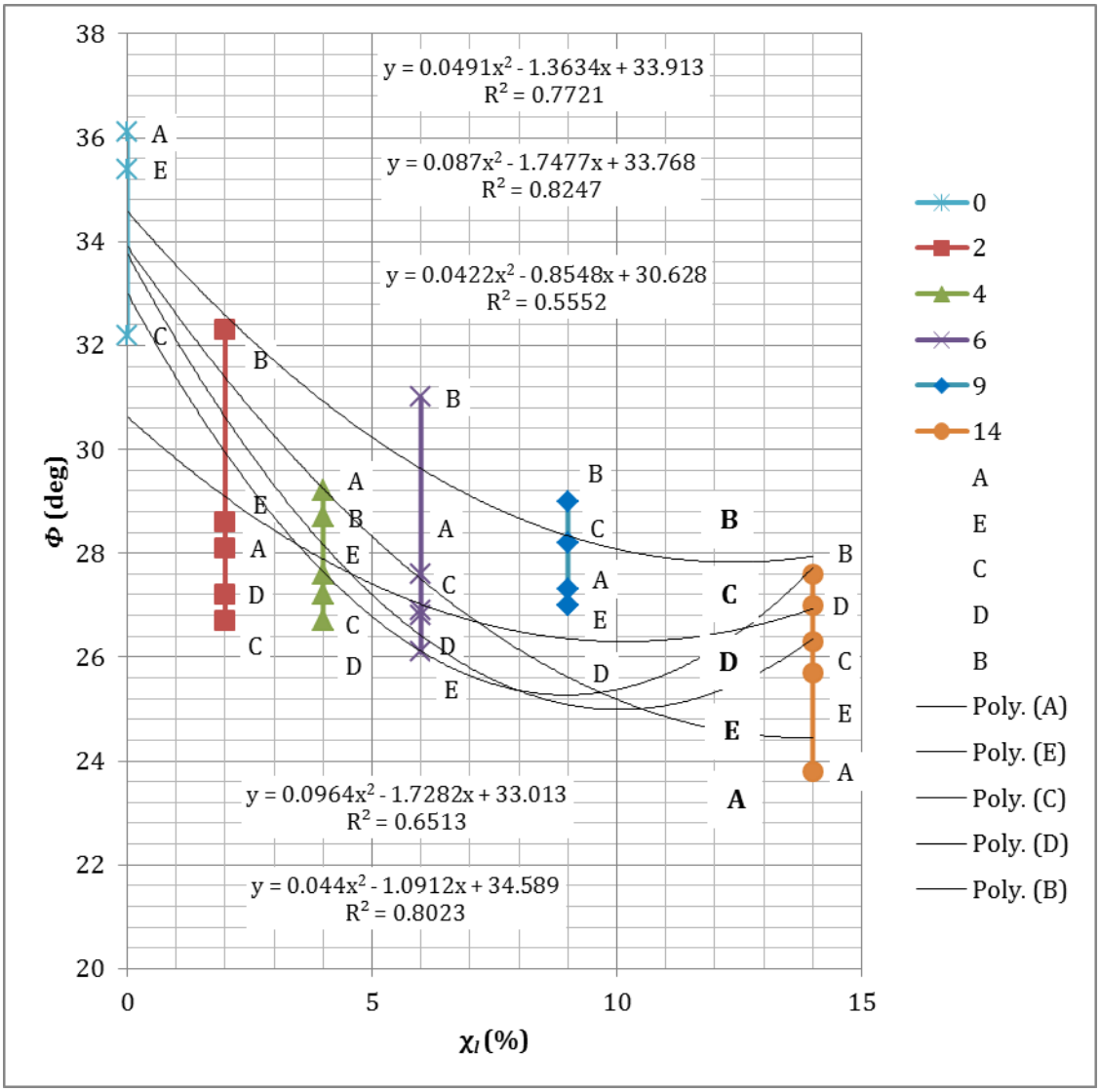

Figure 6-48: Angle of Friction vs. Gravimetric Lignin Content (All pts.)

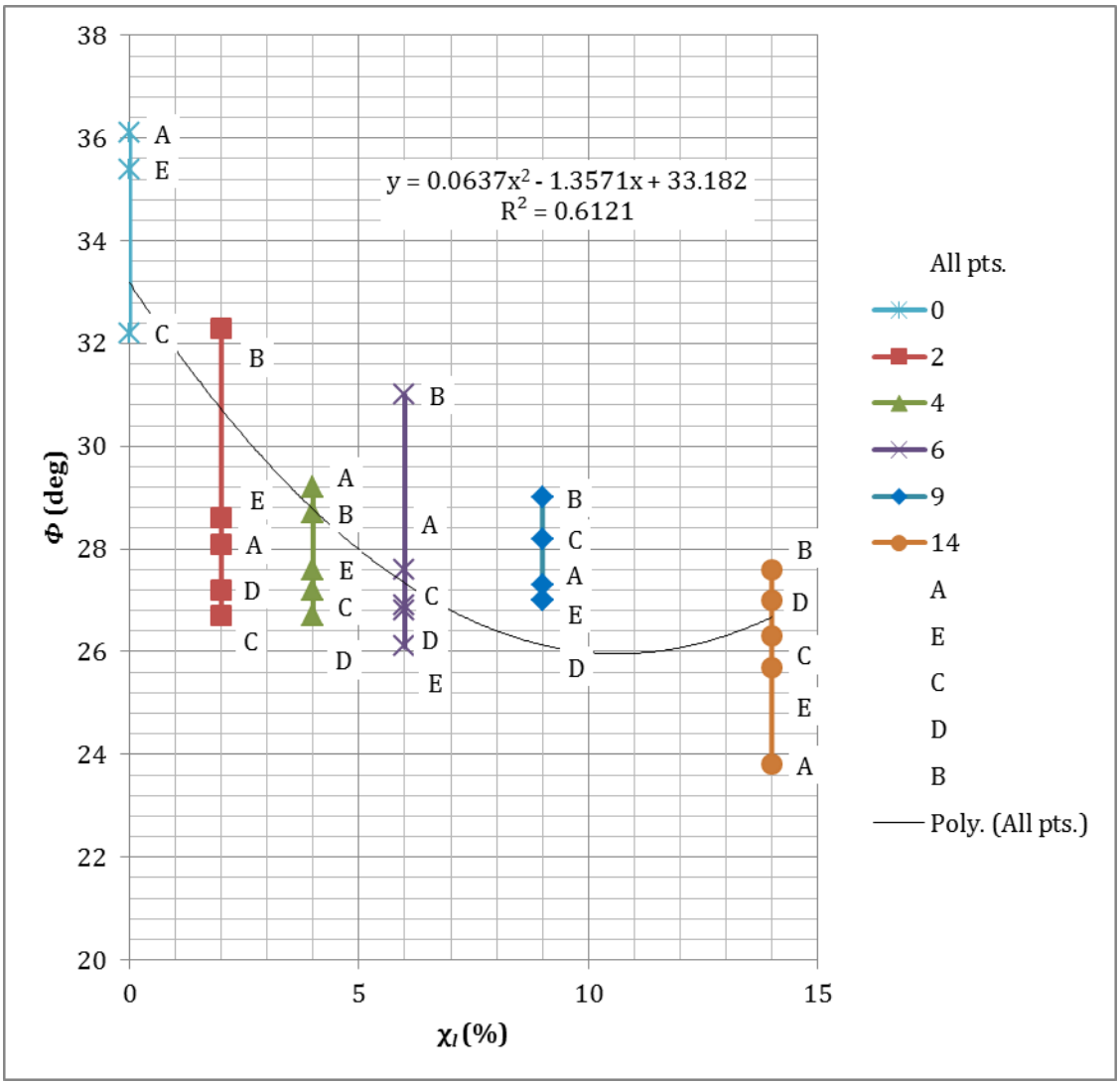

Figure 6-49: Angle of Friction vs. Gravimetric Lignin Content (All pts.)

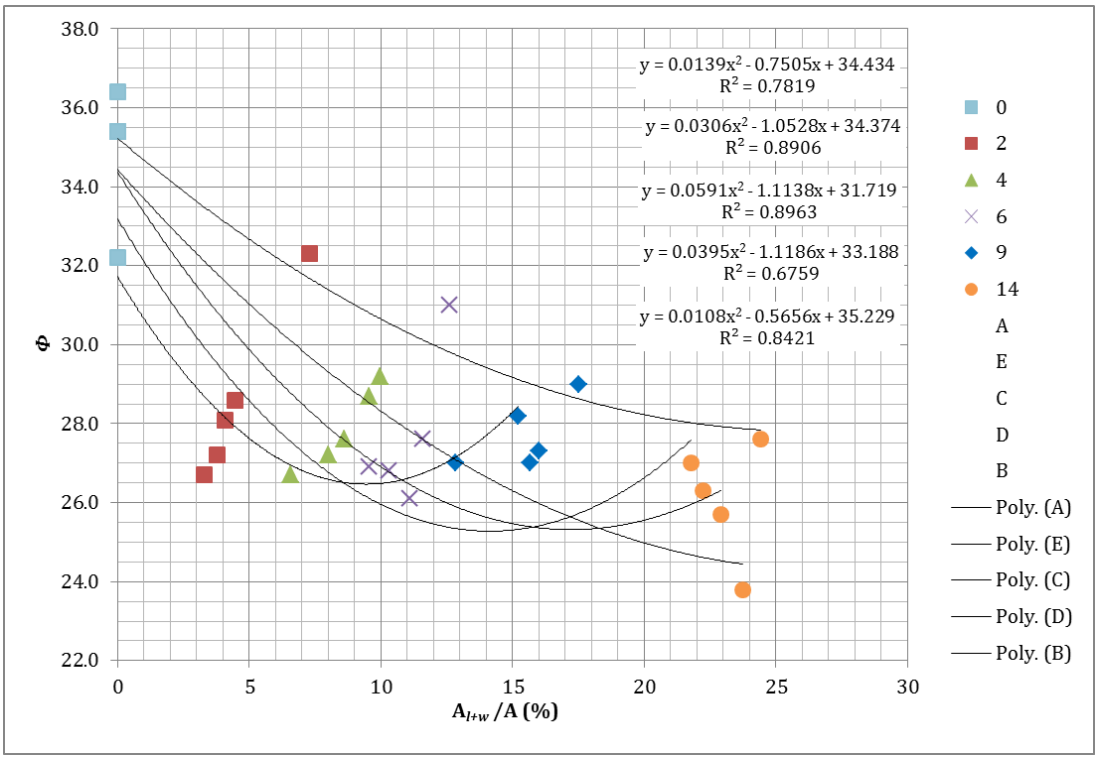

Figure 6-50: Angle of Friction vs. Area Ratio (All pts., individual)

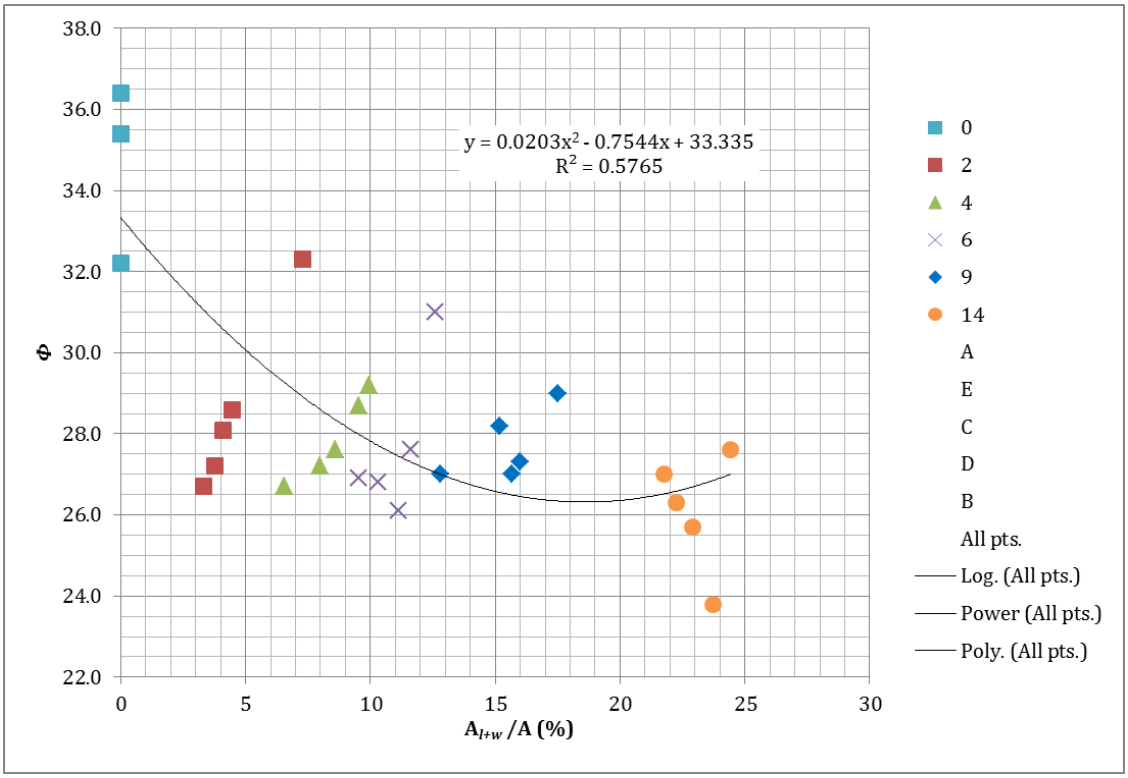

Figure 6-51: Angle of Friction vs. Area Ratio (All pts.)

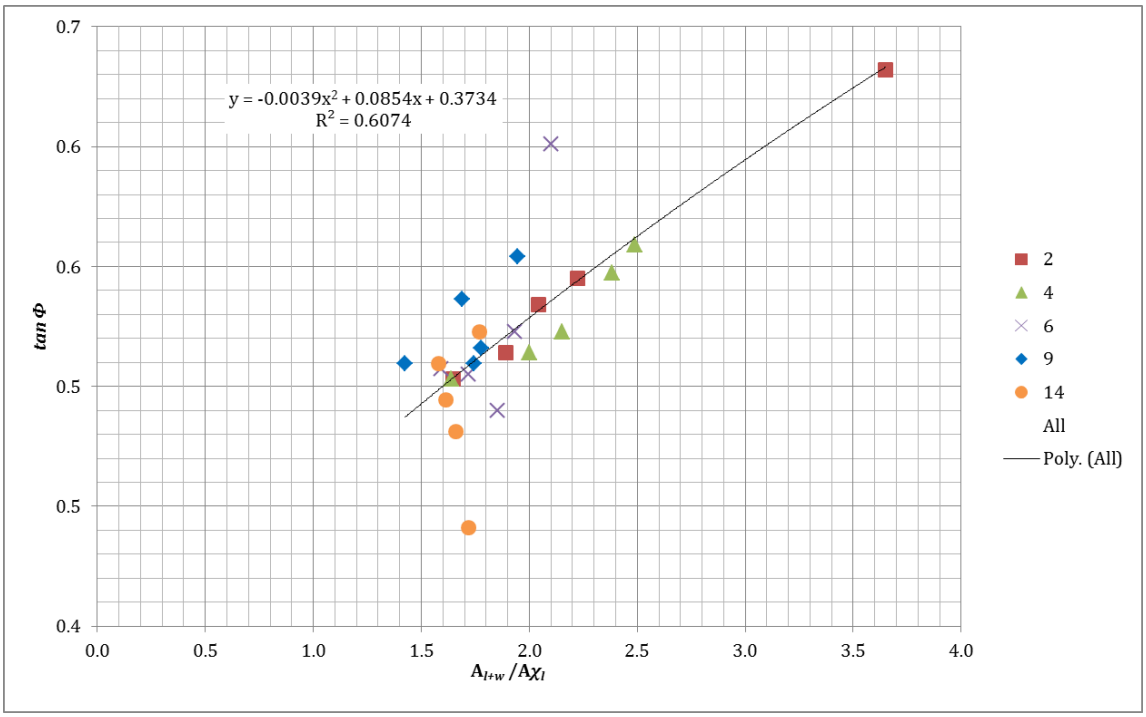

Figure 6-52: Tangent of Friction Angle vs. Normalized Area Ratio (All pts.)

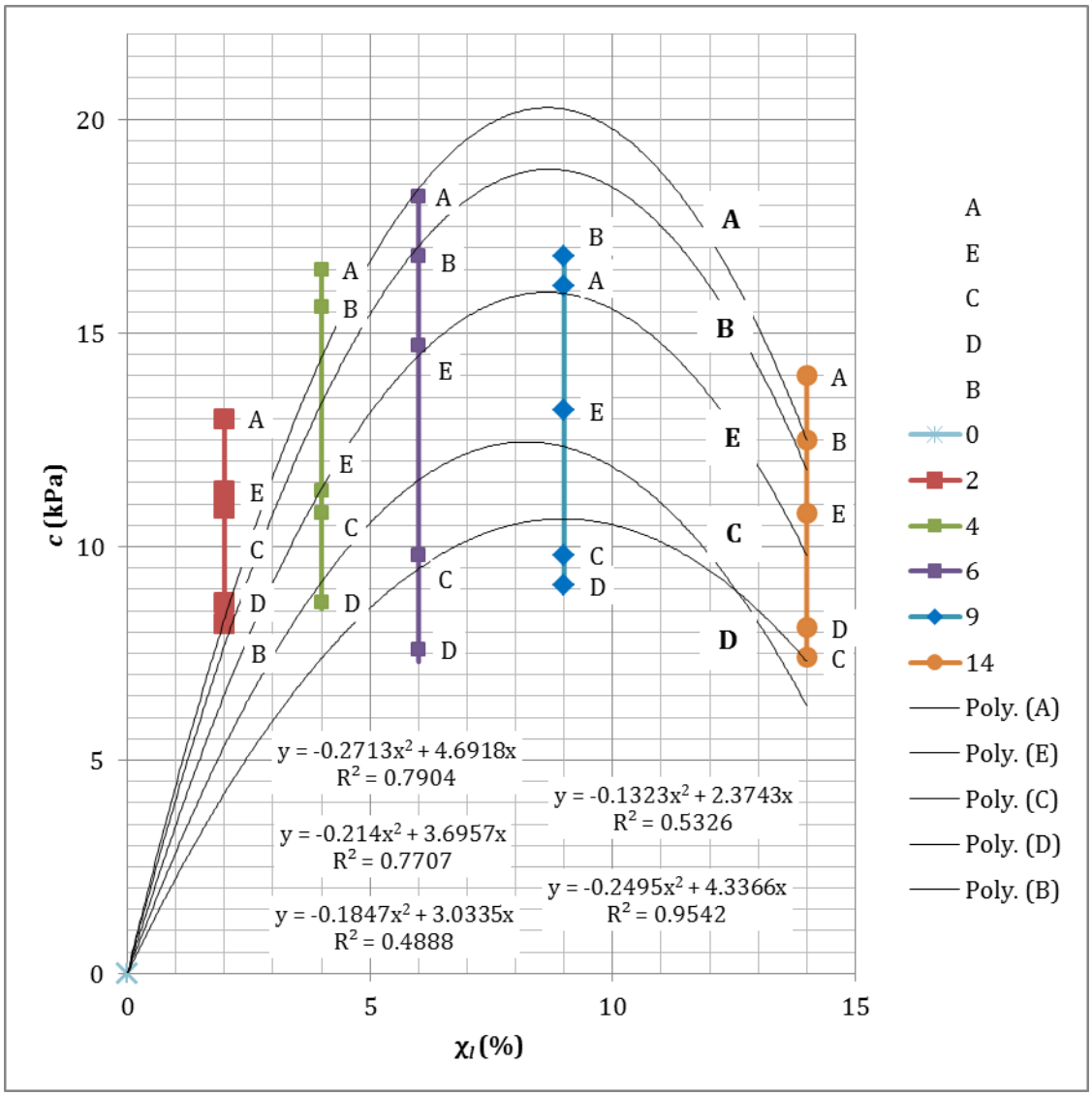

Figure 6-53: Cohesion vs. Gravimetric Lignin Content (All pts.)

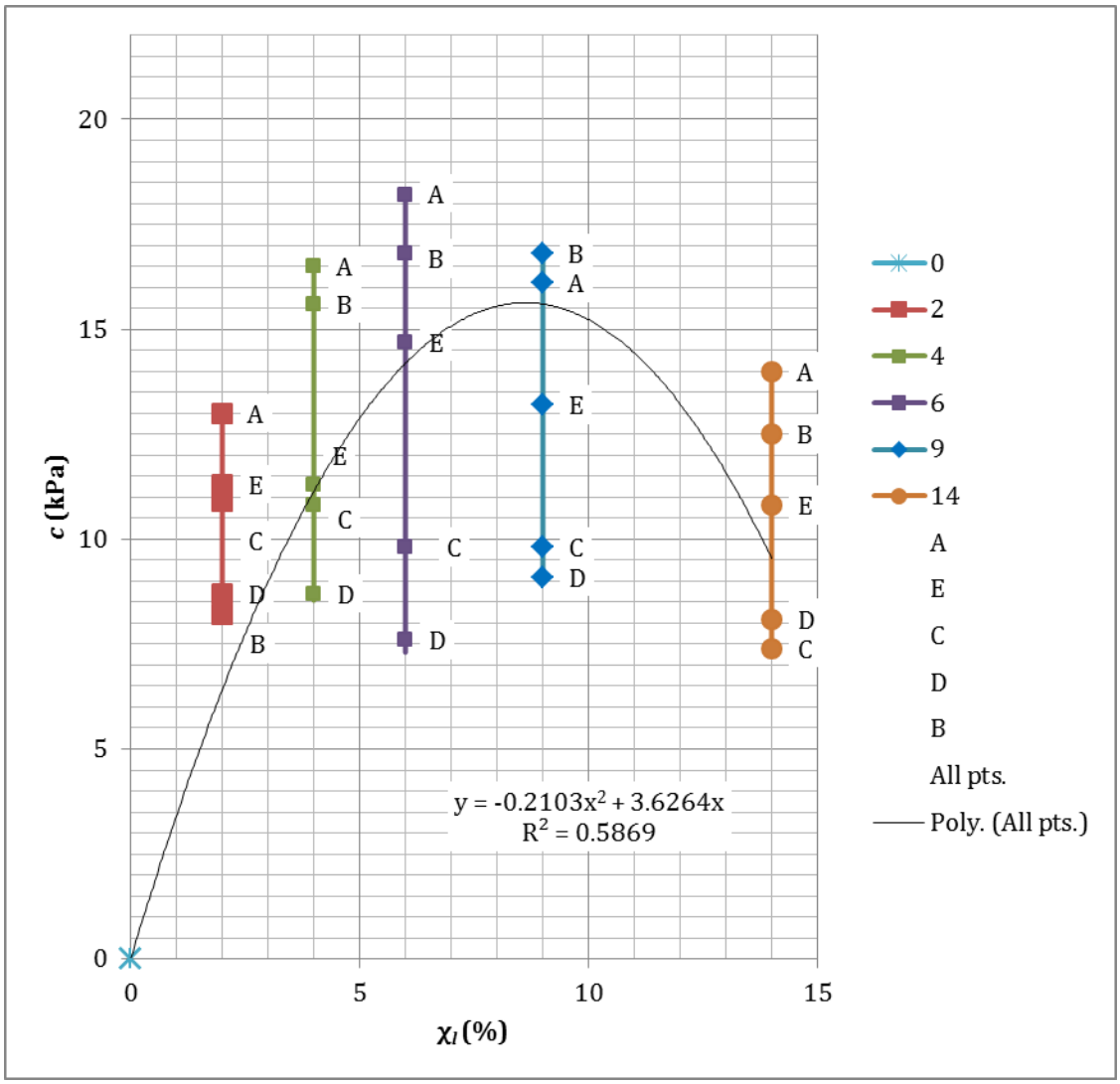

Figure 6-54: Cohesion vs. Gravimetric Lignin Content (All pts.)

Figures 6-50 and 6-51 are Figures 6-47 and 6-48 with cohesion versus gravimetric lignin content and area ratio, respectively. These trends are not as evident, but hold consistent with those of the previous plots depicting the trends for the friction angle.

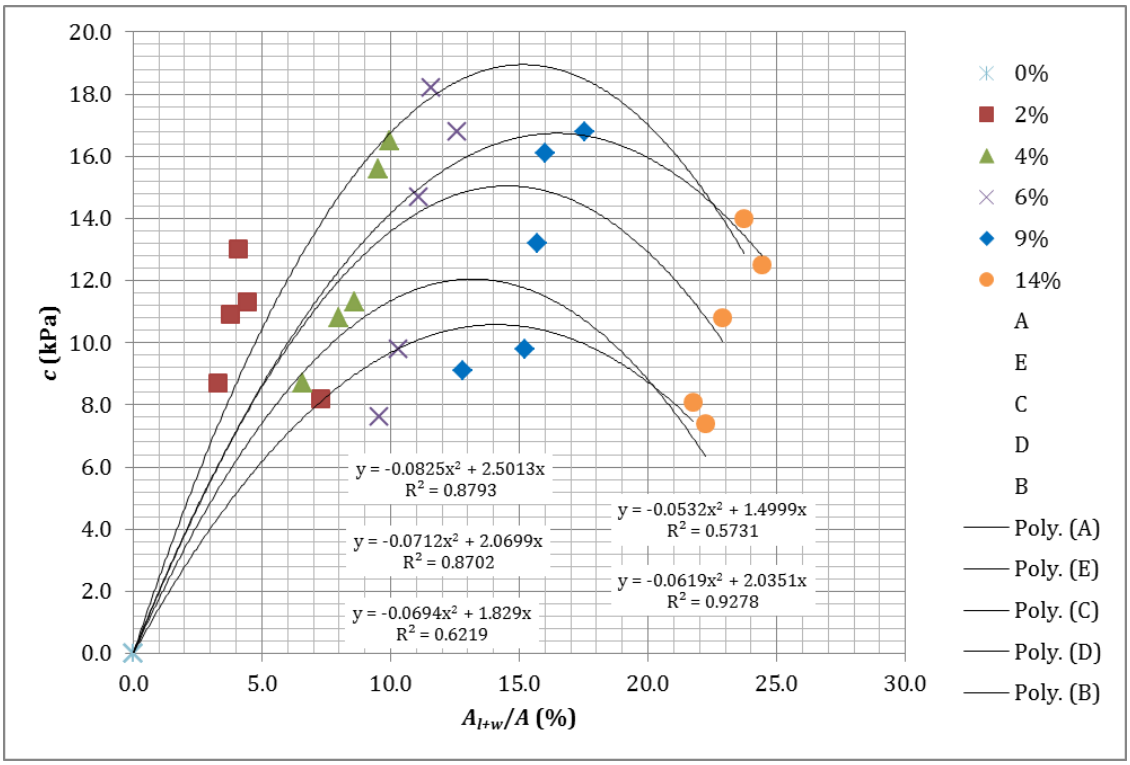

Figure 6-55: Cohesion vs. Area Ratio (All pts.)

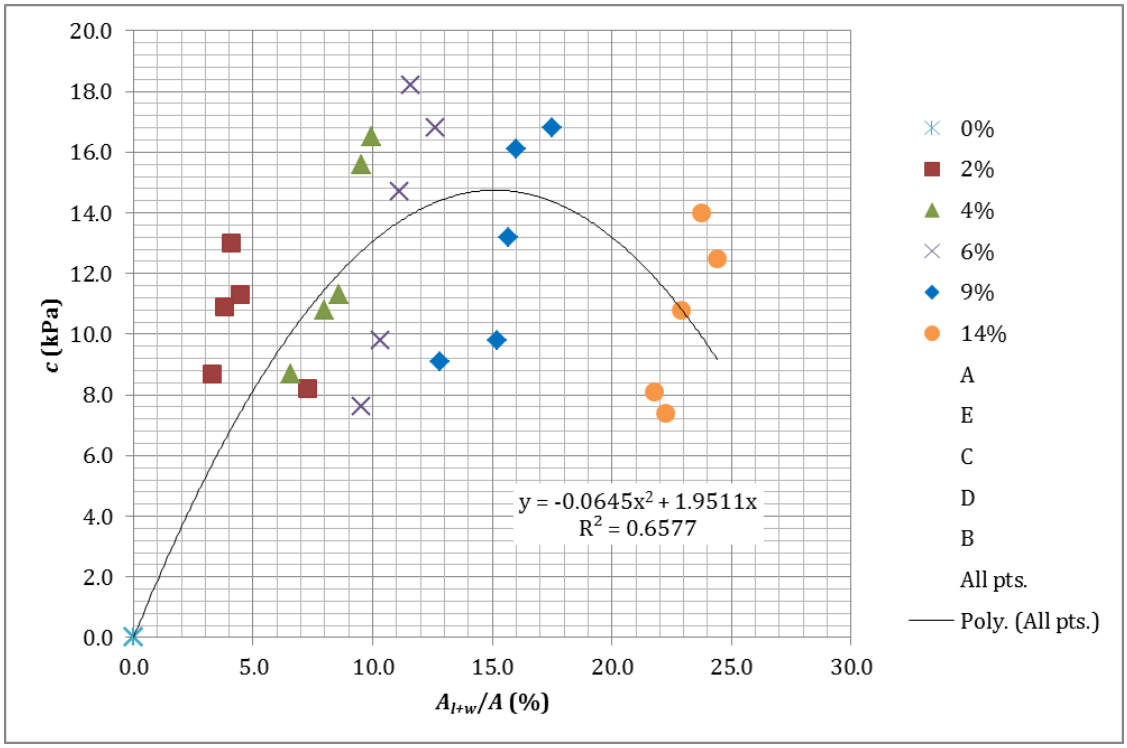

Figure 6-56: Cohesion vs. Area Ratio (All pts.)

Table 6-5 presents the ratios of amount of "fine" materials (lignin and water) and the total amount of materials (lignin, sand, and water) for different gravimetric lignin contents. This table shows that this ratio is smaller than 5% for gravimetric lignin contents 0 and 2%, with 2B being practically equal to the earlier prescribed 5% (4.97%). It is larger than 5%, but smaller than 12% for gravimetric lignin contents of 4, 6% and 9%, with 9B being an exception. Finally, the ratio is larger than 12% for the gravimetric lignin content of 9B and all of 14%. By comparing the ratio of the amount of fines (lignin and water) and the total amount of materials (lignin, sand, and water) with the amount of "fines" that can alter engineering properties of sand, it can be concluded that the former ratio is below 5% for χ_l = 2% at configurations A, E, C, and D, while it is between 5 and 12 % for 2B and χ_l = 4%, 6% and 9% at configurations A, B, E, C, and D, and it is larger than 12% for 9B and χ_l = 14%. It is noted that coefficients of determination were the best for the gravimetric lignin contents of 4, 6, and 9%, whereby 4 and 6% were slightly better due to point 9B being out of the range as noted above. Figure 6-14 shows that χ_l = 2% significantly lowers the coefficient of determination. Figure 6-15 also shows that 14% also lowers the coefficient of determination, though not as significantly as does 2%. These results, in addition to Table 6-6, show that sand and lignin paste can be considered as a binary mixture, which changes its behavior at the threshold values of content of fine materials corresponding to 5% and 12%. This is also known as percolation theory [Peters and Berney, 2010].

It is then concluded that the selected configurations in Table 6-6 represent the most reliable configurations for which the best correlations between normalized cohesion and normalized area ratio were found to exist in this research. Figures 6-57 through 6-70 are notable previous plots altered to only reflect these findings. Figures 6-57 and 6-58 are normalized cohesion versus normalized area ratio for several previous combinations of configurations and Figure 6-70 in tangent of angle of friction versus normalized area ratio. Figures 6-59 through 6-62 are the same as Figures 6-53 through 6-56, but with improved coefficient of determination values due to the exclusion of configurations outside of the "select" range. Figures 6-63 through 6-66 represent the same concept for angle of friction in relation to Figures 6-48 through 6-51. These plots display evident and reliable trends with further improvements in the values of the coefficient of determination.

Table 6-6: Calculation of Amount of Fines in Sand-Lignin-Water Mix

χ_l (%)	w (%)	$(\chi_l+w)/(1+\chi_l+w)$	% Fines
0A	0	0.0000	0.00
0E	0	0.0000	0.00
0C	0	0.0000	0.00
2A	1.13	0.0304	3.04
2E	1.48	0.0336	3.36
2C	1.18	0.0308	3.08
2D	0.77	0.0270	2.70
2B	**3.23**	**0.0497**	**4.97**
4A	**3.30**	**0.0680**	**6.80**
4E	**2.80**	**0.0637**	**6.37**
4C	**2.62**	**0.0621**	**6.21**
4D	**1.52**	**0.0523**	**5.23**
4B	**3.35**	**0.0685**	**6.85**
6A	**3.03**	**0.0828**	**8.28**
6E	**3.08**	**0.0832**	**8.32**
6C	**2.85**	**0.0813**	**8.13**
6D	**2.12**	**0.0751**	**7.51**
6B	**4.02**	**0.0911**	**9.11**
9A	**3.74**	**0.1130**	**11.30**
9E	**4.01**	**0.1151**	**11.51**
9C	**4.08**	**0.1157**	**11.57**
9D	**2.29**	**0.1014**	**10.14**
9B	5.12	0.1237	12.37
14A	5.41	0.1625	16.25
14E	5.48	0.1630	16.30
14C	5.61	0.1639	16.39
14D	4.82	0.1584	15.84
14B	6.38	0.1693	16.93

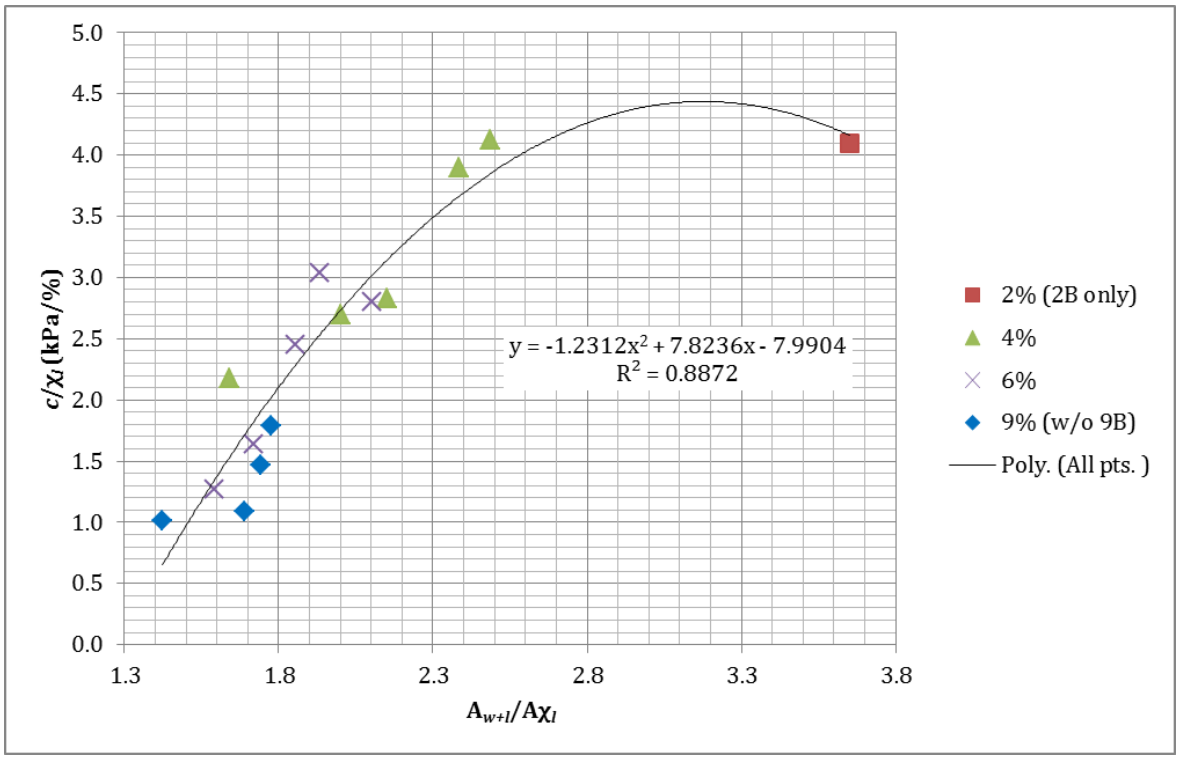

Figure 6-57: Normalized Cohesion vs. Normalized Area Ratio (Select pts., w/o 9B)

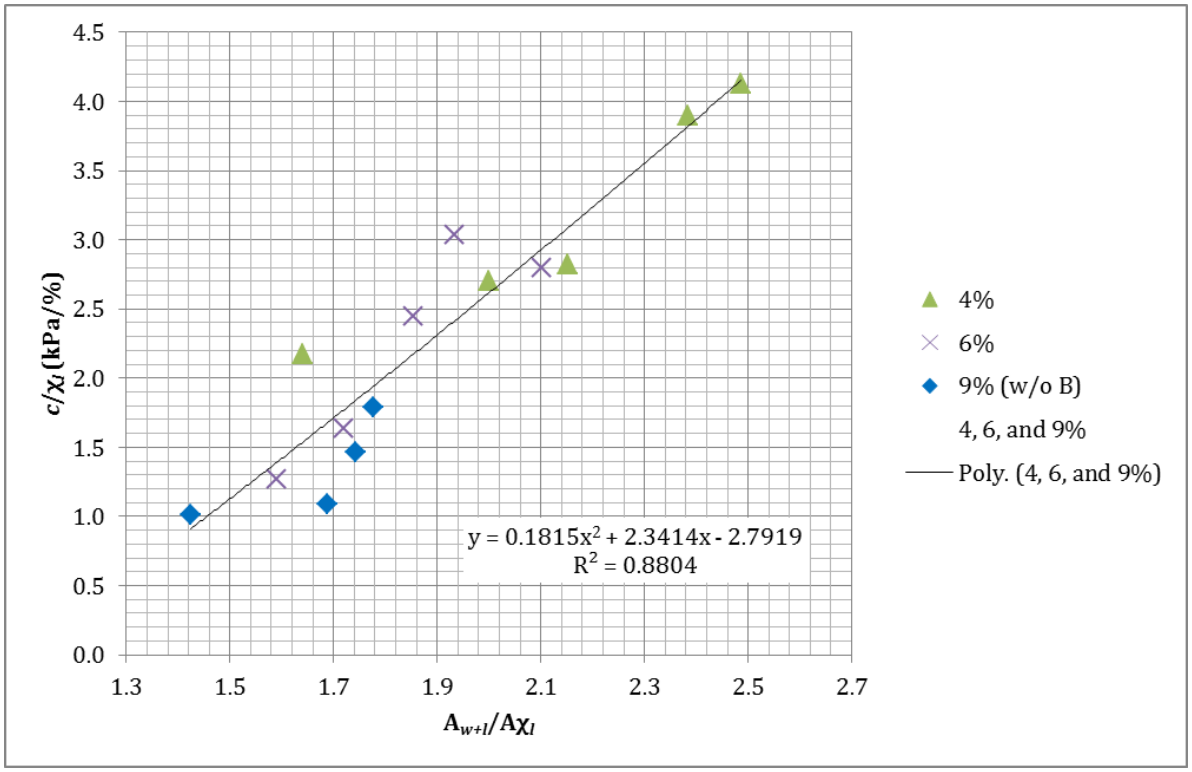

Figure 6-58: Normalized Cohesion vs. Normalized Area Ratio (Select pts., 4, 6, 9% w/o 9B)

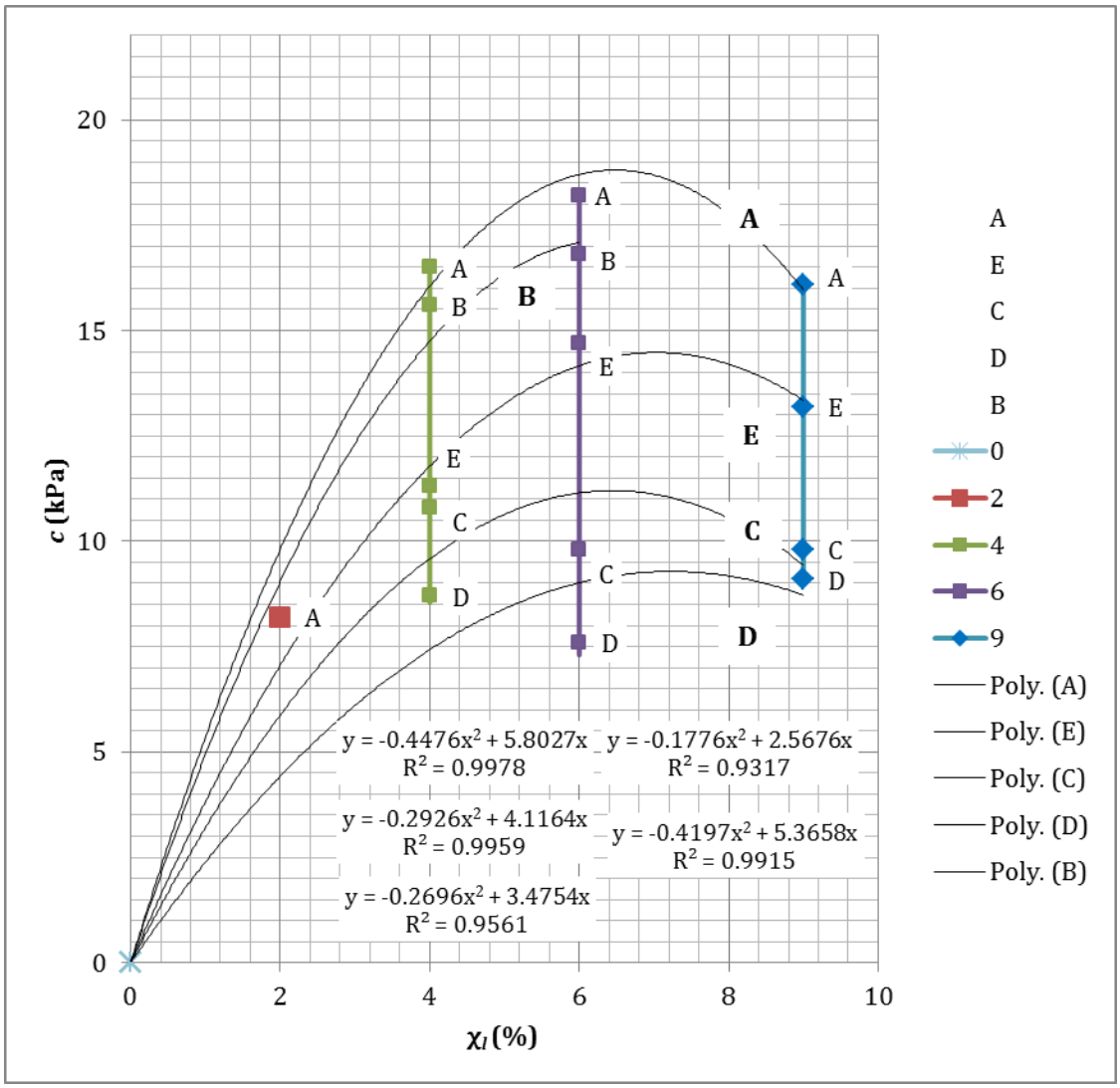

Figure 6-59: Cohesion vs. Gravimetric Lignin Content (Select pts.)

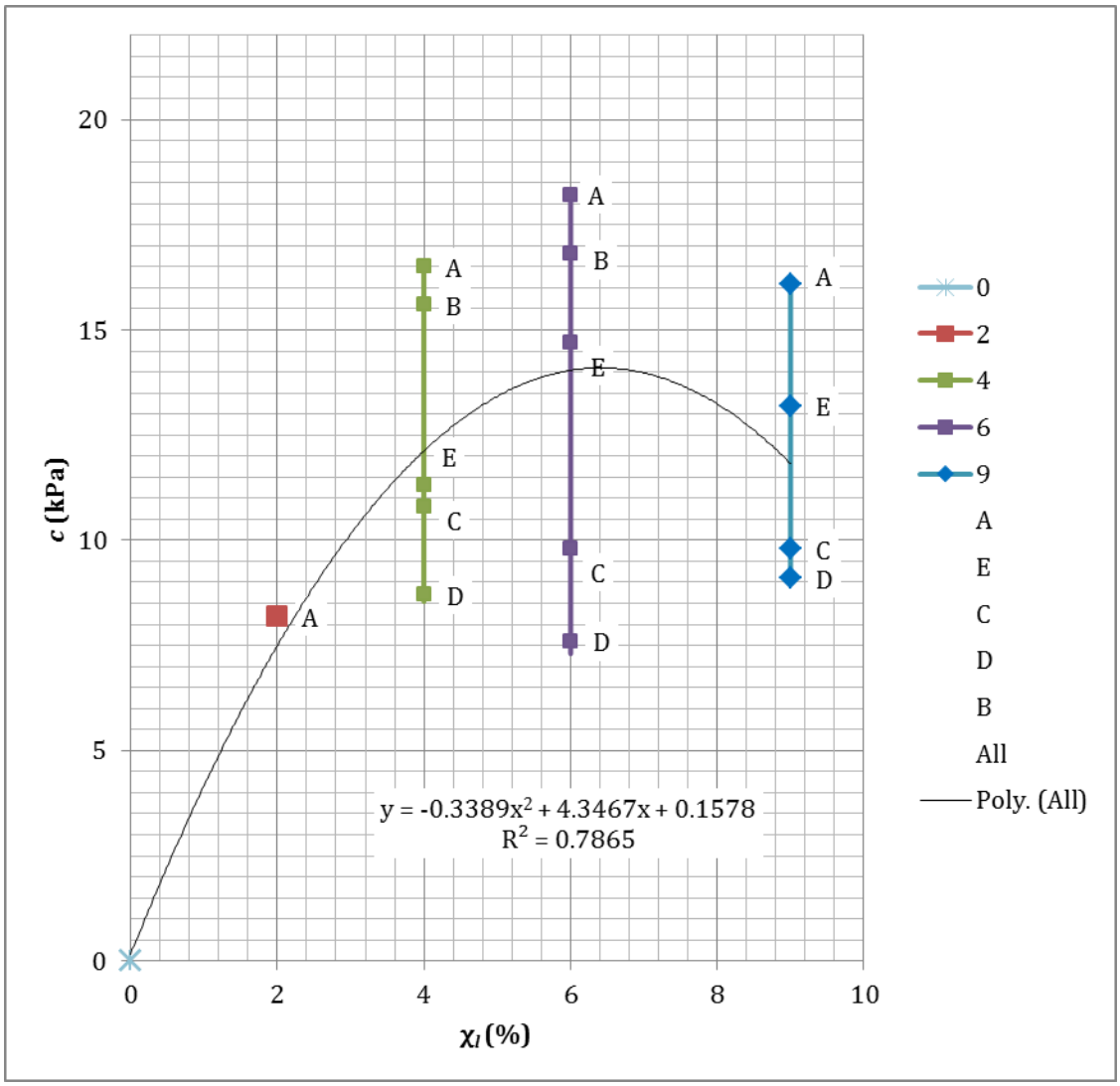

Figure 6-60: Cohesion vs. Gravimetric Lignin Content (Select pts.)

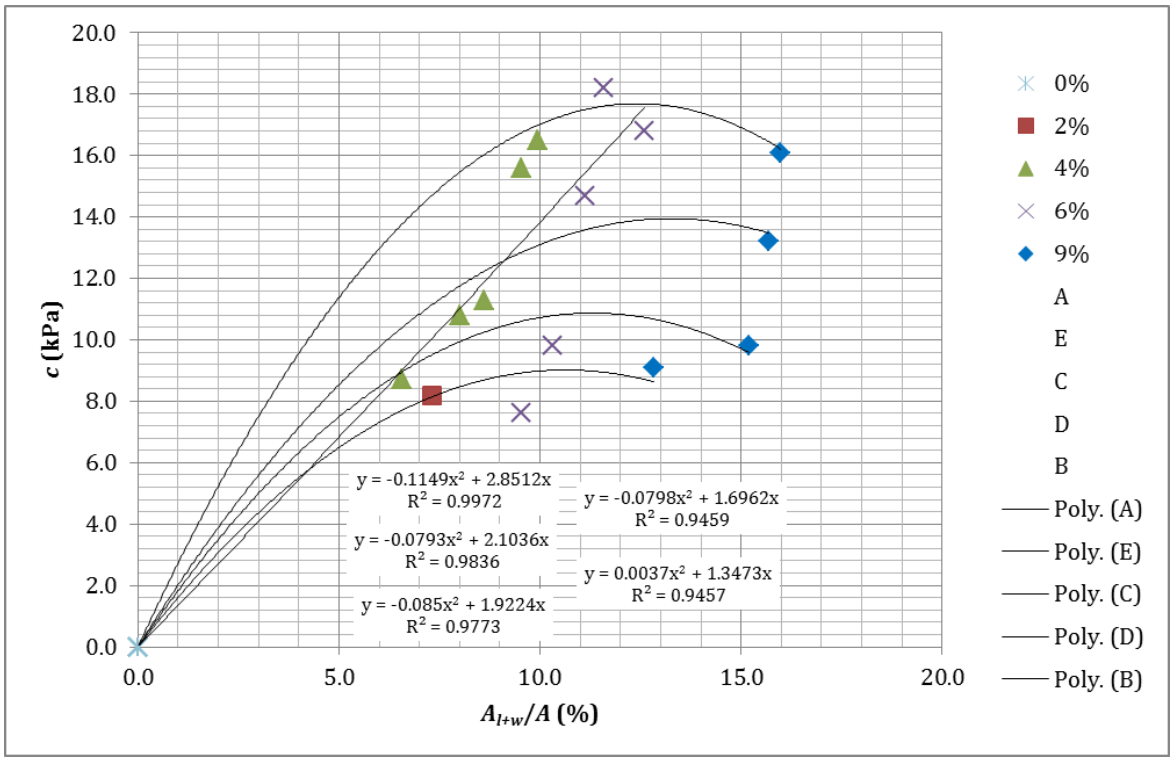

Figure 6-61: Cohesion vs. Area Ratio (Select pts.)

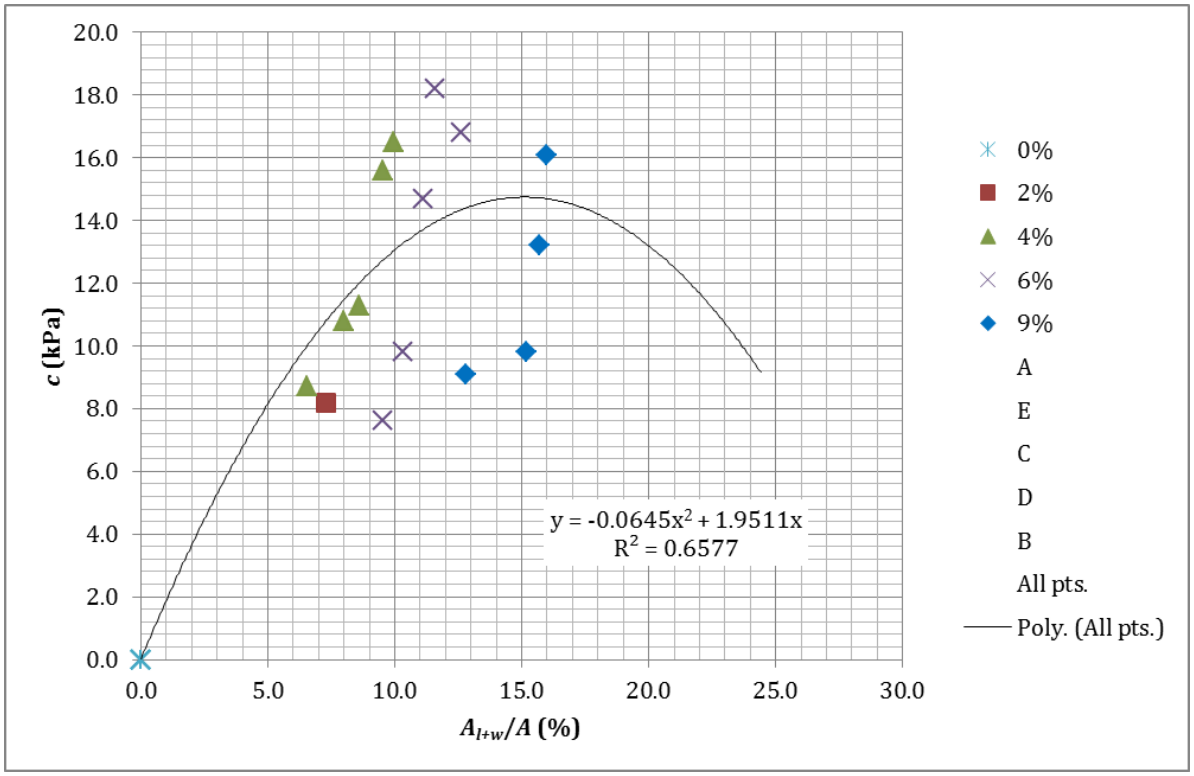

Figure 6-62: Cohesion vs. Area Ratio (Select pts.)

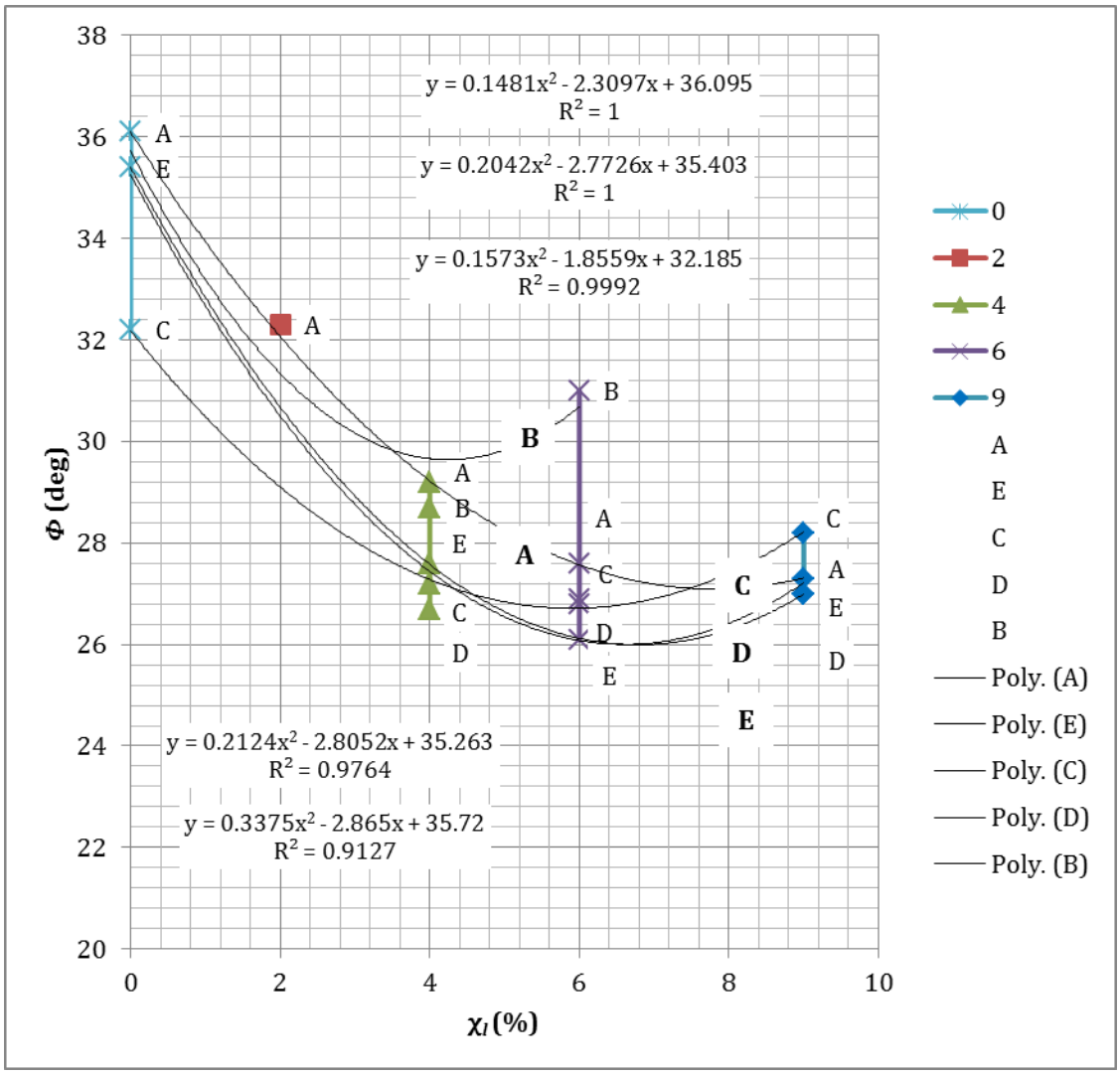

Figure 6-63: Angle of Friction vs. Gravimetric Lignin Content (Select pts.)

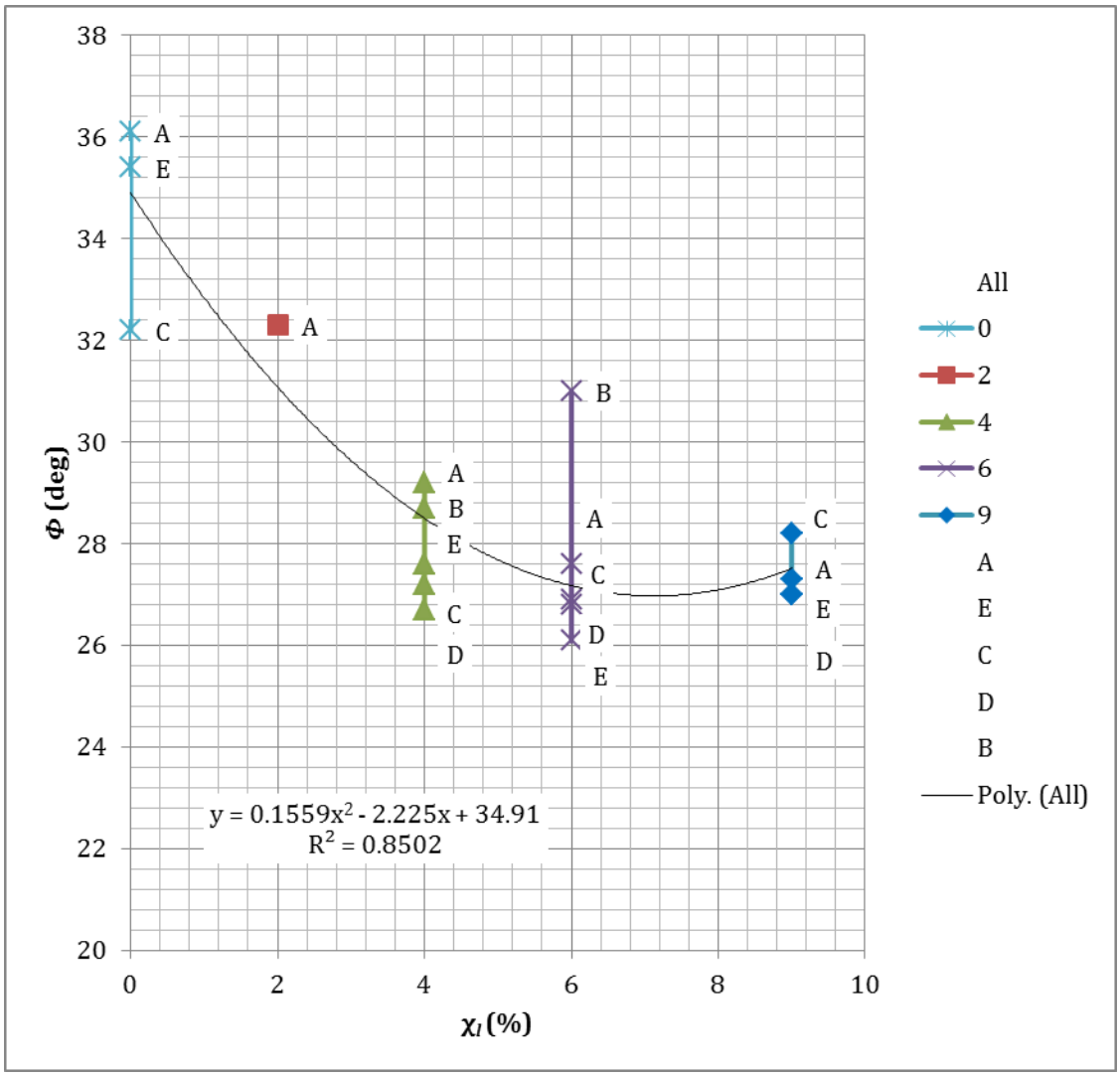

Figure 6-64: Angle of Friction vs. Gravimetric Lignin Content (Select pts.)

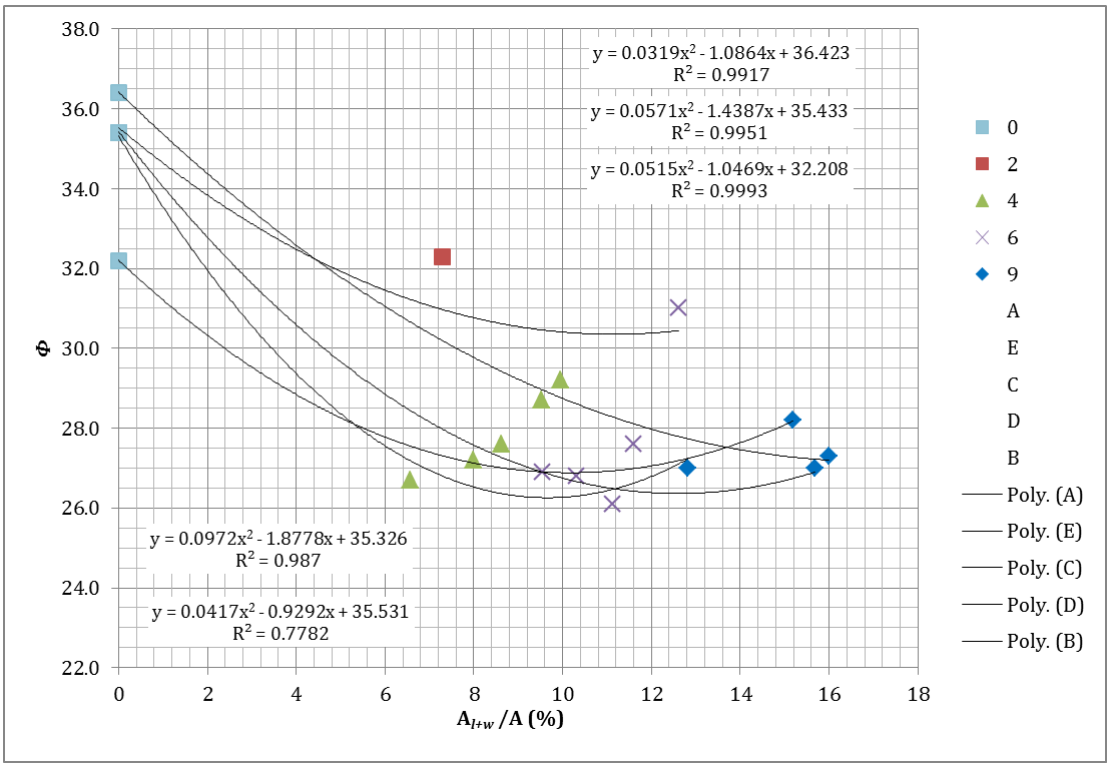

Figure 6-65: Angle of Friction vs. Area Ratio (Select pts.)

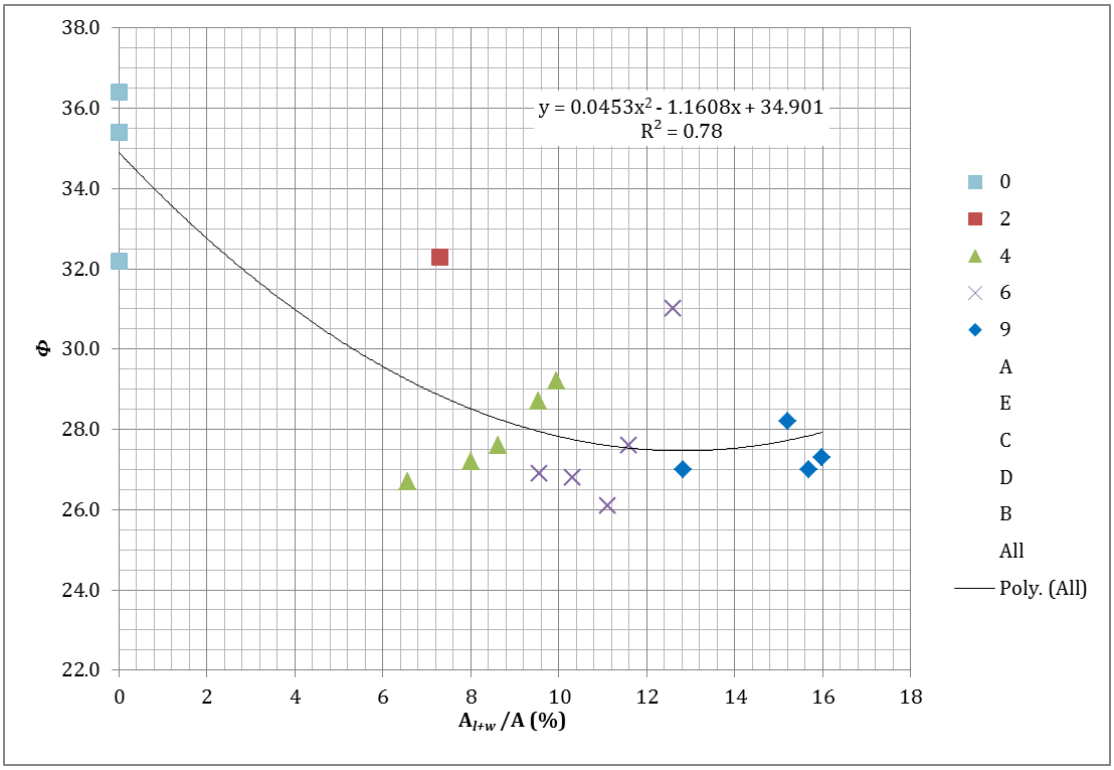

Figure 6-66: Angle of Friction vs. Area Ratio (Select pts.)

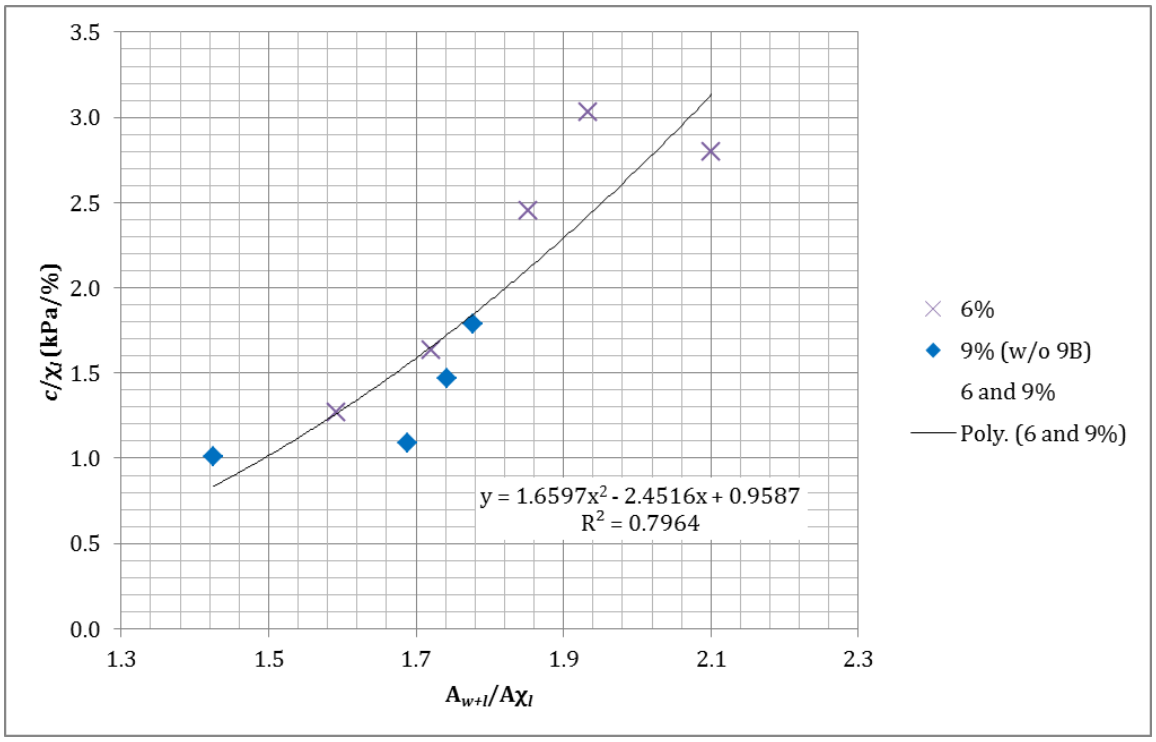

Figure 6-67: Normalized Cohesion vs. Normalized Area Ratio (Select pts., 6 & 9% w/o 9B)

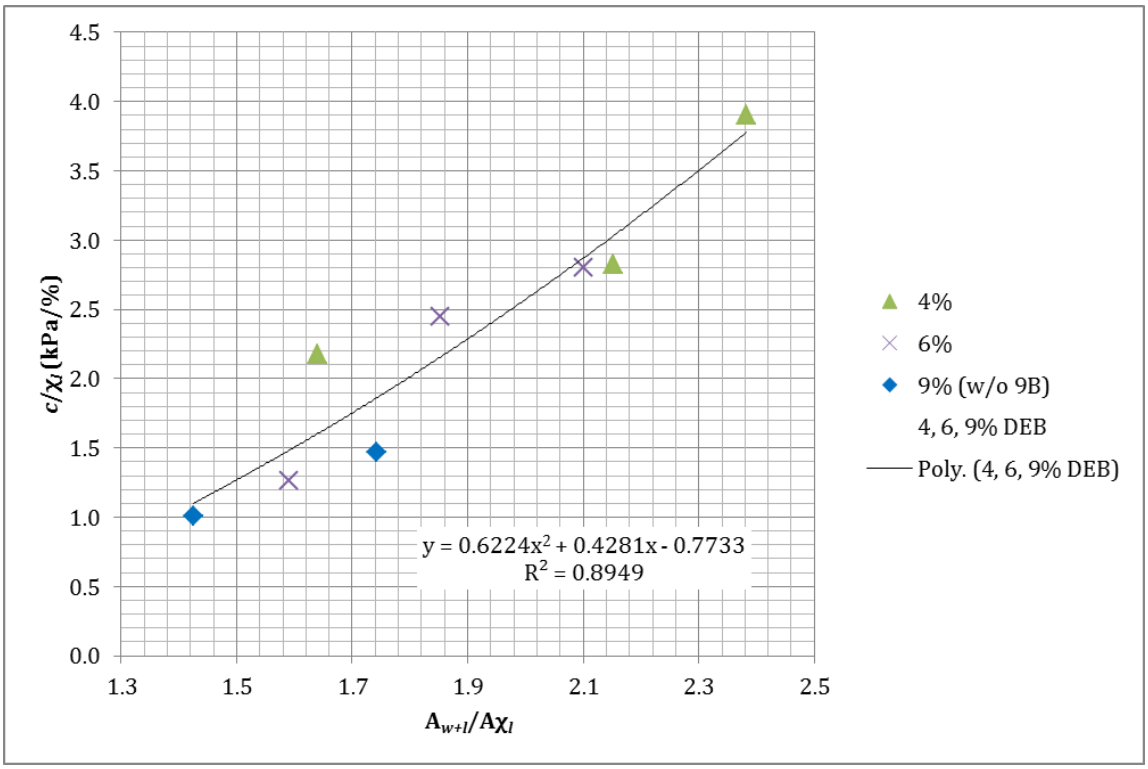

Figure 6-68: Normalized Cohesion vs. Normalized Area Ratio (Select pts., DEB, w/o 9B)

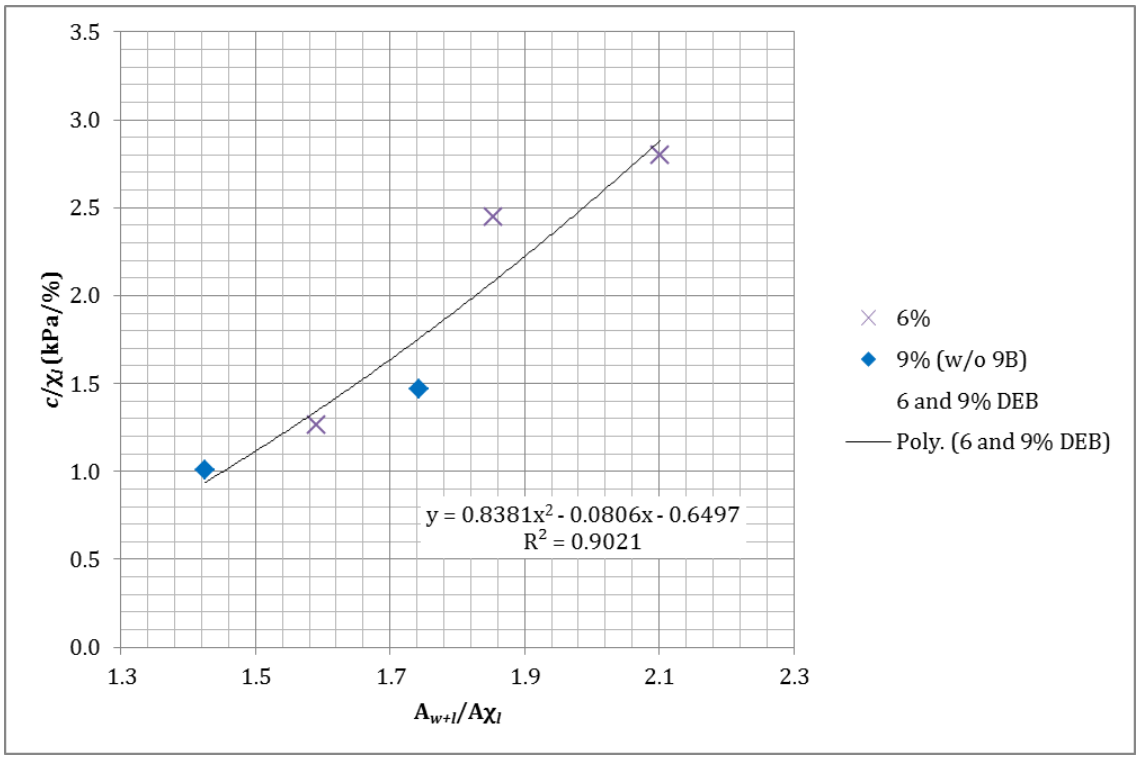

Figure 6-69: Normalized Cohesion vs. Normalized Area Ratio (Select pts., DEB, w/o 9B)

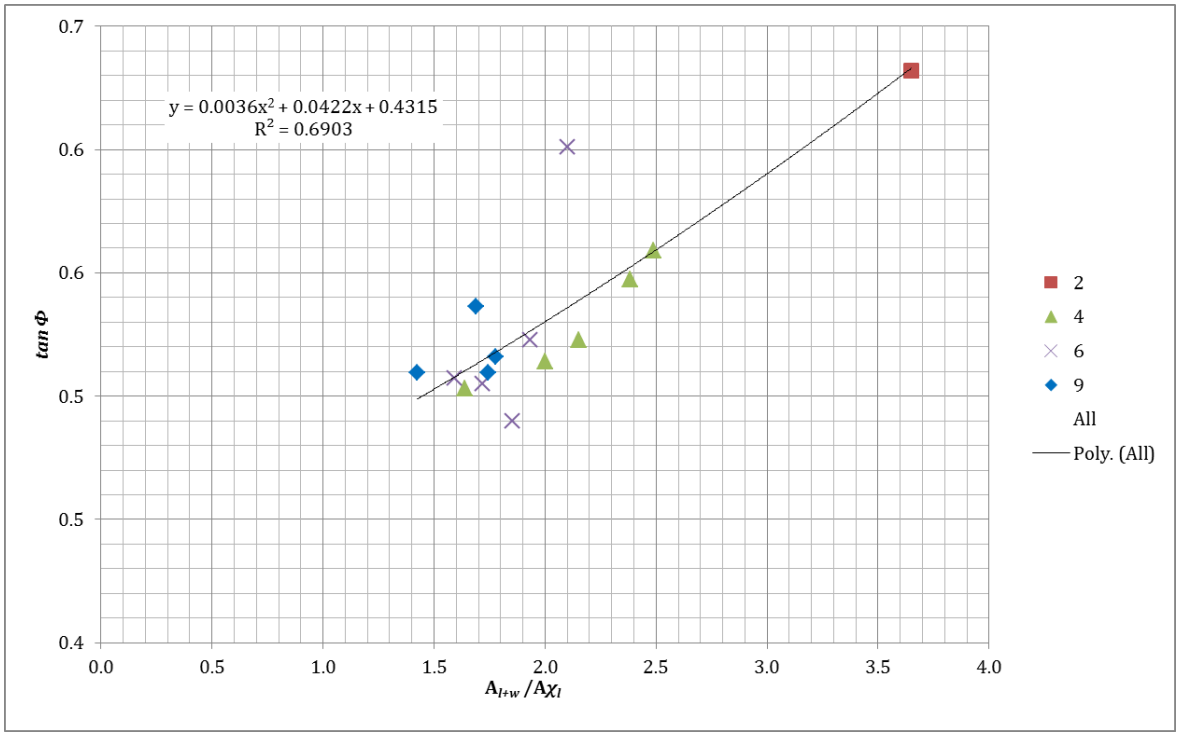

Figure 6-70: Tangent of Friction Angle vs. Normalized Area Ratio (Select pts.)

Chapter 7 - Conclusions and Recommendations

The research described herein produced several conclusions about the stabilization of sand with the plant-derived material known as lignin. This work represents part of a (very) small collection of research conducted so far on sand stabilization with lignin. The experimental results complemented by the extensive analysis lead to the conclusions listed below.

7.1 Conclusions

1. The range in which the cementation benefit is fully realized is between $\chi_l = 2\%$ and $\chi_l = 9\%$ with the maximum benefit likely occurring at $\chi_l = 6\%$. Figure 6-57 represents a baseline design chart in which the amount of cohesion gained can be calculated by the input factors of water content, gravimetric lignin content, and void ratio, for the poorly-graded sand used in this research.
2. Lignin creates particle bonding at the contacts of sand particles. Increasing the portion of cross-sectional area occupied by water and lignin reduces the stress within the lignin and water mixture.
3. Increasing the normalized portion of the cross-sectional area occupied by lignin and water increases the amount of normalized cohesion gained up to a point.
4. It was observed that sand-lignin-water exhibits distinctly different behaviors for different ranges of the ratios of "fines", whereby the mass of water and lignin divided by the mass of water, lignin, and sand solids is defined as the ratio of fines. The ranges closely coincide with the percentages of fines used by the Unified Soil Classification System to assign dual symbols to coarse-grained soils containing fines. This phenomenon is also known as percolation. Thus, the best correlations between the normalized cohesion and normalized area ratio are obtained for the ratio of fines equal to or larger than 5% and smaller than or equal to 12%. This range corresponds to gravimetric lignin contents of 4%, 6%, and 9%.

5. While normalized cohesion increases with normalized area ratio, the cohesion itself reaches the maximum value at 18.2 kPa at χ_l = 6% and then starts to decrease at χ_l = 9%.
6. The cohesion of sand-lignin mixtures is always larger than the cohesion of dry sand, which is non-existent.

7.2 Recommendations

Lignin is a widely-available, sustainable, and safe material to work with. The potential for lignin use as a sand stabilizer and dust suppressant is nearly unlimited. This research has served to introduce this combination of sand and lignin as a viable source of research material and provide baseline values to be further expanded on.

While the ultimate use of lignin-sand mixtures is unknown at this time, there are several considerations and recommendations for work in the future.

1. The specimens tested in this study were freshly-mixed and immediately placed into the direct shear apparatus. Future work should be conducted to establish the effects of drying and curing times on cohesion and friction.
2. In addition, sand-lignin samples should be tested in a triaxial conventional device, which provides more reliable data.
3. Future research could consider testing the specimens at lower normal stresses to determine the bonding effect in this range of stresses.
4. When exposed to water, a dried sand-lignin specimen would likely disintegrate. Future work could consider the effect of infiltration rate on disintegration and possible methods of preventing disintegration. This could possibly widen the use of lignin beyond dry climates.

References

Adams, J.W. (1988). *Environmental effects of applying lignosulfonate to roads* (U05-01R). Research and Development, Daishowa Chemicals Inc.

Booregard Lignotech. *Lignin – Co-Product of the Pulping Process*. Brochure.

Borregaard Lignotech. (2008). *Norlig A Powder Product Descripton Sheet*.

Brady, B, Brush, S, Burmark, B, Corbin, M, & DeMay, J. Washington State Department of Ecology, Air Quality Program. (1998). *Washington state air toxic sources and emission estimation methods* (Publication 98-207). Olympia, WA: Department of Ecology Publications Distribution Center. Retrieved from http://www.ecy.wa.gov/pubs/98207.pdf

Calbinder. (2001). *Calbinder facts*. Retrieved from http://www.calfresno.com/calbnder.html.

Ceylan, H, Gopalakrishnan, K, & Kim, S. (2010). *Soil stabilization with bioenergy coproduct*. Transportation Research Board, (2186), Retrieved from http://dx.doi.org/10.3141/2186-14 doi: 9780309160599

Das, B. (1997). *Soil mechanics laboratory manual*. 5th Edition. Austin, TX: Engineering Press.

DCN Digital Media. (2011, October 18). *U.S. concrete works on supplemental materials to replace cement*. Daily Commercial News and Construction Record, Retrieved from http://www.dcnonl.com/article/id47160/--us-concrete-works-on-supplemental-materials-to-replace-cement

Dissanayake, S, & Liu, L. Kansas Department of Transportation, Kansas State University. (2009).*Speed limit-related issues on gravel roads* (Report No. K-TRAN: KSU-06-5). Topeka, KS: Office of Transportation Information. Retrieved from http://www.ksdot.org/PublicLib/doccontent.dll?LibraryName=PublicDocs^dt00mx38&SystemType=2&LogonId=91961ceee5f872cd78f4cf4207bbeaa3&DocId=003785313

ELE International. (2006). *Operating Instructions: Digital Direct/Residual Shear Apparatus* (Operation Manual). Leighton Buzzard, Bedfordshire, England.

Fox, Carter. (2006). *Chemical and thermal characterization of three industrial lignins and their corresponding lignin esters*: *a thesis*. University of Idaho. Retrieved from http://www.cnrhome.uidaho.edu/documents/Thesis-Carter-Final.pdf&pid=106089&doc=1

Glasser, W. (2000). *Lignin: historical, biological, and materials perspectives*. Proceedings of the ACS symposium series 742 (pp. 2-99). An American Chemical Society Publication.

Head, K. H. (1994). *Manual of soil laboratory testing: Volume 2: Permeability, shear strength and compressibility tests*. 2nd Edition. New York: John Wiley & Sons, Inc.

International Lignin Institute. (2000). *About lignin*. Retrieved from www.ili-lignin.com/aboutlignin/php.

Kestler, M. U.S. Department of Agriculture, Forest Service. (2009). *Stabilization selection guide for aggregate- and native-surfaced low volume roads*. National Technology & Development Program. Retrieved from http://www.fs.fed.us/eng/pubs/pdf/08771805.pdf

Muckel, G. U.S. Department of Agriculture, Natural Resources Conservation Service. (2004). *Understanding soil risks and hazards*. Lincoln, NE: National Soil Survey Center.

Newman, K, & Tingle, J. (2004). *Emulsion polymers for soil stabilization*. Proceedings of the 2004 FAA Worldwide Airport Technology Transfer Conference (pp. 3-4). Vicksburg, MS: U.S. Army Engineer Research and Development Center.

Peters, J., and Berney IV, E. (2010). *Percolation treshold of sand-clay binary mixtures*. ASCE Journal of Geotechnical and Geoenvironmental Engineering (pp. 310-318).

Ragauskas, A. (2011). *Basics of kraft pulping and recovery process* [PowerPoint Slides]. Georgia Institute of Technology. Institute of Paper Science and Technology. Retrieved from http://ipst.gatech.edu/faculty/ragauskas_art/technical_reviews/Kraft%20Pulping%20and%20Recovery%20Process%20basics.pdf

Reddi, L., Howard, J., and Xiao, M. (2010). *Erosion control on roadside embankment using compost*. Applied Engineering in Agriculture. Vol. 26(1): 97-106.

Reed Lignin. *Sulphite Roadbinder: A product of the pulp and paper industry for low cost maintenance of roads*. Publication No. R-13-83. Rothschild, WI.

Santoni, R., Tingle, J, and Webster, S. (2002). *Stabilization of silty sand with nontraditional additives*. Transportation Research Record, (1787), pp. 61-70.

Stapanian, M. and Shea, D. (1986). *Lignosulfonates: Effects on plant growth and survival and migration through the soil profile*. International Journal of Environmental Studies, Volume 27 (p. 45).

Surdahl, R., Woll, J., Marquez, R. (2005). *Road stabilizer product performance: Buenos Aires National Wildlife Refuge*. Federal Highway Administration. Publication No. FHWA-CFL/TD-05-011.

Surdahl, R., Woll, J., Everett, R., Andresen, R. (2008). *Road stabilizer product performance: Seedskadee National Wildlife Refuge*. Federal Highway Administration. Publication No. FHWA-CFL/TD-08-005.

Wang, D. Basic lignin chemistry. (2011). *David Wang's Wood Chemistry Class* [PowerPoint Slides]. National Chung Hsing University. Retrieved from web.nchu.edu.tw/pweb/users/taiwanfir/lesson/8609.pdf.

Appendix A - Additional Direct Shear Testing Results

A.1.1 Gravimetric Lignin Content (4%)

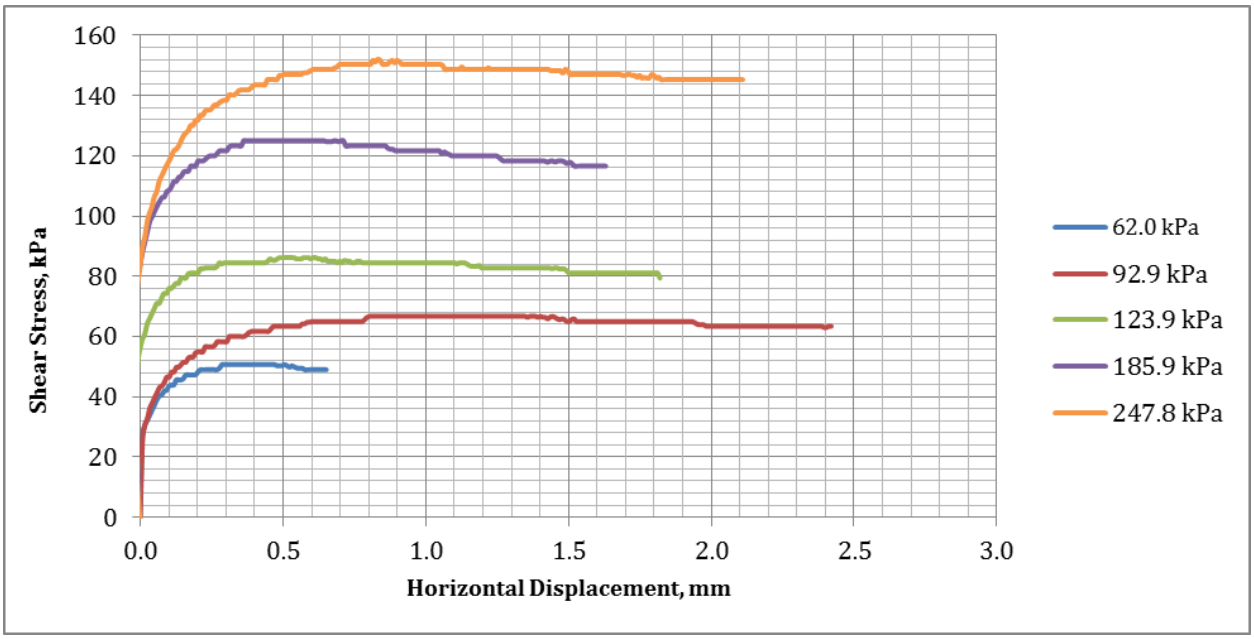

Figure A-1: Shear Stress vs. Horizontal Displacement, χ_l = 4% (A)

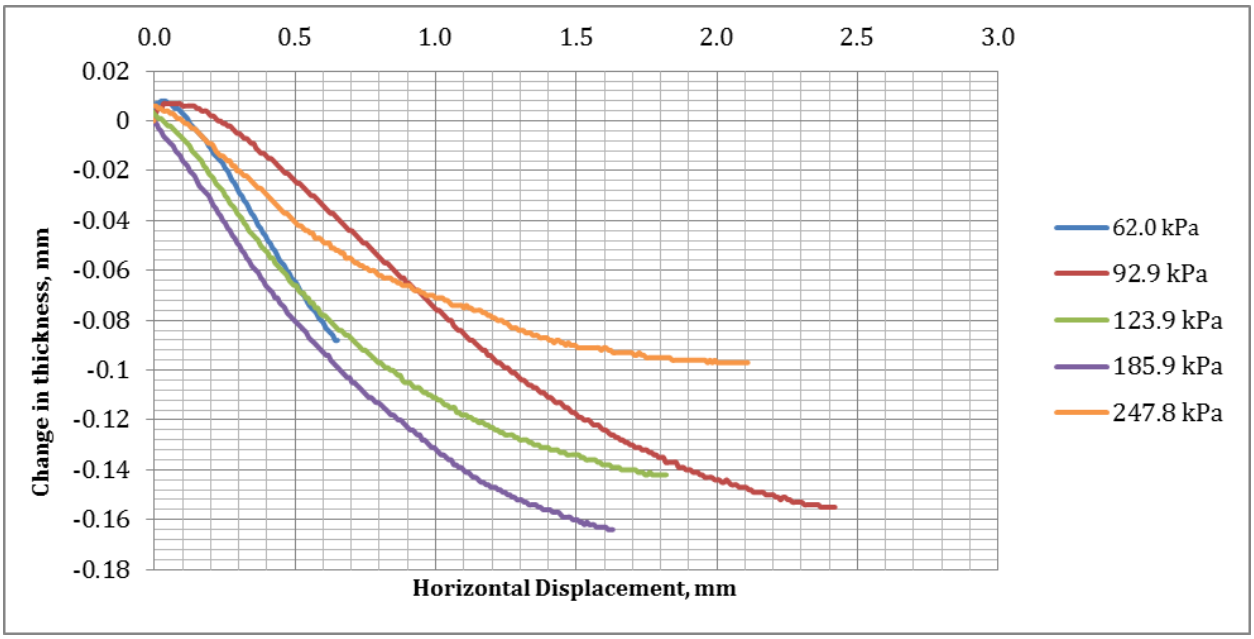

Figure A-2: Change in Thickness vs. Horizontal Displacement, χ_l = 4% (A)

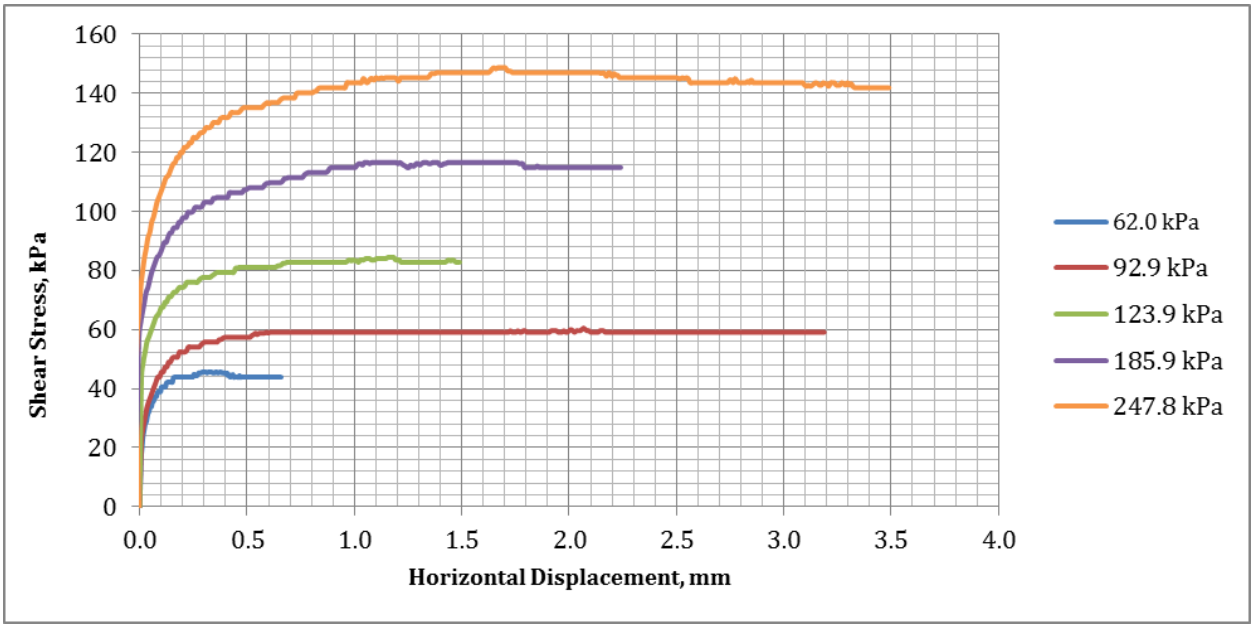

Figure A-3: Shear Stress vs. Horizontal Displacement, χ_l = 4% (E)

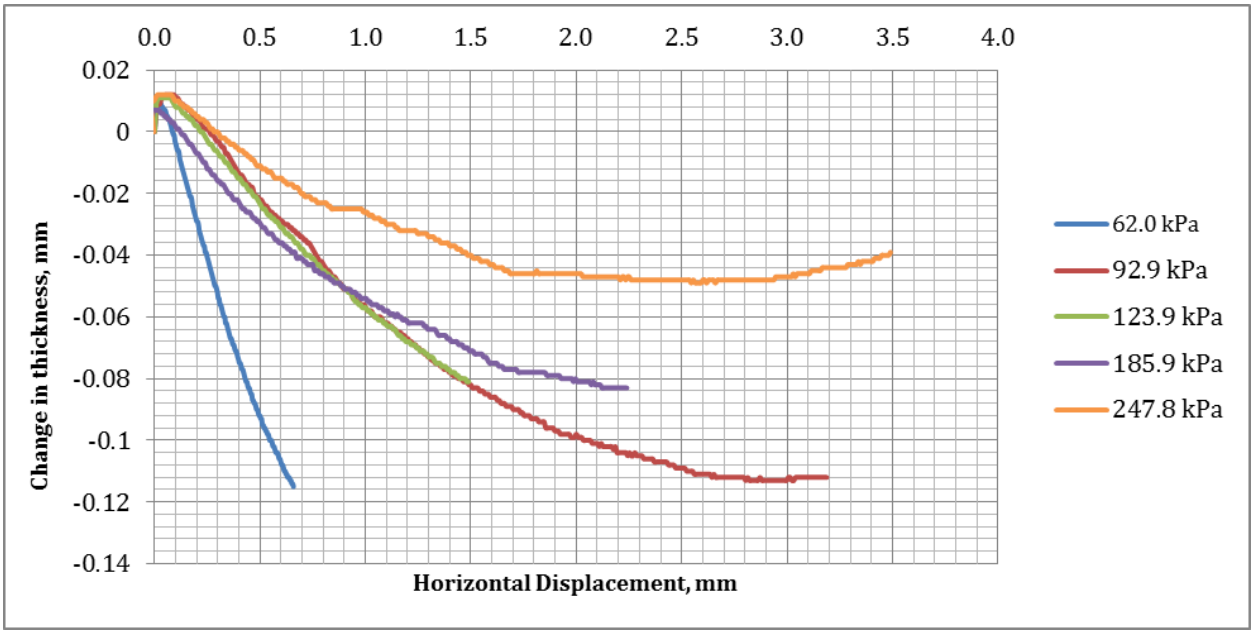

Figure A-4: Change in Thickness vs. Horizontal Displacement, χ_l = 4% (E)

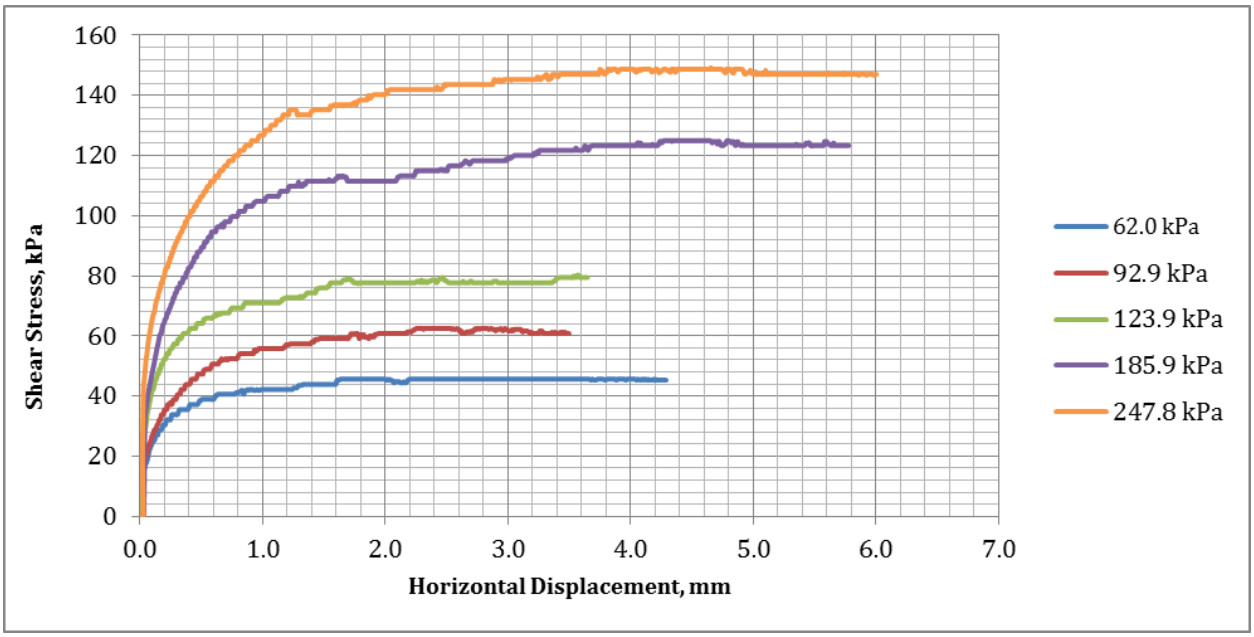

Figure A-5: Shear Stress vs. Horizontal Displacement, χ_l = 4% (C)

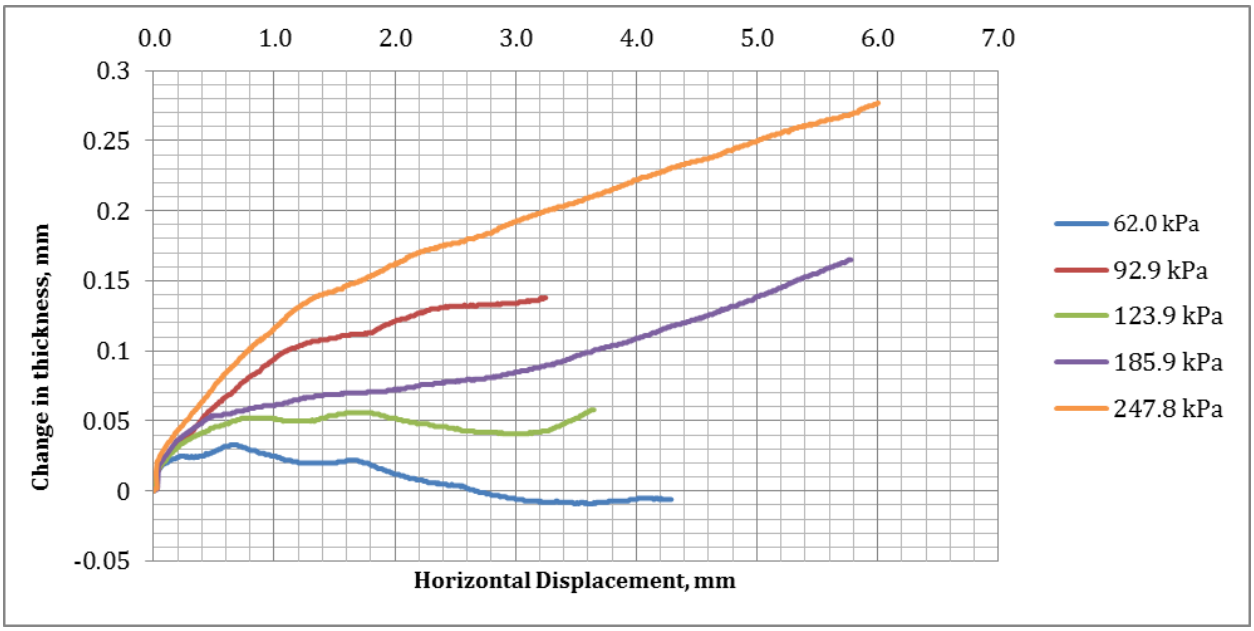

Figure A-6: Change in Thickness vs. Horizontal Displacement, χ_l = 4% (C)

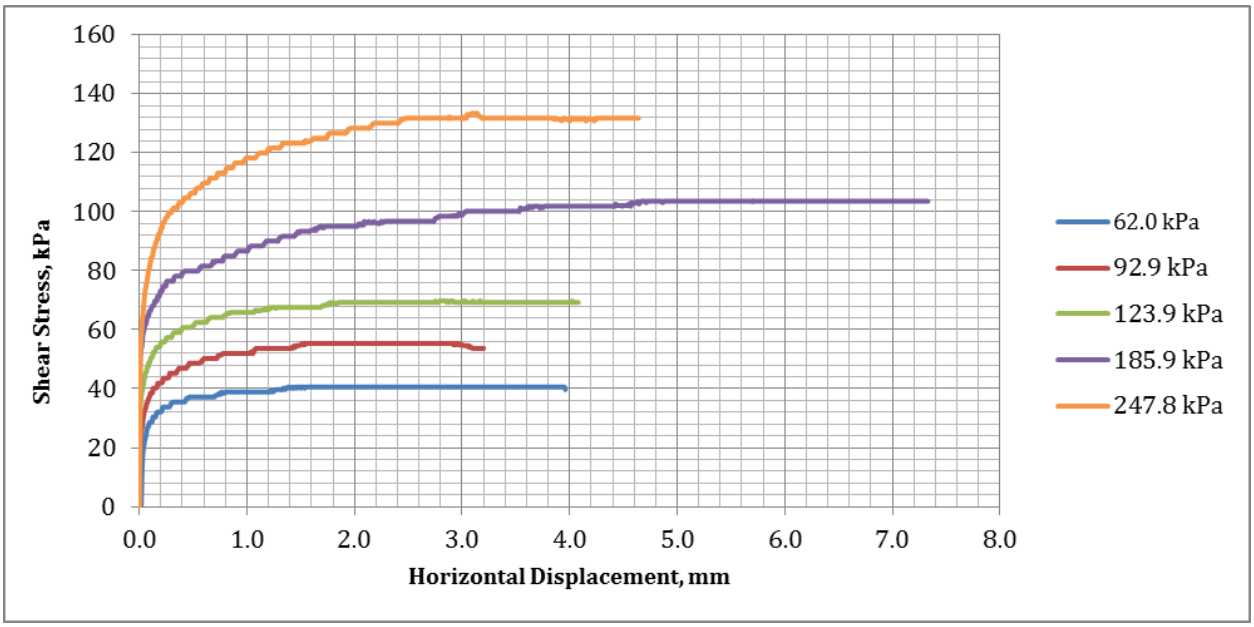

Figure A-7: Shear Stress vs. Horizontal Displacement, χ_I = 4% (D)

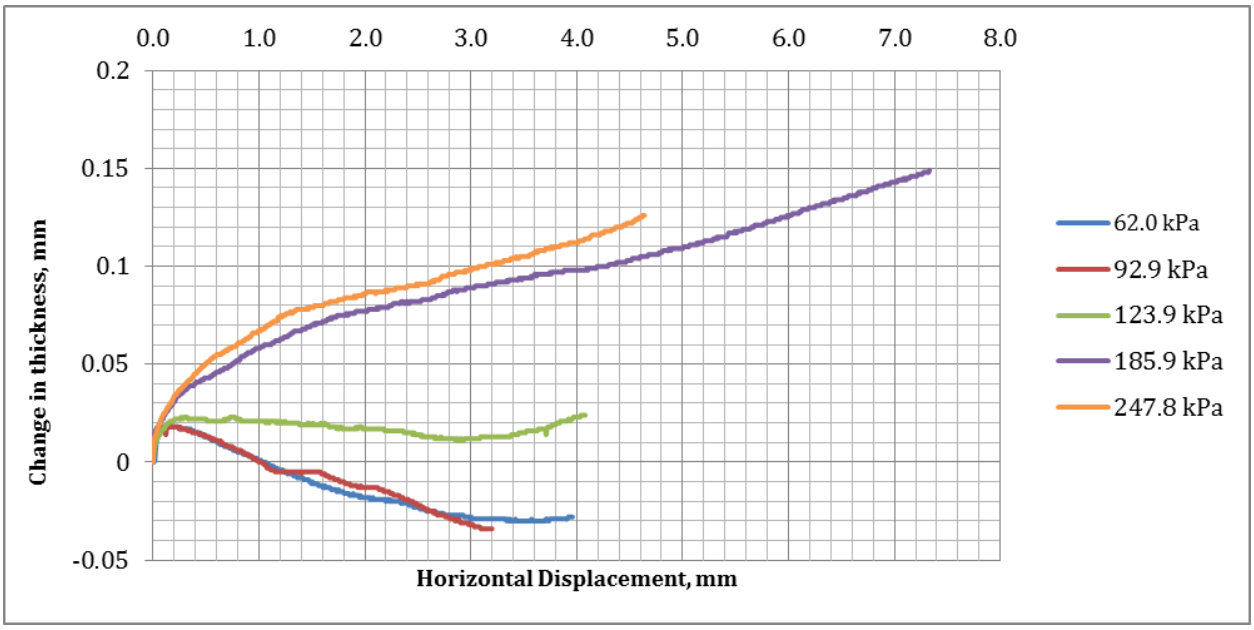

Figure A-8: Change in Thickness vs. Horizontal Displacement, χ_I = 4% (D)

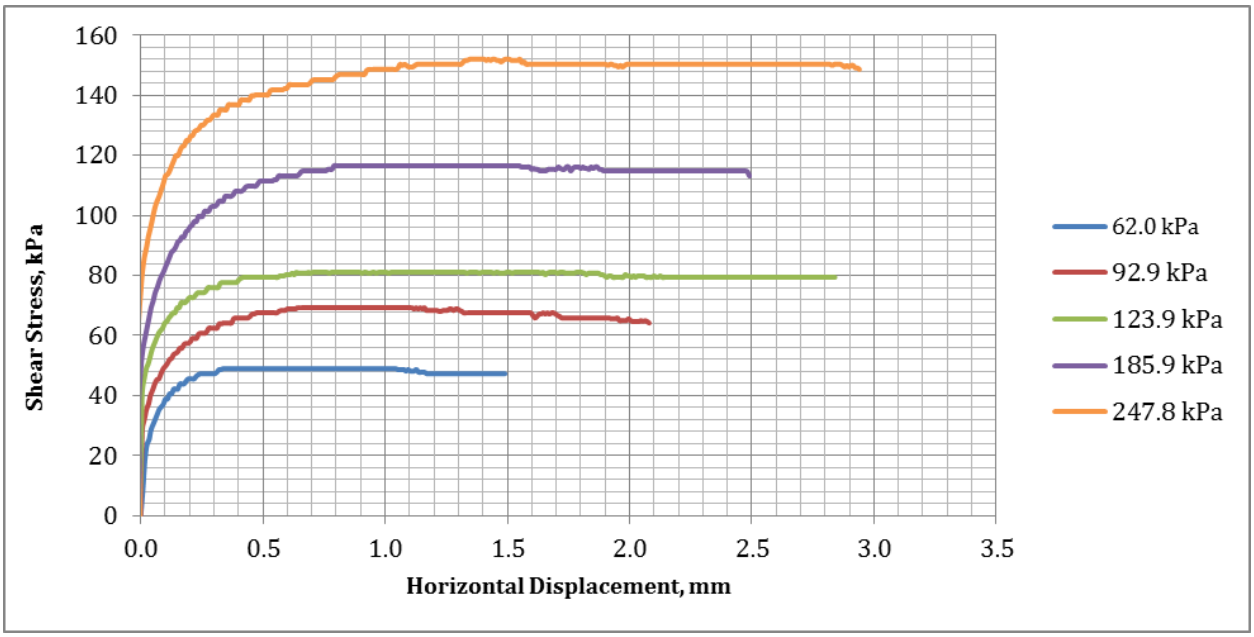

Figure A-9: Shear Stress vs. Horizontal Displacement, χ_I = 4% (B)

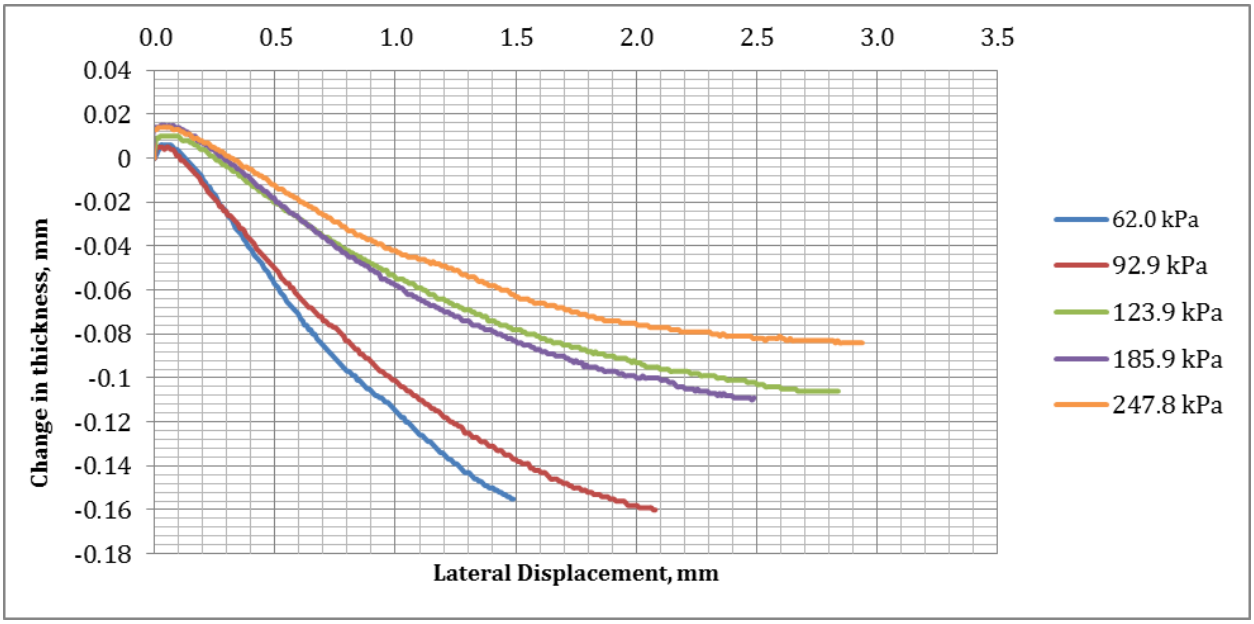

Figure A-10: Change in Thickness vs. Horizontal Displacement, χ_I = 4% (B)

A.1.2 Gravimetric Lignin Content (6%)

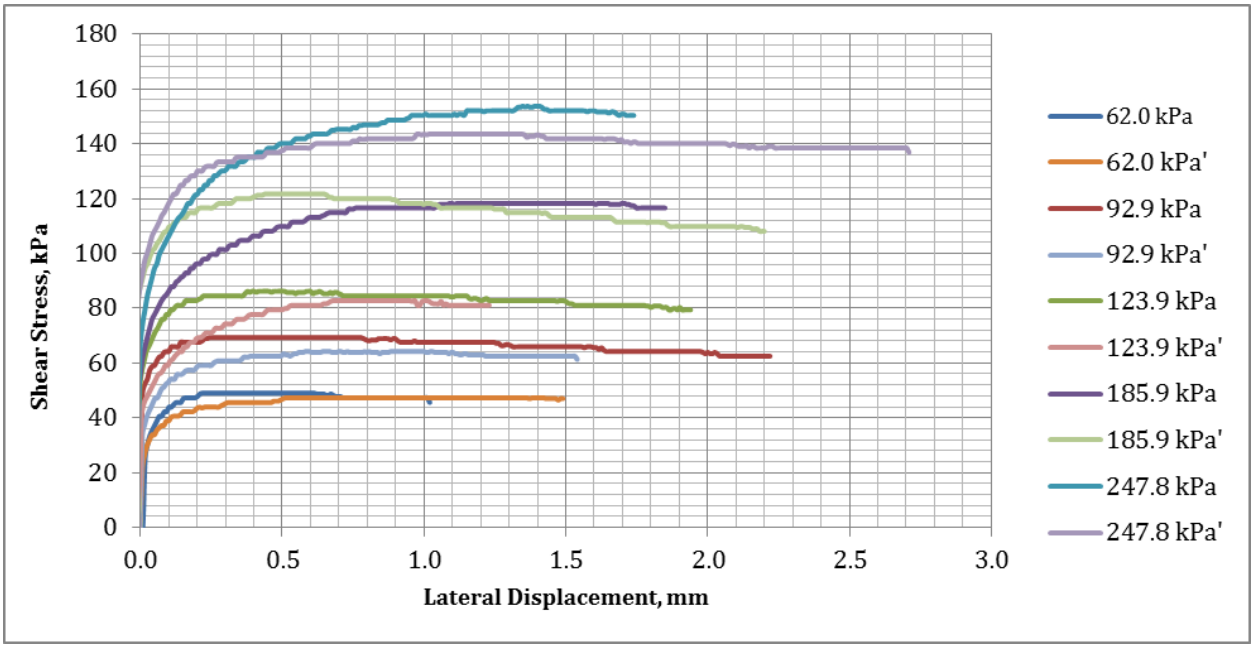

Figure A-11: Shear Stress vs. Horizontal Displacement, χ_l = 6% (A)

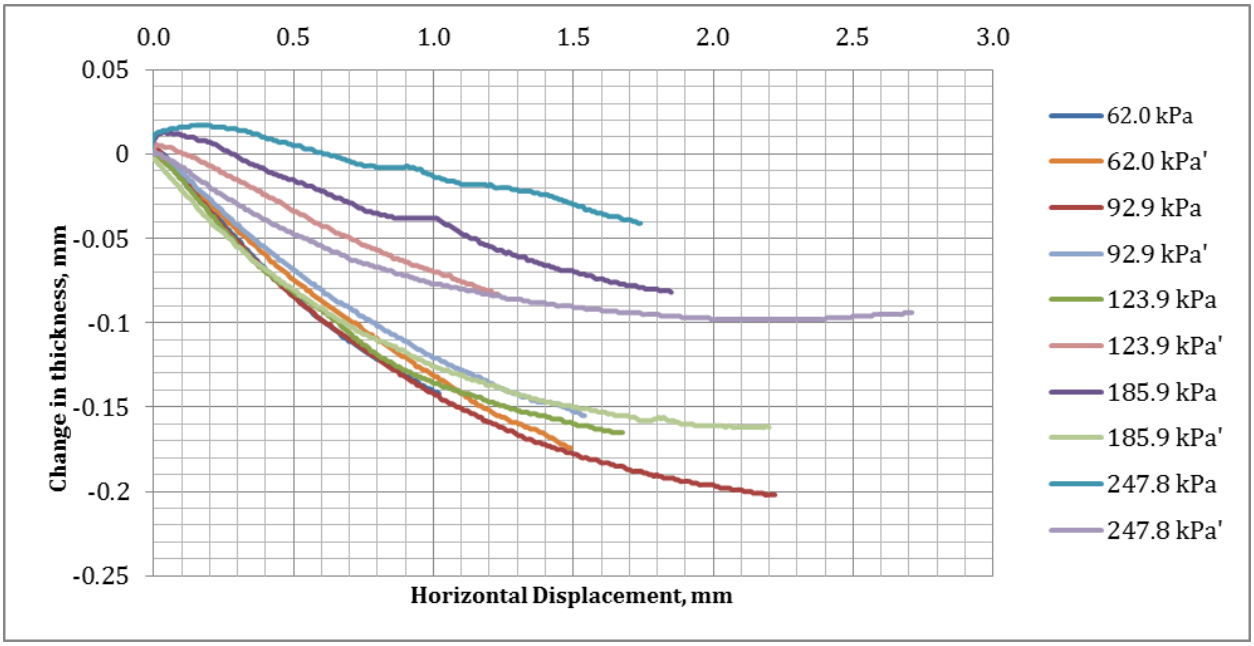

Figure A-12: Change in Thickness vs. Horizontal Displacement, χ_l = 6% (A)

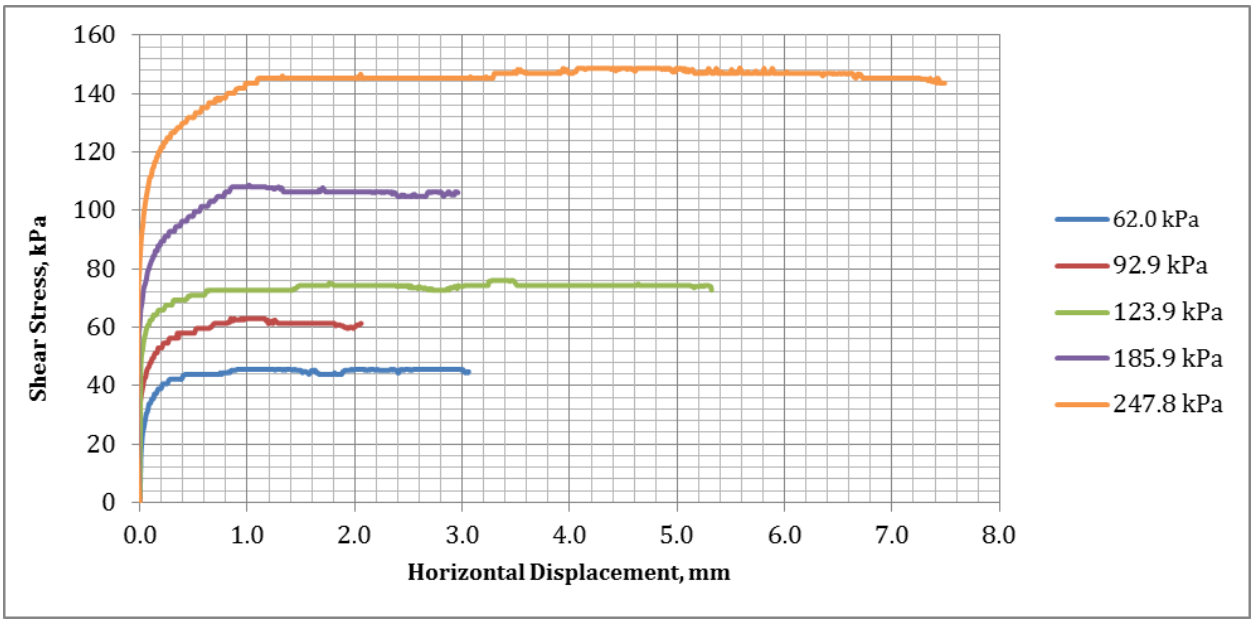

Figure A-13: Shear Stress vs. Horizontal Displacement, χ_I = 6% (E)

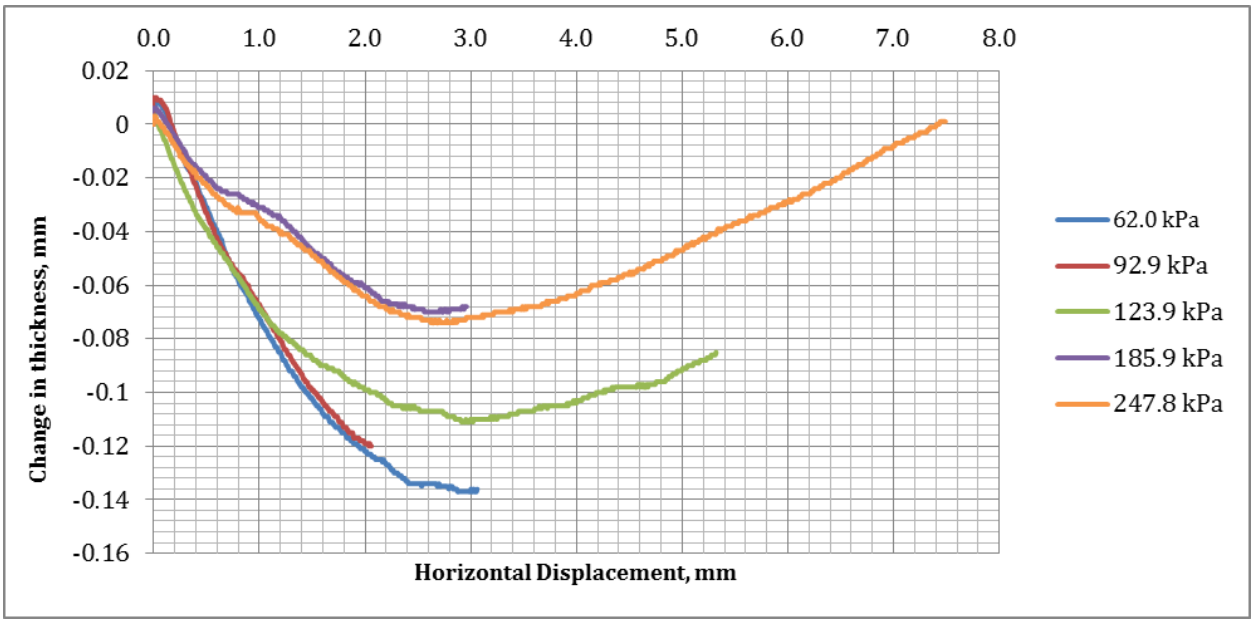

Figure A-14: Change in Thickness vs. Horizontal Displacement, χ_I = 6% (E)

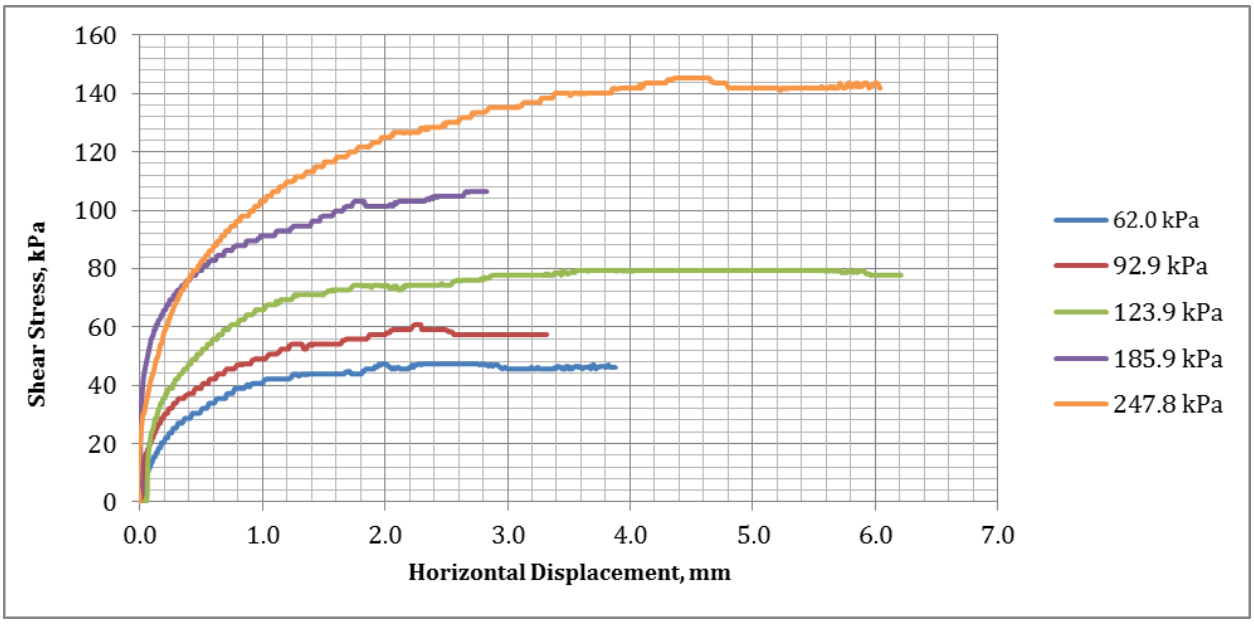

Figure A-15: Shear Stress vs. Horizontal Displacement, χ_l = 6% (C)

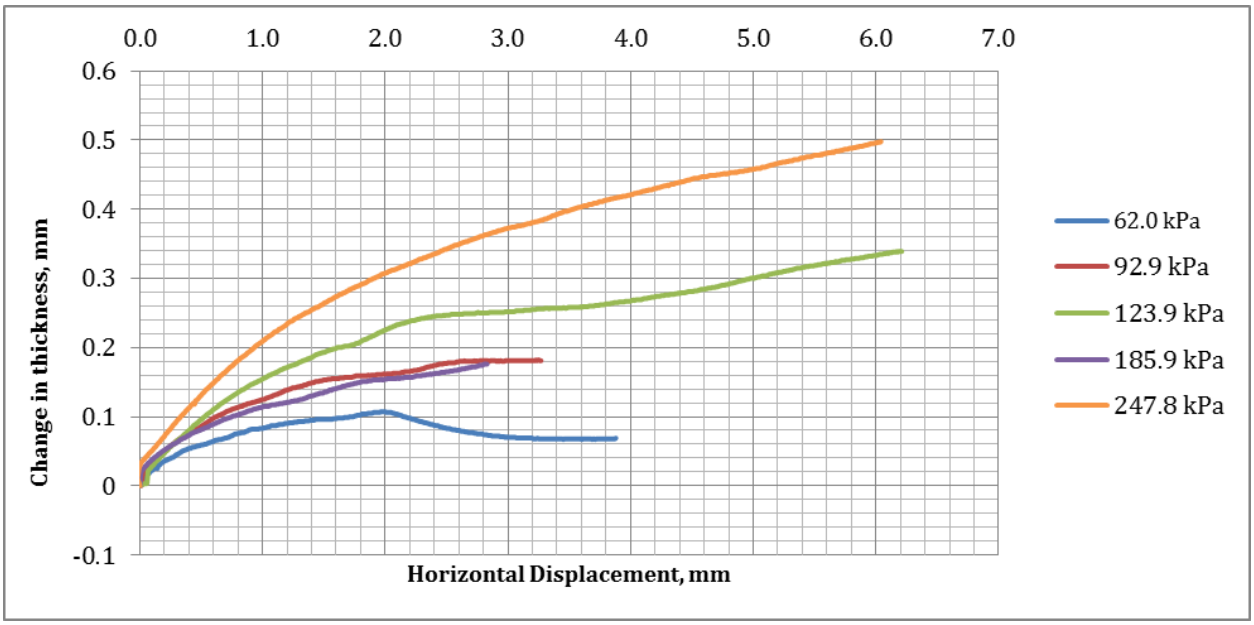

Figure A-16: Change in Thickness vs. Horizontal Displacement, χ_l = 6% (C)

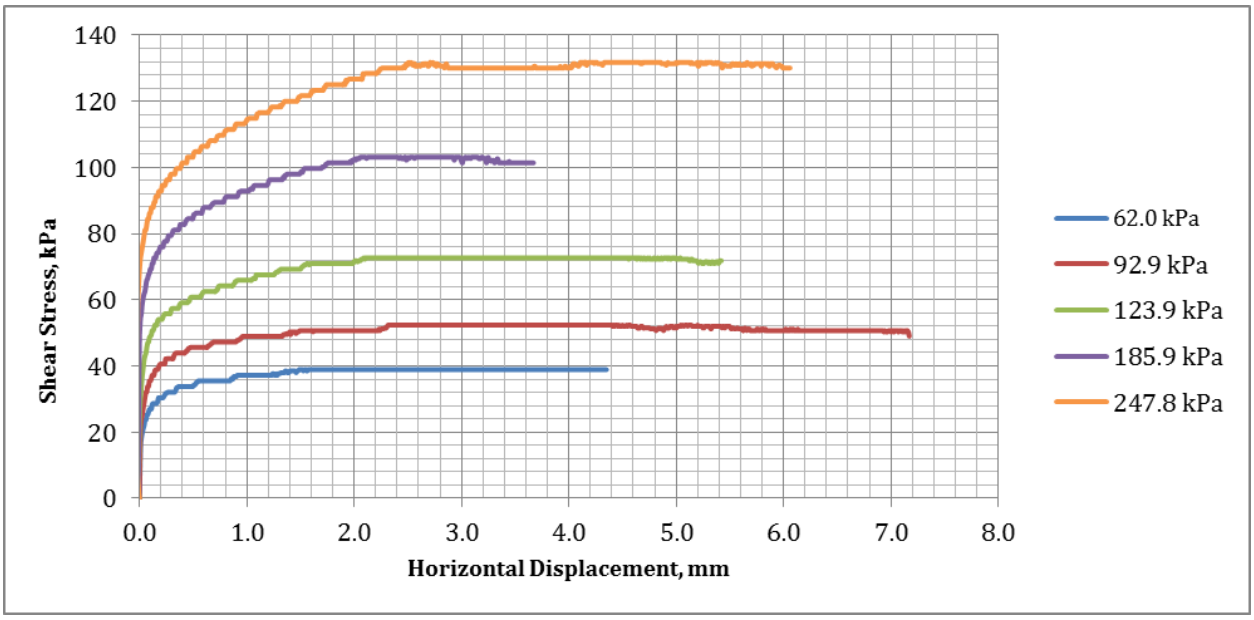

Figure A-17: Shear Stress, vs. Horizontal Displacement, χ_1 = 6% (D)

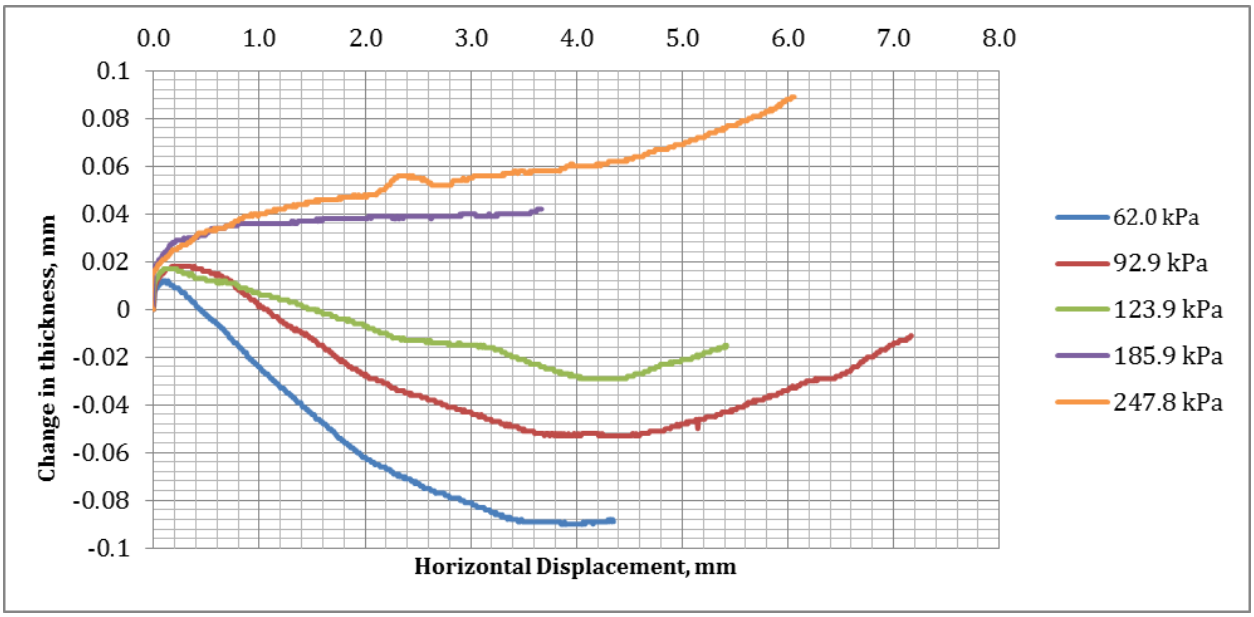

Figure A-18: Change in Thickness vs. Horizontal Displacement, χ_1 = 6% (D)

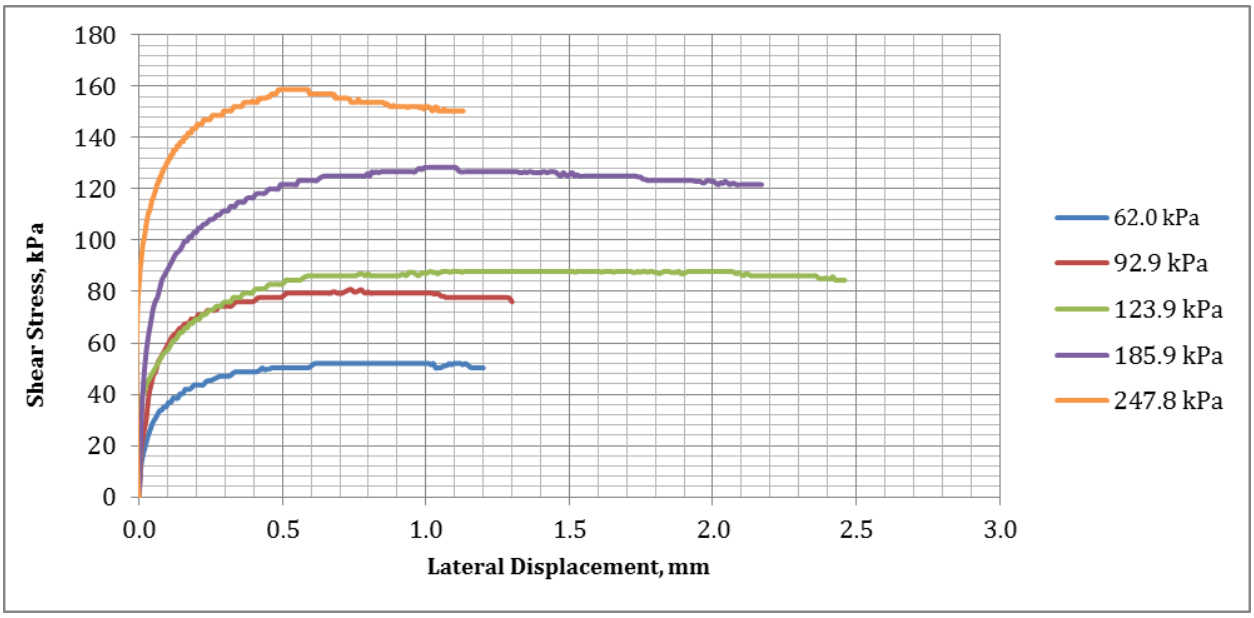

Figure A-19: Shear Stress vs. Horizontal Displacement, χ_I = 6% (B)

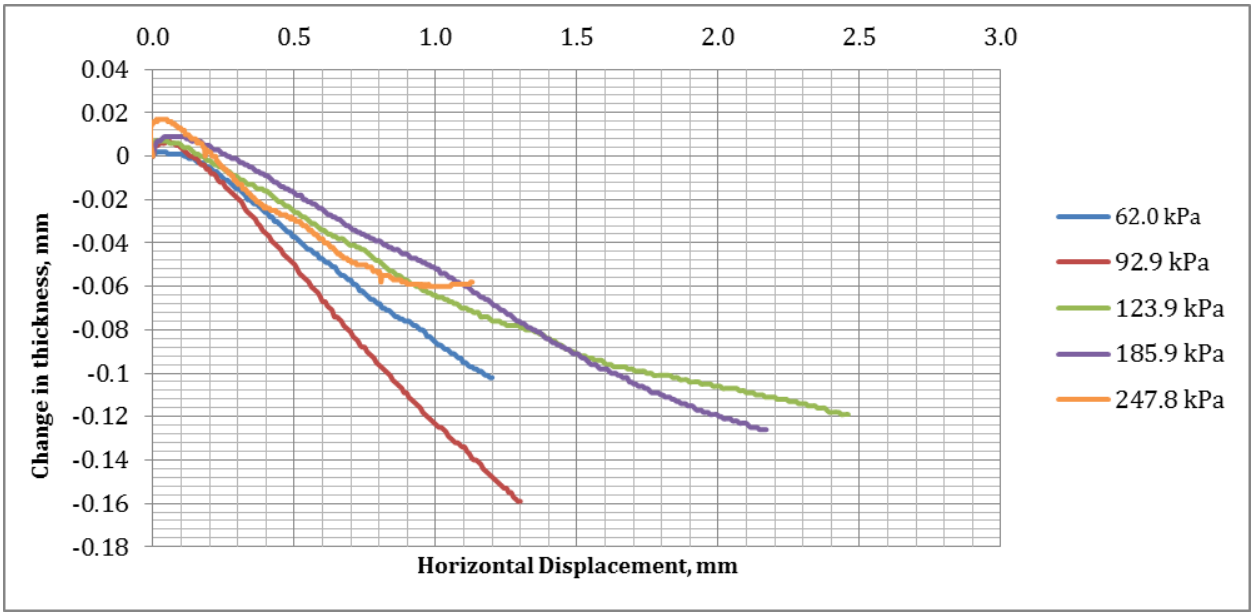

Figure A-20: Change in Thickness vs. Horizontal Displacement, χ_I = 6% (B)

Appendix B - Additional Direct Shear Analysis Plots

B.1.1 Analysis Plots for Determination of c and Φ

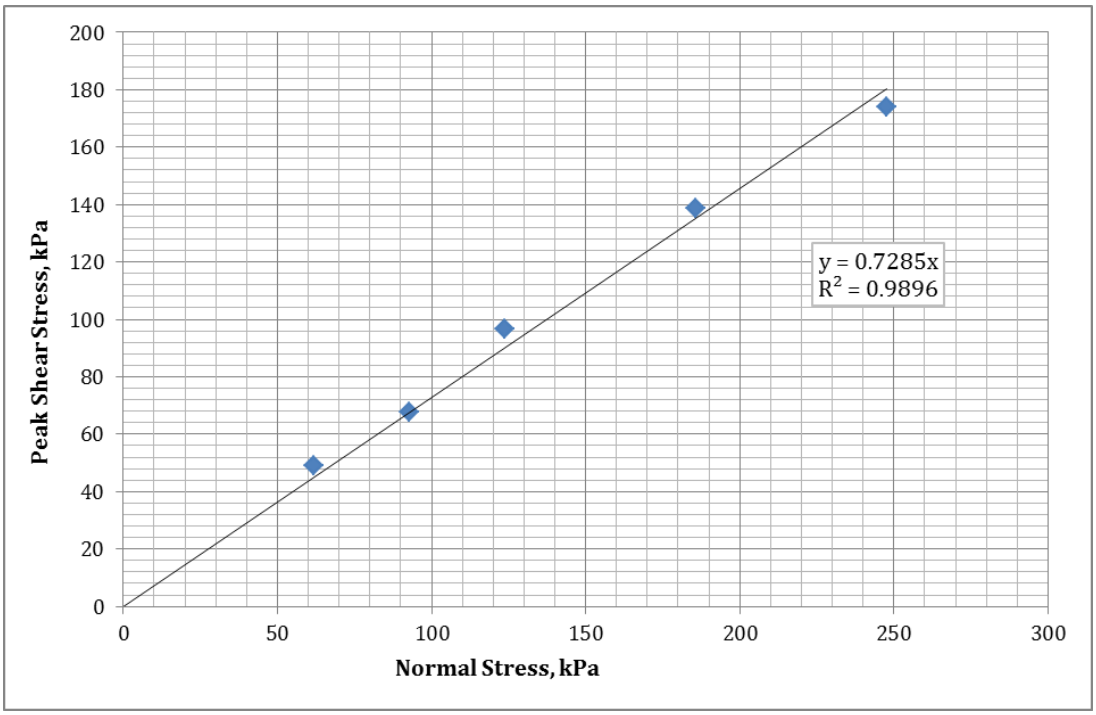

Figure B-21: Plot of Normal Stress v. Peak Stress for χ_I = 0% (A

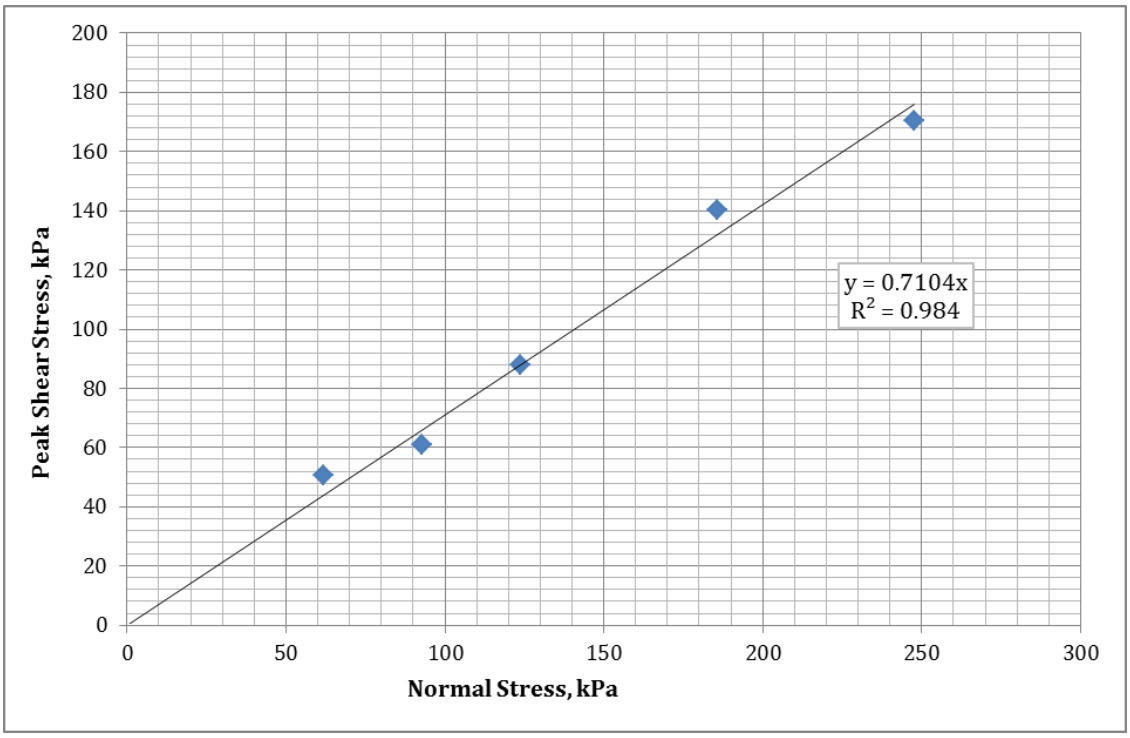

Figure B-22: Plot of Normal Stress v. Peak Stress for χ_I = 0% (E)

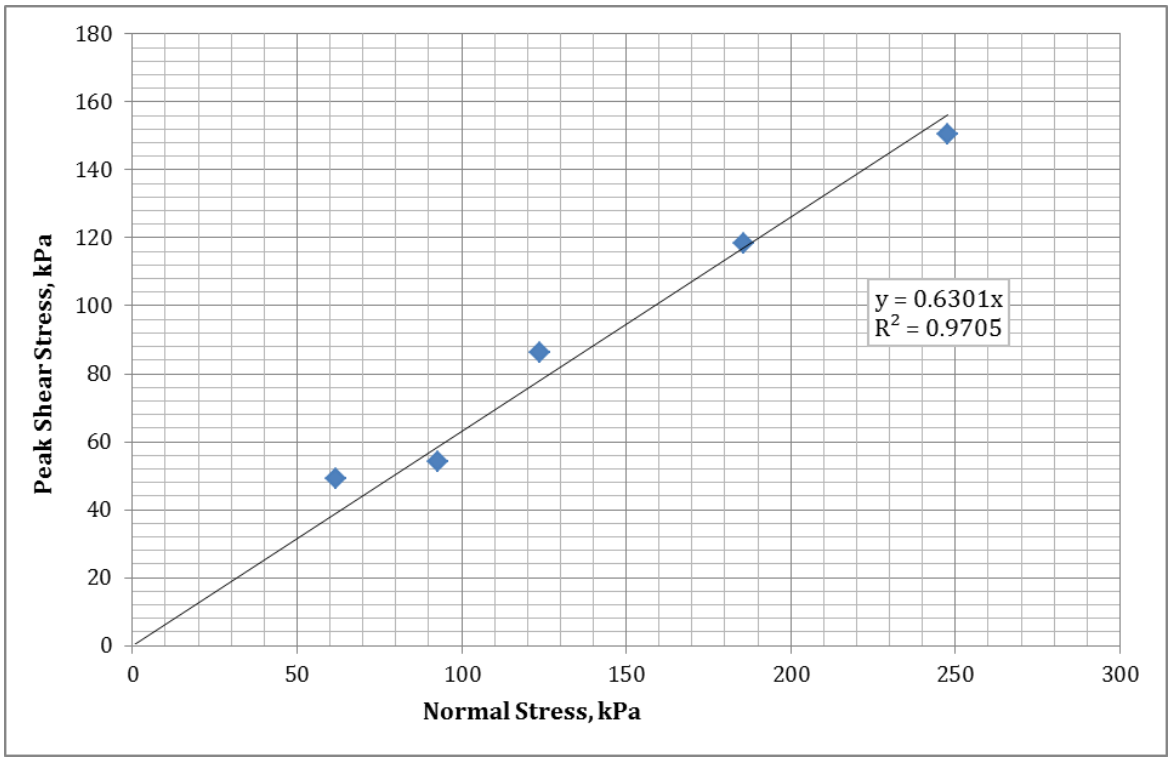

Figure B-3: Plot of Normal Stress v. Peak Stress for χ_I = 0% (C)

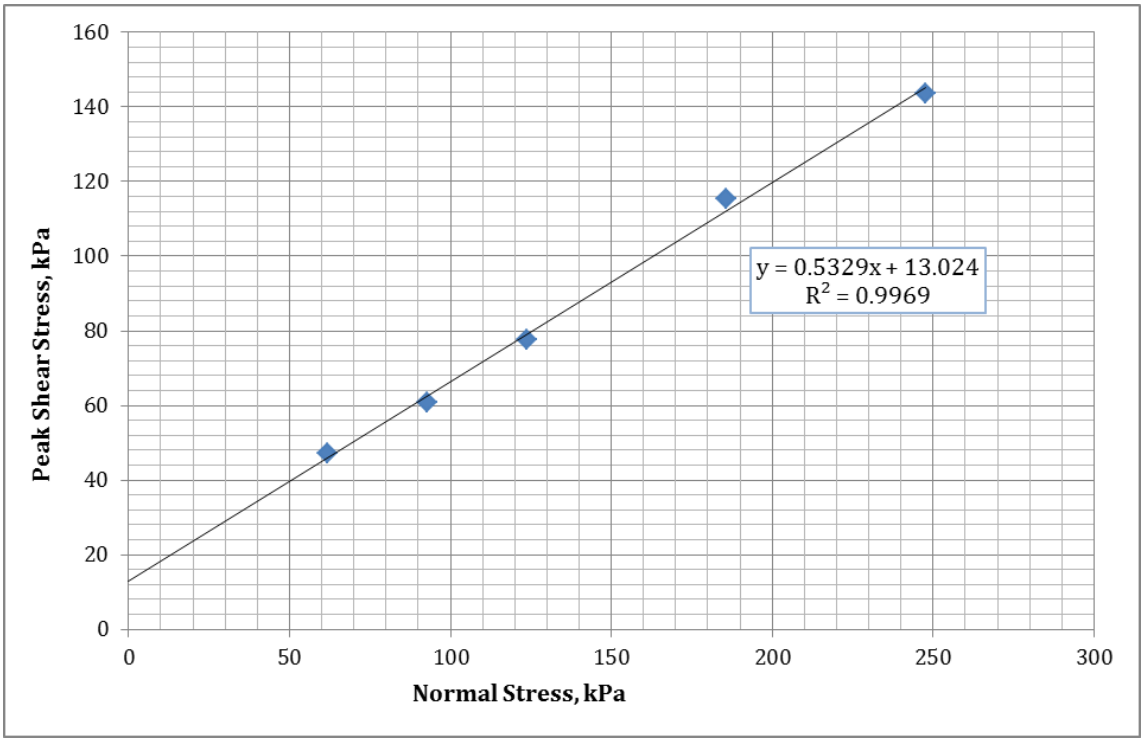

Figure B-4: Plot of Normal Stress v. Peak Stress for χ_I = 2% (A)

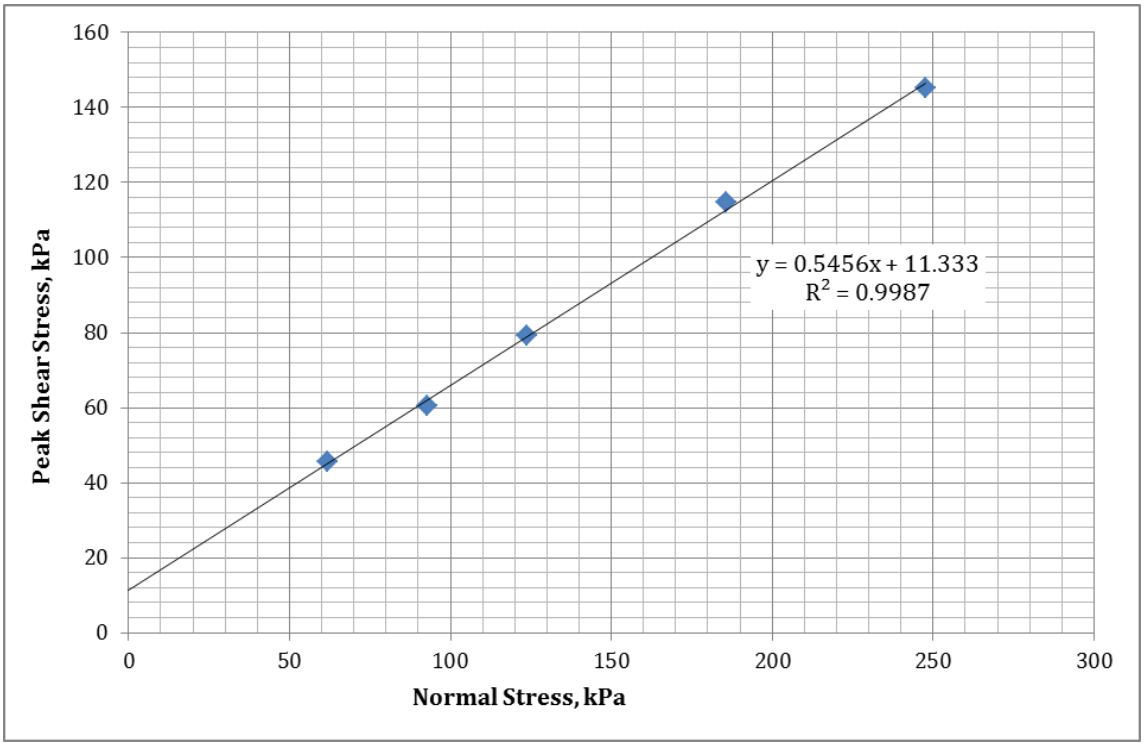

Figure B-23: Plot of Normal Stress v. Peak Stress for χ_I = 2% (E)

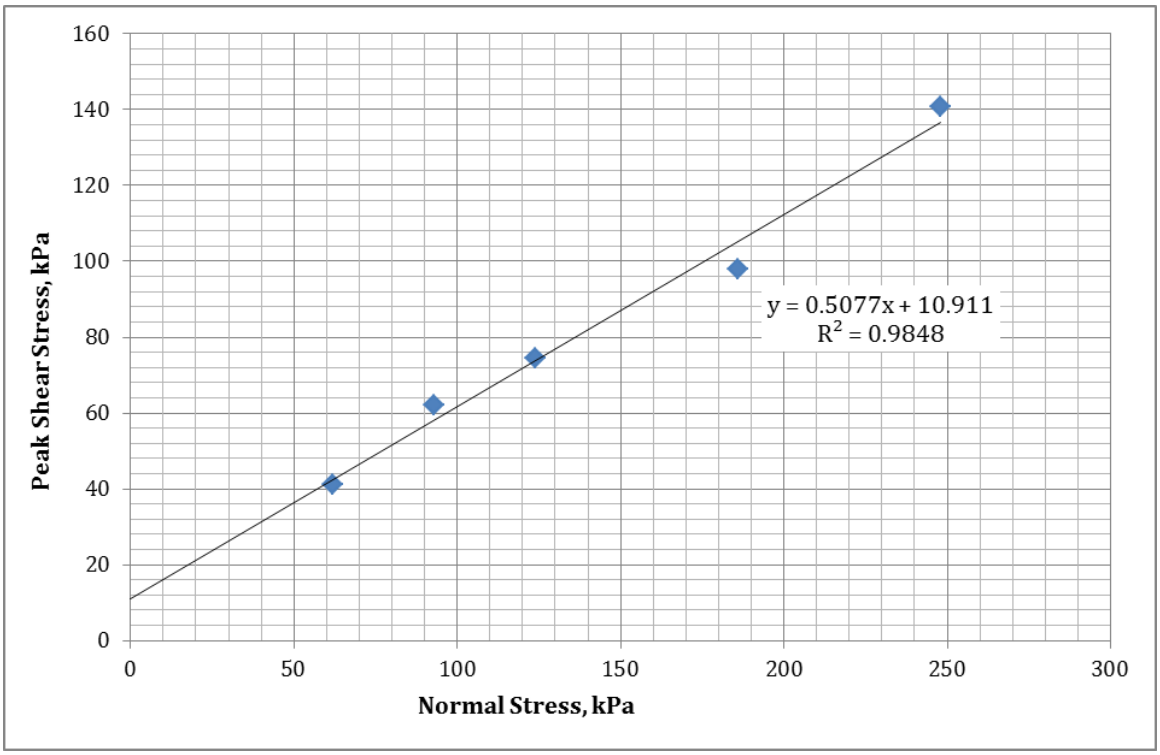

Figure B-24: Plot of Normal Stress v. Peak Stress for χ_I = 2% (C)

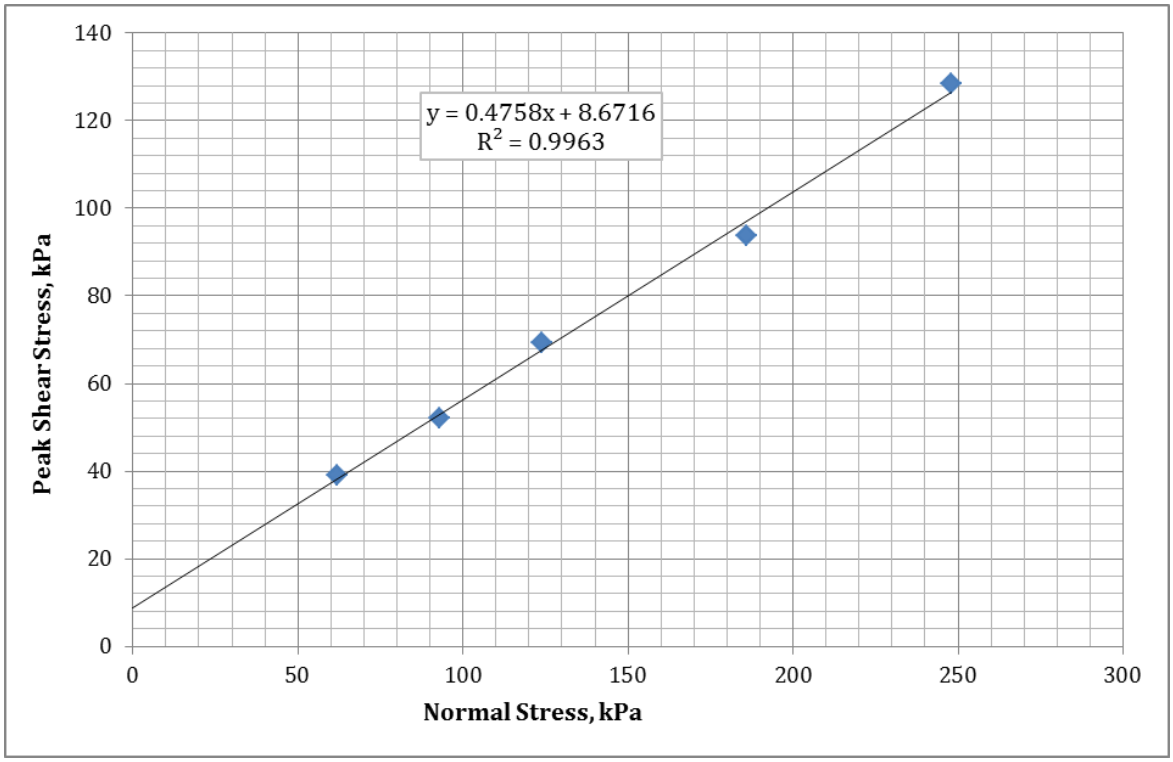

Figure B-25: Plot of Normal Stress v. Peak Stress for χ_I = 2% (D)

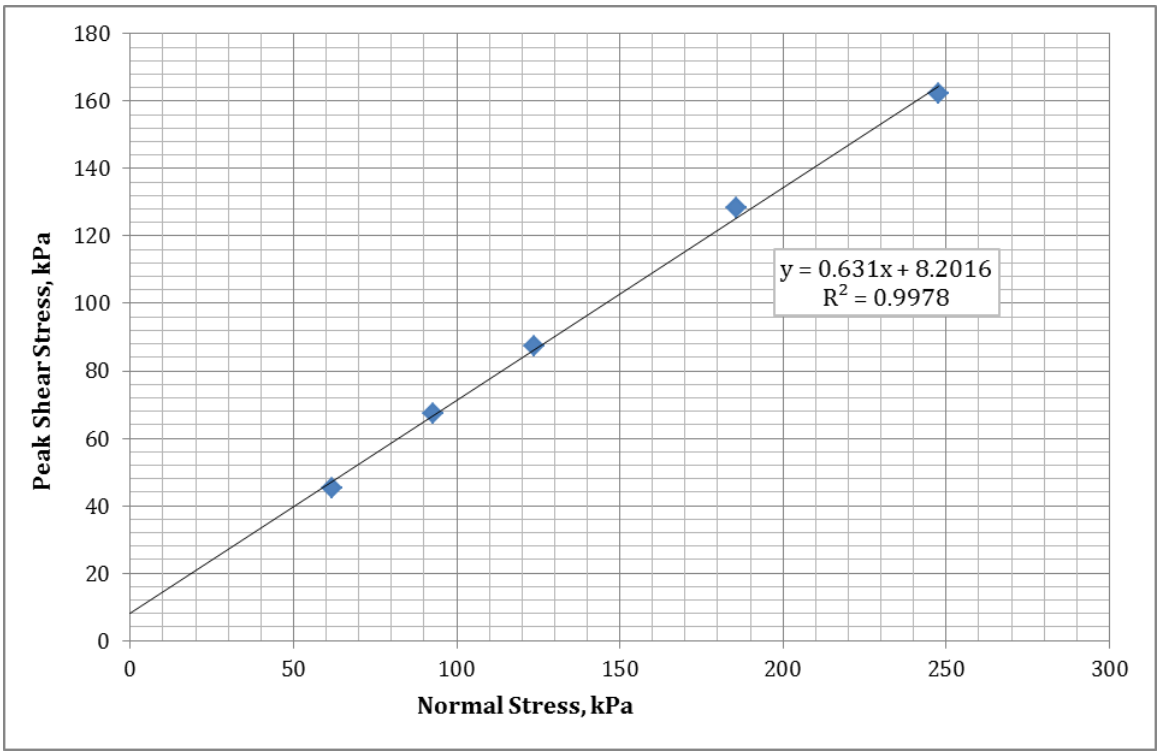

Figure B-26: Plot of Normal Stress v. Peak Stress for χ_I = 2% (B)

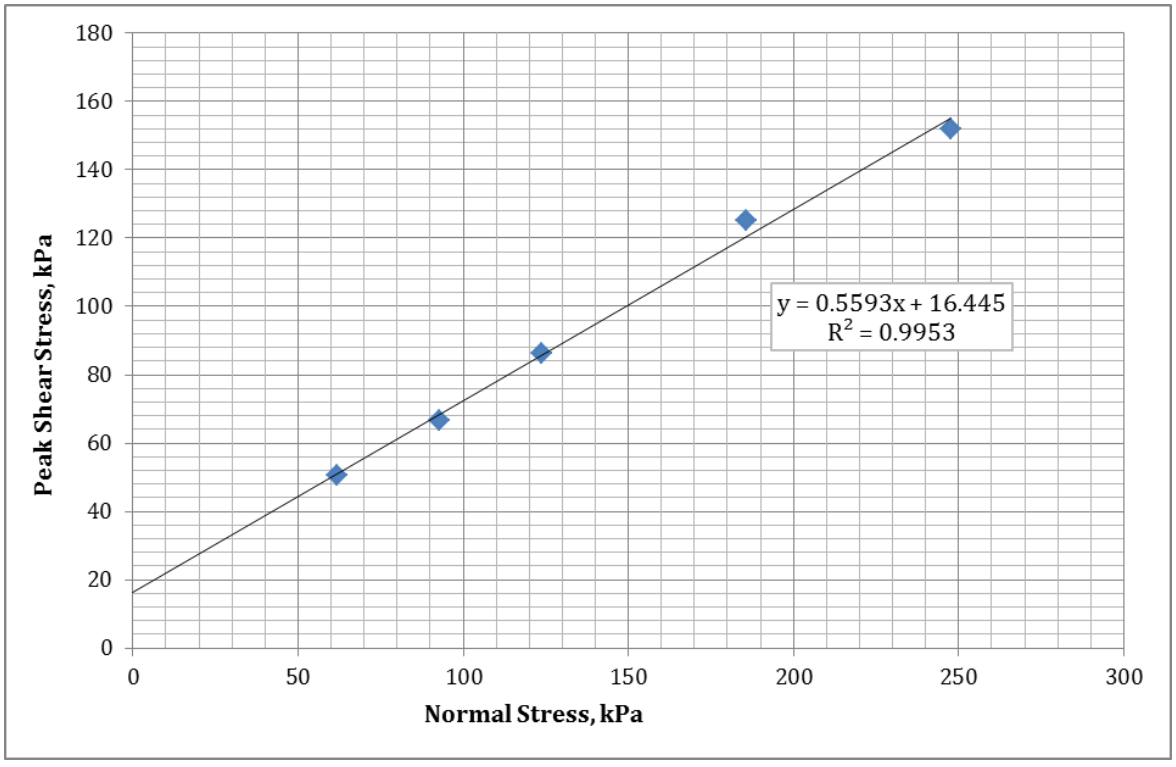

Figure B-27: Plot of Normal Stress v. Peak Stress for χ_I = 4% (A)

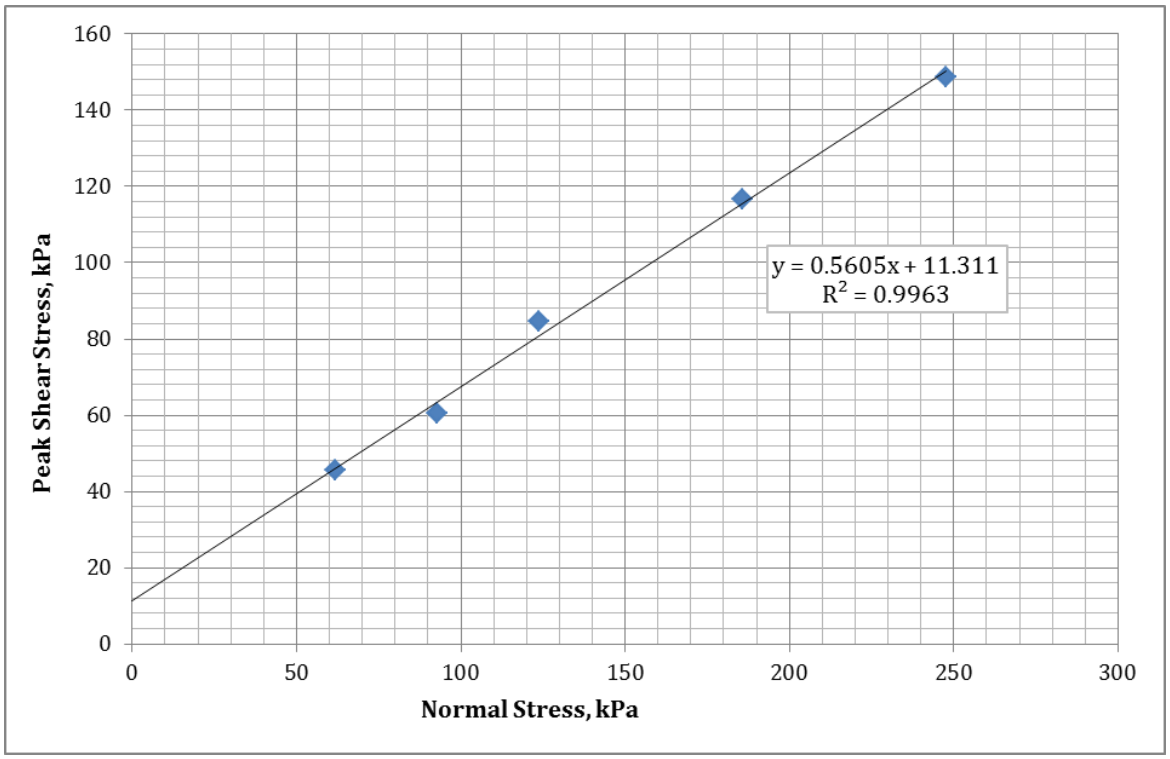

Figure B-28: Plot of Normal Stress v. Peak Stress for χ_I = 4% (E)

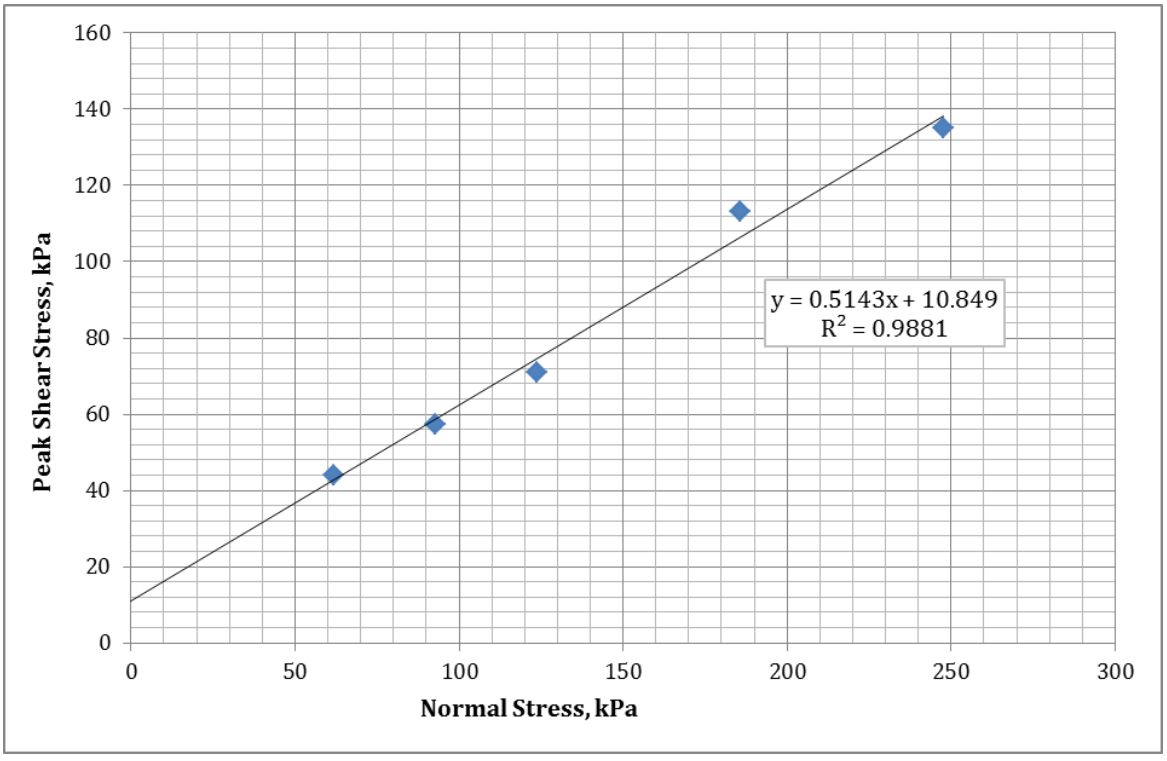

Figure B-29: Plot of Normal Stress v. Peak Stress for χ_I = 4% (C)

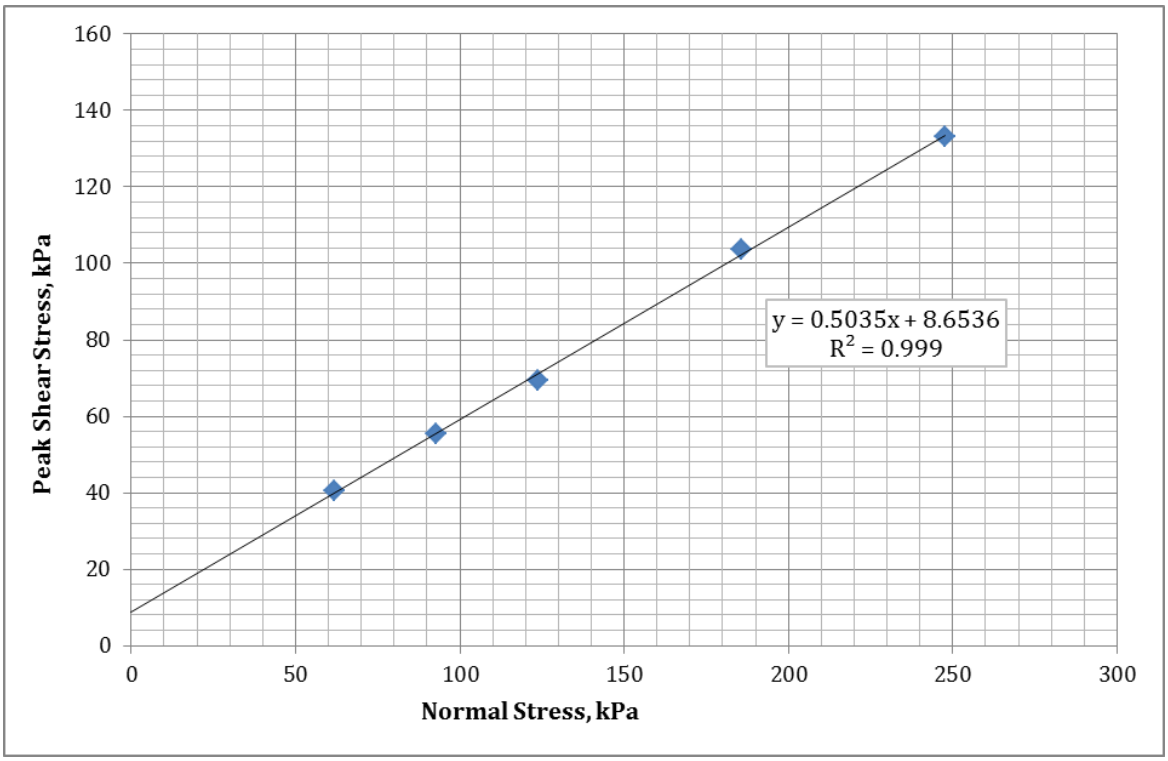

Figure B-30: Plot of Normal Stress v. Peak Stress for χ_I = 4% (D)

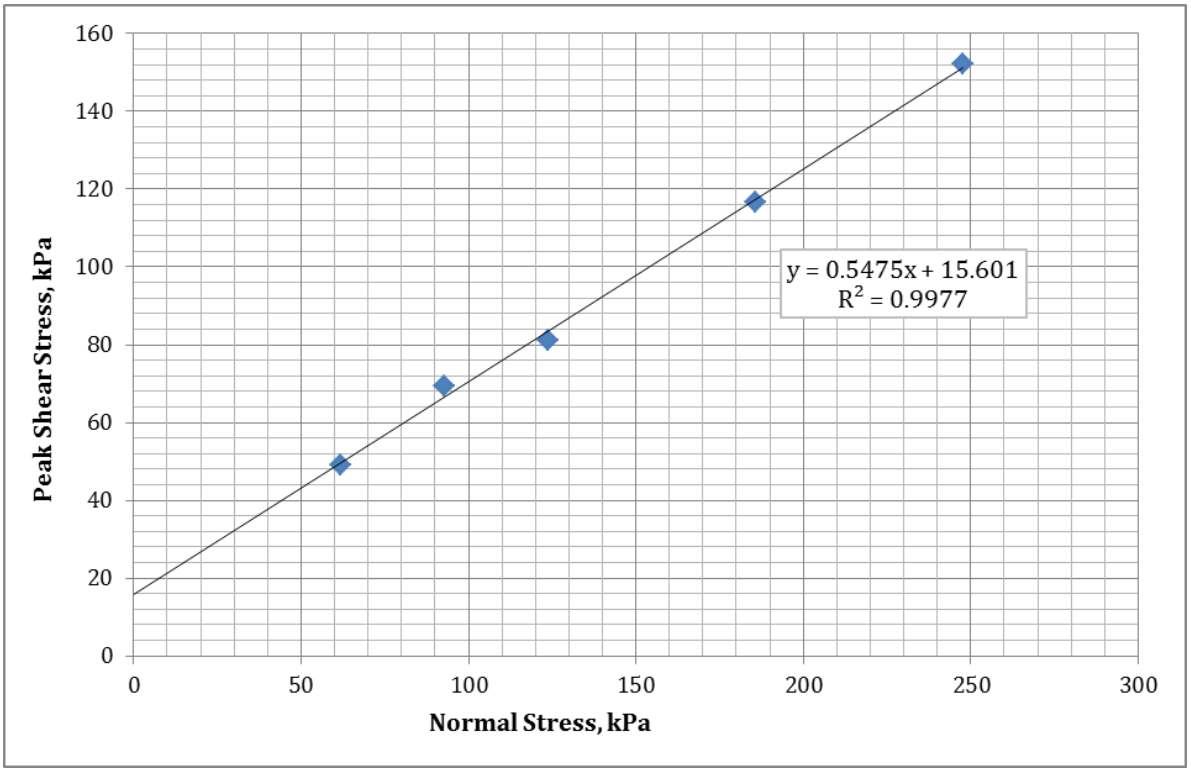

Figure B-31: Plot of Normal Stress v. Peak Stress for χ_I = 4% (B)

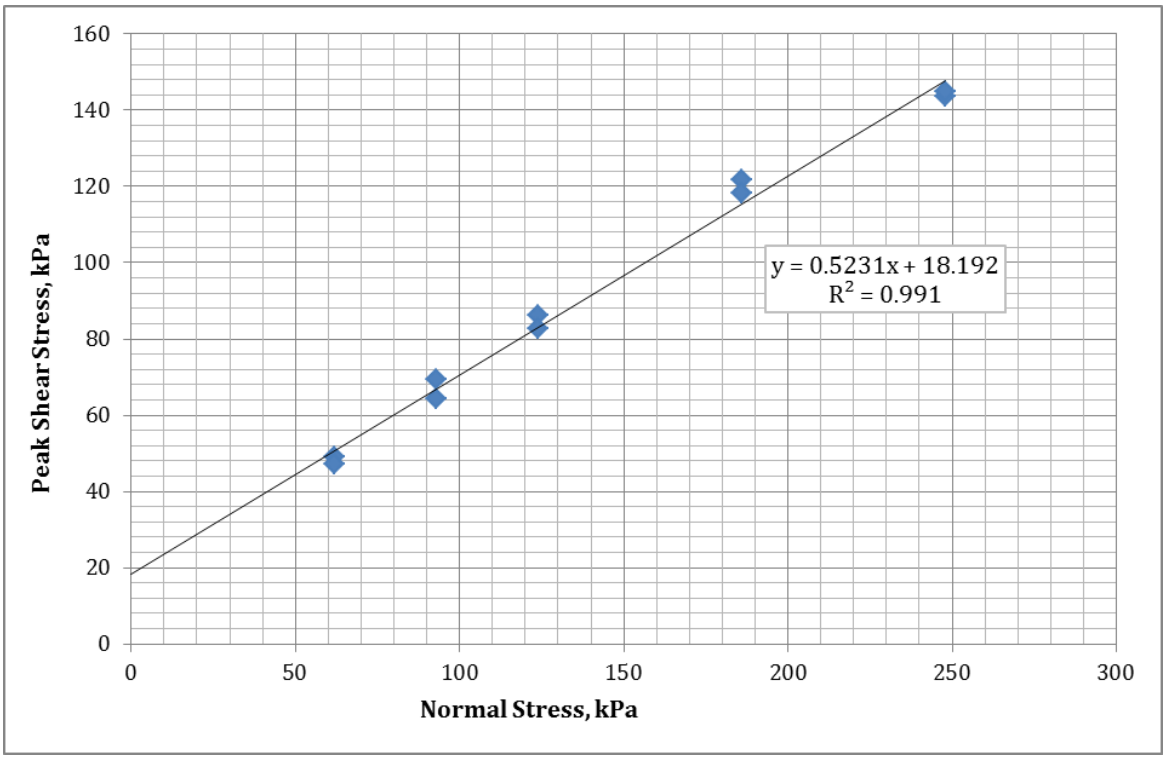

Figure B-32: Plot of Normal Stress v. Peak Stress for χ_l = 6% (A)

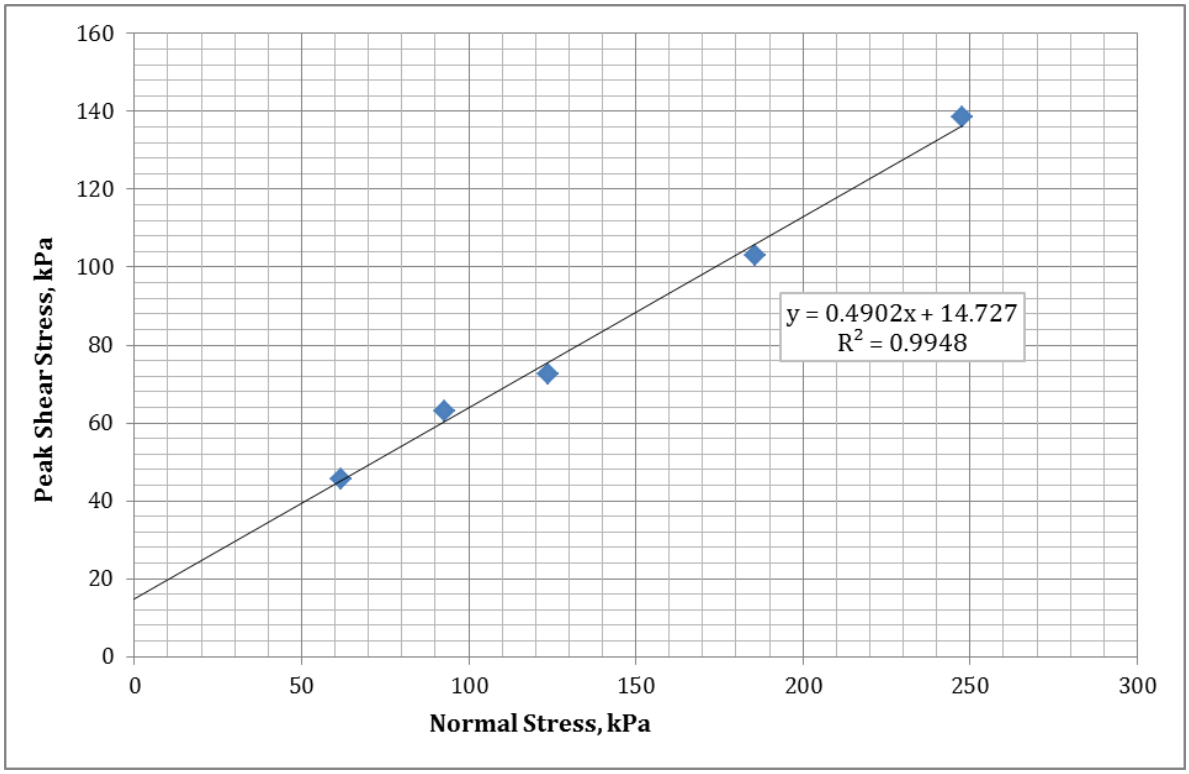

Figure B-33 Plot of Normal Stress v. Peak Stress for χ_l = 6% (E)

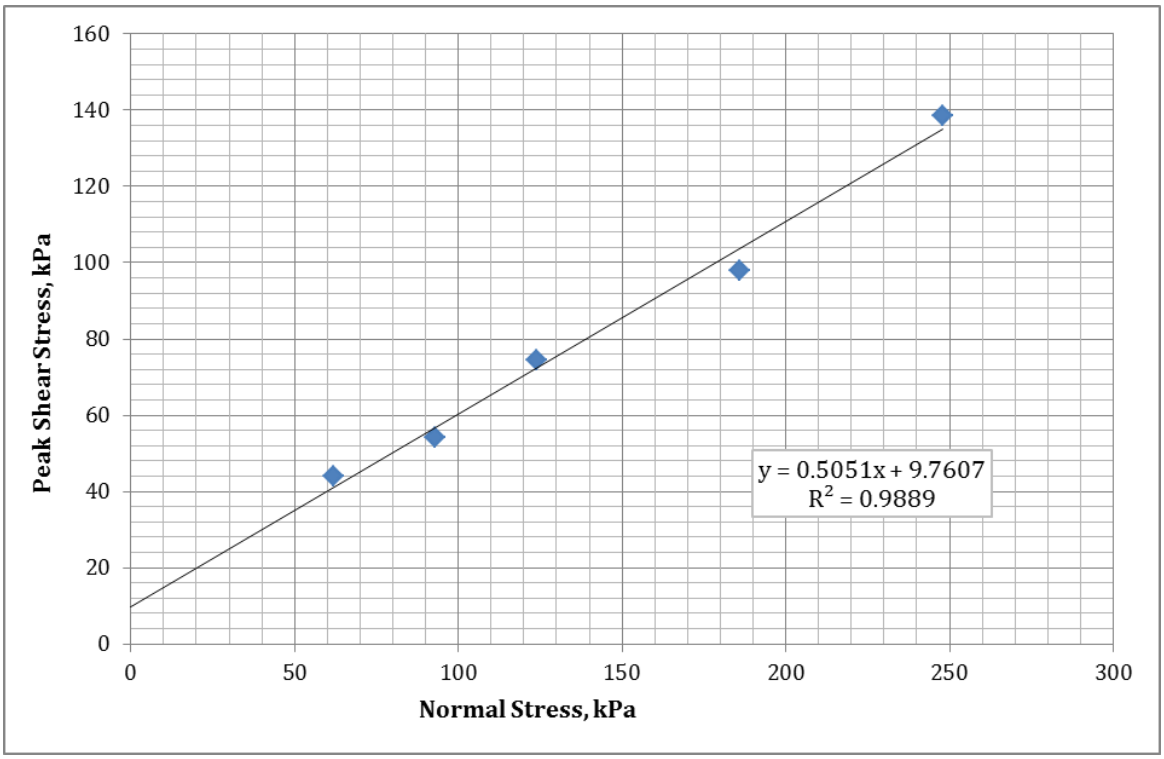

Figure B-34: Plot of Normal Stress v. Peak Stress for χ_I = 6% (C)

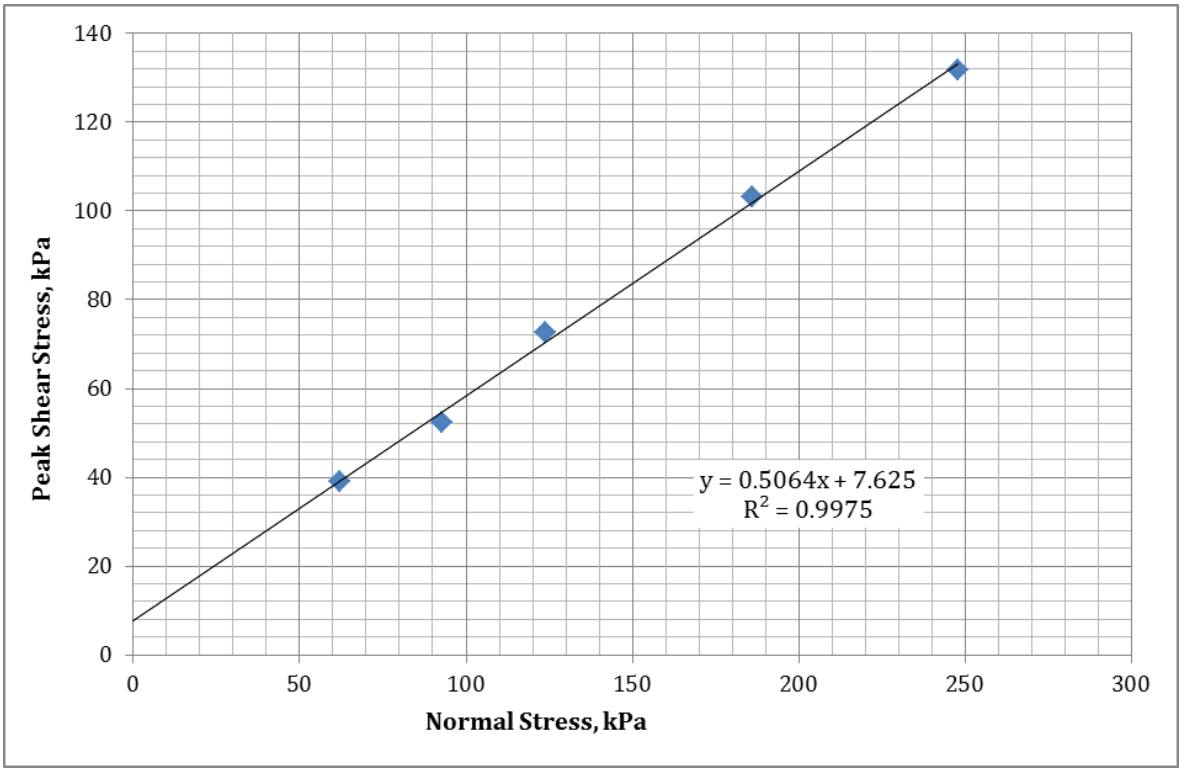

Figure B-35: Plot of Normal Stress v. Peak Stress for χ_I = 6% (D)

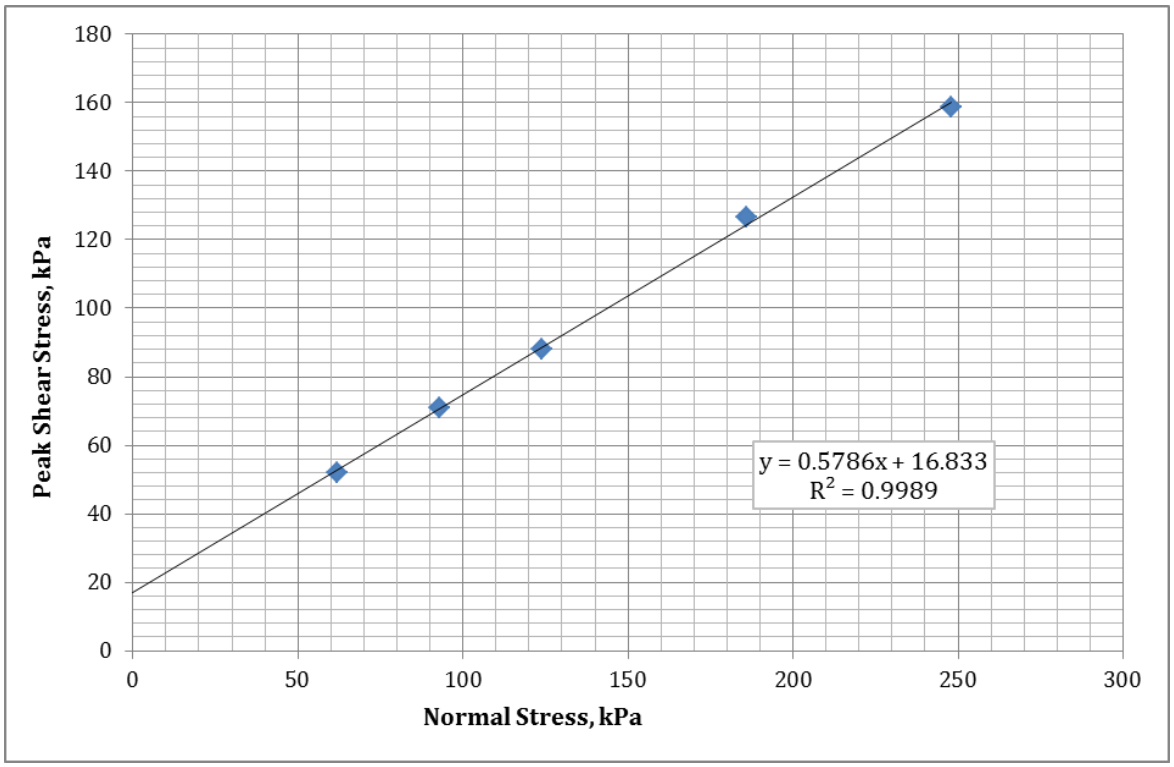

Figure B-36: Plot of Normal Stress v. Peak Stress for χ_I = 6% (B)

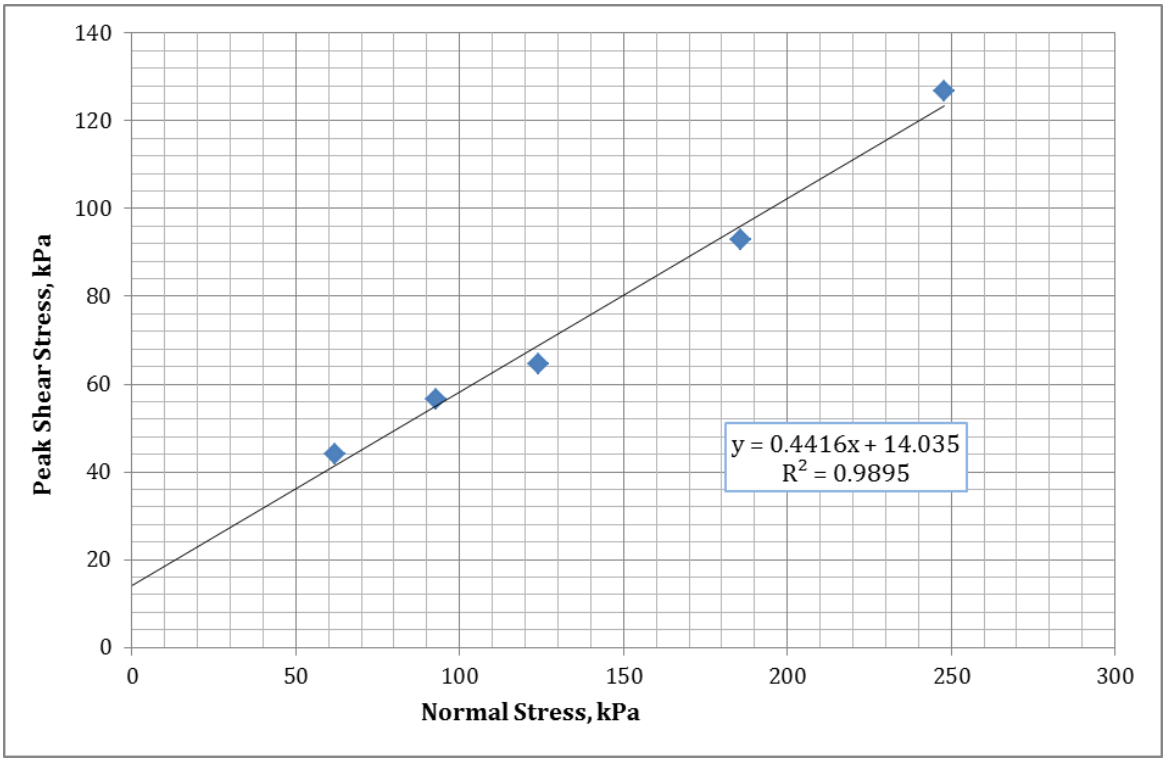

Figure B-37: Plot of Normal Stress v. Peak Stress for χ_I = 14% (A)

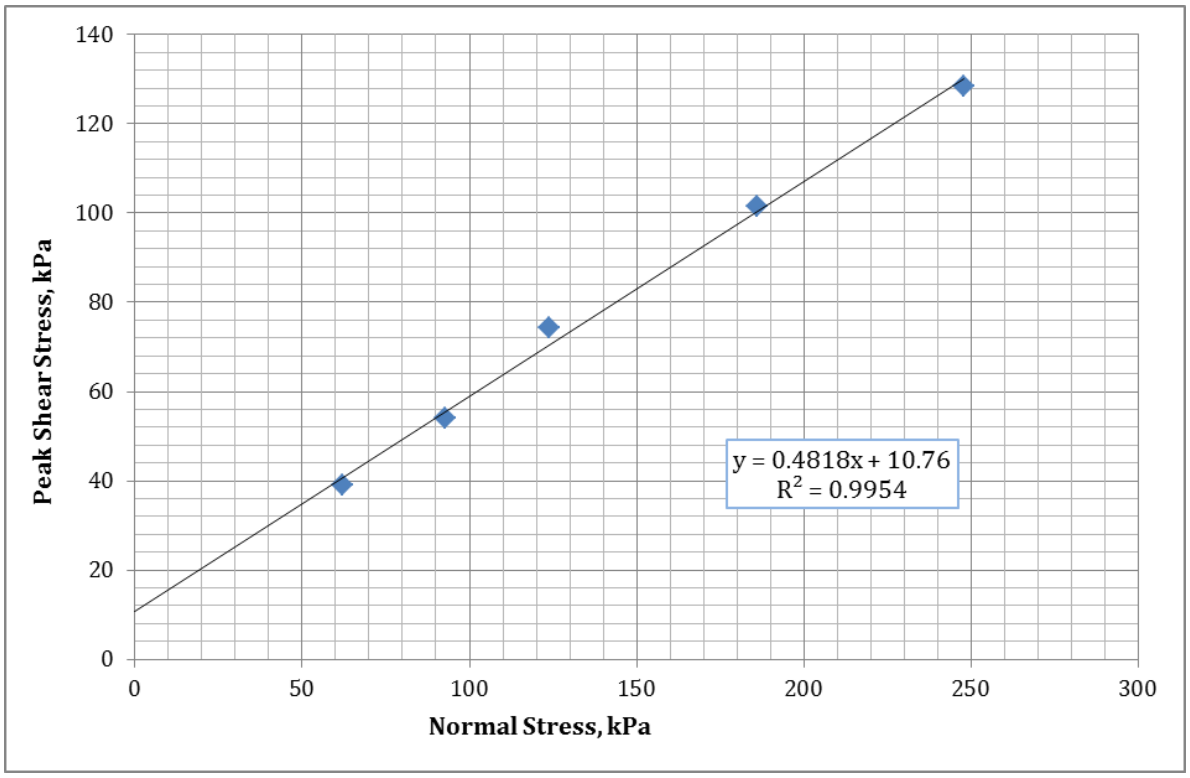

Figure B-20: Plot of Normal Stress v. Peak Stress for χ_I = 14% (E)

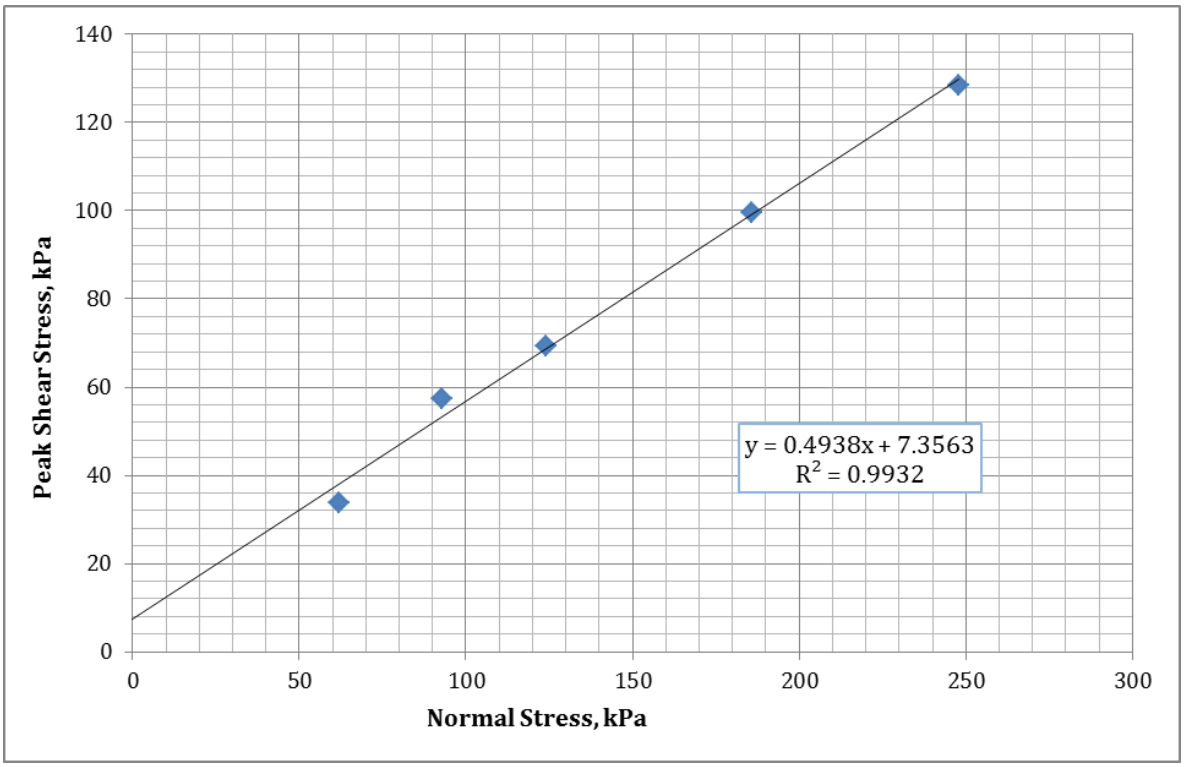

Figure B-21: Plot of Normal Stress v. Peak Stress for χ_I = 14% (C)

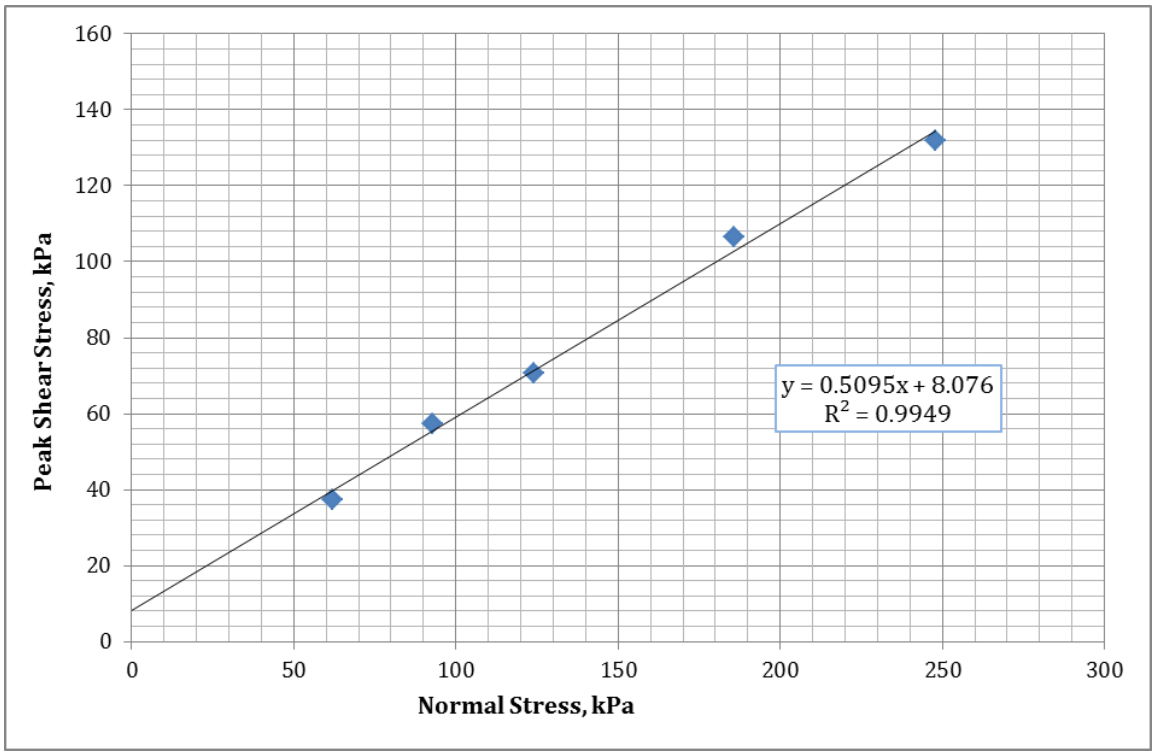

Figure B-38: Plot of Normal Stress v. Peak Stress for χ_I = 14% (D)

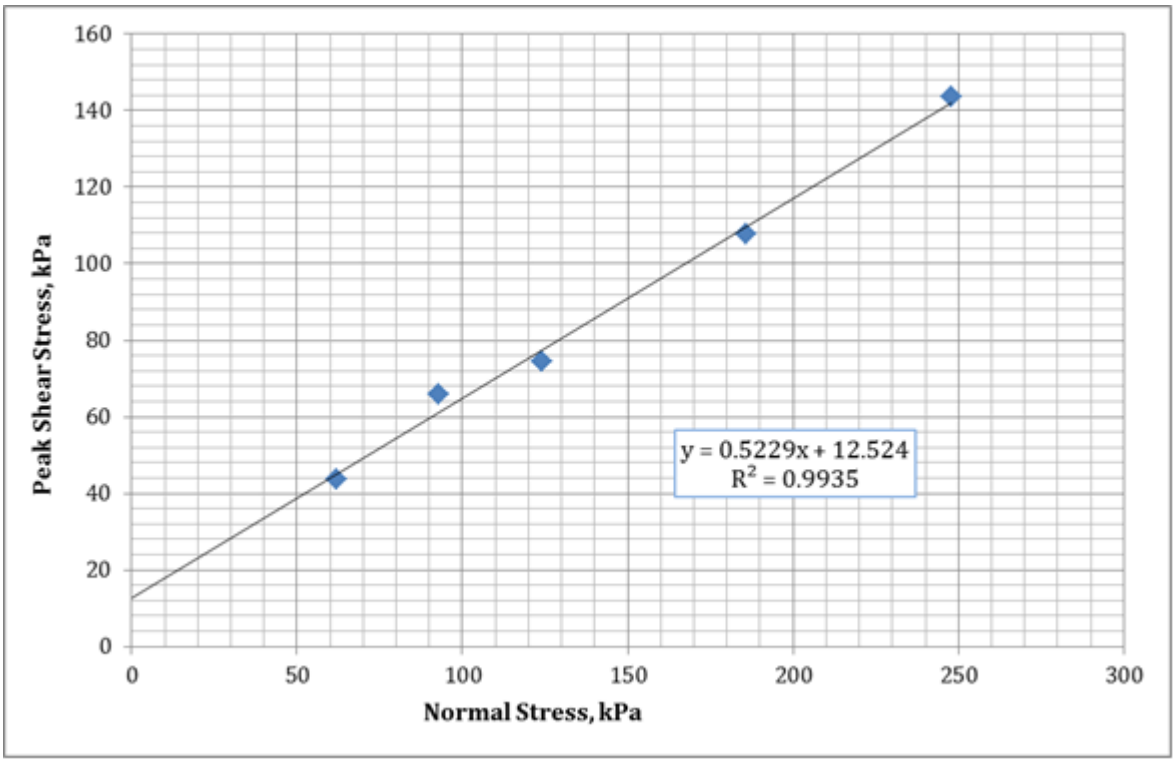

Figure B-39: Plot of Normal Stress v. Peak Stress for χ_I = 14% (B)